The University Of Sheffield.

FABRICATION AND CHARACTERISATION OF NOVEL POLYMERIC AND COLLOIDAL FILMS FOR REFLECTIVE AND ANTI-REFLECTIVE COATINGS

Mahmoud Abdelhafiz Mahmoud Mohamed

Presented for the degree of Doctor of Philosophy
Department of Chemical and Biological Engineering

The University of Sheffield

December 2016

Acknowledgments

This PhD has been a truly life-changing experience for me, and it would not have been possible to achieve without the support that I received from many people. I would like first to express my special appreciation and thanks to my supervisor Dr Jonathan Howse for his excellent guidance, caring, patience, and always providing me with an excellent atmosphere for doing research. He not only provided me with a challenging project that facilitated my growth as a scientist but also recognised my strengths and weaknesses as an individual and taught me how to use them to plan a successful research program of study. Many thanks to Dr Daniel Toolan for his endless help, constructive suggestions towards my research and for the kind conversations over the years. I am also grateful to my group work members: Dr Daniel Wesley, Richard Archer, Richard Hodgkinson and Jacob Lane for their continuous collaboration and advice. Special thanks to Corinne Howse for being always kind and considerate, I would never have been able to finish my dissertation without her support. Words cannot express how grateful I am to my mother, father and sisters for all of you've done on my behalf. Your prayers for me were what sustained me thus far. Especial gratitude and thanks to my beloved wife who spent sleepless nights with and was always my support when there was no one to answer my enquiries. In the end, I would like to express appreciation to the Egyptian Armed Forces for the financial support to my PhD research study.

Abstract

Two-dimensional colloidal crystals, as photonic band gap materials, have a wide variety of interesting and valuable industrial applications as photonic materials as well as simple models to study the basic processes of the atomic model such as phase transition, stability, crystallisation, ordering, and nucleation and growth. Recently, colloidal photonic crystals have got a great interest as templates for the fabrication of two-dimensional (2D) arrays for lithography applications. The dependence of these applications efficiency upon the quality of colloidal ordering during self-assembly process was the motivation for many researchers to perform several investigations in this field. These efforts have been oriented to develop a detailed explanation for mechanisms that took place during the complex self-assembly process of colloids, which may lead to developing a more controllable method to fabricate these structures with better quality. However, we are not yet able to fully understand what exactly happens during the colloidal self-assembly process. Hence, we are still unable to optimise processing conditions and so exploiting the fascinating colloidal optical characteristics is still limited till now.

Several techniques have been used to fabricate highly ordered two-dimensional monolayer photonic crystals such as dip coating, electrophoretic deposition, self-assembly at the gas/liquid interface and electric-field induced assembly. However, these techniques have many drawbacks such as the incompatibility to scale-up from laboratory-scale tests to industrial scale mass fabrication. Also, inability to control the thickness of the final film limits the use of these techniques as fabrication methods for uniform colloidal crystals. On the other hand, spin coating was found to be more feasible due to its advantages over other techniques. Spin coating offers a cheap, simple and straightforward technique for the fabrication of two and three-dimensional colloidal crystals. Spin coating provides easy control of the uniformity, domain size and thickness of the fabricated thin films through tuning the operating parameters such as spinning speed, acceleration rate, solids content and solvent volatility. However, the short duration of the process (5-30 s) and rapidly rotating sample (1000-10000 rpm) makes *in situ* studies challenging and as such we do not yet fully understand colloidal self-assembly, so are unable to optimise processing conditions effectively.

I have developed a laser scattering setup, which facilitates collecting laser scattering patterns diffracted by silica colloids in real time during the spin coating process. Tracking the development of these scattering patterns in real time may help to discover in details the stepwise evolution of the geometrical arrangements of monolayer colloidal crystals (MCCs) during the self-assembly process. Monitoring the colloidal self-assembly mechanisms may help to produce better quality colloidal crystals with a minimum defects density and also may help pave the way to fabricate complete three-dimensional photonic band gaps colloidal crystals with valuable photonic industrial applications.

This work aims to study the critical factors affecting the degree of ordering of colloids as they self-assemble through the development of the *in situ* laser scattering experimental techniques. In addition, samples are investigated with scanning electron microscopy (SEM) to characterise the impact of each factor on the colloidal thin films morphology produced. Further understanding of colloidal self-assembly will allow processing conditions to be optimised so that highly uniform, long range and defect-free colloidal thin films may be easily fabricated.

Table of Contents

4. Results and Discussions for Ex-Situ Investigations Stage

5. Effect of Rotational Speed in Spin Coating

6. Effect of Solid Content in Spin Coating

7. Effect of Solvent Volatility in the Spin Coating

8. Conclusions and Future Work

List of Abbreviations

3-ADMS	(3-aminopropyl) diethoxymethylsilane
Ar laser	Argon-Ion Laser
BSE	Backscattered electrons
CCD	Charge-coupled device
CCs	Colloidal crystals
DAQ	Data acquisition
DI water	Deionized Water
DLVO theory	Derjaguin, Lev Landau, Verwey and Overbeek Theory
DC power supply	Direct current power supply
DTAB	Dodecyl trimethyl ammonium bromide
DLS	Dynamic light scattering
EBP	Emslie, Bonner and Peck model
EDS	Energy dispersive X-ray spectrum
ETPTA	Ethoxylated trimethylolpropane triacrylate monomer
EG	Ethylene glycol
EISA	Evaporation-induced self-assembly
FCC	Face-centred cubic
FFT	Fast Fourier Transform
FTIR spectrophotometer	Fourier transforms infrared spectroscopy
fps	Frames per seconds
HCP	Hexagonal close packing structure
ICC	Ionic colloidal crystal
IPA	Isopropanol
LB	Langmuir–Blodgett
L-PS	Larger polystyrene particles
LSM	Laser scanning confocal microscope
LbL	Layer-by-layer
MCCs	Monolayer colloidal crystals
NTA	Nanoparticle tracking analysis
V.F.	Particles volume fraction

Pe	Peclet number
PBG	Photonic band gap
PCs	Photonic crystals
PS	Polystyrene
QE	Quantum efficiency
rpm	Revolutions per second
SEM	Scanning electron microscope
SE	Secondary electrons
S-PS	Smaller polystyrene particles
SDS	Sodium dodecyl sulphate
Wt. %	Solute weight percentage
Vol. %	Solvent volume percentage
TV	Television
3D	Three-Dimensional
TEM	Transmission electron microscope
2D	Two-Dimensional
UV-vis	Ultraviolet – visible light
UV-vis-NIR	Ultraviolet – visible – near Infrared Spectroscopy
VHS	Video home system

Chapter 1. Introduction and Background

1.0 Introduction

Monolayer colloidal crystals (MCCs), also known as two-dimensional (2D) colloidal crystals, consist of periodically ordered monolayer arrays of monodisperse colloidal spheres. MCCs have been used in several important industrial applications such as low and high reflection coatings [1][2][3], colour changing paints and inks [4][5][6], integrated photonic circuits and electronic devices [7][8][9][10], nanolithographic templates [11][12] and as model systems for studying the fundamental atomic phase behaviour [13][14]. Recently, MCCs have been used as templates for the fabrication of two-dimensional arrays for lithographic applications [15]. The realisation of these applications is highly dependent upon the packing quality of the colloidal thin film, which is determined by complex self-assembly processes. Many researchers have been motivated to perform further investigations in the field of colloidal thin films and their photonic applications. Further understanding of colloidal self-assembly may lead to optimising processing conditions so that highly uniform, long domain size and defect-free colloidal thin films may be easily and routinely fabricated. Development of a more controllable method to fabricate MCCs with a better quality may help to increase the efficiency of photonic devices and so extending the valuable applications of colloidal crystals as photonic materials in the industry.

Colloidal crystals can be fabricated through various techniques such as gravity sedimentation [16][17], electrophoretic deposition [18][19][20], dip coating [21] and self-assembly at the liquid–gas interface due to solvent evaporation [9]. However, these techniques are frequently producing three-dimensional (3D) colloidal crystals, multilayers ranged between two layers up to several hundreds of layers, instead of monolayers colloidal films. These thicker colloidal crystals have found a great interest as templates for the fabrication of inverse opals [22], three-dimensionally ordered macroporous products, which have numerous photonic applications because of their interesting optical properties. However, 3D colloidal crystals are not suitable in the field of lithographic masks which requires 2D arrays. On the other hand, MCCs can be fabricated through Langmuir–Blodgett (LB) [23][24], air–water interfacial floating method [22][23] or rapid convective deposition technique [20]. However, these

processes are often slow and not straightforward, as they often need a surface modification step as well as a pre-coating step [11]. In contrast, spin coating offers a simple, fast and cheap one-step process suitable for the routine fabrication of highly uniform MCCs [27]. This technique involves dispersing colloids in a suitable liquid, which acts as a dispersion medium. Then, deposition of a few drops of the colloidal suspension on a flat substrate, typically (Silicon / Glass), which is then rotated for a specific time. During rotation of the substrate, the excess solution is expelled off edges by shear forces while the volatile solvent is completely evaporated within seconds, forming a uniform monolayer colloidal thin film in its wake.

Many efforts have focused on studying the spin coating process of either polymer blends or colloidal suspensions. The high-speed nature of the process (5-30 s) and rapidly rotating sample (1000-10000 rpm) makes *in situ* studies a serious challenge. Several techniques based upon scattering, reciprocal space, have been used to characterise the morphology of the final colloidal crystals. This helped in optimising processing parameters and so improving the colloidal reorganisation quality. Numerical simulations provided a further understanding of the whole process. Interestingly, *in situ* investigations helped to develop assertive information about many fine details that took place during assembling of colloids such as the development of lateral structures, high-speed dynamics of evaporative spin coating, structural transitions and some crucial forces that significantly affect the colloidal ordering quality. This knowledge acts as a step forward towards the fabrication of long-range, defect-free and highly close-packed MCCs. However, despite all these studies, we are not yet able to fully understand the exact self-assembly mechanism of these micro- and nano-structured colloidal crystals that take place during the spin coating process. Furthermore, the huge number of parameters affecting the colloidal ordering process makes full modelling of the spin coating process of colloidal suspensions a serious challenge. Hence, we are still unable to optimise processing conditions and so the fascinating colloidal optical characteristics cannot be fully exploited yet. It is the aim of this thesis to offer insight and further understanding of the processes taking place during the spin coating fabrication of colloidal crystals.

1.1 Colloidal Crystals

The term "Colloids" was firstly used by Thomas Graham [28] to describe a class of matter at which substances have a low tendency to crystallise in solutions such as starch, gum and gelatine. Nowadays, the term "Colloids" is used to describe particles with a size ranges between (1 nm – 1 μm) dispersed in a fluid (Gas or liquid). Depending on the thermodynamic phases of both colloids and suspension mediums, colloidal systems can be classified as follows; liquid in gas is classified as "Aerosol" such as (Insecticides sprays and fog), solid in gas is classified as "Solid aerosol" such as (Smoke and dust), gas in liquid is classified as "Foam" such as (Shaving lather and whipped cream), liquid in liquid is classified as "Suspension" such as (Mayonnaise and cosmetic lotions) and finally, solid in liquid is classified as "Emulsions" such as (Paint, marshmallow and jelly) [29].

Once spherical colloids are added to the liquid dispersion medium, particles are moving fast under the action of the gravitational force (F_{g}). Over time drag force (F_S) decelerates the speed of particles until reaches a constant terminal velocity (υ_t) at which both gravitational force and drag force are in equilibrium;[30]

$$F_{\mathrm{g}} = \frac{4}{3}\pi a^3 \Delta\rho \mathrm{g} \tag{1.1}$$

$$F_S = 6\pi\eta a v \tag{1.2}$$

$$\upsilon_t = \frac{2a^2 \Delta\rho \mathrm{g}}{9\eta} \tag{1.3}$$

Where a is the radius of particles, $\Delta\rho$ is the difference in densities between colloids and a liquid medium, v is velocity, g is gravity and η is the liquid viscosity.

In colloidal suspensions, continuous random collisions are taking place between liquid molecules and solid particles. These collisions induce a frequently fluctuating net force which forces colloids to move in a random manner in the colloidal suspension continuously. This motion is known as a Brownian motion which was firstly discovered by Robert Brown in 1827 [31]. During Brownian motion, each particle takes several positions over time, but these positions are not correlated. Since

collisions are always random, the total displacement of each particle is always zero. Generally, due to the difference in densities between solid particles and dispersant, colloids may float or sediment under the action of gravity. However, the gravitational force impact in case of very small colloidal sizes (less than 10 μm) was found to decrease significantly due to thermal motion induced by Brownian motion. Herein, the impact of Brownian motion exceeds that of the gravitational force. Hence, once particles come into mechanical contact with each other, they stick together forming irreversible aggregations instead of sedimentation. The only route to avoid these undesirable irreversible aggregations is to modify interaction forces acting between colloids in the suspension to induce a repulsive force at which particles will repel each other. The main interaction forces acting between particles in the colloidal suspensions include Van der Waals forces, electrostatic double-layer forces and depletion interactions.

Van der Waals force is the simplest interaction acting between colloids in the colloidal suspension. It is a weak attraction force arising between uncharged atoms or molecules. Each interaction acting between any pair of particles in the suspension results in a constant random dipole moment. This dipole induces an attractive force with the neighbouring molecules. The strength of Van der Waals potential (U_{dis}) depends on the separation distance between interacting particles as follows;[30]

$$U_{dis} \sim \frac{\alpha^2}{r^6} \tag{1.4}$$

Where U_{dis} is the potential between a pair of atoms or molecules, α is the polarizability and r is the separation distance. The interaction strength between any pair of atoms is approximately 10^{-20} J which is very close to that of the thermal energy K_BT at room temperature.

The electrostatic double-layer force is another important interaction that acts between particles. It was expected that repulsive forces that took place between any two similarly charged particles in a suspension are related to the simple electrostatic repulsion. However, it was found that the origin of these repulsive forces is the difference in osmotic pressure of counter ions in the space between charged particles

in the suspension itself. The interaction between free ions dissolved in the suspension of charged particles is the main reason for the observed repulsion. Thus, a screened Coulombic interaction occurs instead of a simple Coulombic interaction. As shown in Figure 1.1, dissolved ions are neutralised through a layer of counter ions which is attracted to the charged surface forming three regions; (1) electric double layer, which is formed adjacent to the charged surface, (2) diffusion layer, which is created away from the charged surface and (3) an intermediate region, at which excess charges are attached to the counter ions layer. The length of screening is characterised by the Debye screening length (κ^{-1}) which is inversely proportional to the square root of the salt concentration in the suspension. As we can easily notice in Figure 1.1, there is no direct electrostatic interaction between charges at distances higher than κ^{-1} [30].

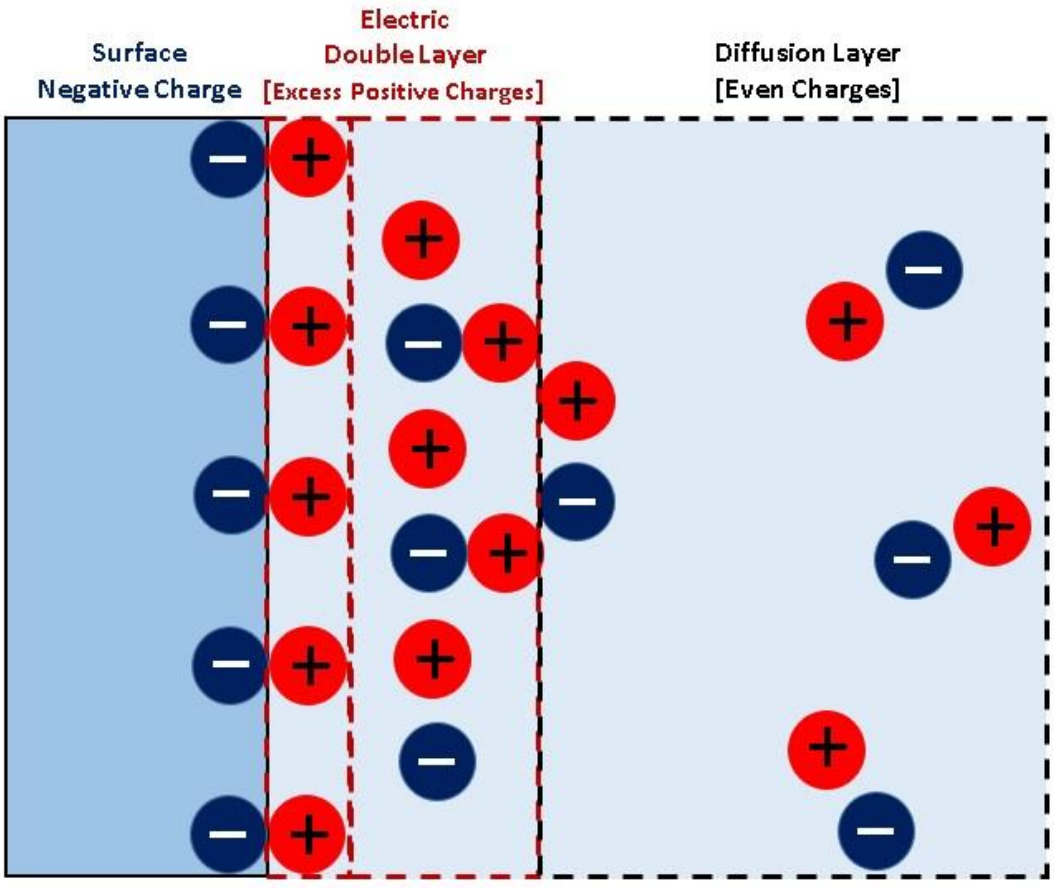

Figure 1.1: Screened Coulombic interaction obtained due to the interaction of free ions dissolved in the suspension with charged particles. Taken and Modified from ref. 78.

Based on the relationship between salt concentration and the Debye screening length, ionic strength has been used to control the colloidal stability through governing the interaction forces acting in the colloidal suspension. As salt concentration increases, the Debye screening length (κ^{-1}) significantly decreases. As a result, the magnitude of electrostatic repulsion potential reduces. Hence, particles are able to come closer to each other which may distort the colloidal stability under the effect of flow. If the salt concentration is not too high, particles still have the ability to rearrange themselves in an ordered structure as shown in Figure 1.2 a by reducing the amount of energy dissipated in the flow process. However, with the continual addition of salt, the recession of repulsive forces continues till reaches a point at which Van der Waals attraction forces dominate. At this stage, particles are attracted together forming irreversible aggregation which leads to a disordered open structure as shown in Figure 1.2 b [30][32].

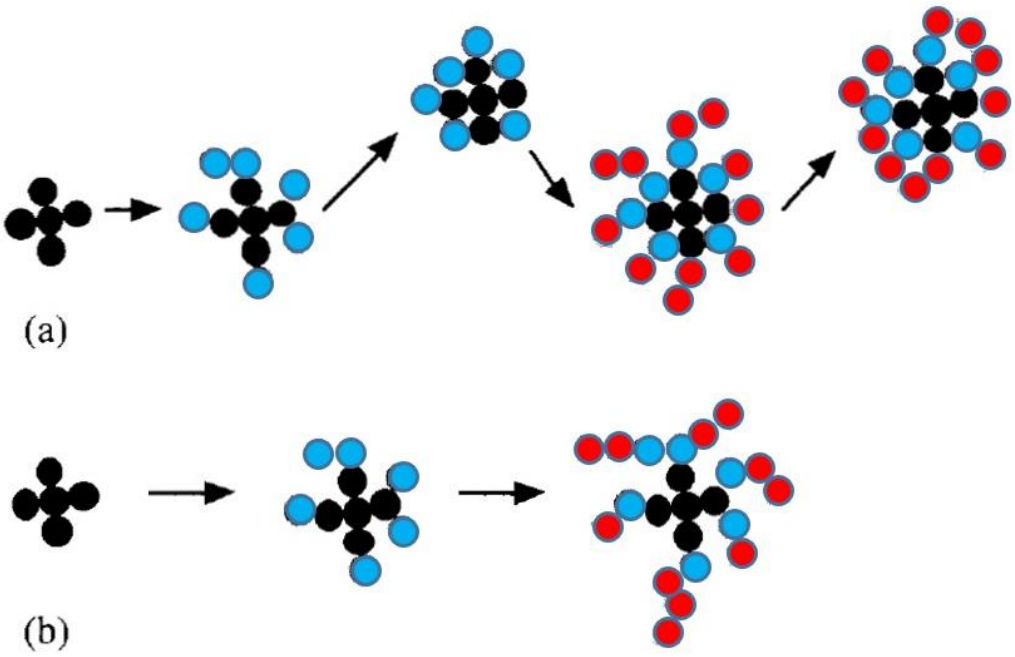

Figure 1.2: Aggregation with and without rearrangement. In (a) the attraction is weak enough to allow the particles to rearrange following aggregation – this produces relatively compact aggregates. In (b) the attractive energy is so strong that once particles make contact, they remain stuck in this position. Particles arriving later tend to stick on the outside of the cluster, as access to its interior is blocked. Resulting in much more open aggregates with a fractal structure. Taken from ref. 30.

Modification in interaction forces can be done either by charge stabilisation, using the electrostatic forces, or by steric stabilisation, at which polymer chains are added to stabilise the colloidal suspension. In steric stabilisation, colloids are coated with a thin polymer layer which is attaching to particles from one end. While the other end is attaching to the solution itself, as shown in Figure 1.3. Consequently, when two particles come in contact with each other, the concentration of polymer at spaces between particles becomes higher than that in the solution bulk. This leads to a significant increase in the magnitude of osmotic pressure between these two particles. This induces a repulsive force between particles which helps particles to repel each other to the extent that it inhibits the irreversible aggregation.

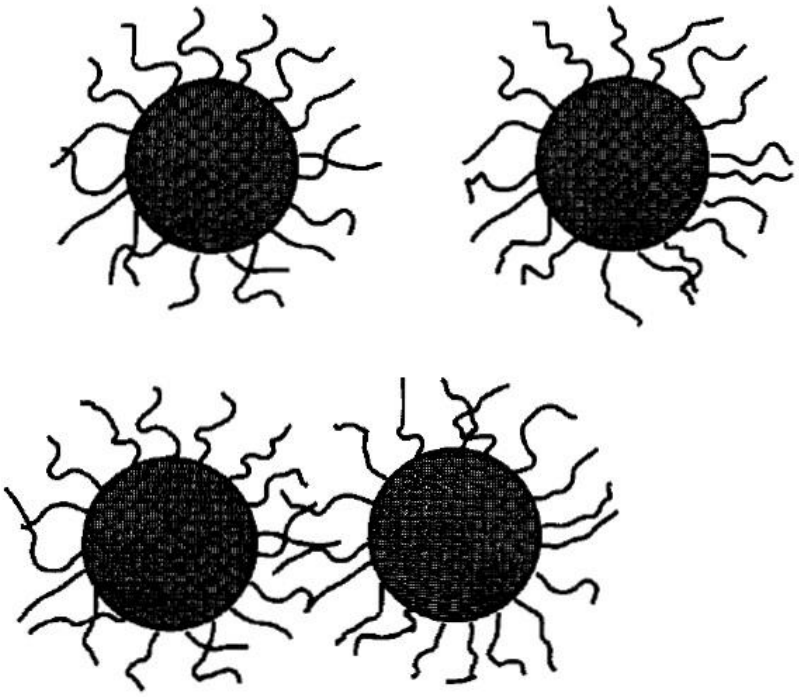

Figure 1.3: Steric stabilisation at which polymer chains are attaching to the particles from one side and the solvent from the other side. When two particles come close to each other, the difference in osmotic pressure induces a repulsive force that inhibits the irreversible aggregation. Taken from ref. 30.

This case is identically explained using the hard-sphere model. In this model, particles are not interacting together unless two spherical particles overlap. At the overlapping, interaction potential between particles changes from zero to infinity. It was found that steric stabilisation process has some limitations that may significantly affect its efficiency. For example, using an incompatible solvent with the polymer will induce an attraction force between polymer layers. Then, a phase separation occurs followed by the attraction between particles themselves. Hence, irreversible aggregation takes place again. Also, the length of polymer chains that governs the interaction range should be controlled in order to have a feasible steric stabilisation. Interaction potential between polymer chains and solvent also should always be controlled to be greater than K_BT. Otherwise, the tendency of polymer chains to leave particles increases. If polymer chains manage to leave the particles surface, as shown in Figure 1.4, a part of the suspension, known as the "Depletion zone", is created at which a lower polymer concentration exists between particles when compared to polymer concentration in the suspension bulk. Variation in polymer concentrations induces a difference in osmotic pressure between depletion zone and suspension bulk. Osmotic pressure deviation creates an attractive force that pushes particles towards each other. As a result, a phase separation occurs distorting the steric stabilisation. Depletion zone phenomenon also obtains either if the grafted polymer was removed or if the added polymer was a non-adsorbing polymer and unable to attach to the particles surface [30].

Many efforts have focused on extending the interaction between two atoms to determine the overall interaction that takes place between two macroscopic molecules. The simplest approach was to add interactions induced between all pairs of atoms in the two macroscopic bodies. However, this approach includes several disadvantages; (1) it considers only the dipole moment resulted from the interacting pair of atoms. However, the overall dipole moment induced by all other neighbouring atoms in the system also affects the interacting pair of atoms and should also be included, (2) as the separation distance between particles increases; retardation impact also increases due to the increase in the effect of the propagation speed in the system. Hence, according to equation (2.4), the change in potential at larger distances should be taken into consideration. Later on, a more advanced approach, known as

Lifshitz theory, was used to determine the interactions between macroscopic bodies. This approach is based on measuring the properties of the electromagnetic field between these two bodies using the quantum field theory [30].

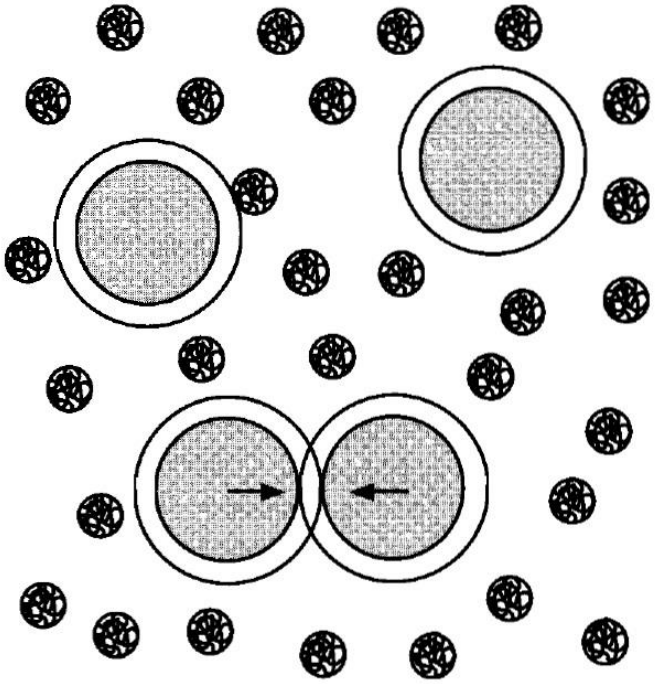

Figure 1.4: Depletion interaction that took place when polymer chains leave the particles surface in the colloidal suspension forming a depletion zone. When the depletion zone of two particles overlap there is a net attractive force between the particles arising from unbalanced osmotic pressures. Taken from ref. 30.

Colloidal suspensions such as glue and paints have an intermediate state between pure crystalline solids and simple liquids. In case of crystalline solids, a shear strain (e) results when a shear stress (σ) is applied to the material, where stress and strain are in direct proportionality through a constant called shear modulus (G);[30]

$$G = {}^{\sigma}/_{\mathrm{e}} \tag{1.5}$$

Similarly, when a shear stress is applied to a simple liquid, it flows in response to a time-dependent shear strain (è) as follows;[30]

$$\sigma = \eta \text{ è} \tag{1.6}$$

Where η is the viscosity of the fluid which is always constant with a constant shear stress.

On the other hand, colloidal systems respond to shear stresses in a more complex way. They response to shear stresses as viscoelastic materials with a more dependency on the timescale similarly to soft condensed matter. Firstly, a constant strain obtains as a result of the applied shear stress. After a certain period of time called relaxation time (τ), they start to flow with a time-dependent strain. If the shear stress timescale is shorter than the relaxation time, colloidal systems will behave like an elastic solid. Conversely, they act as a simple liquid if the timescale of the applied stress is longer than the relaxation time. For that reason, colloidal systems can be classified as soft condensed matter. Also, colloidal systems have another interesting feature that contradicts with Newtonian fluids where their effective viscosity is significantly dependent on the shear rate magnitude as shown in Figure 1.5. It was found that this non-Newtonian behaviour favours concentrated colloidal solutions with a high volume fractions of spherical particles. At larger shear rates, a shear thinning occurs that forces the material to flow easier such as paint that flows easier when applying more stresses using a brush. While in the case of pastes, material resistance to flow increases as a result of a shear thickening at smaller shear rates. This non-Newtonian behaviour can be governed using the Peclet number, Pe;[30]

$$Pe = \frac{6\pi\eta_0 a^3 \gamma}{\mathrm{K}_B T} \tag{1.7}$$

Where η_0 is the viscosity of the dispersion, a is the radius of spherical particles, γ is the shear rate, K_B is Boltzmann constant, and T is temperature.

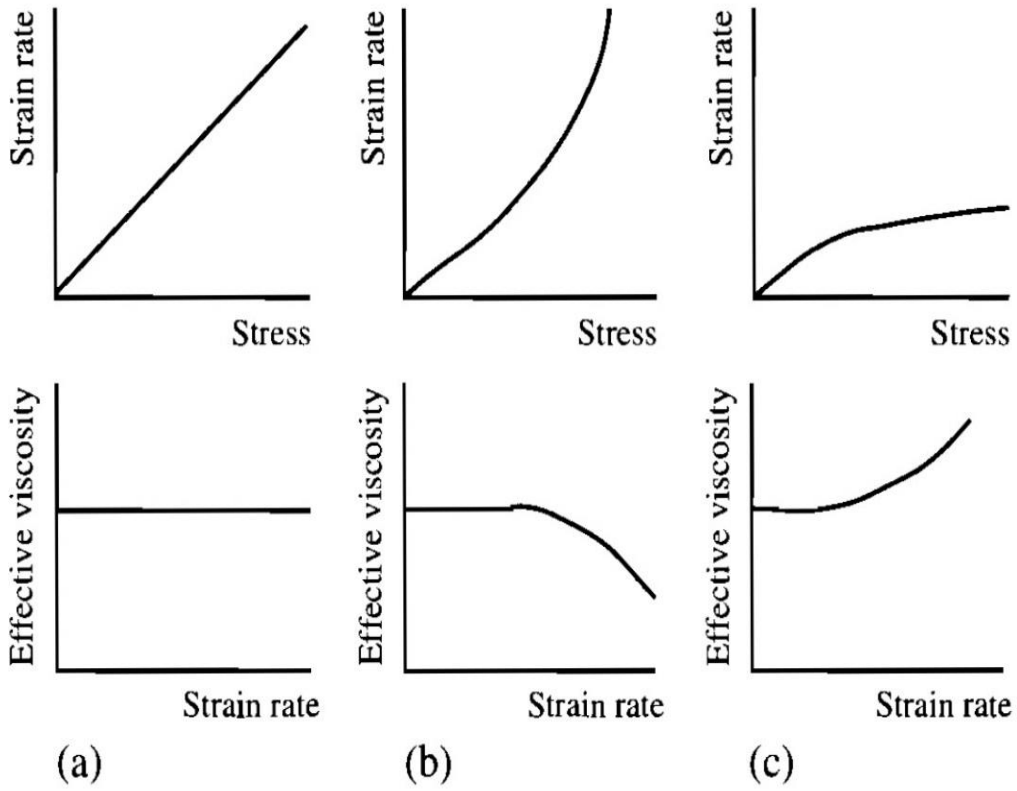

Figure 1.5: Possible fluid responses to an applied shear stresses: (a) Newtonian liquids; (b) shear thinning; and (c) shear thickening. Taken from ref. 30.

Peclet number is a dimensionless value that expresses the impact of both shear and Brownian motion on the behaviour of colloidal systems as follows; (1) if $Pe \leq 1$, Brownian motion can restore particle arrangement and maintain colloidal suspension at its initial state, (2) when $Pe > 1$, Brownian motion will not be able to restore the structure distortion due to shear forces. As a result, colloidal structure will change under the action of flow and depend on the shear rate value [30]

Colloidal systems possess dimensions much larger than that of typical condensed matter which enabled investigations using optical microscopy. This has helped colloidal crystals to act as simple model systems for studying physics of nucleation and growth [33], crystallisation mechanisms [34] and phase transition processes [35] in real time which is extremely challenging in the case of atomic scale processes. Condensed matter is bounded together through intermolecular forces such as Van

der Waals attraction forces and electrostatic double-layer repulsive forces. If Van der Waals forces dominate in the colloidal suspension, particles will stick together and disordered structures forms. However, when repulsive forces between particles dominate, stable suspensions are produced. If solvent evaporates from these stable suspensions, or concentration increases in case of non-volatile solvents, a liquid-solid transition occurs under the action of packing constraints as solids concentration increases. If spherical particles suspended in the dispersant have a low polydispersity index, disorder-order transition forms a long-range ordered structure known as colloidal crystals. Randomly arranged particles can have a maximum packing density of 0.63. However, a maximum packing density of 0.7404 obtains when spherical particles are in a regular close-packed structure. Surprisingly, colloidal crystals can appear at much lower volume fraction than either random or regular close-packed structures. This happens due to a sudden phase transition governed by the difference in entropy at a volume fraction of 0.49 forming a crystal structure with a volume fraction of 0.54 [30].

Two different close-packing structures can retain the maximum packing density of 0.74; (1) face-centred cubic (FCC), shown in Figure 1.6 (a), and (2) hexagonal close-packing structure (HCP) which is represented in Figure 1.6 (b). Both structures are identical in the arrangement of the first layer. However, in the next layers, HCP structures follow the sequence of ababab…, while subsequent layers in FCC structures arrange according to ABC ABC… arrangement [36]. It was found that FCC structure is a little bit lower than HCP close-packing structure with respect to entropy [37][38]. Since disorder-order transition takes place only when two particles come in contact with each other. So, entropy completely governs liquid-solid transition and temperature has no effect. This makes FCC close-packing structure is more stable and so more favourable [30].

Colloidal crystals (CCs) are able to diffract light forming remarkable interference effects. For that reason, colloidal crystals can be named as photonic crystals (PCs). Interestingly, light diffraction through colloidal crystals occurs through a special manner at which light is forbidden to propagate at a certain wavelength. This phenomenon is called photonic band gap (PBG) which makes CCs as valuable materials in photonic application fields [39]. The existence of PBGs is

highly dependent on the colloidal ordering quality. It was found that PBGs significantly reduces in the presence of defects in the colloidal structure. Since, colloidal crystals are normally fabricated with a random HCP arrangements that possess a large number of stacking faults, empty holes and dislocations [30]. Therefore, many efforts have focused on optimising processing parameters which may facilitate the fabrication of highly ordered, defect-free colloidal crystals that possess PBGs.

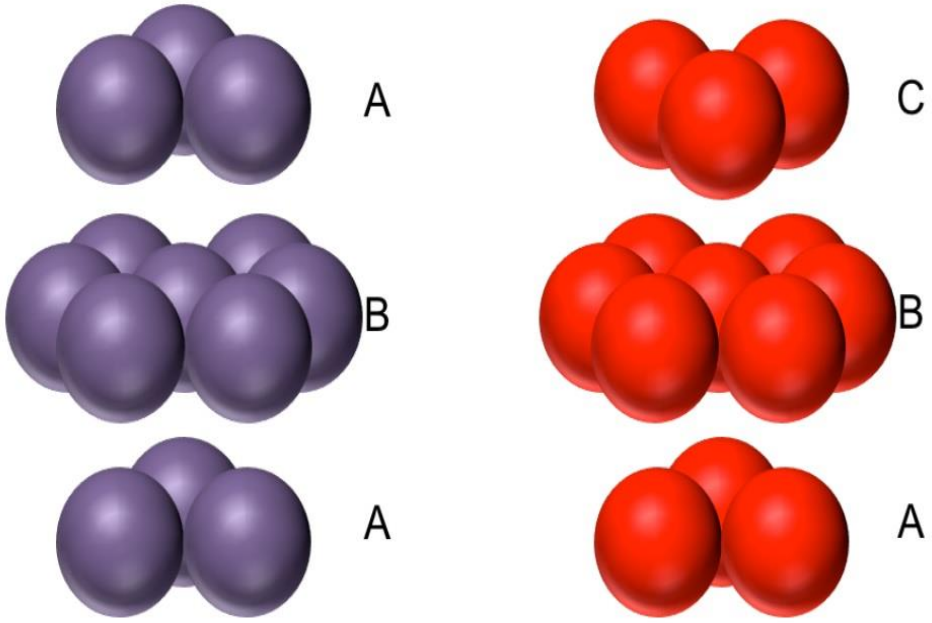

Figure 1.6: Schematic showing illustrating; (a) hexagonal close-packed structure (HCP) and (b) face centred close-packed structure (FCC). Taken from ref. 36.

1.2 Colloidal Self-assembly Process

As mentioned in the previous sections, colloids become very important photonic creatures in the field of flow of light not only for being simple models to study the basic processes of the atomic model such as phase transition, stability, crystallization, ordering, nucleation and growth but also for being used as templates for the fabrication of 2D arrays for lithographic applications. One more advantage for colloidal systems is the ease of formation of highly ordered closed-packing structures through self-assembly of these colloids. Colloidal self-assembly process, as a bottom-up method

for the routine fabrication of highly ordered photonic crystals, has many advantages over the conventional top up methods such as low cost and simplicity of the process [40]. However, the high dependence of their industrial importance upon the perfection of colloidal ordering mechanism is a serious challenge. Improvement of colloidal ordering during self-assembly process, therefore decreasing the defects density and increasing the domain size, may help to fabricate 3D photonic band gap materials.

Colloidal self-assembly process is strongly correlated to the solvent evaporation from the colloidal suspension. 2D array formation process begins when the suspension wetting layer thickness on the solid substrate becomes smaller than the colloidal particles diameter. At this stage, the distance between colloids becomes very small inducing attractive capillary forces between them forming a nucleus. This initiates a crystal growth that takes place in a specific manner where particles are moving towards the more arranged areas in the suspension until forming a highly ordered 2D colloidal photonic crystal. Denkov [41] explained the self-assembly process by describing the case when spherical colloidal particles are immersed in a liquid phase then dropped on a flat solid substrate as shown in Figure 1.7. Due to solvent evaporation, the liquid layer thins gradually with time until particles become partially immersed in liquid causing both contact line pinning and deformations of the liquid-gas interface. Deformation creates two types of strong capillary effects; (1) pressure effect, driven by the difference between pressure in the gas and liquid phases which forces particles towards each other; (2) surface force effect, created due to changing in the liquid surface slope with respect to the horizontal place forming a very strong surface tension forces that leads to increase the ordering efficiency of particles creating a well-ordered packing structure.

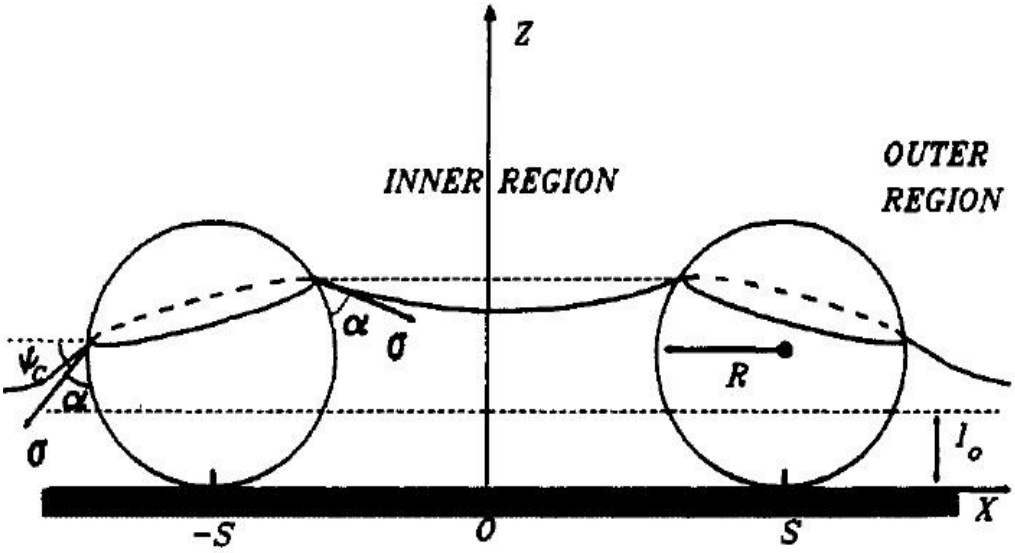

Figure 1.7: Two spheres partially immersed in a liquid layer on a horizontal solid substrate. Taken from ref. 41.

Colloidal packing mechanism begins once the liquid layer thickness becomes close to the particles dimension. Herein, the thinning liquid layer presses particles against the horizontal surface causing contact line pinning which is the crucial factor to enable observation of gradual variations in colloidal crystal thickness with time. Further evaporation beyond this point causes severe deformation in the liquid-air interface leading to a convection flow of particles towards the edges that exhibit a faster rate of evaporation [41]. The same mechanism occurs even if some particles irreversibly adhered to the substrate surface at the drop edges pinning the contact line. Once evaporation starts, a liquid flow towards the edges starts to compensate the liquid loss. Consequently, the flow drags solute from the bulk to edges forming a ring-like deposit at the end of the drying process. Deformation in the liquid surface shape that took place due to partially immersed particles induces immersion lateral capillary forces which are directly proportional to the degree of deformation happened on the liquid surface. These forces tend to attract each two adjacent particles towards each other. Particles weight and their floatation level have a very limited effect on the magnitude of lateral capillary forces. However, capillary forces are highly dependent on the shape and position of contact line as well as contact angle value [42]. As shown in Figure 1.8, evaporative-driven flow of particles is followed by lateral capillary attraction forces between each two adjacent partially immersed particles. Attraction

forces continue until forming a well-ordered colloidal crystal structure [41]. However, forming an ordered pattern after complete evaporation of the liquid is not guaranteed unless factors that govern the deposit uniformity were put under control [43][44].

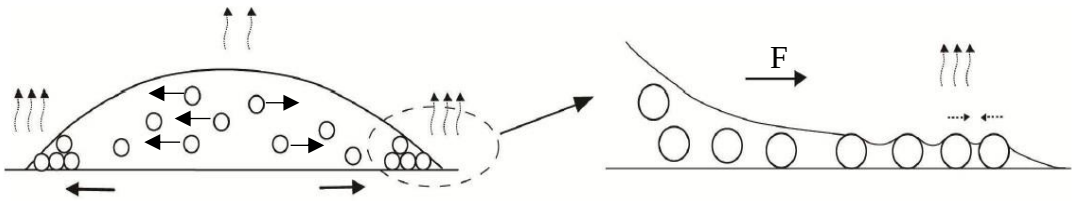

Figure 1.8: An illustration for the hydrodynamic drag force (F_d) that governs the colloidal ordering mechanism during liquid evaporation. Taken and modified from ref. 32.

Crystallisation growth mechanism that took place during the colloidal self-assembly process was found to be highly dependent upon several factors such as particles volume fraction, polydispersity, evaporation temperature, ionic strength and particles mobility. As the liquid evaporates, it was found that the number of particles transferred towards the thinning layer under the action of convective flow increases as particles volume fraction increases. Consequently, the time available for these particles to be self-assembled during the transition stage becomes not enough. This leads to the random ordering of particles leading to the formation of undesirable disordered colloidal films with many defects. In addition, volume fraction was found to dramatically affect the particles adhesion on substrate [32][45]. Particles diameter has no effect on the colloidal ordering. However, polydispersity plays an important role in the self-assembly colloidal growth. Polydispersity is inversely proportional to the uniformity of 2D ordered arrays. As polydispersity increases, dislocations appeared in the final colloidal crystals [46]. It was found that particles with a size distribution more than 8% are not able to self-assemble into well-ordered close-packed structures [9]. Also, evaporation temperature is one of the most crucial parameters to be taken into consideration when dealing with colloidal self-assembly process. When liquid evaporation at higher temperatures, evaporation rates become faster which decrease the opportunity of particles to discover the optimum position to occupy during colloidal growth. In addition, particles kinetic energy is directly proportional to the evaporation temperature. So, as evaporation temperature increases, particles are

moving faster. Herein, particles exhibit more Brownian random motion which increases the collisions between particles. As collisions increase, distortion of the colloidal growth increases leading to the formation of high defect density in the final colloidal crystal. In addition colloidal ordering domain size is highly correlated to the evaporation temperature [45]. Ionic strength plays an important role in improving the colloidal ordering quality. The addition of polar solute to the colloidal suspension changes the electrostatic and steric interactions between colloids by developing a steric barrier. Steric barrier inhibits any direct contact between colloids and increases particles mobility. Higher particles mobility hinders the irreversible aggregations and improves particles arrangement in the growing sites. Therefore, ordering quality is greatly improved. Also, particle-particle interaction forces that took place between colloids in the suspension was found to have a significant impact of the effective close-packing of colloids. Generally, capillary forces impact of particle ordering appears when particles become partially submerged in solution and then protrude leading to a deformation in the air-liquid-substrate contact line. However, particles in colloidal suspension are completely immersed into the solvent. Therefore, capillary forces have no importance at this stage and interaction forces between colloids are the governing key for colloidal ordering [47].

Scanning electron microscope (SEM) and transmission electron microscope (TEM) have been commonly used to characterise final colloidal films after complete drying. Although, they are not able to develop quantitative data, they generate clear images which are magnified enough to provide a morphological monitoring for 2D colloidal growth during the self-assembly process. Also, UV-vis spectrophotometry has been used to investigate direct reflected or direct transmitted beam from colloidal crystals. In addition, colloidal crystals as photonic band gaps materials, they can diffract light. This advantage helps to use optical microscopy to track colloid motion and stepwise colloidal ordering during self-assembly process [32]. Despite all these tools and efforts are done to optimise the colloidal ordering, colloidal self-assembly process still not fully understood. This may be attributed to the complexity of the process that is affected by several independent factors such as environmental conditions, particles parameters, solvent nature, substrate chemistry and interaction between particles. Also, reciprocal investigations and characterization of final

colloidal crystals only are not helping to understand the real-time mechanism that took place during the colloidal self-assembly. However, these studies provided a clear definition of the perfect colloidal crystals that should be highly ordered, large domain size, minimum defects density, minimum angular orientation between domains, minimum cracks and develops a clear reflectance in the visible wavelength range. Many researchers have focused on investigating in this field. In the next few lines, a summary of the main achievements in the colloidal self-assembly process studies is given.

1.3 Development in studies of colloidal self-assembly process

1.3.1 Colloidal self-assembly of uncharged particles

In 1992, Denkov [41] was the first to start *in situ* investigations about the colloidal self-assembly process owing to volatile solvent evaporation from colloidal suspensions. The intentions behind this study were to perform real space investigations for ordering mechanisms and to discover the process stages that take place during the formation of micrometre-size polystyrene (PS) 2D arrays. In addition, Denkov aimed to study factors affecting 2D array formation. To do so, Denkov built up an experimental setup as shown in Figure 1.9 at which 20.0 µl of 1.0 wt. % suspension of polystyrene latex with a particle size of 1.7 µm was placed on a glass plate that was fixed to a microscope table. The whole self-assembly process was observed through a microscope objective.

Denkov's first observation was the Brownian motion of particles in the suspension owing to the presence of a solvent that increases the particles dynamic motion. Secondly, he noticed a partial sedimentation of particles on the glass surface, which increases the solute concentration near the glass when compared to the particle concentration in the bulk. Once water starts to evaporate, the layer thickness thins gradually and particle concentration increases with time. An increase in concentration reduces the distance between particles without any observation of aggregation or irreversible cluster formation. Once the layer thickness reaches the minimum, bright rings can be easily noticed in the cell centre owing to the monochromatic light reflections from glass–water and water–air surfaces. When the layer thickness

becomes very close to the particle diameters, the drying process dominates, initiating an ordering process of the particles as shown in Figure 1.10. No further particle movements were observed after this stage. Denkov showed that during the drying process particles were forced to flow from the centre to the dried edges, just like what happened in the coffee ring experiment performed by Deegan [44] forming well-ordered arrays with hexagonal closed packing. However, Denkov also observed some fringes, which are related to uncovered areas of glass owing to the presence of solvent only.

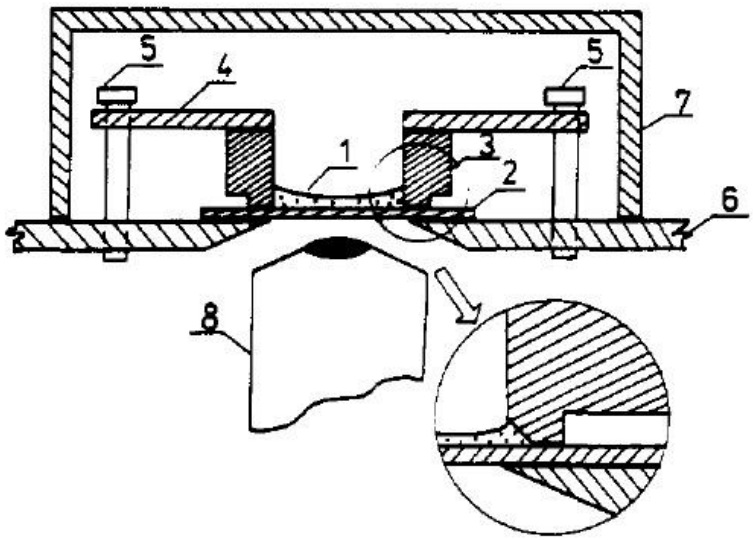

Figure 1.9: A schematic diagram for Denkov's In Situ set up where: (1) latex suspension, (2) glass plate, (3) Teflon ring, (4) braes plate, (5) screws, (6) microscope table, (7) glass cap, (8) microscope objective. Taken from ref. 41.

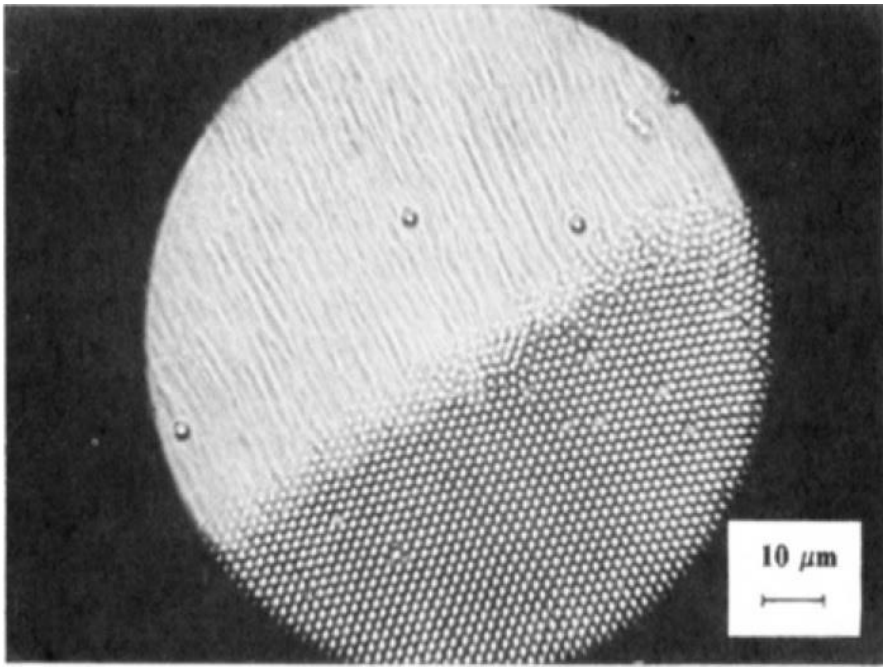

Figure 1.10: Scanning electron microscope image shows the movement of particles towards the ordered array. Taken from ref. 41.

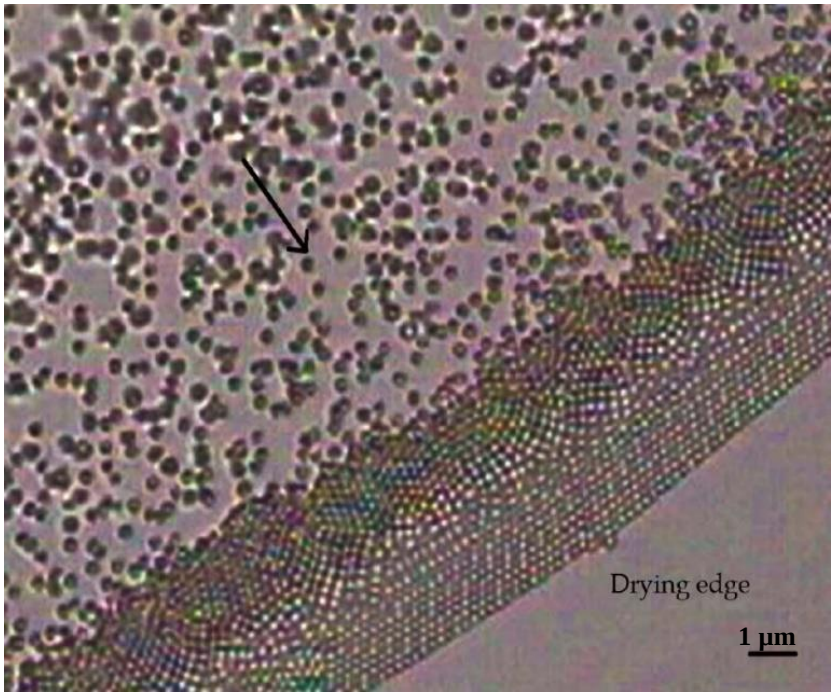

Figure 1.11: Self-assembly of polystyrene particles (860 nm) during the drying stage. Taken and modified from ref. 32.

Denkov's experiment confirmed that both 2D and 3D array formation processes start when the suspension layer thickness becomes equal to the particle diameter and they overflow towards the ordered areas. However, he showed that addition of salts is not crucial in the case of 2D arrays where it reduces the electrostatic repulsive forces but without a great impact on the particle ordering, as in the case of 3D arrays. In addition, he observed that changing the particle concentration does not affect the start of the ordering process in contrast to the 3D array formation mechanism. Based on these observations, he proposed a two-stage mechanism for the formation of 2D arrays. The first stage is the formation of a nucleus of ordered array in the wetting film, while the second stage involves the directional motion of particles towards the ordered array, as shown in Figure 1.11.

The pinning contact line is important to guarantee the observation of gradual variations of liquid layer thickness from the liquid centre to the edges. However, even slow evaporation is not enough to keep the contact line fixed over time. For that reason, the setup shown in Figure 1.12 was used to allow the contact line to move along with the deposition direction. This setup includes a diluted colloidal suspension at which a substrate was partially immersed vertically or inclined at a certain angle in order to favour the convection flow of particles towards the contact line. The temperature of the suspension is kept as low as room temperature to avoid changing the colloidal suspension concentration. Then, the suspension was discharged at an exact speed. Finally, the contact line moving speed was used as a direct measurement of the thickness of the final colloidal crystals formed [32].

Colour phenomena observed from ordered colloidal domains when these structures have been illuminated with white light were first classified by Krieger and O'Neill [48] into (i) colours and (ii) iridescent colours. Colours can be observed from diluted colloidal suspensions owing to Mie scattering that occurs when particles like water droplets and smoke scatter visible light, while the iridescent colours phenomenon is related to Bragg diffraction created from three-dimensional ordered arrays composed of particles that have diameters ranging between 150 and 500 nm in relatively concentrated colloidal suspensions. A third colour phenomenon has been observed owing to the reflection or transmission of white light through two-

dimensional ordered arrays composed of particles with diameters larger than 400 nm [49].

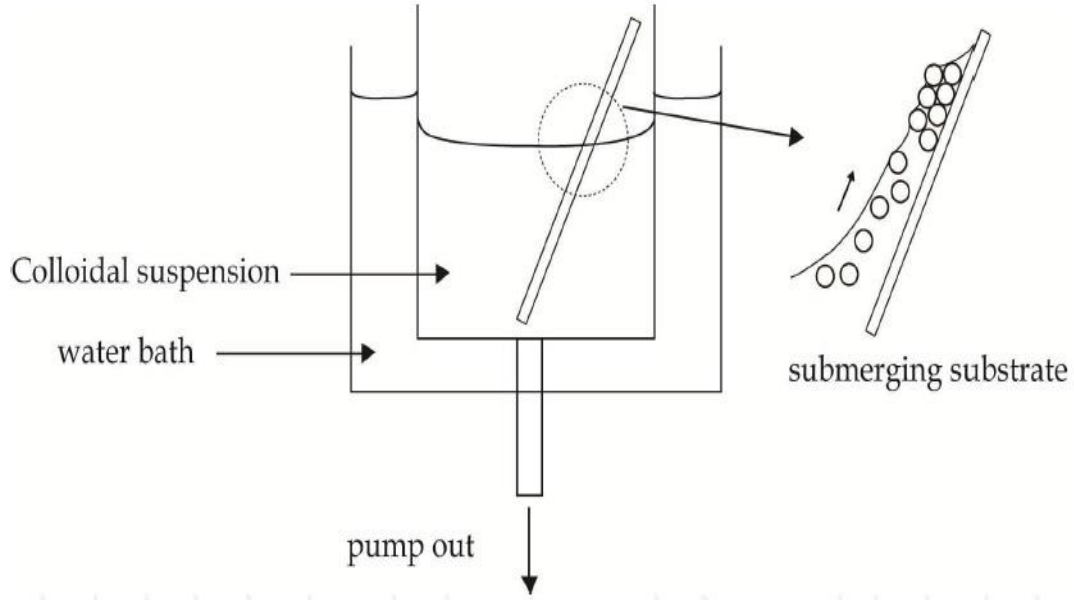

Figure 1.12: An experimental setup to control movement of contact line along crystal growth direction. Taken from ref. 32.

In 1993, Dushkin successfully demonstrated a new colour phenomenon from colloidal particles of diameters ranging between 55 and 144 nm. In this work, an experimental setup was built to allow *in situ* observation of the growth of colloidal crystals from water suspensions. As shown in Figure 1.13, Dushkin's crystallisation cell composed of a 20 x 10 x 5 mm paraffin wax block with a melting point of 70°C. A round hole with a 2 mm diameter has been pierced across the paraffin block, and its bottom was taped up with a transparent flat solid substrate, either a glass substrate prewashed with either chromic acid or a freshly cleaved mica plate. Both glass and mica substrates were coated before the experiment with a thin layer of gold or carbon to improve the colour intensity and enhance the visibility [49].

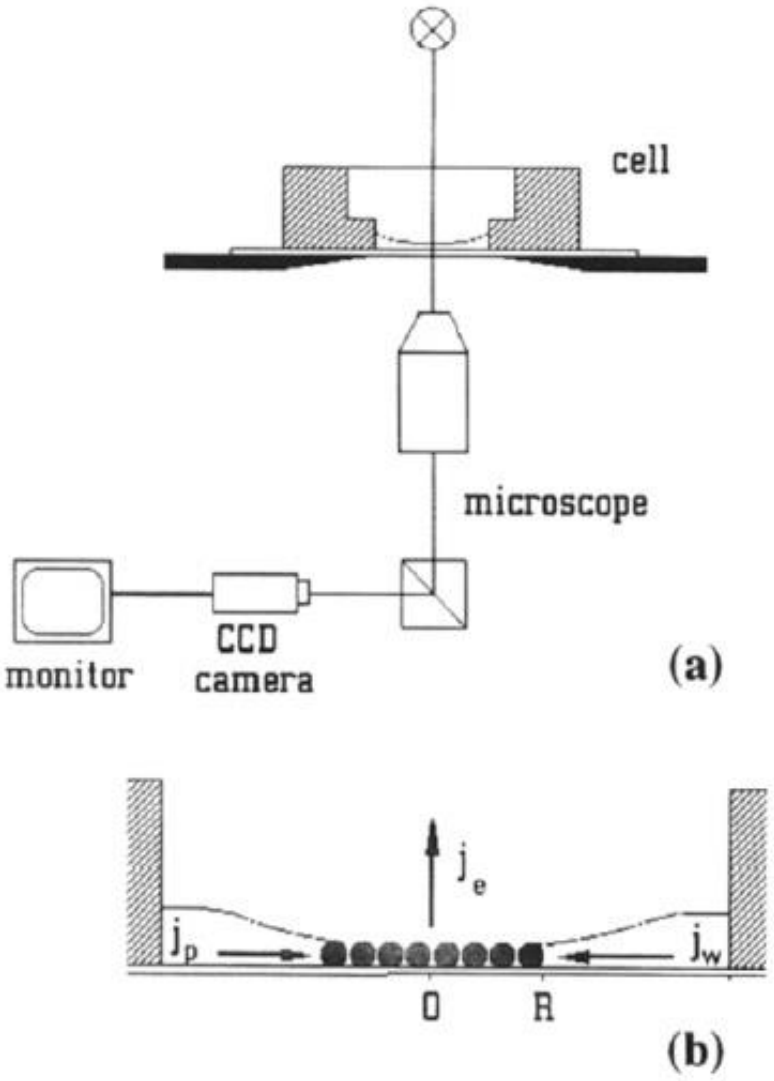

Figure 1.13: Schematic diagram for Dushkin crystallization cell for producing and monitoring 2D crystals: total view (a), and crystallization cell with growing crystal (b). Taken from ref. 50.

Dushkin started his *in situ* investigations by loading his 3.14 mm^2 crystallisation cell with 1.0 µl of colloidal suspension, composed of negatively charged polystyrene particles of 144 nm diameter and 0.001 volume fraction suspended in water, forming a layer with an average thickness of about 300 µm in the cell with a contact angle of about 85° with the paraffin block wall. Both temperature and humidity were kept constant at 20°C and 30%, respectively, by keeping the upper side of the cell open in order to ensure a constant water evaporation rate. Substrates used in this experiment have been pre-coated with a thin layer of either carbon or gold with a thickness of

about 50.0 Å by vacuum evaporation followed by ion sputtering to improve the wettability of substrates and to enhance the uniform deposition of colloidal suspension on a solid surface. Dushkin used an optical microscope (Nikon, transmitted light) together with a Super VHS video system in order to record the progress in the crystallisation stages. The final colloidal crystal structures were characterised through a scanning and a transmission electron microscope (SEM 820 and TEM 1200 EX-11, JEOL) and by a scanning force microscope (SFM, Seiko) [49][50].

Through his real-time investigations, Dushkin deduced that the crystallisation process took place through two stages: (i) nucleation and (ii) crystal growth. Owing to evaporation of water, the liquid layer thins gradually and consequently the polystyrene particle concentration increases. Dushkin observed that layers in the centre were always thicker when compared to those at the cell edges because of the concave meniscus. After about 15 minutes, a thin liquid layer was formed at the cell centre with an average thickness of about 200 µm, which is still greater than the particle diameter. As evaporation proceeds, the liquid layer becomes thinner and subsequently presses colloidal particles towards the solid substrate. At this stage, particles start to attract each other by the action of the lateral surface forces forming an ordered rounded monolayer nucleus on the substrate surface. Once the liquid layer thickness becomes smaller than the particle diameter, particles from the bulk start to attach themselves to the nucleus and the crystal grows gradually until forming a multilayer colloidal crystal. However, the number of multilayers formed was not constant owing to the uncontrollable meniscus profile. Therefore, Dushkin recommended that the best way to obtain only a monolayer colloidal crystal is to keep the meniscus profile always uniform by either adding or pulling water from the colloidal suspension. Through video observations, Dushkin observed a convection flow for particles from the bulk towards the more ordered areas in the cell edges where water evaporates at a faster rate [50].

Dushkin observed that the final colloidal arrays have a hexagonal close packing (HCP) lattice structure where a tetragonal packing was found between each two consecutive hexagonal packing multilayers as shown in Figure 1.14. In addition, he showed that the colour intensity is highly dependent on the final film thickness formed

on the individual substrate, and he confirmed this result by showing the gradual change of colours with respect to the number of multilayers formed where the colour changes each time when the upper layer is removed from the multilayer array. As shown in Figure 1.15, it is easy to observe the uniform colour strips clearly with sharp boundaries. Different layers have different colours starting from ochre for the monolayer and brown for the bilayer, and then a variety of colour strips appeared for each consequent layer depending upon the layer thickness as listed in Table 1.1. In addition, one can easily see the colour strips for the same latex in different colours in the case of mica as a substrate given in Figure 1.16. The difference in colours is related to the lower reflectivity of mica in comparison with the coated glass substrates. In addition, Dushkin's investigation clarified the vital role of gold or carbon coating for the glass/mica substrates before deposition of the colloidal suspension. Colour observation was very difficult in the case of uncoated substrates. Nevertheless, gold-coated glass substrates exhibit higher intensity (Figure 1.15 a) when compared to intensity for carbon-coated glass substrates (Figure 1.15 b). Finally, Dushkin showed that the colour phenomenon observed from polystyrene particles of diameter less than the wavelength of visible light, 55–144 nm, is not related to either Bragg diffraction or Mie scattering. However, he showed that the observation of colour stripes, in this case, is attributed to the light interference at parallel films [49],[50].

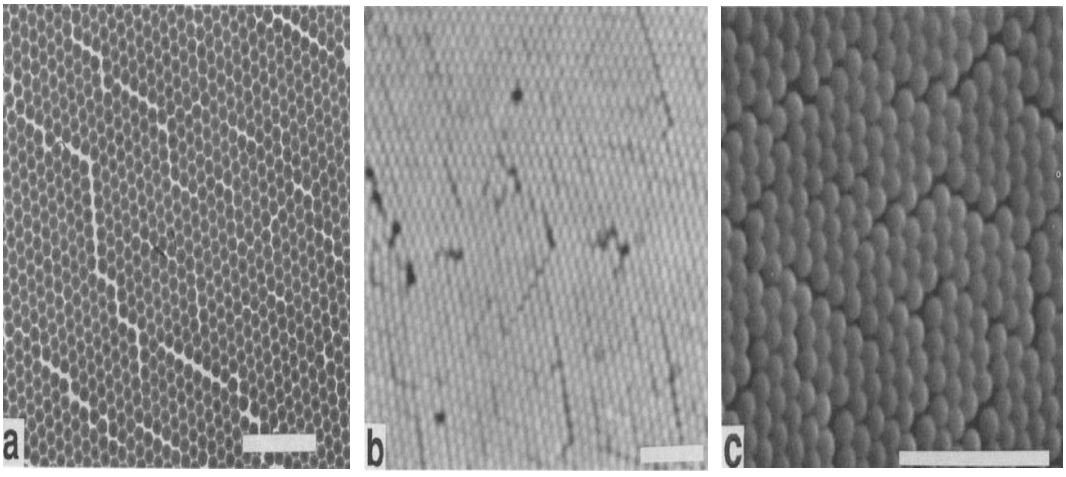

Figure 1.14: Hexagonal-close packing images for polystyrene monolayers: (a) TEM, (b) SFM and (c) SEM. Scale Bars: 1 µm. Taken and modified from ref. 50.

Table 1.1: Colour strips observed from nanometer polystyrene multilayers formed on Gold-coated glass substrates. Taken from ref. 49.

No. of layers	Colour in reflected light	Thickness, nm
1	Ochre	47
2	Brown	85
3	Navy Blue	124
4	Sky Blue	162
5	Yellow	201
6	Orange	239
7	Magenta	277
8	Blue-Purplish	316
9	Green	354
10	Yellow-Green	392
11	Orange	431
12	Red	469

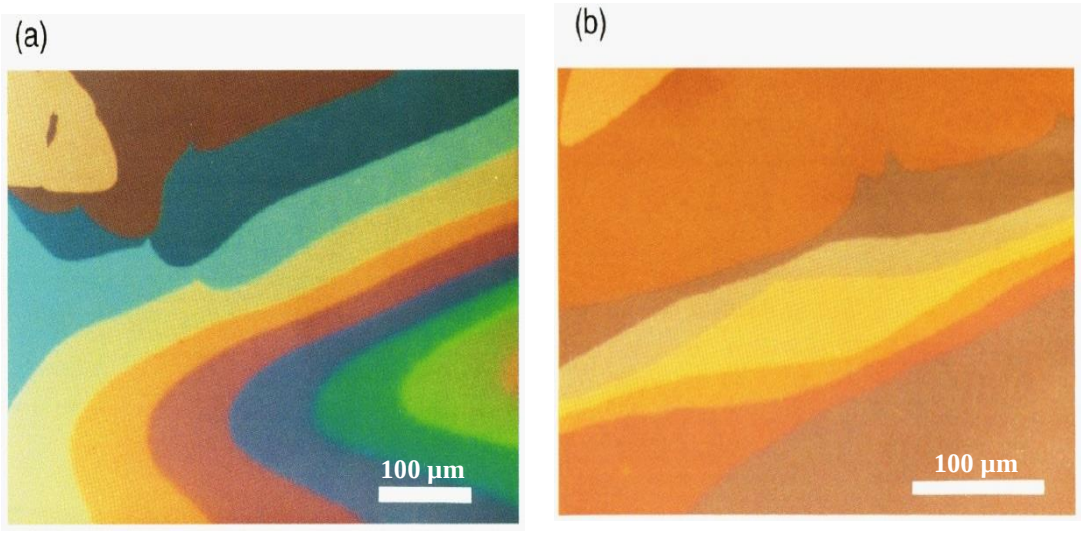

Figure 1.15: Images for colour stripes observed due to light interference at plane parallel films from polystyrene particles with a diameter of 55 nm dispersed in water: (a) Gold-coated glass substrate, (b) Carbon-coated glass substrate. Taken and modified from ref. 49.

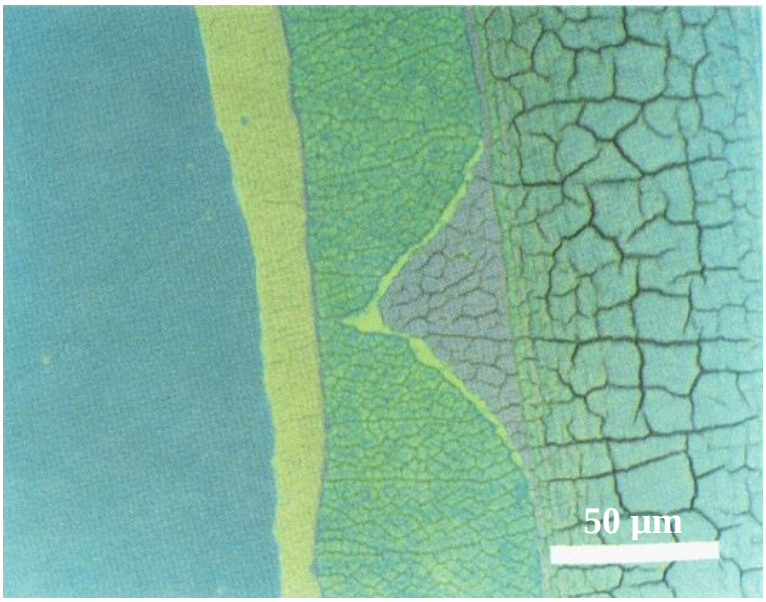

Figure 1.16: Images for colour stripes observed due to light interference at plane parallel films from polystyrene particles with a diameter of 55 nm dispersed in water in case of using mica as a substrate. Taken from ref. 49.

One of the drawbacks in Dushkin's work was the incapability to validate the responsibility of the lateral capillary attraction force for collecting particles together forming ordered particle arrays during the crystallisation process. Hence, the hypothesis is still not verified, and the reasons behind the formation of ordered structures are still doubtful. In addition, the extent of nucleation has not been studied, and Dushkin did not determine the value of colloidal film thicknesses during the nucleus formation stage.

Dimitrov [51] continued Dushkin's work through studying the nucleation stage, as the first step in the crystallisation process, leading to the formation of ordered monolayer colloidal films on different substrates. He studied the nucleation process in the case of mercury as a liquid substrate as well as glass and mica as solid substrates. In the case of solid substrates, Dimitrov used a similar experimental cell to Dushkin's cell. A halogen lamp was used as a light source with a wavelength of 546 nm, controlled via a transmission filter, together with an Olympus optical microscope equipped with a 10× objective. The whole nucleation process was recorded using a video system and displayed on a TV monitor connected with an image analyser to

calculate the interference fringe radii. However, Dimitrov used this cell not only to observe the crystallisation process but also to trace the liquid film thickness variations with time during the nucleation stage, which was one of the missing points in Dushkin's work. In the case of mercury, he controlled the whole process by obeying Dushkin's recommendation that liquid should be expelled or added continuously to the latex suspension in order to keep the meniscus profile constant. This modification led to the formation of a monolayer colloidal film without the intervention of any multilayers. Herein, Dimitrov used a high-pressure mercury lamp as a light source instead of the halogen lamp that was used with the solid substrates, but with the same transmission filter, which allows transmission of a wavelength of 546 nm only. Besides, Dimitrov's experiment also involved the study of the particle–substrate interaction impact on the nucleation process by changing the electric potential value applied to the mercury surface.

Dimitrov built up an experimental cell, shown in Figure 1.17, to study the growth of monolayer colloidal crystals on mercury surface. Dimitrov's cell was composed of a glass container with a diameter of 5.0 mm at which the high-purity mercury (99.9%) was placed. The container cover was made of bronze in order to conduct electricity and so could be used as a reference electrode for mercury polarisation. A plastic ring was used as a cell wall, which adhered to the bronze cover in a way that allowed the plastic ring to be gently attached to the mercury surface and so restricting the colloidal solution volume in the cell. The solution volume was controlled via the syringe needle pierced in the plastic wall. Dimitrov was able to control the electrode potential applied to the cell by connecting two electric wires, one to the bronze cover and the other to the mercury itself, and the actual applied potential difference was measured by a voltmeter. In this experiment, the latex suspensions were composed of 1.0 wt. % negatively charged polystyrene particles of different diameters of 1696.0, 814.0, 144.0 and 55.0 nm dispersed in deionized water. The temperature was kept at room temperature and the humidity ranged between 30 and 70 %. Sodium dodecyl sulphate (SDS) was added at a concentration of 0.01 mol/L together with 0.15 mol/L sodium chloride in order to improve the mercury surface wettability. A clean polyethylene syringe was used for mercury sampling and injection into the cell to avoid any contamination after the cleaning process.

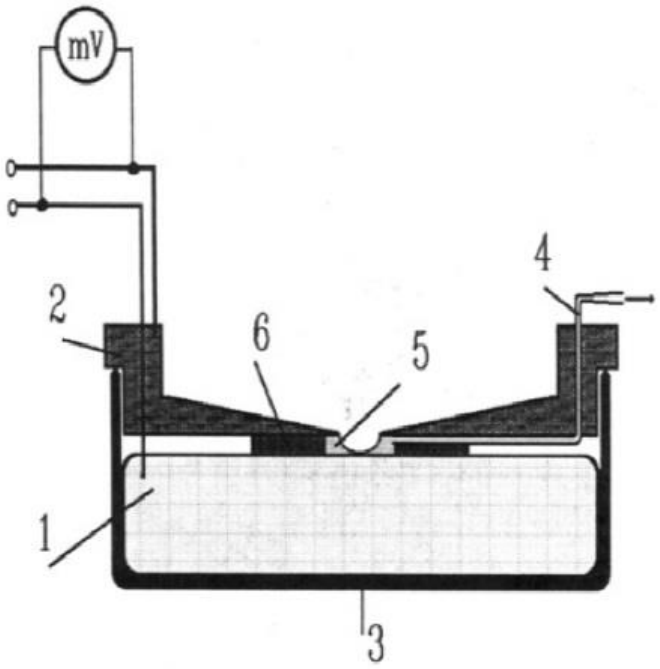

Figure 1.17: Schematic diagram for Dimitrov's experimental cell used for preparation of latex arrays on mercury: (1) mercury, (2) bronze cover, (3) container for mercury, (4) syringe needle, (5) latex suspension, (6) plastic ring (cell wall). Taken from ref. 51.

Dimitrov deduced through his *in situ* observations that the applied electric potential value is one of the crucial factors that significantly affect the nucleation stage on the mercury surface. A negative potential of about 200 mV led to the formation of non-stable hexagonal domains that could not survive when the suspension latex was withdrawn, while at negative potentials below 200 mV, the ordered domains successfully pressed the particles towards the mercury surface. However, these particles suddenly left the arrays forming particle-free films. When positive potentials of more than 100 mV were used, a temporary film appeared owing to the precipitation of particles on the mercury surface. Ordered arrays were observed with open areas at which the suspension drives particles back to the bulk owing to the abrupt increase in the contact angle between mercury, particles and air, causing deterioration of the formed film. In contrast, positive electric potentials between 3 and 15 mV developed the optimum medium for the nucleation process to proceed. Herein, ordered films were obtained, and surfactant particles still adsorbed at the mercury/water interface, which improved the wettability of the mercury surface. As a result, the wetting layer became stable, and the particles were able to resist the film thinning action and did not leave

the film. Dimitrov noticed that at the first stage of the nucleation process, particles that were originally close to each other were aggregating closer and closer forming clusters. Conversely, particles that were originally apart separated much more, forming high- and low-density areas in the latex film, shown in Figure 1.18 a, under the action of the capillary immersion forces. In the second stage, clusters are aggregated together, shown in Figure 1.18 b, and consequently the nucleus area starts to grow, shown in Figure 1.18 c, and finally defects in the nucleus start to disappear, forming a highly ordered hexagonal lattice structure, shown in Figure 1.18 d, governed by the action of the lateral capillary immersion forces. At this stage, capillary forces were able to overcome the friction forces between latex particles and adsorbed sodium dodecyl sulphate particles.

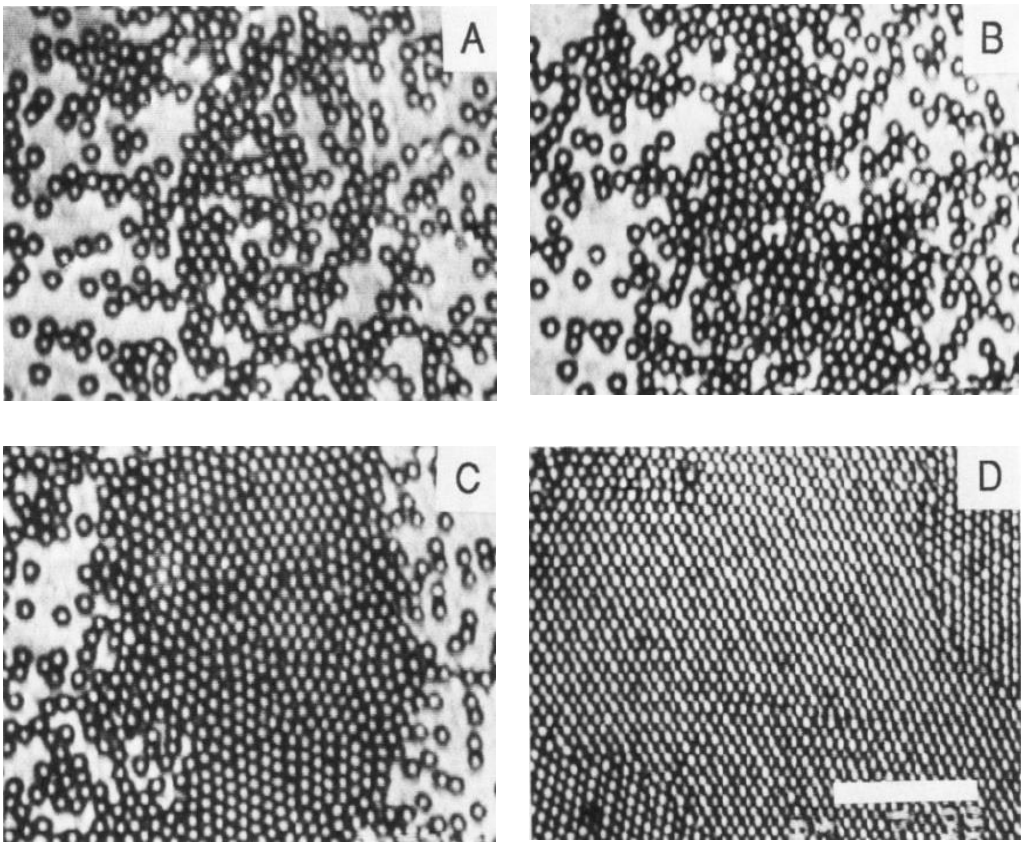

Figure 1.18: Nucleation stages that took place during crystallization of 1696 nm polystyrene latex where (A) attraction of close particle to each other, (B) formation of clusters, (C) growing of nucleus and (D) Formation of highly-ordered hexagonal lattice structure. The reference bar corresponds to 20 µm. Taken from ref. 51.

Dimitrov [46] followed on from his *in situ* study on mercury by trying to control the crystallisation growth of 2D particle arrays formed on flat solid substrates. The interesting industrial importance of the controllable periodicity colloidal crystals in a variety of fields, such as optical gratings, anti-reflection coatings, solar cells, photovoltaics, data storage and microelectronics, was Dimitrov's motivation to start a new series of *in situ* experiments. However, there were many obstacles in front of Dimitrov, such as that the crystallisation growth process that took place on glass substrates was not yet controllable, and so formed films were full of defects, such as voids and undesirable multilayers, which have a significant negative impact on the performance of formed films. In addition, large-sized arrays were not achievable at this stage and parameters that govern the whole process were not studied yet.

Hence, Dimitrov's target was to develop a simple procedure to control the continuous growth of ordered monolayer arrays with a large-sized domain on a glass surface. In order to do so, Dimitrov developed a new technique in which a clean glass substrate was immersed in a colloidal suspension and kept stationary during the experiment, and then gradually pulled out from the solution at the same rate as that of the growing arrays as described in Figure 1.19. The solid substrate width was large enough to avoid any disturbances that may take place at the plate edges. As shown in Figure 1.20, Dimitrov's experimental setup was composed of a cell that was made by attaching glass micro slides together using a polymeric glue. A 1 mm hole was made at the top of the cell in order to withdraw the substrate at a constant rate and to minimise the solvent evaporation rate, so increasing the time available for particle ordering. The cell was kept stationary by attaching it to a fixed string that was attached to a 2.0 cm inner diameter wheel. Dimitrov used a stepper motor to rotate the wheel and consequently withdraw the substrate at a rate ranging between 0.1 and 30 μm/s, which coincides with the array formation rate. A video system composed of a CCD camera connected to a microscope with a resolution power of about 350 nm was used to record the growth process. The real-time growth process was displayed on a TV monitor, and the final film structures were characterised using a field-emission scanning electron microscope.

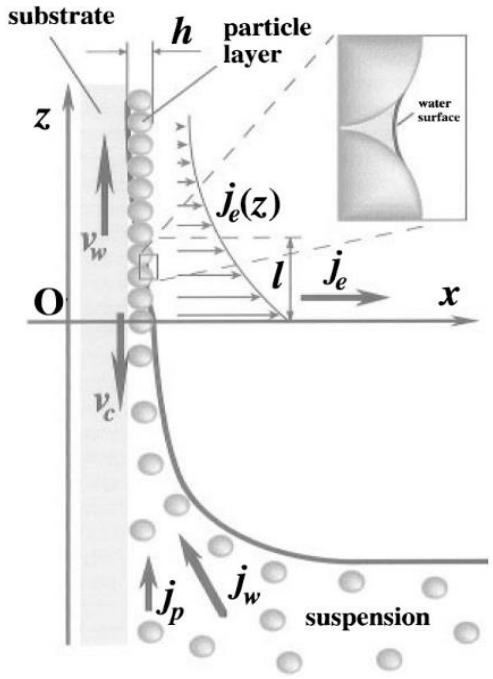

Figure 1.19: Schematic diagram showing the growing of monolayer particle arrays on a substrate plate that is being withdrawn from a colloidal suspension at a rate of v_w while arrays growing rate is given by v_c and j_w is the water influx, j_p is the respective particle influx, je is the water evaporation flux, and h is the thickness of the array. Taken from ref. 46.

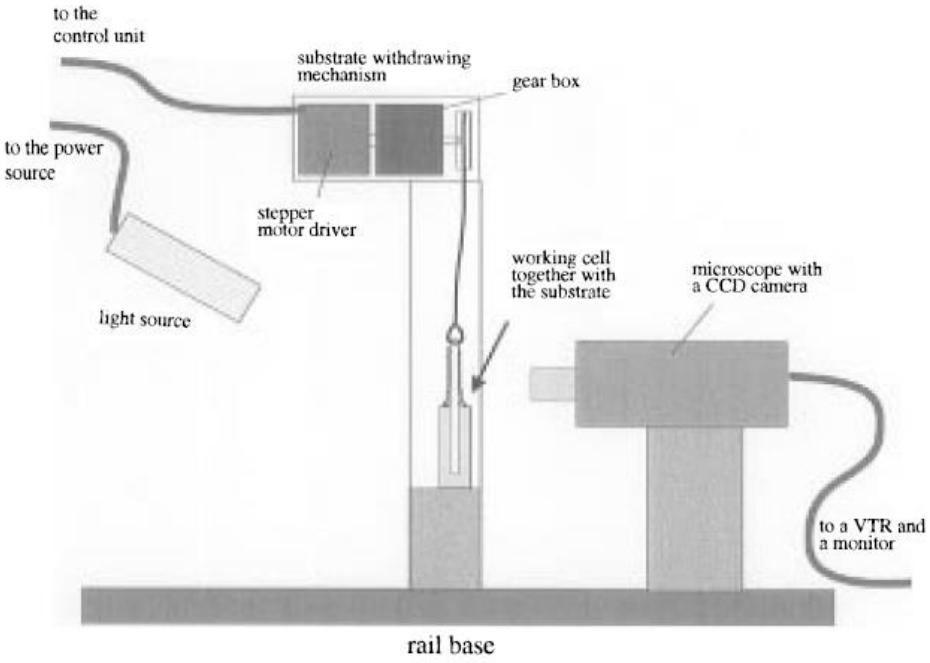

Figure 1.20: Schematic diagram for Dimitrov's layered particle array formation setup. Taken from ref. 46.

Brilliant colours were clear and easily observed from the final films by the naked eye. However, the coating was fragile and not stable. For that reason, Dimitrov coated the formed particle films with a thin layer of gold or silver using a vacuum-coating technique to increase the films' stability. Polystyrene particles with different diameters, [79 nm – 2106 nm] as listed in Table 1.2, have been suspended in water collected from an MILLI-Q SP.TOC reagent water system. 1.0 % volume fraction polystyrene-water suspensions were prepared and filtered through cellulose acetate membranes to remove any particle aggregations and then fed to 76 x 26 x 1 mm glass micro slides. Glass plates were subjected to a treatment procedure in order to increase their wettability prior to addition of colloidal suspensions. First, glass substrates were kept overnight under the surface of chromic acid then have been rinsed with water. Secondly, they have been fully immersed in 0.1 M sodium dodecyl sulphate (SDS) solution for about 1 hour then rinsed with water and let to dry. In addition, the open atmosphere existing around the cell created a good medium for organic traces in air to settle down on the glass plates, causing dewetting and so destroying the films formed upon these glass surfaces. Hence, Dimitrov added 0.01 mg/mL of ferritin to the suspension together with the SDS solution in order to increase the wettability of glass substrates. The cell itself has been sonicated before starting the experiment in a water bath, washed with a soap solution, rinsed with water and finally dried.

Dimitrov observed from electron micrographs that hexagonal close-packing ordered 2D colloidal arrays were formed on glass substrates. It was found that the domain size of the central areas was always larger than that in the cell peripheral regions. This observation was attributed to the lower water evaporation rate at the cell centre. Therefore, wetting films formed at the cell peripheries always have smaller thicknesses. In this experiment, Dimitrov showed that particle diameter has no impact on the total water evaporation flux per unit length, which remained constant at the array's leading edges. Particles in thin films with thicknesses smaller than the particle diameter were aggregated together under the action of lateral capillary immersion forces, forming ordered 2D hexagonal packing areas. On the other hand, wetting films with thicknesses close to the particle diameter were governed by the hydrodynamic flux, which forces them to occupy free positions in the growing domain.

Table 1.2: Specifications of the Latex Particles used in Dimitrov's experimental cell. Taken from ref. 49.

Latex Code	Particles diameter (nm)	Polydispersity (nm)
SS-021-P	2106	±17
SC-171-S	1696	±47
SC-108-S	1083	±10
SC-953-S	953	±9
SC-081-S	814	±23
SC-051-S	506	±10
SC-048-S	479	±5
SC-032-S	309	±4
SC-015-S	144	±2
SC-008-S	79	±2

Furthermore, Dimitrov deduced that polydispersity significantly affects the uniformity of 2D ordered particle arrays formed on flat solid substrates. He observed that large uniform oriented domains were formed in the case of low polydispersity of about 1.0 %. However, particles with a higher polydispersity of 2.8 % showed many dislocations along the formed ordered domains, which can be easily noticed through the disturbances in colour uniformity that resulted when these films were illuminated with white light. Impurities or the existence of much larger particles in the suspension considerably disturbed the array growth and resulted in the formation of undesirable multilayers in different locations along the formed films. Dimitrov successfully controlled the formed domain size by either changing the evaporation rate of water, which is the main driving force in the whole process or by controlling the thickness of the wetting film. He also realised the high dependence of large-size domain formation on the wettability of the substrate surface as well as the wetting layer thickness and polydispersity of the suspension particles.

Yamaki [52] reported that two-dimensional ordered arrays of colloidal particles formed on mercury surface are governed by a size-dependent phenomenon by which larger particles form arrays that occupy the centre and these arrays are bordered by smaller particles as shown in Figure 1.21. Yamaki deduced this new separation phenomenon from an experiment in which two-dimensional ordered colloidal arrays were obtained from suspensions containing polystyrene particles with a diameter of 144 nm together with polystyrene particles with a diameter of 55 nm with a volume ratio of 1:3, respectively. Images obtained from electron microscopy showed the occurrence of a clear separation only when the size of the large particles is two times the size of the smaller particles. Otherwise, a mixed array was obtained.

Yamaki's experiment confirmed that the size-separation phenomenon is governed by two types of force: (1) lateral capillary forces that are obtained during particle ordering owing to the variations in the liquid surface curvatures; and (2) convective flow, which is derived from gradual liquid evaporation, which forces particles to flow towards highly ordered areas. However, the separation mechanism under the action of convective flow was not explained clearly, which was a drawback of Yamaki's work. Later on, Yamaki defined an order parameter that gives the ratio of the number of large particles surrounding a large particle as six, which is the maximum number of large particles that can border any particle in a well-ordered close-packing structure. This order-parameter enabled Yamaki to judge the degree of separation, so confirming results obtained from electron microscopy images where a high value means the existence of a clear separation while a small order parameter indicates the occurrence of a poor separation and the formation of mixed areas.

Yamaki followed his experiment by doing a computer simulation through which he was able to mimic the separation that took place in a real binary system. This helped to study in detail the self-assembly process of particles suspended in wetting films. The behaviour of particles in binary mixtures of large and small particles under the action of lateral capillary force and convective flow was successfully simulated by using the Monte Carlo method [53]. Structures containing an overlapping of particles were excluded for simplicity. Particles were represented as disks in the x-y plane and the interaction energy between particles was given by the following equation [52]:

$$E = 0.5 \log r \tag{1.10}$$

Where r is the distance between the centres of the particles and E is the non-dimensional interaction energy.

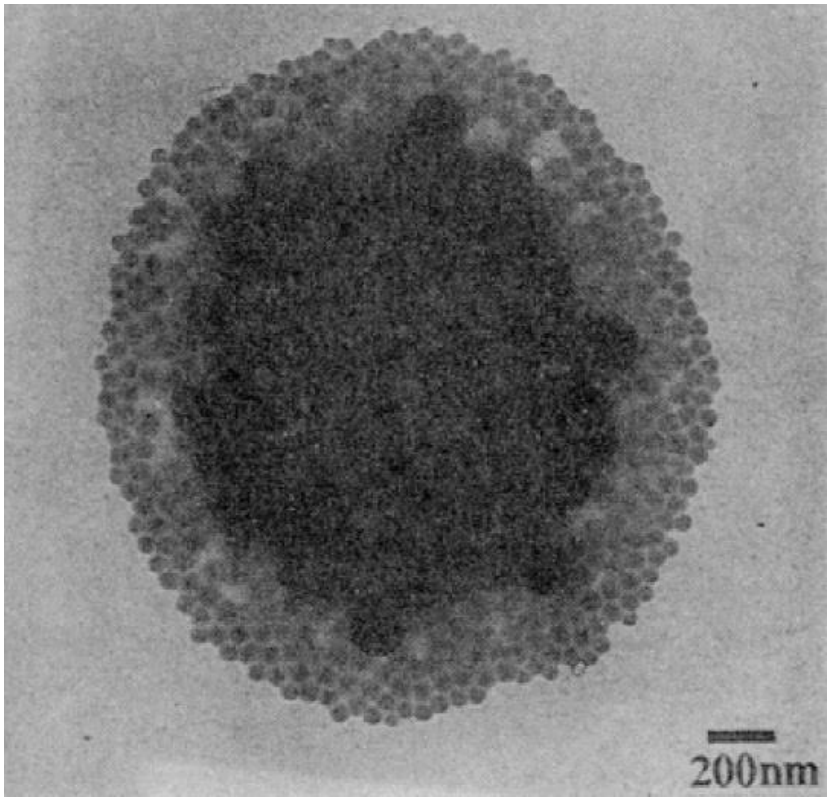

Figure 1.21: Transmission electron microscope images of two-dimensional arrays obtained from a binary mixture composed of polystyrene particles of 55 ± 3.4 nm and 144 ± 2.0 nm in diameter. Taken from ref. 52.

The diameter of the larger particles was taken as the wetting layer initial thickness, which regularly thins during the self-assembly process until reaching zero at the end of the experiment. A gradual decrease of solution layer through the program was obtained by setting the water evaporation to take place at a constant rate. Evaporation of water was considered to be the driving force for both the lateral capillary forces and the convective flow. During this investigation, different rates of evaporation and various particle diameters as the smaller specious (R_s) have been used while larger particles diameter (R_L) were kept constant as 144nm in all experiments and each simulation has been repeated 10 times to confirm the results.

Profiles obtained from Yamaki's simulation program were identical to the real profiles developed from electron microscopy. The results showed that a clear separation took place, as shown in Figure 1.22, if and only if the ratio between the small and large particles diameters was 0.5 [R_s / R_L = 0.5]. Otherwise, a mixture area appeared containing both different diameters, which deteriorates the size separation process. In addition, simulation profiles confirmed that both lateral capillary forces and convective flow were not only responsible for the 2D colloidal assembly, which leads to the formation of highly ordered colloidal films, but they also governed the size-separation phenomenon where the convective flow was mainly effective on larger particles, especially in the early stages of the assembly process. Yamaki explained this phenomenon by classifying the particle separation process into two stages: (1) the first stage takes place in the early stages of self-assembly when the thickness of the wetting layer is larger than the smaller particles' diameter and smaller than that of the larger ones. At this stage, smaller particles were completely dipped under the water surface while larger particles were partially immersed in water. Hence, only larger particles were able to interact with neighbouring particles under the action of convective flow. (2) The second stage starts when the wetting layer thickness becomes smaller than the smaller particles' diameter. At this stage, both larger and smaller particles were protruding from the water surface, and both can interact. Particle interactions in the second stage with the nearest neighbours took place under the action of lateral capillary forces while interactions with other particles in the suspension were governed by convective flow.

In 1996, Nagayama [54] reported that observation of thin liquid film surfaces is governed by the separation that takes place between any two immiscible mediums, such as water and air as shown in Figure 1.23. He showed that the difference in refractive indices between these mediums is responsible for the appearance of geometric boundaries, which are known as colloidal films. Changing the nature of the suspension in which colloids are dispersed was found to have a great impact on the quality of the developed films after solvent evaporation owing to the reduction of the inhomogeneous distribution of colloids through the colloidal suspension.

In addition, Nagayama confirmed that colloidal films start to form once the liquid layer thickness reaches the particle diameter, as shown in Figure 1.24. In this situation, particles were protruding from the liquid layer surface causing a deviation in the meniscus profile. This led to a clear observation of the developed colloidal films. Thin liquid films with small thicknesses act as a container for particles in which particles are in continuous motion under the action of convection flow. Owing to the steady evaporation of water, particles became partially submerged. Herein, particle movement was governed by the surface tension force and ordering of particles in 2D arrays starts to take place under the action of the lateral capillary forces.

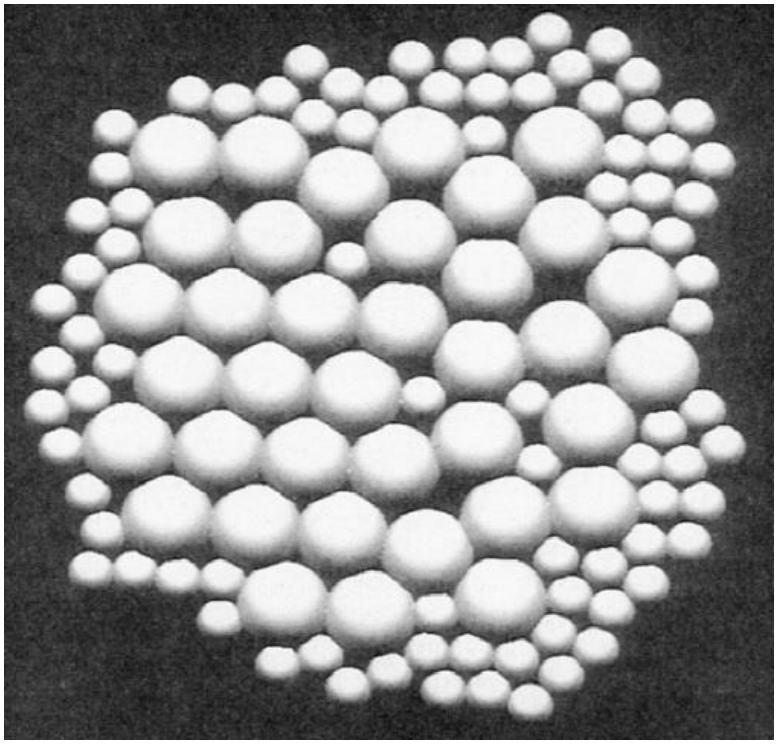

Figure 1.22: Profile obtained from Yamaki's simulation program showing the separation of particles that took place during self-assembly process when R_s/R_L = 0.5. Taken from ref. 52.

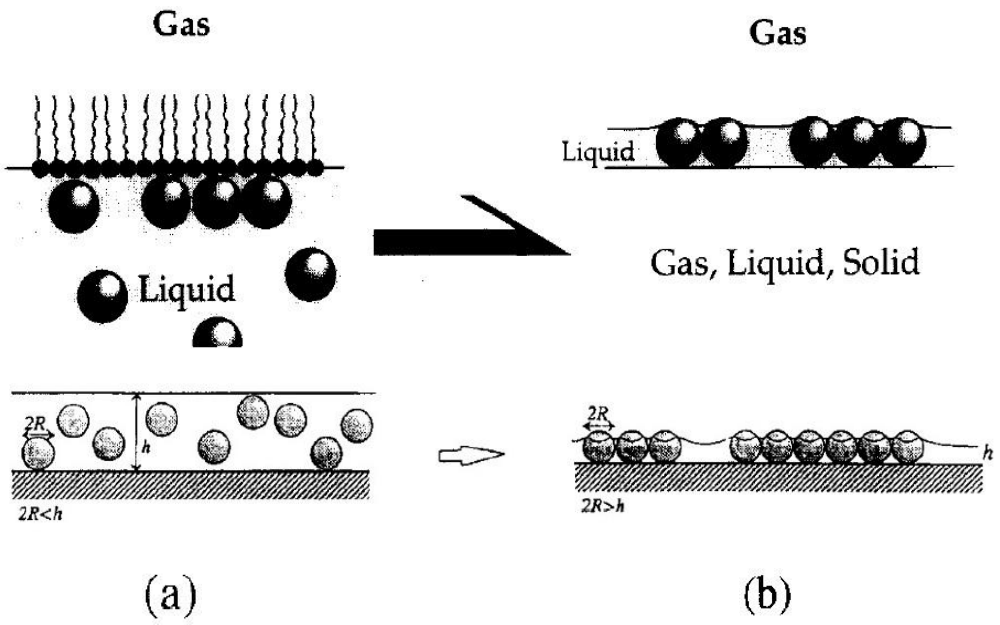

Figure 1.23: A schematic diagram illustrating the growth of 2D colloidal arrays through liquid medium. (a) Particles Brownian motion due to the water evaporation. (b) Ordering of particles governed by lateral capillary force once liquid layer thickness reaches particles diameter. Taken from ref. 54.

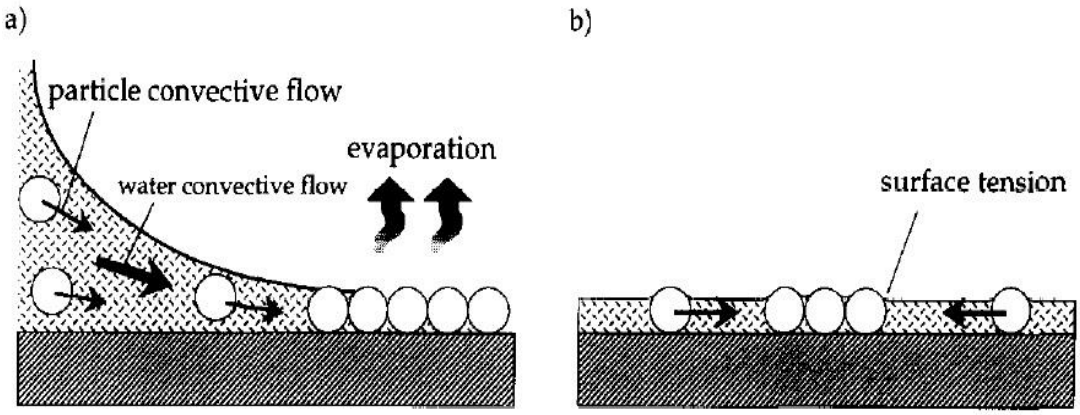

Figure 1.24: A schematic diagram illustrating the two steps for the particles crystallization. (a) Directional motion of particles due to convection flow stimulated by water evaporation. (b) Attraction between particles that partially immersed in liquid due to lateral capillary force. Taken from ref. 54.

Substrate surface roughness was one of the factors investigated by Nagayama in order to study its impact on the quality of ordering of the fabricated monolayer colloidal films. Monodisperse polystyrene latex particles were able to be uniformly ordered on the glass substrate regardless of the surface roughness. However, protein molecules were too small to do so. For that reason, Nagayama used liquid substrates, such as mercury and glucose solution, instead of solid substrates, such as glass and mica, for the development of 2D arrays of colloidal crystals. For mercury as a substrate, Nagayama set up a chamber as shown in Figure 1.25, which was filled with oxygen gas with a pressure not less than 1 atmosphere. Mercury was placed in the bottom of the chamber, and its surface was cleaned under vacuum. Then, 10.0 μl of the protein solution was added to the mercury surface through a microsyringe. After about 10 s, a protein monolayer had spontaneously formed on the mercury surface. Finally, the dried monolayer film was transferred through a carbon supporting film in order to be investigated by electron microscopy.

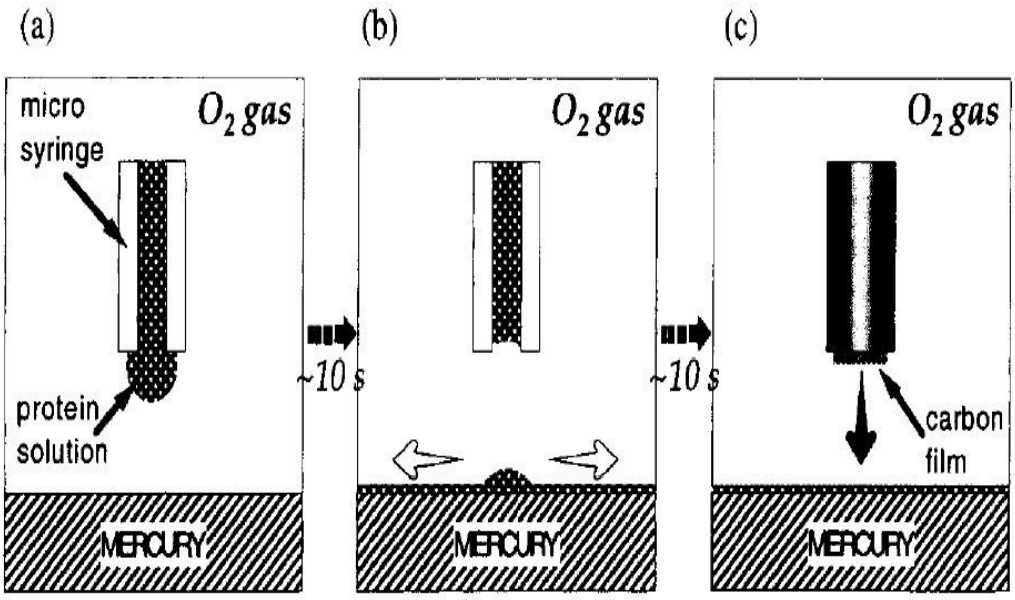

Figure 1.25: Schematic diagram for Nagayama's set up used for the development of protein monolayer arrays on mercury surface. Taken from ref. 54.

Nagayama followed on his investigations on mercury surface by trying to develop protein monolayer films on glucose solution as a liquid substrate instead of mercury. In order to do so, 1.0 µl of protein solution was injected into a freshly prepared primary solution as shown in Figure 1.26. The primary solution, which is composed of 0.5 ml of 10 mM morphine ethyl sulphate (pH 5.7) together with 2.0 % glucose and 150 mM NaCl, had a higher density than that of the protein solution, which allows the protein solution to float and spread over the primary surface and consequently form a thin monolayer protein film at the water/air interface after about 10 minutes. The developed thin films formed on the glucose surface were transferred to the electron microscopy specimen grid through porous carbon grids that were placed on the surface of the glucose solution. Finally, the collected protein arrays on carbon grids were stabilised by the deposition of an additional thin carbon layer with a thickness of about 5.0 mm on the protein arrays. TEM images showed that hexagonally packed 2D highly ordered arrays of protein were successfully formed on the surface of glucose solution surface with a large area of about 1.0 µm^2. Furthermore, small standard deviations of magnification, elongation and rotation deduced from analysis together with the Gaussian distribution observed in histograms confirmed that the monolayer crystals produced have only a slight distortion.

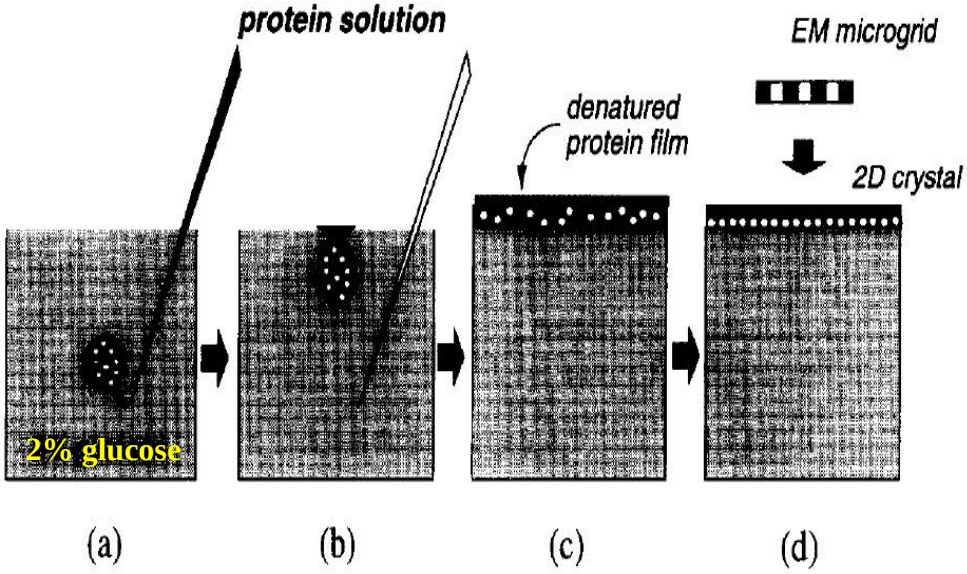

Figure 1.26: Schematic diagram for Nagayama's set up used for the development of protein monolayer arrays on glucose solution surface. Taken from ref. 54.

In 1997, Deegan performed an experiment to study the formation of a ring-like deposit when a drop of coffee is placed and dried on a solid surface. He claimed that the coffee-ring phenomenon is related to the evaporation of solvent from edges. Liquid evaporation is followed by a spontaneous compensation by liquids from the interior of the drop, leaving a ring with an empty centre on the solid surface. Deegan explained that by assuming the occurrence of a power-law growth of the ring mass with time, which had been initiated by the drying of the liquid at the edges of the droplet. He confirmed the self-assembly growth from the drop centre to its edge by performing microscopic investigations as shown in Figure 1.27 using a variety of substrates, solutes and volatile solvents.[55]

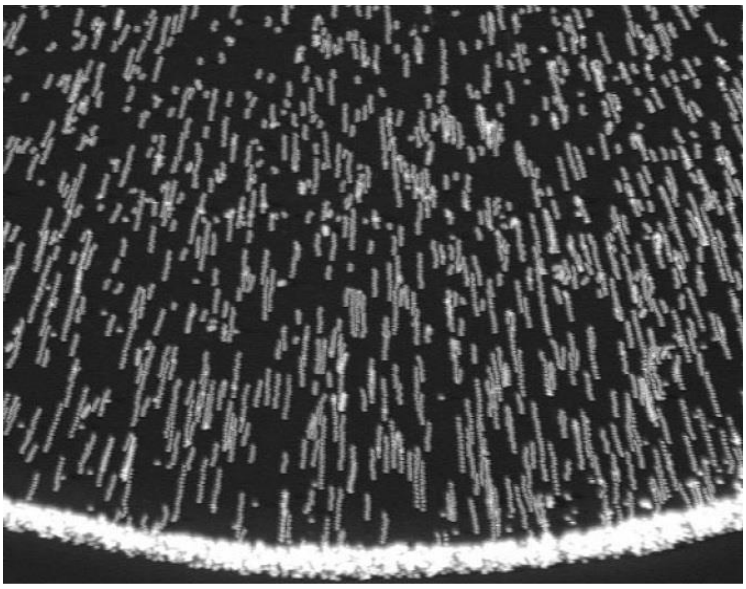

Figure 1.27: A microscopic pictures shows the motion of microspheres form the interior to edges. Taken from ref. 55.

Deegan followed on from previous studies by trying to study the exact ring formation mechanism and factors that govern the whole process. As a start, Deegan performed an experiment to observe the behaviour of a deionized water drop with a volume of 0.5 mL placed on a freshly cleaved mica as a flat substrate and left to dry where its radius against time was recorded. Then, he prepared different solutions by adding a variety of solutes such as sugar, dye molecules, 10mm colloidal polystyrene particles independently as different solutes with different volume fractions ranging from 10^{-6} to 10^{-1} on the same mica substrate. The drop behaviour in each case has been recorded. Afterwards, he used glass, metal, polyethylene, roughened Teflon, ceramic,

and silicon instead of mica as different substrates to study the effect of the chemical composition of substrate surfaces on the ring-like deposit behaviour. Also, he tried acetone, methanol, toluene, and ethanol instead of water as a different solvent medium. Then, he changed the environmental conditions such as temperature, humidity, and pressure. Deegan realised through his observations that none of the mentioned factors has any effect on the behaviour of drop behaviour during the ring formation. Afterwards, Deegan started a new series of investigations to study effects of other factors such as solute diffusion, Gravity and electric field. However, advection motion of 1 mm polystyrene colloids towards the drop edges that took place when liquid starts to evaporate showed that gravity is not a considerable reason in the case of ring formation phenomenon. Also, similar observations resulted from both a pendant drop that was dried upside down and a sessile drop which was dried right side up were enough to neglect gravity from the list. Finally, electrostatic fields with different configurations also had no visible effects on the drop behaviour during the drying stage.

He discovered that the whole process is governed by two crucial factors: (1) Contact line pinning, where a drop deposited on a smooth Teflon substrate was found to shrink in size without the ring formation at the end of liquid evaporation. (2) Liquid evaporation rate was found to be an important factor on ring uniformity where covering the drop after deposition on glass substrate with a lid, which includes only one small hole in the centre in order to reduce the rate of evaporation, gave a uniform ring instead of a ring with a high solute concentration at the edges. As liquid starts to evaporate, it was expected that the liquid layer would recede and consequently the contact line would go back to the initial air–liquid interface from position A to position B, as shown in Figure 1.28. However, the contact line, in reality, will not move and will still be pinned in position A. That action could not happen unless liquid loss owing to evaporation process was compensated. Evaporation of liquid from the drop edges induces outwards radial flows. These flows drag solute towards the contact line and after some time the accumulation of solute causes self-pinning of the contact line, which is accompanied by the formation of a characterised coffee-like pattern as shown in Figure 1.28 b.

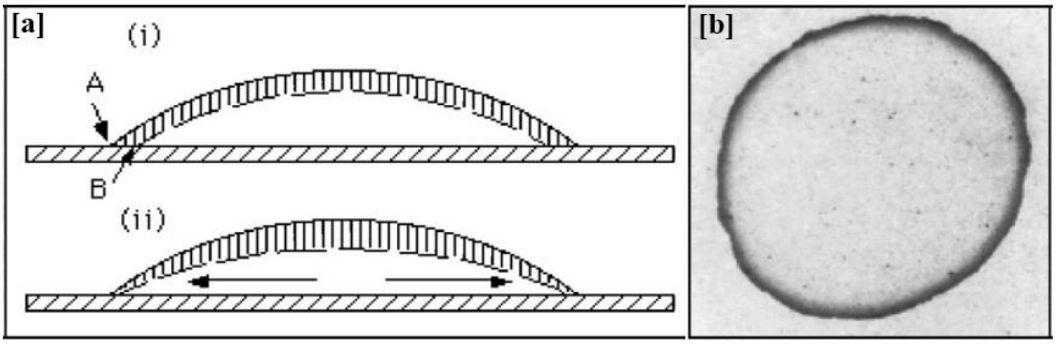

Figure 1.28: [a] Schematic illustration of the origin of the adventive current. (i) If the contact line were not pinned, uniform evaporation would remove the hashed layer, the interface would move from the solid line to the dashed line, and the contact line would move from A to B. However, if the contact line is pinned then the retreat from A to B is not possible, and there must be a flow that replenishes the lost fluid. (ii) Shows the actual motion of the interface and the compensating current. [b] A photograph of a dried coffee drop. The dark perimeter is produced by a dense accumulation of coffee particles. The radius is approximately 5 cm. Taken from ref. 44.

In 1999, Jiang [9] was the first to study the impact of close-packed silica–air array thickness on the optical spectrum developed from these periodically dielectric colloidal crystals. The high dependence of these dielectric materials' industrial applications upon both symmetry and sample length scale was the motivation behind this study, especially with the great demand at that time to overcome the difficulty in fabricating three-dimensional photonic band-gap materials with nanometre-scale structures. Matching refractive indices between colloids and suspensions was a good approach to increase the stability of the obtained colloidal crystals. However, it decreases the diffractive properties of these structures to a great extent. Gravity-sediment colloidal samples showed high transmission spectra. However, these samples have been limited to specific volume fractions of colloids, characterised by polycrystalline domains, and their array growth was very difficult to control. Therefore, deposition of colloidal dispersions on different substrates was found to be the optimum method for fabricating uniform monolayer colloidal films [54]. However, the effect of sample thickness on the optical properties of colloidal films fabricated through this method has not been studied yet.

Jiang's work resembled Nagayama's self-assembly method in which capillary forces were used to organise 1.0 μm polystyrene colloids into uniform monolayer arrays on flat substrates. However, Jiang exploited that technique to fabricate uniform colloidal multilayers with thicknesses ranging from two layers up to hundreds of well-ordered colloidal layers instead of monolayers. In order to do so, monodisperse silica nanospheres have been prepared through Stȍber-Fink-Bohn method with different particle sizes ranging between 200 to 700 nm with a standard deviation less than 7% where sizes and sizes distributions have been measured using scanning electron microscopy (SEM) and dynamic light scattering (DLS) instruments. Glass micro slides which have been used as flat substrates were kept under the surface of chromic – sulphuric acid cleaning solution overnight, then washed with distilled water and finally dried with nitrogen gas just before the experiment. Then, clean micro slides were immersed into silica alcosol solution and covered by a crystallisation dish to avoid any contamination, and the whole solution was kept at a constant temperature of about 22^{o}C. Fabricated samples were then coated with a thin layer of gold to enhance imaging through SEM and then some gold-coated samples were scratched with a sharp razor blade in order to facilitate edge imaging of samples to measure the sample thickness. Jiang prepared different volume fractions of 0.1%, 0.5%, 1.0%, 1.5%, 2.0%, 2.5% and 3.0% in order to study the effect of volume fractions on the samples thicknesses. Also, he used three different evaporation conditions; the open atmosphere, covered in a crystallising dish and covered in a crystallising dish with an ethanol environment in order to study the effect of evaporation rate on samples thicknesses. Jiang was able to control the output film thickness through controlling: (1) the type of solvent used in the colloidal suspension; (2) the solid content ratio in the solution; and (3) the colloid particle size and size distribution.

Scanning electron micrographs showed the formation of highly ordered close-packed silica colloidal crystals with a large domain area of about 10 μm. This conclusion was confirmed through the two-dimensional Fourier transforms of SEM images as shown in Figure 1.29. Jiang continued his work by investigating the degree of alignment of domain boundaries of silica colloidal crystals in order to fully characterise the spatial structure of fabricated colloidal crystals. Different images were compared to check the alignment of the hexagonal registry of the array lattice over

these long length scales. As shown in Figure 1.30, it was found that all the examined samples exhibited perfect alignment and no grain boundaries were observed. It was also found that the colloidal films formed through Jiang's method exhibited a uniform thickness and regular arrangement from top to bottom, both in the case of the 15 layers sample, shown in Figure 1.31 A and the thicker sample of 50 layers as shown in Figure 1.31 B [9],[56].

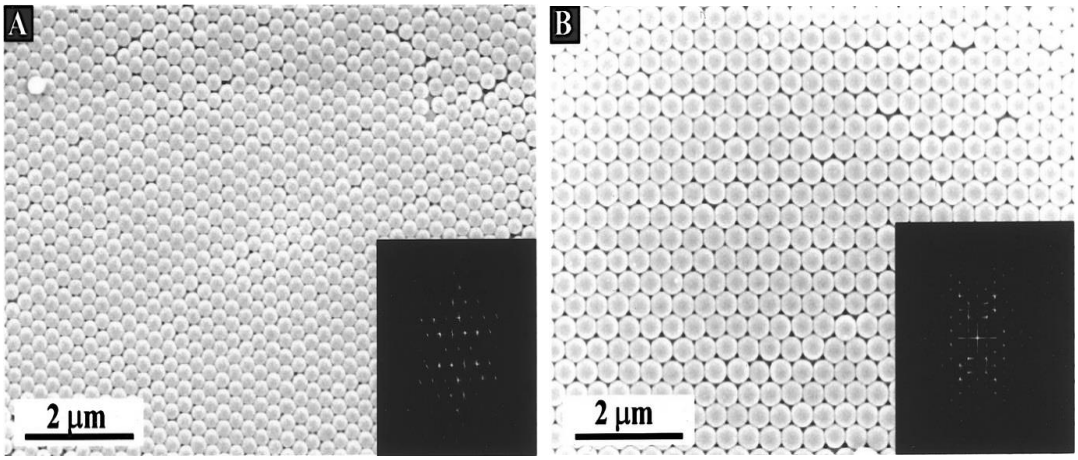

Figure 1.29: Scanning electron images (SEM) of two samples with different particle diameters (x 12 000 magnification) showing highly ordered arrays with a long domain size. The insets show Fourier transforms of 40 x 40 µm2 regions. Key: (A) 298.6 nm; (B) 437.4 nm. Taken from ref. 9.

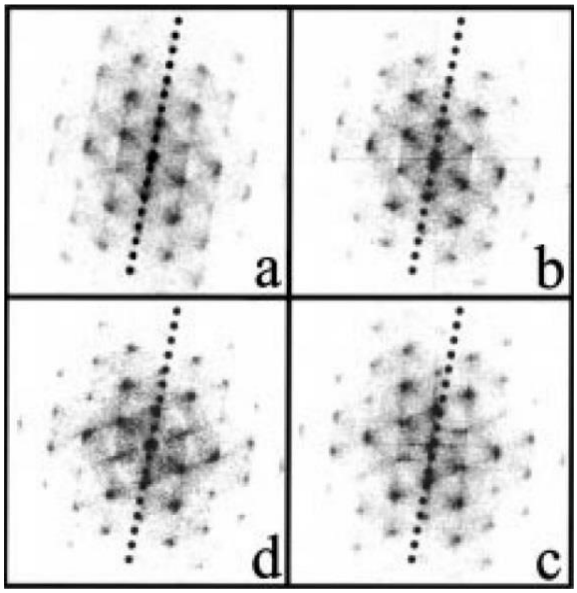

Figure 1.30: Fourier transforms (FFT) of four images of a 1 cm^2 colloidal silica single crystal representing four corners where image c was closest to the edge of the sample. The four parallel dashed lines indicate one reference direction, and demonstrate that the four images are of the same orientation with a maximum deviation of 1.6 degrees. Taken from ref. 9.

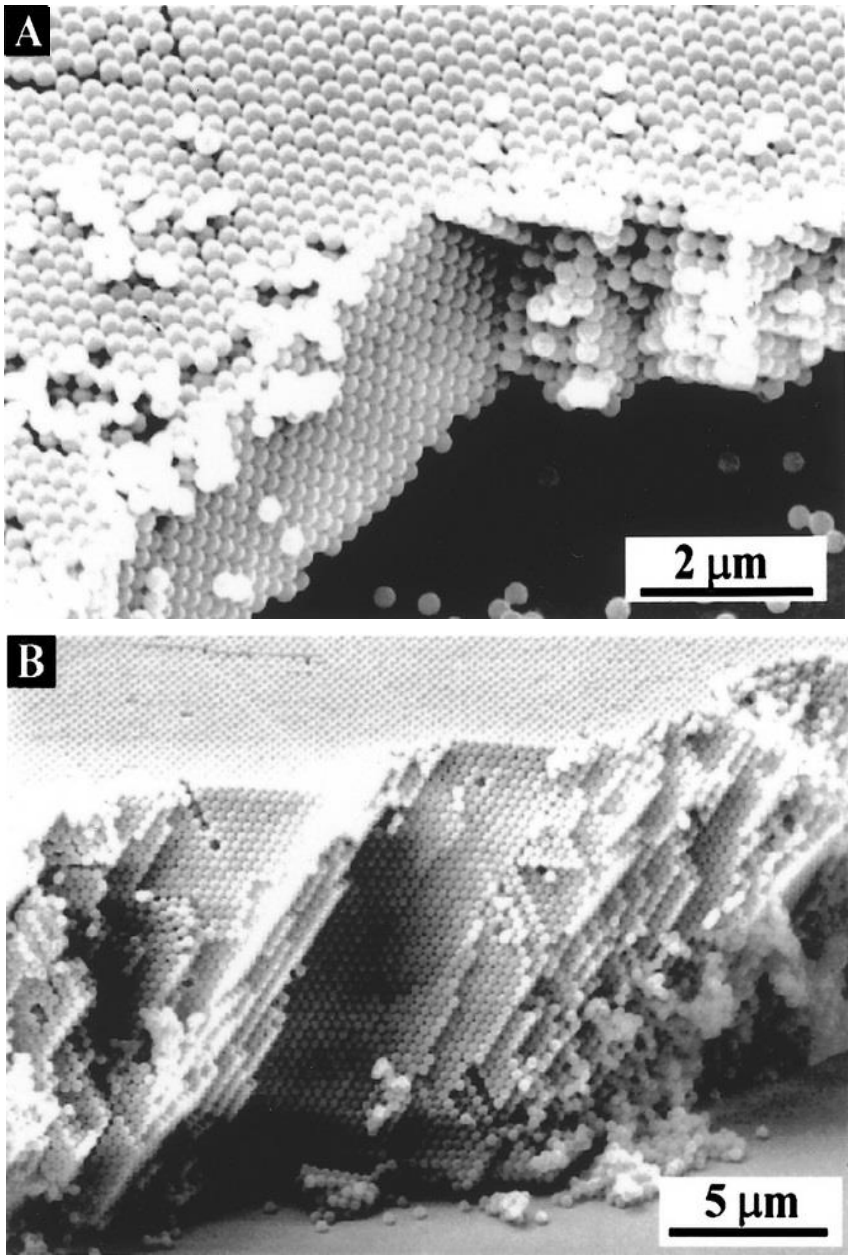

Figure 1.31: Scanning electron images (SEM) of two silica samples with different thicknesses (x 12 000 magnification) showing regular arrangement from top to bottom regardless to number of layers. Key: (A) 15 layers; (B) 50 layers. Taken from ref. 9.

Jiang also proved that the standard deviation of colloids is a, if not the, crucial factor in the ordering quality of the fabricated arrays. He revealed that the standard deviation of particle size distribution should be less than 8 % in order to form ordered colloidal crystals with a long domain size. As shown in Figure 1.32, the sample with a higher standard deviation of 14.2 % exhibits a diffuse ring in the Fourier transform. This is an indication of lower order quality. In contrast, the sample with a narrow size distribution of 3.8 % gives a well-ordered array over a long length scale, and its scattering pattern in the Fourier transform exhibits sharp peaks. This confirms that the hexagonal close-packed structure formed. In addition, polydispersity was found to have a great effect on the optical properties of colloidal crystals formed. It was observed that samples fabricated using the lower standard deviation particles gave brilliant colours. However, films formed using the higher standard deviation particles were white and opaque, even in the case of very thin films.

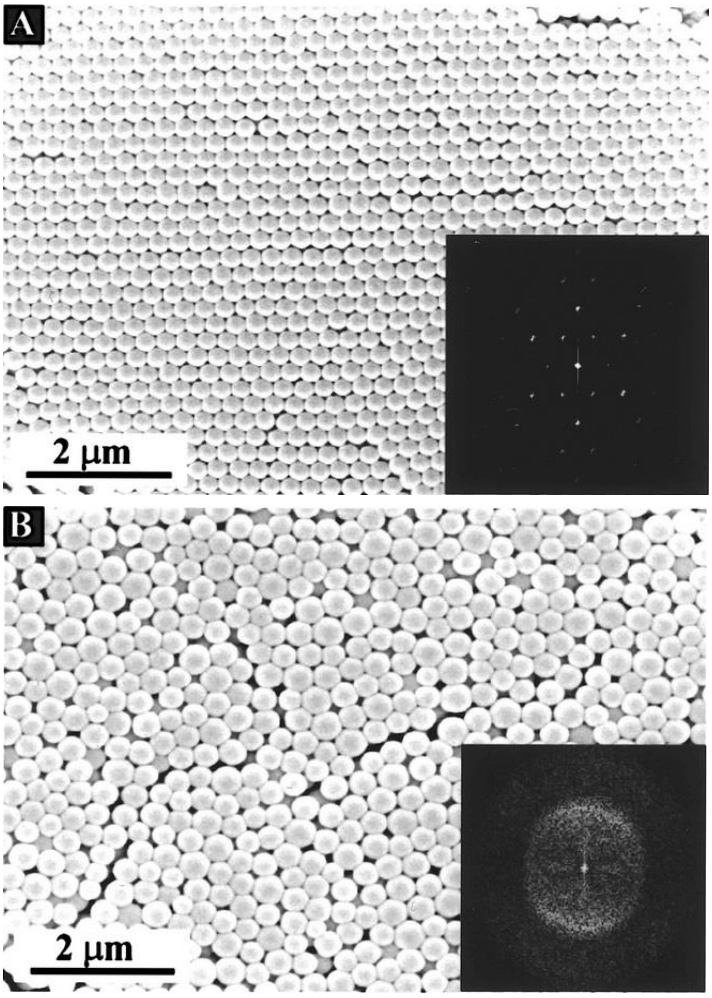

Figure 1.32: Scanning electron images (SEM) of two silica samples with different particle size distributions (S.D.) (x 12 000 magnification): (A) S.D. = 3.8%; (B) S.D. = 14.2%. The insets show Fourier transforms of 40 x 40 µm² regions. Taken from ref. 9.

Jiang followed on by studying the crucial factors governing the film thickness. In order to do so, he performed many experiments where multilayers were fabricated through multiple depositions. Fabricated monolayers were allowed to dry first and then were reimmersed in the colloidal dispersion where the stepwise coating was done successfully as shown in Figure 1.33. Jiang showed that film thickness is highly dependent on two parameters: (1) particle diameter (d), which is inversely proportional to the number of layers formed in the colloidal film; and (2) particle volume fraction (V.F.), which is directly proportional to the layer thickness. As shown in Figure 1.34, as the particle size decreases from 396.6 nm to 206.4 nm the number of layers increases gradually from 7 to 14 layers, (2) particle volume fraction (V.F.) which is directly proportional to the layer thickness where at higher colloidal suspension concentrations, thicker films with a higher number of layers were produced as clearly shown in Figure 1.35.

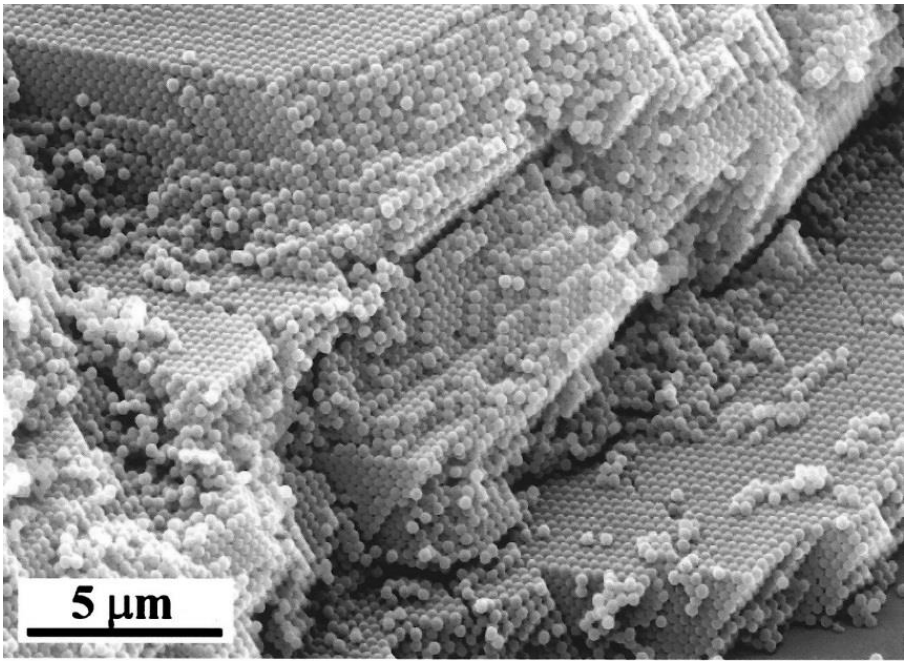

Figure 1.33: Scanning electron micrographs (SEM) for multilayer silica colloidal crystal fabricated through four successive coatings. Each deposition provides 12 colloidal monolayers. Taken from ref. 9.

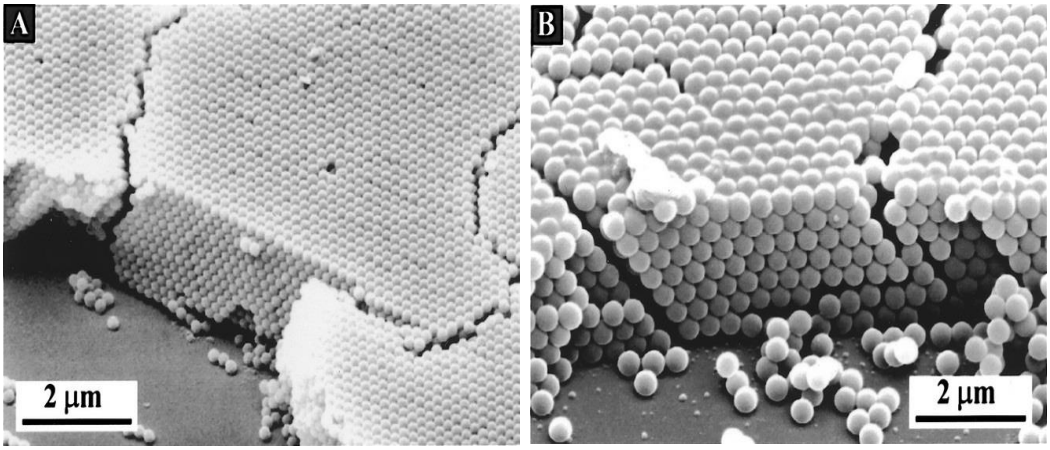

Figure 1.34: Scanning electron images for two silica samples with different particle diameters (206.4, 396.6 nm), grown from solutions with the same volume fraction (0.5%). (A) The 206.4 nm particle size produced a film with 14 layers, and (B) The 396.6 nm particle size produced a film with 7 layers. Taken from ref. 9.

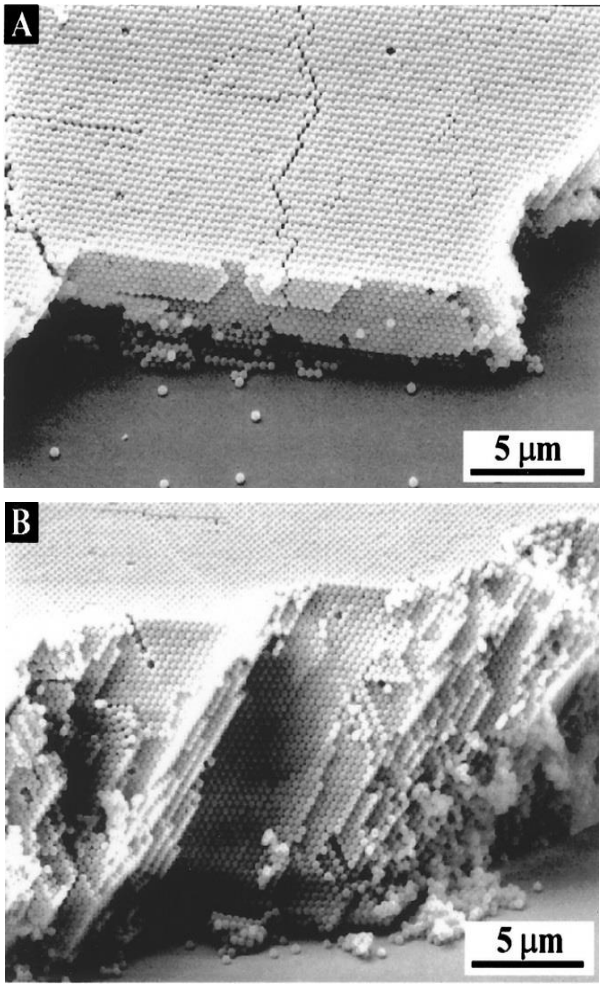

Figure 1.35: SEM cross-sectional images of two samples grown from solutions with different particle volume fractions. In both parts A and B, the spheres are 298.6 nm in diameter. (A) V.F.) 0.8%, 18 layers; (B) V.F.) 3.0%, 50 layers. Taken from ref. 9.

Im *et al.* [57] performed a new series of investigations on how to control colloidal crystal thickness using a different technique. Unlike Jiang's technique, which relies on changing the concentration of the colloidal suspension, a glass substrate was dipped with various tilting angles in a colloidal suspension with a constant concentration. For this study, freshly cleaned glass substrates have been immersed into 0.2 wt. % polystyrene colloidal suspension with different tilting angles as shown in Figure 1.36. Then, colloidal suspensions have been placed in an oven at 60°C to keep the water evaporation rate constant at about 0.7 mL/h. Colloidal crystals formed on a glass substrate have been characterised through scanning electron microscope. Observations showed that colloidal assembly successfully occurred at two interfaces: (1) colloidal assembly at the air–water interface, which starts as explained before by Nagayama [54]; and (2) colloidal assembly at air–water–glass substrate interface as shown in Figure 1.37.

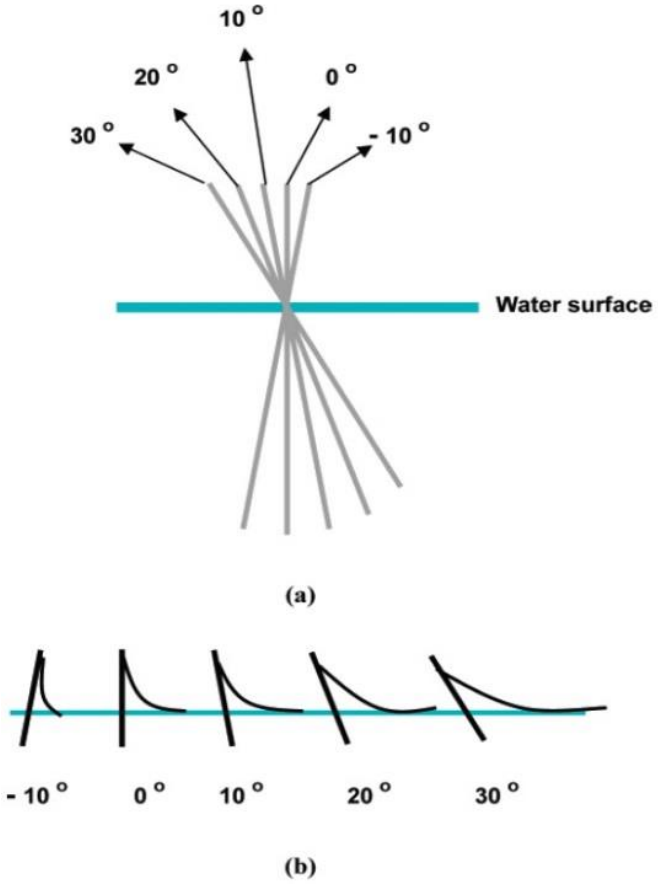

Figure 1.36: (a) The normal to the water surface plane is defined as 0° and established tilted angles -10°, 0°, 10°, 20°, and 30°, respectively. (b) Contact line shapes with tilted angles. Taken from ref. 56.

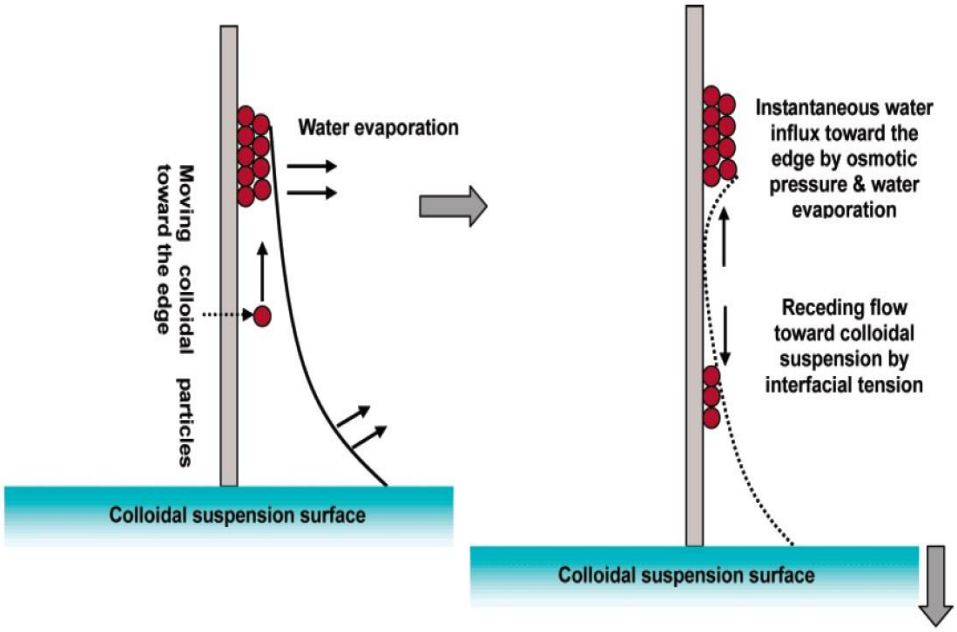

Figure 1.37: Systematic illustration of the formation of multiple contact line patterns. Taken from ref. 56.

Colloidal particles pinned once the glass substrate was immersed in the colloidal suspension. Consequently, the contact line was also pinned. As water evaporation proceeds, the contact line will only thin without moving back. This happens owing to influx water flow that took place towards the edges, which exhibit the highest evaporation rates. That theory coincides with Deegan's explanation [55] for how a coffee ring forms when a drop is deposited on a flat solid substrate surface. As a result, a colloidal assembly that took place at the air–water–glass interface produced highly ordered face-centered cubic colloidal structures with (111) planes parallel to the glass substrate. However, the thickness was found to be highly dependent on the tilting angles of the glass substrate dipped in the colloidal suspension. Angles between -10° and 0° gave very small thicknesses, which were not sufficient for particles to be assembled, while angles between 20° and 30° produced even surfaces with smooth contact line shapes. A tilting angle of 10° produced an intermediate thickness, which ensures that uniform surfaces will be obtained if and only if the glass substrate is dipped into the colloidal suspension at a tilting angle higher than 10°. In addition, Im et al. showed that increasing the colloidal crystal thickness decreases the photonic band gaps depth. However, that increase in thickness will increase PBGs width.

However, both relationships were found to be disabled at thicknesses above 10 layers, at which both PBGs depth and width became saturated and were not affected anymore by any changes in thickness.

More attention, such as the study conducted by McLachlan [45], focused on different factors that may have a key role during the colloidal self-assembly process. Firstly, McLachlan showed that temperature has a significant impact on the colloidal thin films produced through colloidal self-assembly. This result contradicts with Jiang's [9]. McLachlan noticed through his SEM and optical micrographs, shown in Figure 1.38, that increasing the temperature from 25°C to 45°C increases the domain size from less than 50 µm to about 50 –100 µm in any direction. In addition, the domain size continues to increase up to 250 – 300 µm as temperature increases to 65°C, which confirmed the directly proportional relationship between temperature and domain size. Samples grown at 25°C were found to display very weak spots with the formation of ring patterns as shown in Figure 1.39, which confirms the formation of short-range order. However, FFTs calculated from colloidal thin films grown at a higher temperature of 65°C showed spots with a higher intensity without the appearance of ring patterns, which indicates the formation of higher domain order. From SEM micrographs, McLachlan also concluded that domain direction was not affected by the change in temperature where domains formed in all cases occurred along the close-packed <110> directions. However, crack depth had a great dependency on the growth temperature where cracks formed at 25°C were isotropic, and their uniformity decreased as temperature increased from 25°C to 45°C. Similarly, increasing the growth temperature from 45°C to 65°C led to the formation of rough cracks when compared to those formed in the case of 25°C and 45°C as shown in Figure 1.40. These results indicate that colloidal crystals' crystallographic orientation is not dependent on the cracks that formed during the drying stage. In addition, McLachlan reported that even the degree of adhesion between the colloidal sample and the substrate is greatly affected by the temperature. It was found that working at higher growth temperature reduces sample flakes and increases the adhesion strength with the glass substrate.

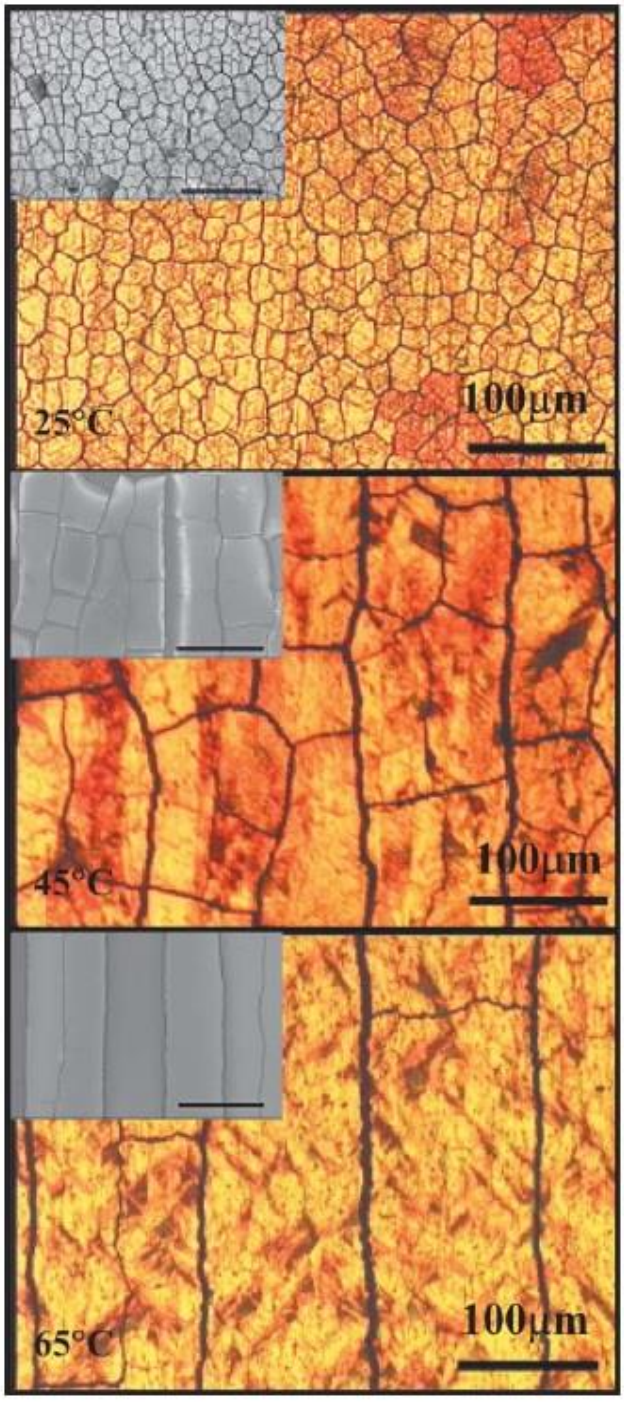

Figure 1.38: Increasing growth temperature leads to a direct increase on the size of domain produced, as shown in the optical micrographs. SEM images (inset) confirm that smaller cracks are not present and that the majority of cracking occurs during drying (inset scale marker 200 mm). Taken from ref. 45.

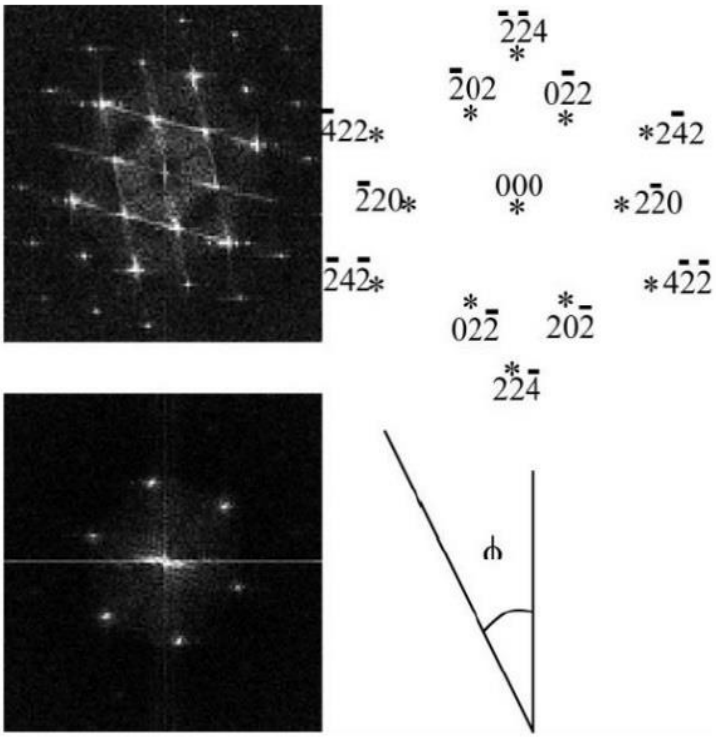

Figure 1.39: 2-D Spatial frequency diagrams obtained at 25 and 65°C with schematic illustration of the measurement technique used to determine the angle of rotation. Taken from ref. 45.

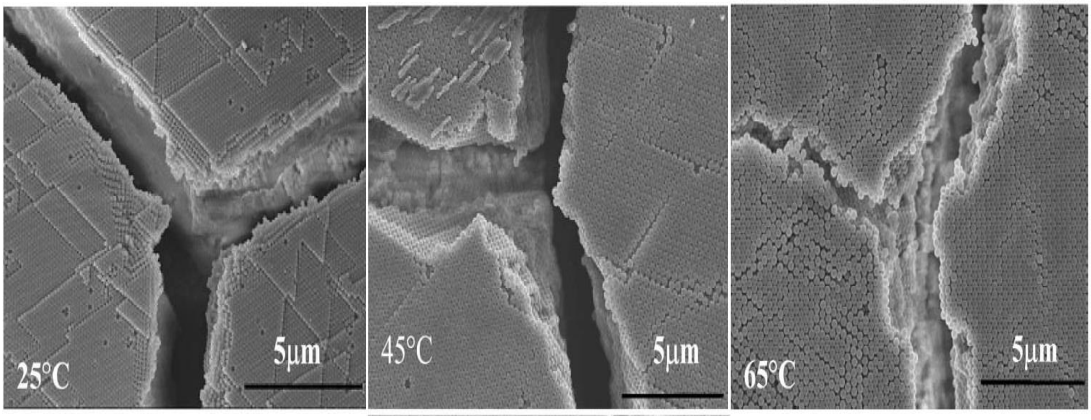

Figure 1.40: SEM images of typical cracks observed at the temperatures indicated. The images reveal that there is no change in the direction of the cracking with change in growth temperature. Taken from ref. 45.

McLachlan followed on his studies by trying to investigate the effect of changing relative humidity on the self-assembly process of PS colloidal crystals. It was found that working at low relative humidity (10 – 20 %) together with high temperature (45 – 65°C) is a must in order to produce colloidal crystals with good quality accompanied by even coverage and good adhesion with the substrate. In addition, the colloidal volume fraction of polymer (V.F.) was found to have a significant effect on both film thickness and adhesion quality with the substrate. A volume fraction of 1.0 % was found to be the optimum to produce a good optically colloidal thin films. Films grown at V.F. below 1.0 % were very thin and optically useless, while those grown at V.F. greater than 1.0 % were highly flaked and not well bonded to the glass substrate. In addition, McLachlan reported that the domain size grown at a substrate angle of 75° was nearly the same as that grown at an angle of 90°. This result coincides with Im's results [57], which indicated that substrate angle should be greater than 10° in order to fabricate good quality colloidal crystals.

In 2004, Teh *et al.* [58] initiated an investigation on band formation during 3D colloidal crystal growth from vertical deposition. They were motivated by Nagayama's group's work [41], in which a good explanation has been given for the forces governing the self-assembly process on a horizontal solid substrate during droplet evaporation. Herein, polystyrene colloids with a diameter of 148 nm and a polydispersity of 7.4 % were fabricated via emulsion polymerization. PS particles with different volume fractions of 2.96 %, 0.59 %, 0.30 %, 0.15 %, and 0.10 % have been added to water. Then, each colloidal suspension was vertically deposited on a flat silicon wafer placed in a vial. The whole setup was placed in a temperature controlled oven to enable studying the effect of evaporation rate on the colloidal growth behaviour. A UV-vis spectrometer was used to monitor the morphological variations during colloidal growth. The observed colloidal growth was found to exhibit three different zones. Firstly, cracks were observed parallel to the silicon substrate as shown in Figure 1.41. The proposed explanation for the formation of these cracks at the initial growth stage was the presence of water between colloids in the suspension. Once the drying stage starts, water was evaporated leaving cracks in its wake. Then, these cracks were found to move in the same direction as the continuous supply of spheres to the growth front. Afterwards, a final colloidal structure was formed after complete drying

of water. The final colloidal crystal ordering quality was found to be independent of these cracks where SEM micrographs showed that final films exhibited FCC structure with a close-packed (111) plane and the crystallographic orientation was stable during the growth zones.

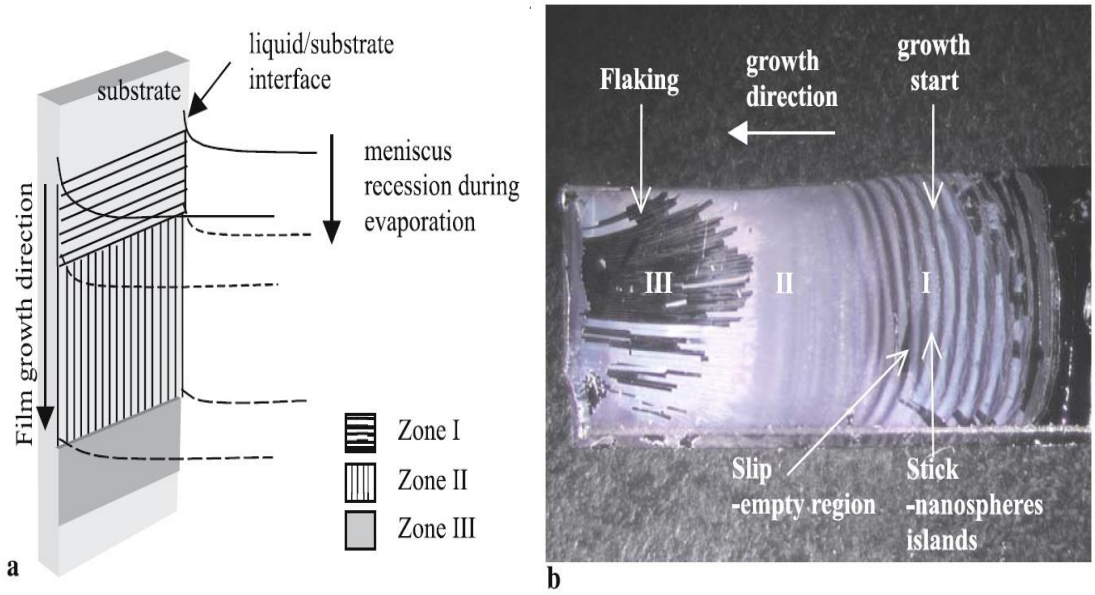

Figure 1.41: (a) Schematic diagram for the growth zones observed during 3D colloidal crystal growth from vertical deposition, (b) In situ spectrometer images for different growth stages. Taken from ref. 58.

Teh *et al.* hypothesised that the reason behind the formation of these growth patterns is the competition between suspension surface tension ($T_s = \gamma_o \text{ Cos } \theta$) and wetting-film surface tension (γ_f) at the substrate–suspension–air contact line. Initially, a concave meniscus was formed by immersing the silicon substrate in the colloidal suspension. At this point, the suspension surface tension reaches its maximum. As the suspension level recedes slowly owing to water evaporation, a convection flow induced, driving particles from the bulk to the contact line. Increasing volume fraction in this situation induces capillary attraction forces, which initiates a colloidal ordering. At this point, the wetting film surface tension becomes greater than that of suspension ($T_s < \gamma_f$) and a thin ordered colloidal crystal film is formed. At further evaporation, suspension level recedes back with a great decrease in the wetting angle (θ), which is accompanied by an increase in the suspension surface tension value (T_s). A 'stick-slip' motion, shown in Figure 1.42, was observed when T_s exceeds the wetting film surface

tension value (γ_f). Herein, the contact line slips down and occupies a lower level at which $T_s < \gamma_f$ again. At this point, suspension surface tension (γ_f') becomes smaller than the original suspension surface tension (γ_f) and the 'stick-slip' motion cycle repeats itself as the solution level continues to go down because of further drying. It was found experimentally that banding which occurred at the first stage took place at very low concentrations (approximately less than 0.31 vol. %). However, uniform colloidal growth took place in zone II at higher concentrations (0.31 – 0.64 vol. %). This result shows that the colloidal crystal tendency to form bands during crystallisation is greatly affected by the suspension concentration.

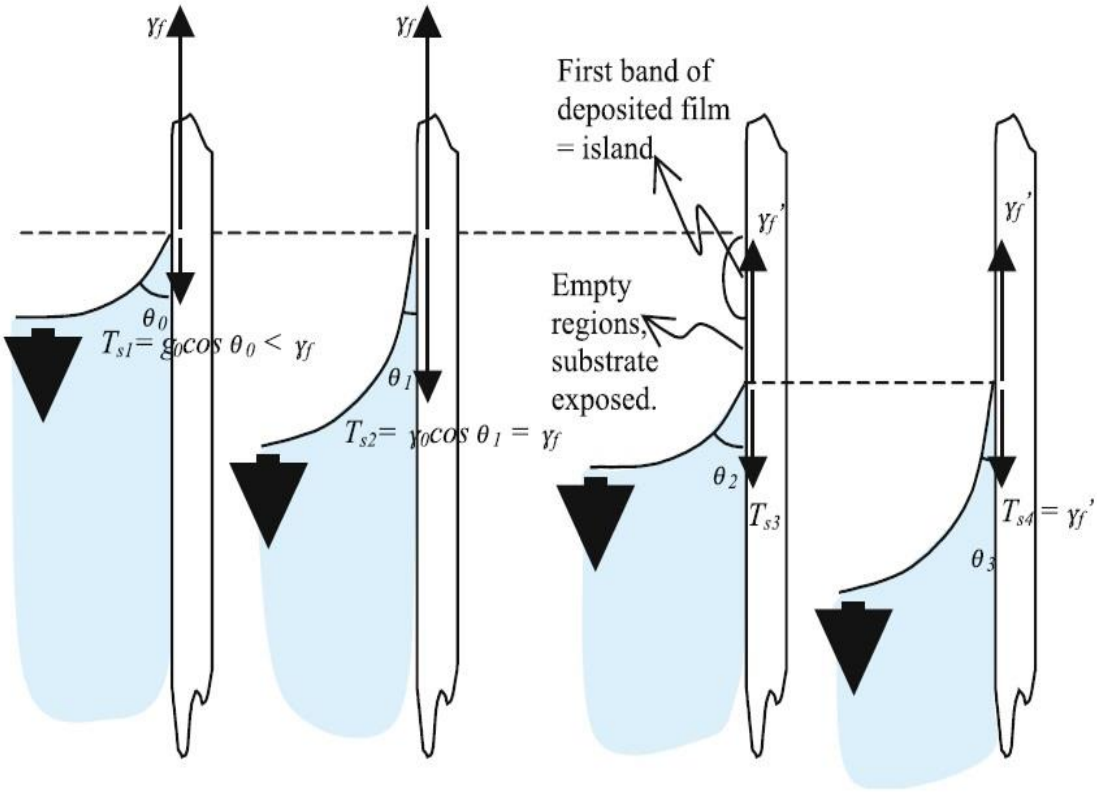

Figure 1.42: Schematic of one cycle of stick–slip motion. Taken from ref. 58.

Crack morphology was greatly affected as the concentration increases from the zone (I) to zone (III) as shown in Figure 1.43. In addition, it was found that in some cases even a high concentration was not enough to ensure quality ordering where the time available was not enough for these colloids to be self-assembled, which led to many imperfections in the final films. For that reason, Teh *et al.* deduced that better colloidal ordering with minimum imperfections can be achieved by (1) eliminating cracks from the first zone of colloidal growth by drying the colloidal suspension in wet environment under controlled rate of evaporation and humidity; and (2) colloidal suspension volume fraction, type and amount of surfactant added are essential factors, to reduce suspension surface tension force and increase substrate wettability, and should be adjusted before vertical deposition of the substrate into the colloidal suspension.

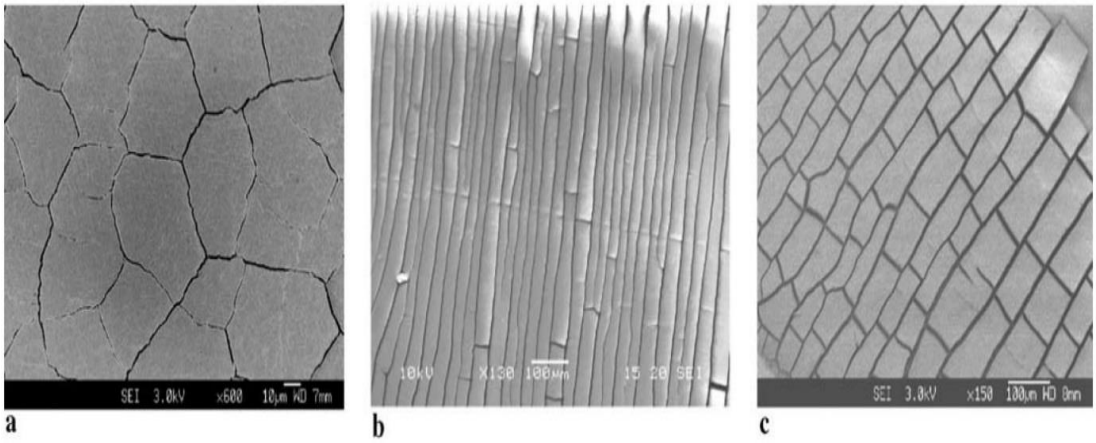

Figure 1.43: SEM micrographs showing different crack patterns at different zones. (a) Hexagonal cracks, (b) parallel cracks, and (c) rectangular blocks. Taken from ref. 58.

Interaction forces that took place between colloids during self-assembly process may have a significant effect on the degree of ordering of colloids. One of the most important interaction forces is the ionic strength which is greatly correlated with the electronic forces between colloids and so may affect the colloidal crystal quality. Based on that fact, ionic strength has been added to the parameters list that probably may enhance ordering of colloidal crystals. Koh *et al.* [40] reported that the colloidal self-assembly process is characterised by the formation of an intermediate face-centred cubic (FCC) structure as shown in Figure 1.44. This structure resembles the final FCC structure but with a greater lattice constant. The intermediate structure acts as a transition state between the primary and the final FCC colloidal structure. In this

state, particles are surrounded by a solvent layer that hinders the direct mechanical contact between these particles. The transition state maintains stable as long as evaporation flux is in balance with the capillary attraction forces between colloids in the solvent. At the end of the drying stage, the solvent layer becomes insufficient to support that structure and faces a sudden rupture. Consequently, cracks appear in the final structure. These observations coincide with McLachlan's results [45], which showed that cracks are formed at the end of the drying stage regardless of the colloidal self-assembly process. Koh also reported that the solvent layer surrounding colloids in the transition state is significantly dependent on the ionic strength force. This observation initiated a huge motivation to study the effect of ionic strength on the colloidal self-assembly process.

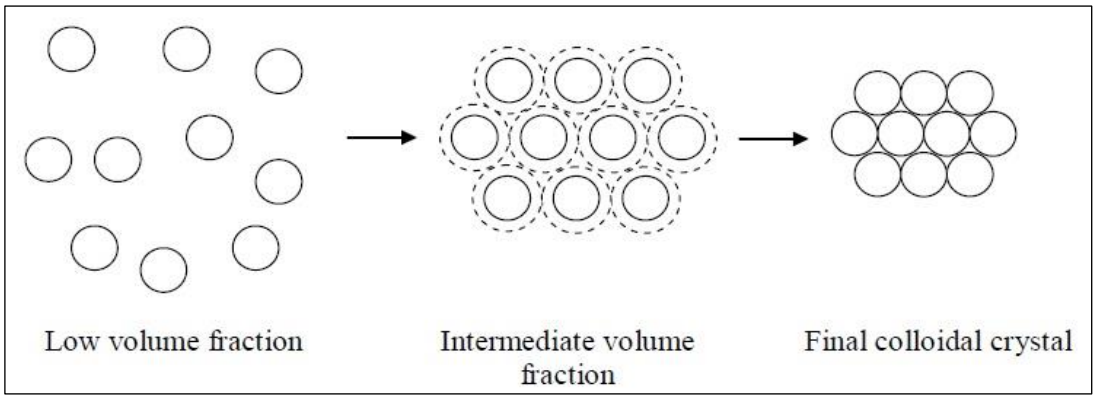

Figure 1.44: The proposed mechanism for colloidal self-assembly. A transition structure with a larger lattice constant has been observed. Taken from ref. 59.

Later, Koh *et al.* [59] started an investigation of the effect of ionic strength on the colloidal crystal quality. SEM micrographs indicated that colloidal crystals obtained from the original suspension without any addition of salts were less ordered, and their structure included many defects, such as empty voids between colloids. Better ordering was obtained with 1.0 mM potassium chloride (KCl), but a lot of voids were still included. This may be attributed to the larger lattice constant of the transition structure. However, increasing ionic strength to 10.0 mM KCl led to a decrease in the transition structure lattice constant. Consequently, a better colloidal ordering appeared with fewer undesirable voids. Surprisingly, the addition of a higher concentration of salts (100.0 mM KCl) formed a colloidal glass phase as shown in Figure 1.45 D. Higher ionic strength causes an aggregation of colloids, at which they are strongly

attached to each other. During self-assembly, capillary attraction forces were very weak to break down these aggregations, and disordered structures were formed at very high ionic concentrations instead of enhancing the colloidal crystal quality.

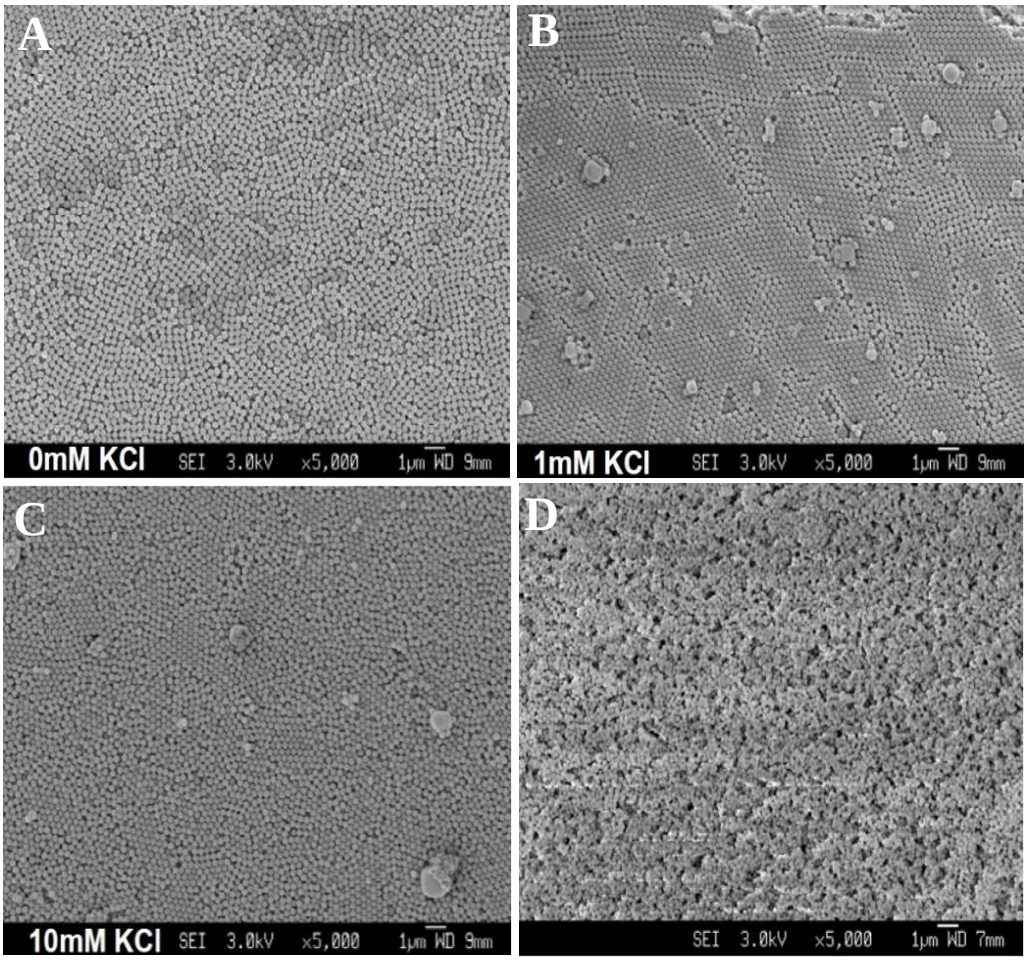

Figure 1.45: SEM images of colloidal crystals grown from different starting ionic strength of suspension; (A) No salt, (B) Low ionic strength, (C) Intermediate ionic strength and (D) high ionic strength. Taken from ref. 59.

Koh *et al.* [40] further utilised reflectance spectroscopy to record changes in photonic band gaps that took place during the colloidal self-assembly process. The spectrometer was adjusted to collect reflectance using only the specular reflectance. Avoiding diffuse reflection increased the accuracy of the results where disorder in the colloidal structure will not be picked up. A peak appears in the reflected spectrum once the incident light strikes the PBGs area. This happened to owe to the impossible propagation of light through the PBG wavelength band. It was found that PBGs' properties are strongly correlated to the colloidal structure. Consequently, Koh et al. related the recorded PBGs changes to the variations in the colloidal structure. For this

study, Koh used a UV-Vis light source (deuterium-tungsten halogen type) together with an optical fibre (200 µm diameter) to develop an incident light beam. Incident light was directed towards the drop using mirrors. In addition, the reflected spectra were collected with the spectrometer during the colloidal self-assembly process using a similar series of mirrors as that shown in Figure 1.46. The experiment was repeated several times at different incidence angles.

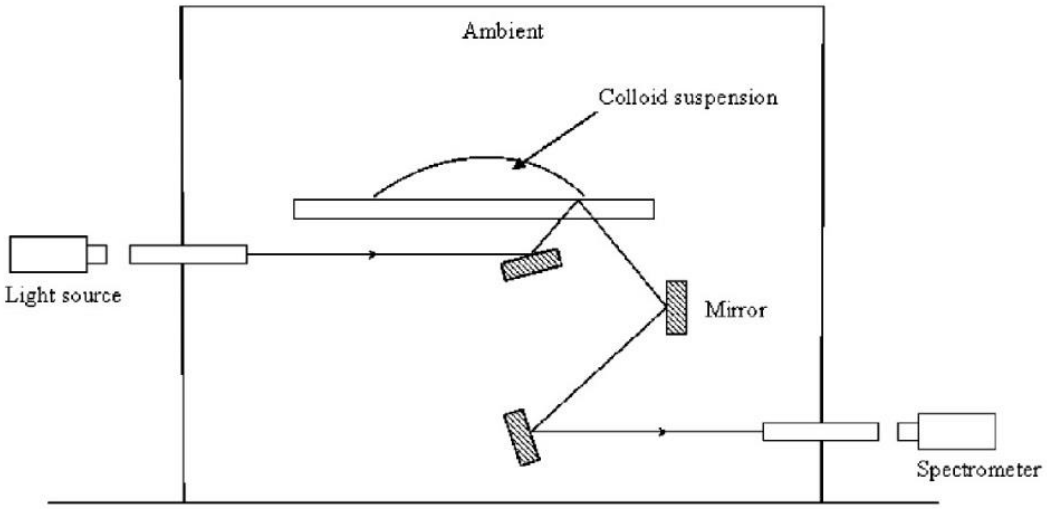

Figure 1.46: Schematic diagram for Koh's set up used to record PBGs changes during colloidal self-assembly process. Taken from ref. 40.

Initially, the reflectance spectrum showed no peaks. Uniform scattering of incident light from the homogeneous colloidal suspension prevented observation of any peaks. As the water starts to evaporate, the contact line is pinned with an angle of 30°. At this stage, a very low-intensity peak starts to appear in the spectrum. The emergence of a reflectance peak indicates the initial appearance of PBG structure. As for drying proceeds, the contact angle decreases accompanied by a gradual increase in the intensity of the collected peak. As the intensity increases, the reflectance peak was found to be shifted towards the shorter wavelength band. Reflectance peak position shift is attributed to the change in structure lattice parameter, which can be given by modified Bragg's law [40]:

$$\lambda max = 2d\sqrt{n^2(\lambda) - \sin^2\theta} \qquad (1.11)$$

Where d is the spacing between each (111) plane where d = 0.577a, and a is the lattice parameter, θ is the angle of incidence and $n(\lambda)$ is the effective refractive index, which is given as [40]:

$$n(\lambda) = n_{medium}(1 - f) + n_{colloid}(\lambda)f \tag{1.12}$$

At a certain point, the intensity of the reflectance peak becomes constant with a fixed position. Stabilisation of the reflectance peak indicates the complete drying of solvent with the formation of a ring-like deposit. SEM micrographs showed that the formed deposit exhibits an ordered FCC close-packing structure. The Colloidal structure exhibits an (111) plane, which is parallel to the glass substrate. The diameter of the deposit was found to be 10mm with 2.5mm width. The thickness of the formed ring-shaped deposit was found to be 24 µm which is equivalent to 160 layers.

Koh followed on by trying to study the dynamics of the colloidal self-assembly process. *In situ* reflectance spectra taken at the different incident, angles enabled the tracking of both peak position and lattice parameter during the self-assembly. Plotting lattice parameter against time as given in Figure 1.47 showed that lattice parameter was decreasing at a constant rate of 1.14 nm/min after the appearance of the first peak. A gradual decrease in the lattice parameter indicates a shrinkage of FCC structure over time. As evaporation proceeds, colloids become more restricted at the drop edges. Consequently, Brownian motion reduces over time and reduces the spacing between colloids. An increase in the intensity of the reflectance peak at this stage confirms better colloidal ordering. The presence of solvent around the colloids keeps this transition state stable. However, complete evaporation of solvent at the end of the drying stage causes a sudden drop in the lattice parameter. Therefore, a distortion in the final FCC colloidal structure appears. Reflectance spectroscopy showed that peak position appeared clearly sharp just before the end of the drying stage. This *in situ* observation confirmed the occurrence of an abrupt decrease in the value of the lattice parameter followed by the appearance of cracks in the final FCC structure. Koh reported that the transition structure has an advantage over the final rigid FCC structure in that the colloids have some degree of mobility. Extending this stage may

give a chance for particles to anneal themselves. Consequently, it may improve colloidal ordering by reducing defect density in the final colloidal crystal.

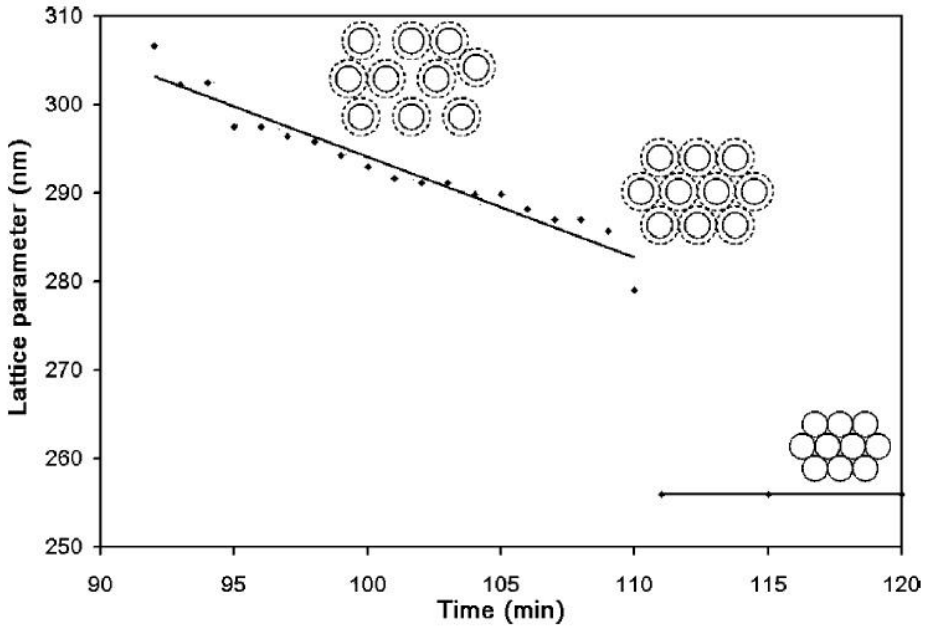

Figure 1.47: Plotting lattice parameter against time showing that FCC structure is shrinking over time. Taken from ref. 40.

In 2008, Koh *et al.* [47] developed a transmission setup for mapping the colloidal ordering growth during self-assembly process of negatively charged PS colloids suspended in water. Their intention was to study the kinetic stages that took place during the colloidal self-assembly process. Herein, he followed on his previous investigation on the colloidal structure variation via the edges of a drop deposited on a flat substrate by studying kinetic stages of self-assembly process through vertical deposition of a colloidal suspension. During vertical deposition, particles at the meniscus region may sediment back towards the suspension or remain on their position. Tendency of particles to sediment back is governed by the Peclet number which is given as follows [47];

$$Pe = m_B gR/KT \tag{1.13}$$

Where m_B is the buoyant mass of a particle with radius R and g is the gravitational acceleration. Peclet number is a good indicator of the colloidal suspension stability.

For $Pe \leq 1$, particles will stay at their position at the meniscus region and colloidal self-assembly proceeds. However, at $Pe >> 1$ tendency of particles sedimentation increases and irreversible aggregation occurs. Aggregation inhibits particles from ordering via self-assembly and leaves a glassy colloidal structure in its wake [32].

Transmission spectra were used instead of reflection to monitor the changes in the meniscus contact line over time, which helps to study the kinetics stages of self-assembly process. The transmission setup, shown in Figure 1.48, was composed of a balanced deuterium tungsten halogen lamp as a light source. The light beam is directed towards a plastic cuvette, which contains the colloidal suspension. The light beam level is adjusted to be above the meniscus at the beginning of the experiment. A glass substrate is fixed on one of the cuvette sides that faces the light source to increase the wettability and consequently provides a better line of sight for the transmitted beam. The temperature was kept constant during the experiment using a temperature-controlled chamber in order to develop a constant evaporation rate. Transmitted spectra were collected using a spectrometer connected to gratings working in the wavelength range between 300 – 900 nm.

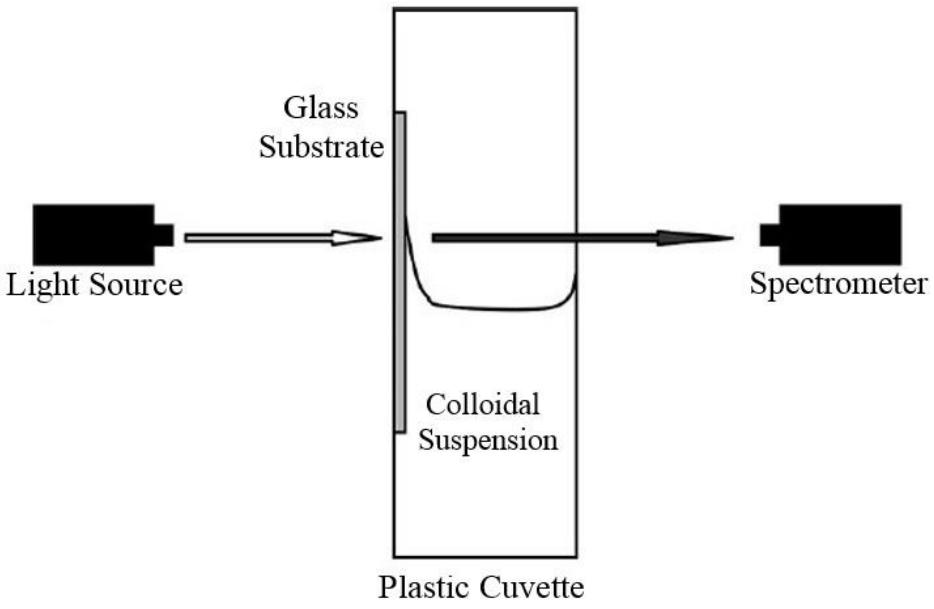

Figure 1.48: Transmission set up used for mapping the colloidal self-assembly growth. Light beam is directed towards a plastic cuvette at which colloidal suspension is placed. Glass substrate on the cuvette side improves wettability and ensures better line of sight for the spectrometer. Taken from ref. 47.

Initially, disordered colloidal structure scattered light randomly preventing light beam from transmittance and no features were observed. As evaporation proceeds, the volume fraction of colloids decreases gradually. As a result, the distance between colloids reduces and transmittance was observed at t_1 = 300 minute, as represented by feature (A) in Figure 1.49. This feature can be considered as the first kinetic stage in the colloidal self-assembly process at which a photonic band gap structure starts to appear. Since colloids at this stage were still completely immersed in water, the driving force for the observed onset of colloidal ordering can be attributed to the interaction forces between colloids. This result changes the previous understanding that colloidal ordering is governed only by lateral capillary forces. Furthermore, it was concluded from the previous studied that colloidal ordering during the self-assembly process starts once the particle diameter goes below the solvent layer thickness, which also contradicts the present case. The proposed explanation for this new result is given by combining macroscopic forces, such as capillary attraction forces, with microscopic forces between colloids, such as electrostatic, steric interactions and Van der Waals forces between closely arranged particles. In the case of large particles, the colloidal ordering mechanism is initiated under the action of lateral capillary attraction forces. Microscopic forces in this situation have no impact on the colloidal ordering. However, in the case of particles much smaller than the surrounding volume, colloidal self-assembly is initially governed by the microscopic interaction forces. Later, as evaporation of water proceeds, capillary attraction forces have the chance to drive the next stage of self-assembly process.[47] Interaction forces between particles can be described by DLVO theory [32]:

$$V_{DLVO} = \frac{64\pi a c_0 \Gamma_0^2 \mathrm{K}T}{\kappa^2} \exp(-kr) - \frac{Aa}{12r} \qquad (1.14)$$

Where a is the particle radius, c_0 is the concentration of ions, K is the Boltzmann constant, T is the temperature, κ is the inverse Debye length, r is the separation between the particles, A is the Hamaker constant and Γ_0 is the surface potential of the particles, which is given as follows [32]:

$$\Gamma_0 = \tanh\left(\frac{ze\varphi_0}{4KT}\right) \quad (1.15)$$

Where z is the valence of the counter ions, e is the electronic charge, and φ_0 is the surface potential.

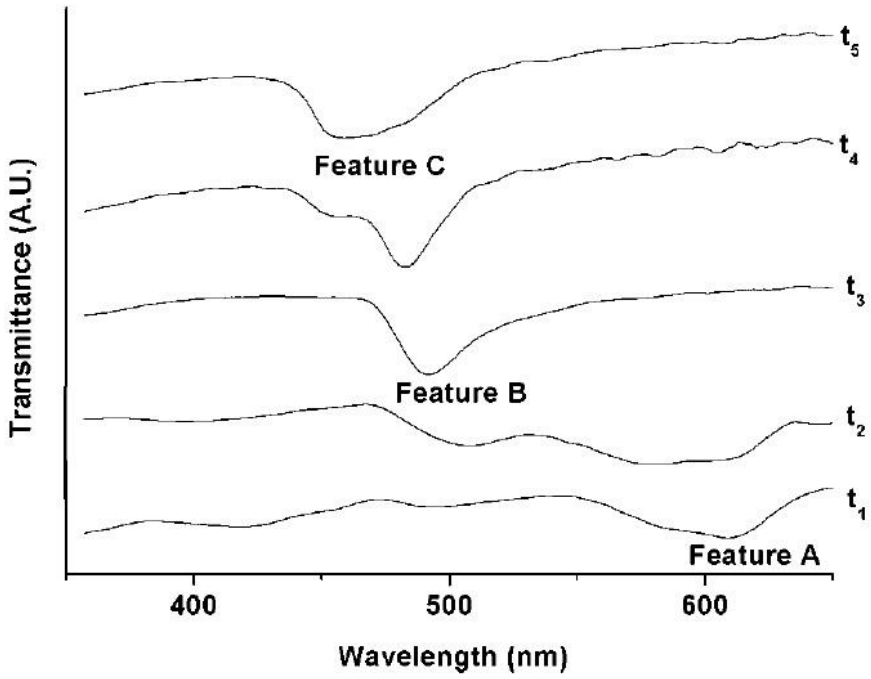

Figure 1.49: Transmission spectra showing the appearance of the features A (608 nm) at t_1 =300 min, B (491 nm) at $t_2 - t_3$ =320-400 min, and C (462 nm) at $t_4 - t_5$ =770-800 min from the beginning of the experiment. These features summarise the three kinetic stages of the colloidal self-assembly process through vertical deposition. Taken from ref. 47.

The calculated DLVO potential vs. experimentally particle surface-to-surface separation shown in Figure 1.50 showed the presence of an energy barrier that inhibits the permanent aggregation of particles and paves the way for particles to be self-assembled over time. However, a large dielectric barrier was found to increase shrinkage stress during the transition between features A and B. Increasing shrinkage stress leads to the formation of undesirable macroscopic cracks that may distort the whole colloidal structure. SEM micrographs showed that the colloidal structure formed at feature (A) exhibits FCC close packing with a (111) plane that is parallel to the glass substrate. PS particles with a diameter of 195 nm were expected to produce an equilibrium colloidal crystal with a lattice parameter of about 276 nm. However,

the FCC structure formed at feature A was found to exhibit a lattice parameter of 368 nm, which is larger than the expected value. A higher value of lattice parameter confirmed the presence of a transition structure in which the energy barrier increases the colloidal separation and inhibits the mechanical contact between particles.

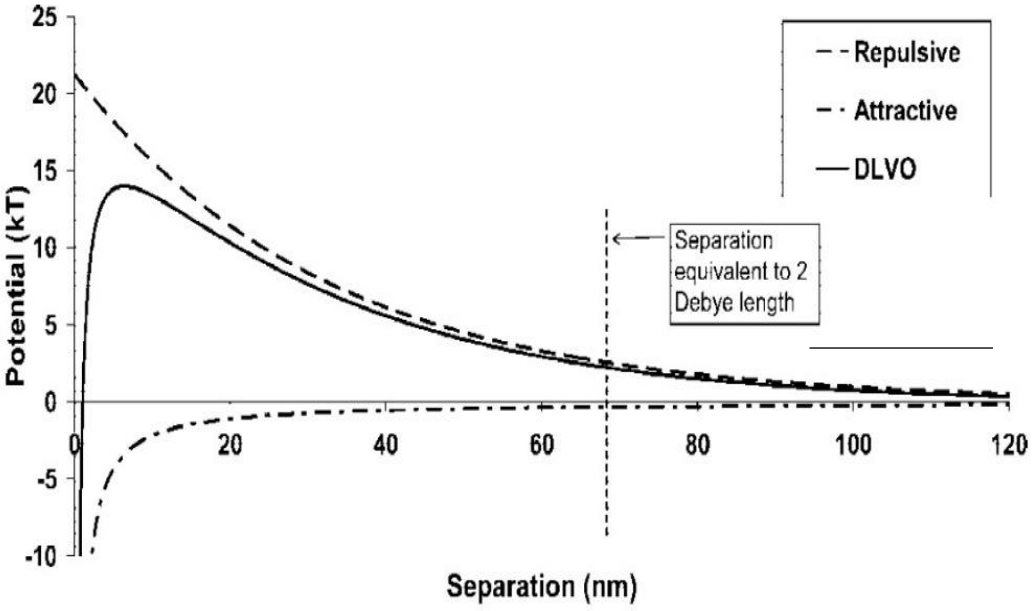

Figure 1.50: The calculated DLVO potential of the colloidal suspension used in our experiments, plotted against the surface-to-surface separation between the spheres. The surface potential is taken as the measured zeta potential of -38 mV at an ionic strength of 0.1 mM KCl. The dashed vertical line denotes the separation equal to 2 times the Debye length. The energy barrier has a magnitude of ~15 kT. Taken from ref. 47.

As liquid evaporation continues over time, colloidal ordering growth proceeds until the meniscus recedes below the top of the particles in the colloidal suspension. At this stage, lateral capillary forces increase to the extent that enables these macroscopic forces to overcome the energy barrier between particles. Therefore, particles become in physical contact where water occupies the cavities between them. The colloidal ordered structure in this situation develops the second transmittance feature (B) at t_2 = 320 min. At the end of the drying stage, complete evaporation of water occurs and air occupies cavities between particles instead of water. Consequently, a change in the dielectric contrast takes place, which develops the third kinetic stage at t_4 = 770 min, represented by feature C in Figure 1.49. The third transmittance feature (C) represents

the emergence of dry colloidal crystals, which is the final kinetic stage in the colloidal self-assembly process. Interestingly, features (A) and (B) were observed simultaneously at t_2 and t_4, which confirms the gradual shrinkage of the transition structure. In addition, the intensity observed between t_4 and t_5 describes the gradual transfer from the wet colloidal crystal to the final dry colloidal structure as water evaporates stepwise during this period. Once the dry structure is completely formed, the colloidal crystal becomes sufficiently stable to protect the final colloidal structure against liquid infiltration process [32],[47].

As in previous studies, the deposition of a colloidal suspension on a flat substrate either horizontally or vertically was found to develop colloidal crystals with an FCC close-packed structure. However, the process leading to the formation of these equilibrium structures was not clearly described from the thermodynamic point of view. In addition, the detailed crystalline arrangement mechanism was not obvious. These mysteries motivated Meng et al. [60] to utilise a real-time microscopic visualisation together with scanning electron microscopy and scanning confocal microscopy to study in detail the crystallisation mechanism that took place during the convection process, which is a crucial stage in the colloidal self-assembly process. In this study, silica colloids with a diameter of 1.0 µm and a polydispersity of 1.5 % was added to deionized water to obtain the colloidal suspension. The crystallisation cell, shown in Figure 1.51, used in this study was composed of a transparent thin wall with an inclined angle of about 30°. The evaporation rate inside the cell was adjusted by flowing nitrogen gas around the cell. Deposition of silica spheres on the inclined wall and subsequent colloidal growth mechanism were recorded in real-time through an oil immersion microscope objective (Nikon Plan Fluor 100×, 1.3 numerical aperture).

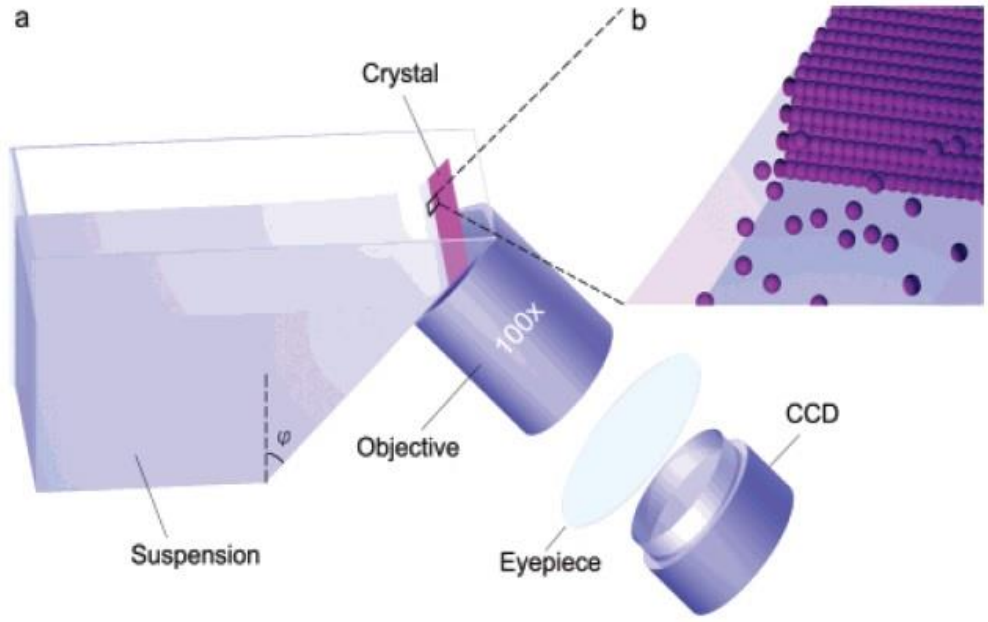

Figure 1.51: (a) Schematic diagram for the in situ set up utilised for real-time observation of colloidal growth mechanism using an oil immersion microscope objective. (b) Idealized view of the growth front, which exhibits a "ramp" shape. Taken from ref. 60.

Real-time observations showed that once the meniscus goes down the substrate, particles were continuously added in a regular manner to the growth front, as shown in Fig. 1.51 b, until the liquid–air contact line touches the growing colloidal structure. This induces a strong capillary attraction force in the holes between colloids, which drives colloidal ordering to form a monolayer colloidal thin film parallel to the substrate. During this stage, water was found to remain within the close-packed colloidal structure under the action of capillary forces. As water evaporates, additional spheres have been pulled under the action of the liquid flow towards the growing structure. No particle sedimentation was observed during the whole vertical deposition process. Meng et al.'s proposed explanation for this observation was that particle sedimentation is not preferred in this situation, where it needs 10 times longer than that needed for the same particle to travel towards the growing colloidal structure.

Meng *et al.* followed on from this study by focusing on the early stages of colloidal growth. The motivation behind this study was to understand the reason for the formation of the initial FCC wet structure, which spontaneously propagates until

forming the final dry FCC colloidal crystal. Their strategy was to use a scanning electron microscope together with a confocal electron microscope in order to characterise the packing plane orientation as well as detecting spheres' position within the structure during the transition state from a bilayer to a triple layer. In addition, they utilised a computerised simulation to assemble a structure 'by hand'. The simulation code was based on some assumptions. Firstly, particles were assumed to be hard spheres with an initial close-packed structure that is maintained firmly during the transition. In addition, the growth front was assumed to preserve its ramp shape during the colloidal transition stage. Finally, structure thickness was assumed to increase gradually as the colloidal structure converts from two to three layers.

Under these assumptions, particles were continuously added to the growth front forming rows of close-packed colloids. These rows were then shifted between parallel and perpendicular directions with respect to the growth front in order to allow the gradual increase of structure thickness. Consequently, colloidal structure close-packing transformed from hexagonal to rectangular and finally stabilised as square close-packed structure. Once the three layers exhibit the square close-packing structure, propagation takes place, adding several square close-packed rows to the growth front. Finally, three hexagonal close-packed layers were formed. From this study, we can learn that square close-packed transition structures have a significant impact on the final hexagonal colloidal crystals. In addition, it was expected that final colloidal structures prefer to have an FCC close-packing structure. However, simulation predicted that the final structure exhibited a hexagonal close-packed structure rather than an FCC structure. Confocal microscopy real-time observations confirmed this unexpected prediction, showing that 90% of the obtained trilayer structure exhibited a hexagonal arrangement (ABA). In addition, SEM images, shown in Figure 1.52, either for top surface or for the growth front replicated the simulation model. Agreement between real-time observations and simulated model confirmed that the transition stage plays a crucial role in controlling the propagating colloidal structure in the case of thin films.

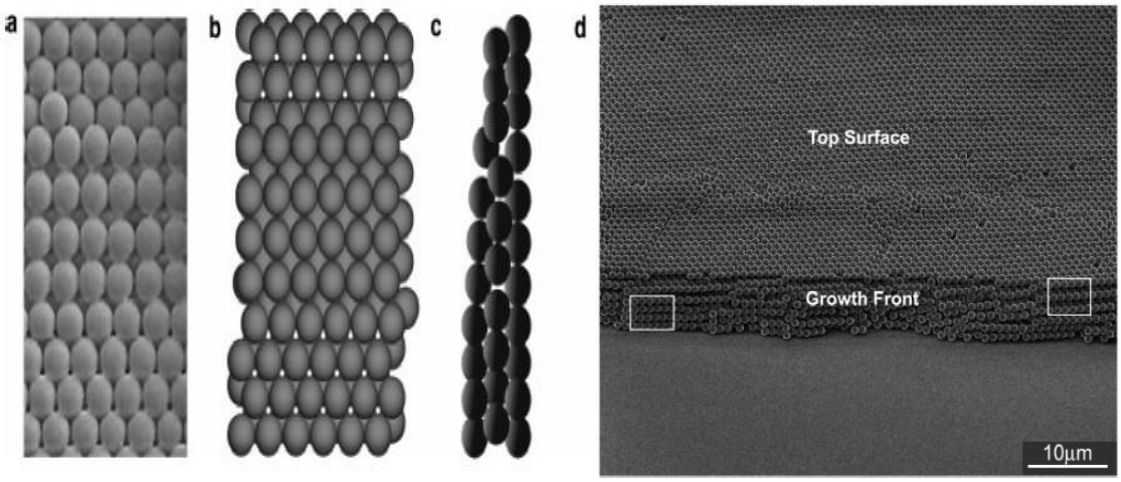

Figure 1.52: Bilayer to trilayer transition. (a) Scanning electron micrograph (top view) of the transition region of 1 µm silica spheres. The bilayer of hexagonally packed spheres is at the top of the image; the trilayer is at the bottom. (b) and (c) Simulated structure (top view and cross section, respectively. (d) Typical scanning electron micrograph of a growth front revealed after arresting convective assembly. Taken from ref. 60.

Moreover, Meng *et al*. tried to extend the last experiment on thicker colloidal films. To do so, they tried to visualise the colloidal growth mechanism that takes place during the three-layer to four-layer transition stage. Herein, the simulation program developed a structure with an ABAC arrangement. However, experimental results showed the possibility of the formation of two structure arrangements: (1) ABAC arrangement, which was formed 40 % of the time; and (2) ABCB arrangement with a 30 % probability of being observed. The ABCB structure successfully allows the thickness to gradually increase as the transition took place from three to four layers. However, the ABCB structure was found to be less tightly close-packed when compared to ABAC close-packing. Meng's results gave a better understanding of the convection assembly process. However, increasing the structure thickness during the transition stage was found to decrease the ease of either simulation measurement or real-time observations, which was one of the drawbacks found in this study. In addition, Meng's *in situ* results were unable to explain how particles preferably choose to propagate according to one of the available two stacking structures. Moreover, Meng's experiment did not explain how the FCC structure originally formed. Furthermore, they failed to describe the mechanism that leads to converting the observed hexagonal close-packed transitional stacking to the final FCC colloidal structure.

Ishii *et al*. [61] performed another set of *in situ* experiments in order to investigate the impact of the growth rate on the crystallographic growth direction of colloidal array. To do so, colloidal ordering process during self-assembly process has been studied using confocal laser scanning microscopy. They integrated a fluidic cell that allows real-time observations of the colloidal growth process. The cell shown in Figure 1.53 composed of two glass substrates together with two double-stick tapes as spacers. Spacers were assembled between the glass substrates to sandwich the feeding colloidal suspension and enable *in situ* investigations for the ordering changes. An Ar laser with a wavelength of 458 nm was utilised as a light source. *In situ* observations have been recorded using an inverted-type laser scanning confocal microscope (LSM) (Carl-Zeiss, LSM5 Pascal) with a 636 oil immersion objective (numerical aperture (NA) 1.4, Plan-Apochromat). Colloidal suspension was fed through one of the cell sides while the other side was used for both water evaporation as well as recording the colloidal growth that took place at the growth front. Evaporation occurred under the action of ambient conditions (Temperature 20 °C and relative humidity 28%). Glass substrates have been subjected to a series of cleaning steps; (1) Cleaning with Piranha solution (H_2SO_4 : H_2O_2 = 3:1, volume ratio) for 10 min, (2) Sonication with NH_3:H_2O_2: H_2O = 1:2:5, volume ratio) for 5 min, (3) Rinsing in (HCl : H_2O_2 : H_2O = 1:2:7, volume ratio) for another 5 min, (4) Washing with plenty of deionized water. Finally, Cleaned glass substrates were dried by a nitrogen gas just before the experiment [61][62].

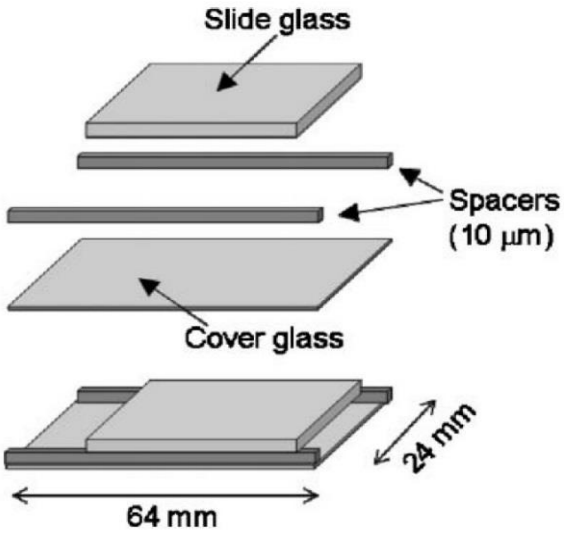

Figure 1.53: Schematic drawing of the fluidic cell used for the real-time observations of ordering growth of PS colloids. Taken from ref. 61.

Confocal scanning microscope snapshots showed that crystallographic growth direction was highly dependent on the growth rate. At low growth rates, ordered spheres grew in the <112> plane direction. Moderate growth rates led to colloidal growth in the <110> plane direction. However, highly undesirable disordered colloidal structures were formed at a high growth rate of 120 μm/min. At very high growth rates, particles were delivered to the growth front during convective assembly at extremely high rates. Hence, the time available for these particles to be self-assembled was not enough. Consequently, random orientation occurred developing disordered colloidal structures. The difference in growth direction with respect to the growth rate was attributed to the water-flow resistance. During convective assembly, particles were pulled towards the growth front and forced to self-assemble under the action of capillary forces. As a result, water occupied the vacancies between spheres in the growing close-packing structure. Hence, variations in the colloidal arrangement were governed by the difference in water-flow resistance. The porosity of both the <112> and <110> directions was found to be the same for particles with a large enough size and both have a continuous shape. However, the <112> direction was found to be not linear, which decreases the permeability of the <112> direction. Hence, the <110> direction with more permeability than the <112> direction will develop lower water-flow resistance. Consequently, the <110> direction will develop a dominant colloidal growth rate that is more favourable. Based on these results, Ishii et al. hypothesised that the colloidal structures growing in the <112> direction that were observed in Meng's experiment [60] were representing early growing stages only. Later on, spheres will propagate towards the preferable orientation, which is the <110> direction, until forming the final equilibrium FCC structure with <111> close-packed structure.

Ishii *et al.* further investigated the emergence of planar defects during convective assembly using the same setup. Confocal laser microscopy snapshots showed dark spots between spheres at the early stages. Through careful observations, it was found that particles with smaller diameters than the average were occupying these dark spots. As colloidal growth proceeds, these particles were found to act as the origin of planar defects in the structure. Furthermore, these planar defects were growing as the ordered array growth propagates until forming cracks that may deteriorate the final colloidal

structure. Ishii *et al.* claimed that these defects may be stabilised at moderate growth rates as the colloidal growth front changes its shape stepwise over time. However, a detailed explanation of defects annealing was missing and the mechanism into which the growth front changes its growth direction from <112> to <110> was not obvious. Another drawback in this study was the deformation in the cell opening that took place during the focus adjustment of objective lens. Cell opening deformation forced *in situ* growth front observations to focus on an area that is several millimetres away from the cell opening. Hence, it was impossible to observe the early stage of colloidal growth, which was crucial information to understand the nucleus formation mechanism.

Pisist *et al.* [20] performed a new series of investigations on the critical processing parameters; such as deposition rate and particle size, governing the rapid convective deposition process. In addition, the impacts of the deposition blade hydrophobicity and deposition angle on both the coverage density and the packing quality of the final monolayer thin film have been studied for the first time. Their intension behind that was to control the convective deposition of particles of various compositions on substrates to improve the light extraction efficiency of light emitting diodes (LEDs).

Pisist utilised the “coffee ring effect” principle, at which particles are pulled towards the suspension drop drying edges, to control the particles convective deposition by drawing a meniscus thin film across the substrate. In continuous convective deposition process, colloidal crystallisation took place while substrate is vertically withdrawing from the particles suspension at a constant rate. However, in this investigation the horizontal deposition of the particles suspension on a glass substrate has been used as shown in Figure 1.54. Initially, a concentrated suspension is injected between the deposition blade and the substrate. Then, the substrate is pulled away from the bulk suspension at a designated speed using a linear motor. As the substrate moves, the meniscus is overextended along the substrate and particles motion became governed by the convection flow from the bulk suspension towards the drying front. As evaporation proceeds, particles crystallisation takes place forming a hexagonal close-packing two-dimensional array. Scanning electron microscopy together with confocal laser scanning microscopy have been used to analyse the local

and long-range microstructure of the thin film deposited on the glass substrate. In addition, the coverage density, distributions of the number of nearest neighbour and the local bond order were investigated to enable defining the distribution and arrangement of the particles after deposition.

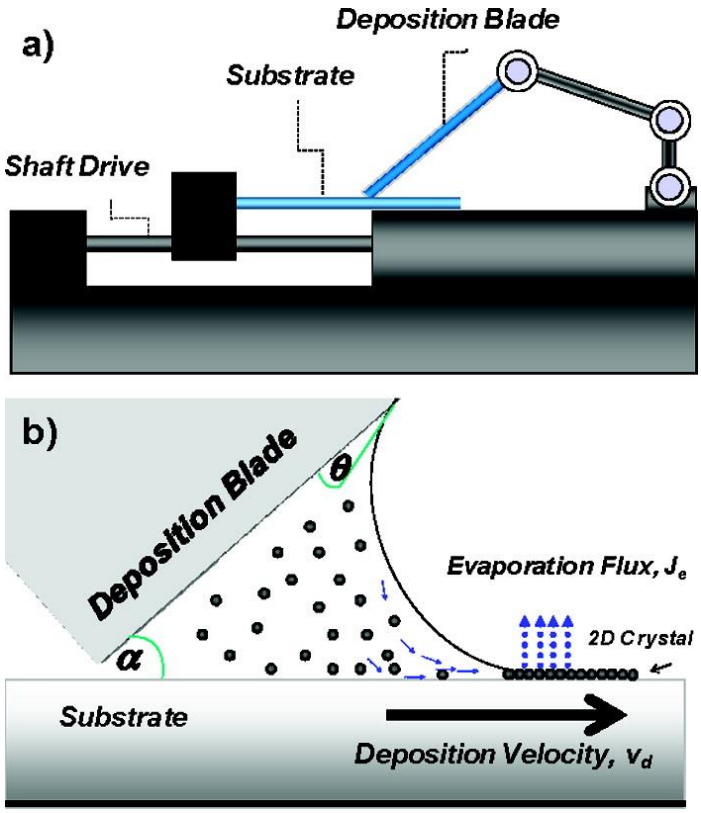

Figure 1.54: Experimental setup showing equipment (a) and the local deposition process (b) where a meniscus is pulled relative to the substrate to induce deposition and the local ordering of particles. Taken from ref. 20.

This work discovered the great impact of the blade hydrophobicity on the shape and curvature of the meniscus formed on deposition, as shown in Figure 1.55. The hydrophilic blade enables wetting the underside of the blade along the full width of the substrate dominating the surface tension force. Surface tension drives the suspension drop to wet both the blade and the full width of the substrate equally forming a concave free surface. On the other hand, the hydrophobic back and bottom edges of the deposition blade prohibits any flow neither on the back side nor down the blade. So, governing the bulk pressure and the profile of the extended meniscus on deposition. In addition, it was found that deposition speed has a significant effect on the packing quality of particles. Increasing the deposition speed favoured the

fabrication of sub-monolayer structures with lower coverage density, while decreasing the deposition speed led to the fabrication of multilayer thin films. Pisist's work also shed the light on the importance of the blade angle in the deposition process. Results showed that blade angle has a limited impact on deposition in the case of the hydrophilic deposition blade, which coincides with previous predictions. However, it was found that the deposition speed is dramatically dependent on the angle of the hydrophobic deposition blade. Thus, increasing the blade angle should be accompanied by an increase in the deposition rate for achieving a highly ordered monolayer thin film deposited on the substrate [20].

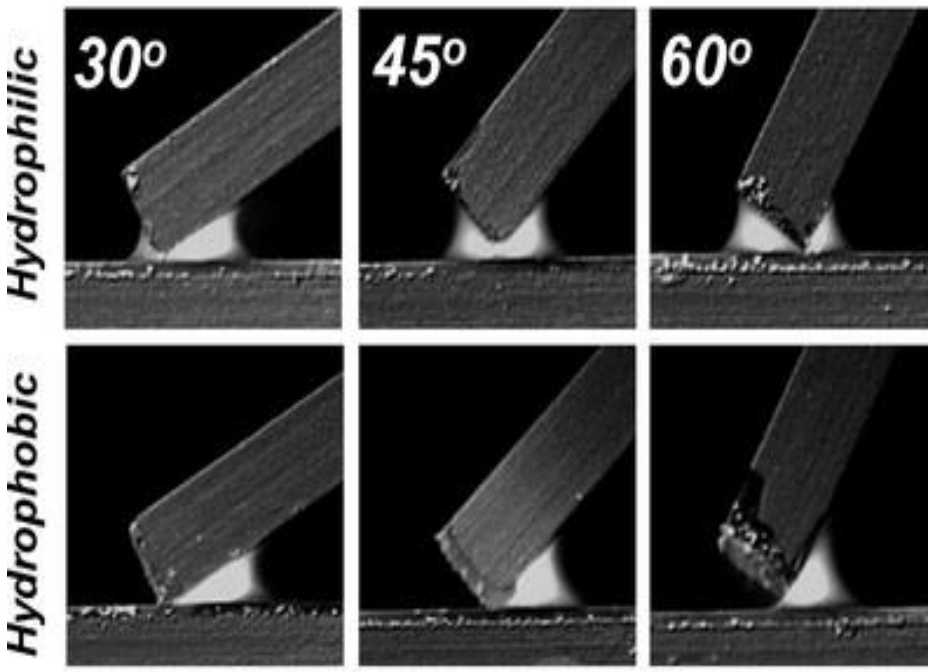

Figure 1.55: Radius of curvature shown as a function of contact angle. (a) Images of meniscus curvature (hydrophilic, top; hydrophobic, bottom) Taken from ref. 20.

1.3.2 Colloidal self-assembly of charged particles

In 2008, Yan *et al.* [63] integrated a direct video monitoring apparatus to investigate the effect of surface charge on the colloidal ordering quality during the dynamic self-assembly process in a sessile colloidal drop. The *in situ* device was composed of an optical microscope (Olympus, BX51TRF), adjusted to operate in transmission mode, and connected to a charge-coupled device (CCD) camera (Sony, SSC-DC58AP) in

order to record the real-time ordering variations that took place at the colloidal sessile drop edge. In this study, PS colloids with a particle size diameter of 860 nm and 738 nm and a polydispersity of less than 5.0 % were prepared through the emulsifier-free emulsion polymerisation method using different initiators. Potassium persulfate has been used as an initiator in order to attach a negative charge on PS spheres (860 nm). However, 2,2′-azobis (2-methylpropionamidine) dihydrochloride has been used as an initiator when a positive charge is required to be attached on PS (738 nm) colloids. The measured zeta potentials for negatively and positively charged spheres were – 55.87 mV and +85.52 mV, respectively. Igepal CO-720 as a nonionic surfactant, sodium dodecyl sulfate (SDS) as an anionic surfactant and dodecyl trimethyl ammonium bromide (DTAB) as a cationic surfactant have been used individually to investigate the effect of charged surfactants on the colloidal ordering process. Glass microscope slides were negatively charged by rinsing in acetone followed by mixing with Piranha solution. Positively charged glass substrates were prepared by submerging freshly prepared negatively charged glass substrates in (3-aminopropyl) diethoxymethylsilane (3-ADMS) overnight then rinsing with acetone, ethanol, deionised water and finally immersing substrates in 0.1 M hydrochloric acid overnight. Colloidal suspensions were prepared with different volume fractions between 0.05 and 1.0 %. Then, 10 µL of each colloidal suspension was dropped on the glass substrate under ambient environment at 23°C and 31 % relative humidity. The self-assembly process was recorded using the integrated direct video device.

In situ observations showed that colloidal ordering quality was highly affected by the charges type on both PS spheres and glass substrate. Positively charged PS colloids on positively charged substrates gave ordered colloidal crystals. In addition, negatively charged PS spheres deposited on negatively charged glass substrate was found to develop an ordered structure. However, neither positively charged PS sphere on negatively charged glass substrate nor negatively charged colloids on positively charged substrate led to an ordered colloidal structure. These results confirmed that obtaining ordered colloidal arrays could be achieved if and only if colloids and substrate possess the same electric charge. Yan *et al.* claimed that opposite charges develops strong Coulombic interaction forces between colloids and substrate surface, which is responsible for increasing the attraction forces between spheres and substrate.

As a result, attraction reduces the particles' mobility on the glass substrate, inhibiting them from ordering properly forming an undesirable disordered colloidal structure. In contrast, same charged surfaces induce repulsion forces, which increase the particles mobility in the colloidal suspension. Mobility helps particles to be arranged in an orderly manner during the self-assembly process, avoiding the irreversible colloidal agglomeration.

In addition, real-time monitoring records showed that colloidal ordering quality was highly affected by the surface charge on the surfactant added. In the case of nonionic Igepal CO-720, video snapshots showed that negatively charged PS spheres deposited on positively charged substrate developed a disordered structure, while negatively charged colloids deposited on a negative charged substrate formed a highly ordered colloidal crystal. Observations in this case coincided with results observed in the absence of a surfactant. Hence, the nonionic surfactant had no effect on the ordering of colloids because it did not possess any surface charge. However, it was found that addition of either anionic or cationic surfactants to oppositely charged surfaces had a significant impact on the colloidal ordering of spheres. Addition of charged surfactants highly reduced the surface charge density. As a result, colloidal ordering improved significantly. On the other hand, it was found that addition of DTAB as a cationic surfactant to negatively charged PS spheres deposited on a negatively charged substrate led to the formation of an unexpected disordered structure. Yan *et al.* hypothesised that these odd results may be attributed to the effect of hydrophobic interactions between DTAB and spheres. Hydrophobic interaction increases the adhesion of PS spheres on the glass substrate. Hence, the surprising disordered structure was obtained. Similarly, the addition of SDS as an anionic substrate to positively charged PS colloids deposited on positively charged glass substrates was found to develop hard-sphere like interactions. Herein, hydrophobic interaction between SDS layers absorbed on the negatively charged substrate and negatively charged PS particles increases particle adhesion to the substrate. Strong adhesion develops lower particle mobility, which distorts the particle ordering during the self-assembly process.

Afterwards, Tan *et al.* [64] started a new investigation on the effect of ionic strength on the layer-by-layer (LbL) crystallisation growth of oppositely charged colloids. Their intention behind this study was to develop an additional control route in the crystallisation growth of binary colloidal systems. Consequently, better control may help to enhance the colloidal ordering in the subsequent layers. Attraction forces expected between oppositely charged particles make the whole colloidal growth prone to irreversible aggregations. This aggregation inhibits particles from regular ordering and led to the formation of disordered structures. Hence, crystallisation of oppositely charged particles in this study was one of the major challenges. Their strategy was to grow a positively charged colloidal monolayer above a negatively charged monolayer where ionic strength was measured during the process to reveal its impact on colloidal ordering quality. In this study, PS spheres with different diameters of 550 nm and 250 nm were fabricated through the emulsifier-free emulsion polymerisation method. A sulfate-type initiator was used to add negative charge on larger polystyrene particles (L-PS), while smaller polystyrene particles (S-PS) were positively charged through the usage of an amandine-type initiator. Zeta potential values for both negatively and positively PS particles were found to be -41.87 mV and +80.98 mV, respectively. Igepal CO-720 and DTAB were added to the colloidal suspension as nonionic and cationic surfactants, respectively, to reduce the surface tension of the PS suspension. Firstly, a colloidal suspension of negatively L-PS particles with a volume fraction of 0.5 % was grown on the glass substrate through a controlled pumping velocity of 0.5794 μm/s to fabricate the first monolayer on the glass substrate. Then, the substrate was vertically deposited in the positively charged PS colloidal suspension in the same manner to give a positively charged monolayer the chance to grow upon the initial negatively charged monolayer forming, a bilayer of oppositely charged PS spheres.

SEM micrographs showed that addition of DTAB cationic surfactant led to the formation of a disordered structure. Tan claimed that dissociation of DATB into water to DAT^+ and B^- was the main reason for inhibiting regular colloidal ordering on glass substrate, where B^- was attracted to the positively charged PS particles inducing strong electrostatic repulsion forces. The induced repulsion forces led to irreversible agglomerations and disordered colloidal structures being formed. However, an ordered structure appeared when Igepal CO-720 was used as a nonionic surfactant.

Herein, no electrostatic repulsion forces appeared and positively charged PS spheres were dispersed regularly in the colloidal suspension. Hence, positively charged PS spheres were able to be deposited on the first negatively colloidal monolayer, leading to ordered LbL growth. These results confirmed that the type of surfactant used in LbL colloidal growth has an important role in the formation of ordered colloidal structures. Optimum surfactant should reduce the water surface tension and consequently improve the adhesion of colloids with the substrate. In addition, it should not affect the interaction between charged particles to avoid irreversible aggregation. Furthermore, SEM results showed that the effect of lateral capillary forces in this case can be ignored. The Peclet number for positively S-PS particles was calculated to be approximately 10^{-3}. Based on Koh's previous work [47], particles with a Peclet number (Pe) < 1 remain suspended in the solution. In this case, lateral capillary forces are too weak to overcome the interaction forces between charged particles. Real-time observations in this experiment confirmed previous conclusions that capillary forces' impact on colloidal ordering of charged colloidal crystals can be ignored.

Tan *et al.* [64] followed on by trying to discover the exact impact of increasing the ionic strength in the colloidal suspension on the monodisperse colloidal crystal growth. In this study, KCl was used as a solute to adjust the ionic strength value in the colloidal suspension. Low ionic strength developed owing to the addition of 10 µM KCl improved the colloidal ordering forming LS_2 structure, shown in Figure 1.56 b, with respect to structure formed when no KCl was added as shown in Figure 1.56 a. KCl was dissociated into to K^+ and Cl^- ions in the suspension. Attachment of these ions to the oppositely charged PS spheres in the colloidal suspension significantly reduced the interaction between the two oppositely charged PS layers. As a result, attraction forces reduced and particle mobility increased. Particle mobility allowed PS spheres to be self-assembled more regularly, forming a more ordered colloidal structure. Increasing the concentration of KCl to 1000 µM led to the formation of more ordered 2D-superlattice structures, such as LS_3 and LS_4. These results confirmed the significant impact of ionic strength value on the growth of attractive binary colloidal films (LbL).

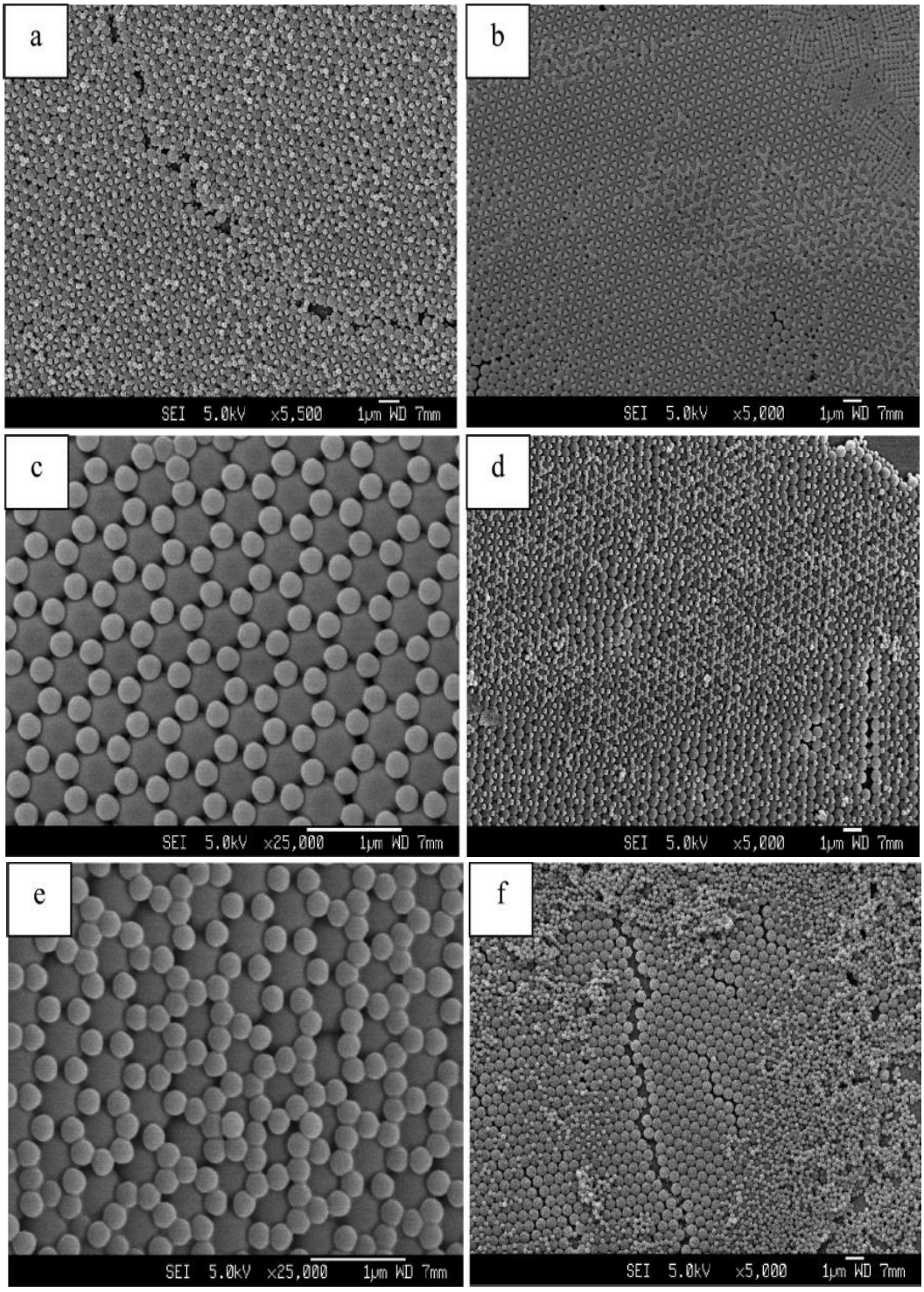

Figure 1.56: Positive-charged S-PS monolayer pattern is grown on negative-charged L-monolayer in (a) deionized, (b) low ionic, and (d) high ionic conditions with Igepal CO-720 and (f) high ionic conditions with DTAB. Panels (c) and (e) show the magnified views of the LS_2 and more close-packed LS_n structures, respectively. In general, order is vastly improved with the addition of small amounts of KCl. Taken from ref. 64.

Since both ionic strength and the Debye screening length of the oppositely charged PS sphere were found to be independent of the particles size, then the effect of ionic strength impact on the ordering of oppositely charged PS particles can be quantified using Debye screening length (κ^{-1}) given in Gouy–Chapman theory, as follows [65]:

$$\kappa^{-1} = \left(\frac{e^2}{\varepsilon_0 \varepsilon_t k_B T} \sum z_i^2 c_i^*\right)^{-1/2} \quad (1.16)$$

Where e is the elementary electron charge, ε_t is solvent dielectric constant, k_B is Boltzmann's constant, T is temperature, z is valence and c_i^* is the ion concentration.

It was found that the Debye screening length for deionised water is 865.584 nm. Then, it decreased to 98.197 nm as 10 µM KCl was added. Furthermore, the Debye screening length was continuously decreased to 9.869 nm at high ionic strength (100 µM KCl). Therefore, the thickness of the electric diffuse double layer of counterions surrounding the charged colloidal particles will also decrease as the ionic strength increases. Hence, oppositely charged particles will be closer to each other and should experience very strong electrostatic attraction forces. These attraction forces should lead to an irreversible coagulation of particles forming randomly disordered structures. However, the formation of ordered 2D-superlattice, structures such as LS_2 at low ionic strength and LS_3 and LS_4 at high ionic strength, contradicts that expectation. In LBL technique, stepwise growth of alternate layers of oppositely charged particles prevented the irreversible aggregations of particles. Firstly, addition of negatively charged L-PS particles developed repulsion forces with the negatively charged glass substrate. Repulsion forces provide particles with high mobility to be able to reorder themselves upon the glass substrate forming the first negative L-PS template. Secondly, addition of positively charged S-PS induces two different pairs of electrostatic interactions: (1) repulsive interactions between similarly charged (S-S repulsion); and (2) attraction interactions between oppositely charged particles (L-S attraction). As ionic strength increases by the addition of KCl, the Debye screening length decreases. As a result, S-S repulsion interactions also decrease, which allows like-charged S-PS particles to approach each other more closely as shown in Figure

1.57. As a result, a 2D ordered LbL structure was successfully formed. This study confirmed the importance of ionic strength impact in ionic colloidal crystal (ICC) binary systems for either increasing particles mobility or decreasing screening effect in order to achieve regular colloidal structures [64].

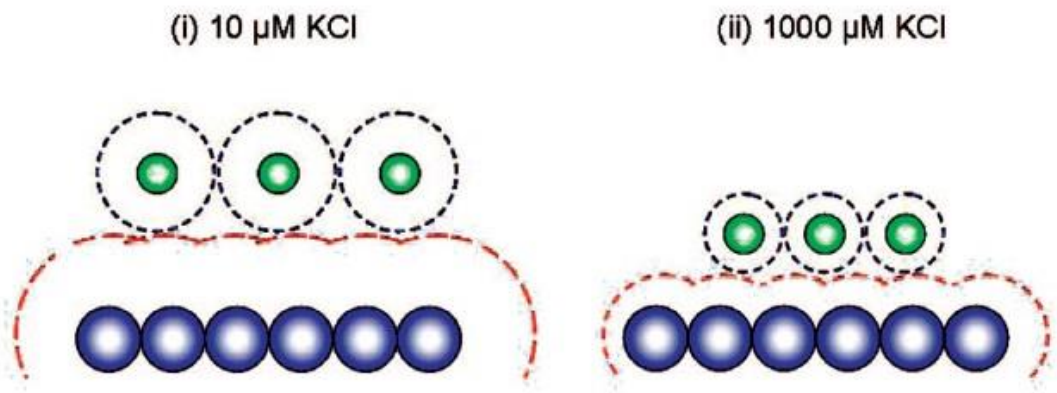

Figure 1.57: Schematic illustration of the range of L-S attraction and S-S repulsion at (i) low ionic strength and (ii) high ionic strength. The Debye length and range of electrostatic interactions decreases with increasing ionic strength in the suspension. Taken from ref. 64.

Tan *et al.* [66] then investigated the combined effect of evaporation temperature, volume fraction, ionic strength and electrostatic interaction on particle mobility during the LbL colloidal growth in ionic colloidal crystals. The intensions behind this were to optimise the conditions required to develop a well-defined close-packed 2D-superlattice structure of oppositely charged colloidal films. Firstly, particle volume fraction was found to have a significant impact on controlling particle flux and improving crystallisation growth quality. Once positively charged S-PS spheres were introduced at low ionic strength (10 μM KCl), great attraction took place with the negatively charged glass substrate. Attraction forces immobilise spheres and inhibit their opportunity to order. However, evaporation of water over time forces the meniscus to recede and deformation appears. A convective flow drives particles from the bulk of the suspension towards the more ordered regions in order to keep the contact line pinned. This flow reduces interparticle distance to the extent that it helps particles to reorder at the meniscus. At this stage, it was found that high concentrations prohibit any hexagonal close-packed structures from appearing. However, lower

volume fraction helps to reduce the number of particles transported to the meniscus. This gives particles at the meniscus more time to be self-assembled forming a more ordered hexagonal arrays. In addition, reducing the volume fraction decreases the interparticle distance and minimises the probability of particle collisions. Hence, particles gain a degree of mobility that allows them to order themselves. This result shed light on the importance of low particle volume fraction in improving the colloidal ordering for oppositely charged particles. However, particles with low volume fraction of 0.1 vol. % examined at high ionic strength (1000 µM KCl) were found to lose all their mobility, leading to irreversible aggregation. In a word, improving oppositely charged particles ordering were achieving at a combination of low volume fraction (Ø $\leq$ 0.05) together with low ionic strength ($c_i \leq 10$ µM) at a constant temperature of 25^{o}C. In this situation, oppositely charged particles and negatively charged substrate achieve an equilibrium state between repulsive forces between like-charged particles and attraction forces induced between positively charged (S-PS) particles and negatively charged glass substrate. This equilibrium gives particles the crucial mobility they need to reorder forming close-packed hexagonal colloidal crystals.

Secondly, the impact of evaporation temperature variation on the colloidal crystallisation growth was investigated with respect to both particle volume fraction and ionic strength. It was found that as temperature increases from 25 to 35°C, less ordering took place and more defects were noticed in the close-packed structure as shown in Figure 1.58. As evaporation temperature increased, the particulate mobility of charged particles was found to be highly affected. Increasing the evaporation temperature causes several sequential variations: (1) increasing the particles flux transferring towards the more ordered growing areas: and (2) increasing particle kinetic energy. Consequently, particles will experience faster Brownian free motion, which increases the collisions between particles. Collisions favour the appearance of defects through the colloidal crystal formed. Furthermore, increasing the rate of particles growth at the growing cluster will minimise the time available for particles to self-assemble. Hence, particles will not be able to effectively explore favourable sites during growth. Then, a less ordered colloidal close-packed structure with a high defect density is formed after complete liquid drying. Conversely, when liquid evaporates at lower temperatures (25°C) it dries slowly. Slower growth rates give the

positively charged S-PS particles a good chance to stabilise with both negatively charged L-PS particles as well as the negatively charged glass substrate. Stabilisation of S-PS particles helps them to reorganise in the favourable thermodynamically LS_2-superlattice plane in the colloidal suspension. As liquid dries, the growth of a more ordered hexagonal close-packed colloidal structure with lower defects density takes place.

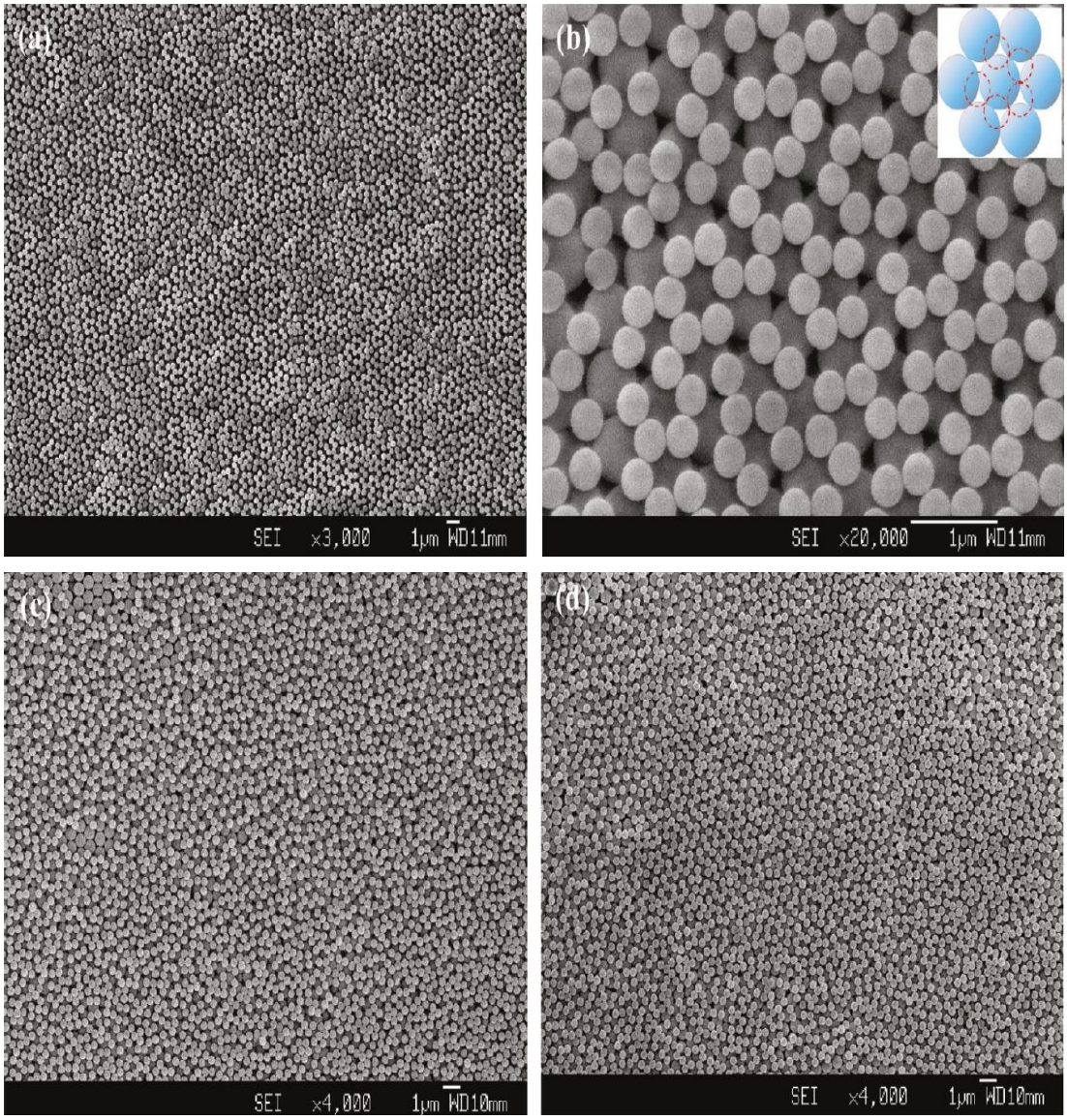

Figure 1.58: SEM micrographs showing the growth of LS_2 superlattice at (a) 25, (c) 30, and (d) 35 °C at various magnifications. The highest density of well-defined LS_2 superlattice is found under the conditions of lower evaporation temperature of 25°C, low ionic strength of 10 μM and low particles volume fraction of 0.05. (b) The LS_2 schematic (drawn to scale) in the inset panel shows the L-colloidal template could only accommodate five S-particles at the interstitial sites for the size ratio d_S/d_L=0.614. Taken from ref. 66.

This study showed that it is possible to control the mobility of charged particles during the layer-by-layer (LbL) growth of oppositely charged particles through the electrostatic interactions. These interactions were found to be highly dependent on a combination of evaporation temperature, ionic strength and particle volume fraction in colloidal suspension as shown in Figure 1.59. Evaporation temperature controls both the particles' kinetic energy and the amount of particles transferred to the growing clusters, while ionic strength can mitigate the surface charge and then enable oppositely charged particles to come closer to each other in a suitable interparticle distance to allow them to order. However, particle volume fraction plays an important role in LbL growth by decreasing the amount of particles at the favourable site, hence increasing the time and space available for these particles to explore the optimum sites to occupy, leading to improved colloidal ordering. In this study, the most organised 2D-LS_2 superlattice structure with a hexagonal close-packing and low defect density was formed at an evaporation temperature of 25°C, low ionic strength of 10 µM KCl and low particle volume fraction of 0.1 vol %.

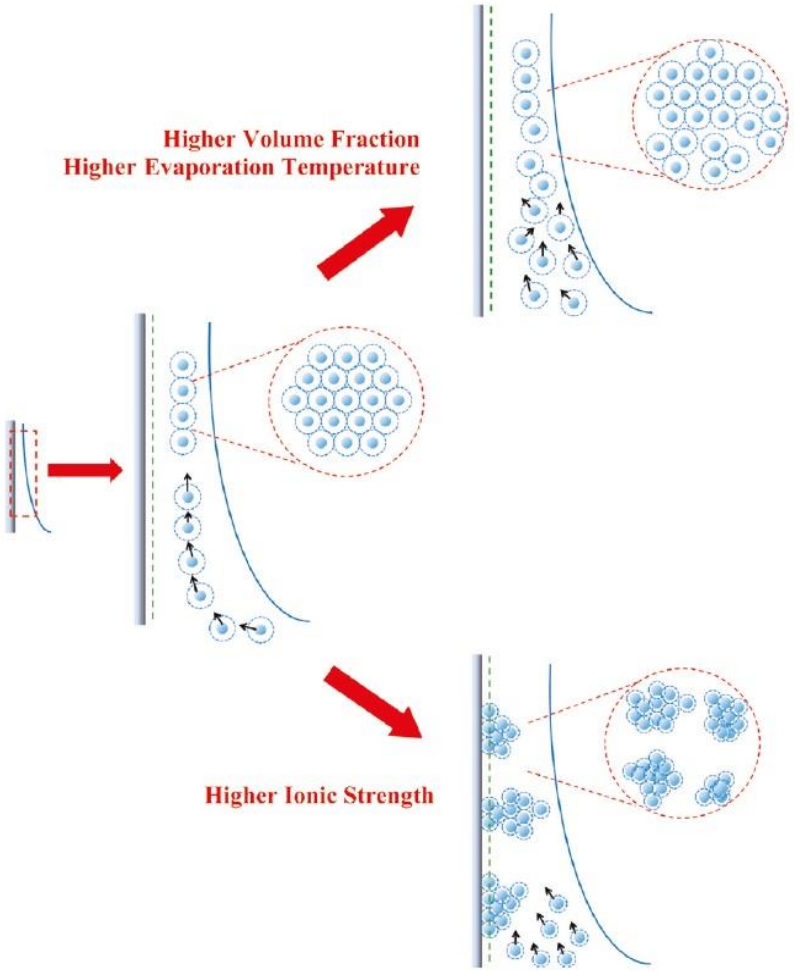

Figure 1.59: Schematic of attractive monolayer colloidal crystal self-assembly process (not drawn to scale). High-density compact hcp monolayer arrays are grown ideally when φ ≤ 0.05 vol. % and c_i ≤ 10 μM KCl at 25°C. However, at higher volume fraction or evaporation temperature, more particles are delivered to the meniscus edge and kinetically trapped into locally ordered arrays due to the faster crystal growth rate. Aggregation of the colloids occurs at high ionic strength conditions. Taken from ref. 66.

1.3.3 Colloidal self-assembly during spin coating process

1.3.3.1 Spin Coating

Spin coating technique offers a simple, fast and straightforward route for the routine fabrication of two-dimensional colloidal crystals, which have a wide variety of potential industrial applications as photonic materials and as templates for the fabrication of 2D arrays for lithography applications [15]. Spin coating process provides easy control of the uniformity, domain size and thickness of the fabricated thin films through tuning the spinning parameters such as spinning speed, acceleration and spin time [67]. The spin coating process can be simply described by four consecutive stages, as shown in Figure 1.60. It starts with deposition stage at which a small amount of the colloidal solution (50µl) is dropped on the surface of a flat substrate (Glass or Silicon) using a micropipette. The colloidal solution is spreading quickly on the whole surface reducing the height to the minimum under the action of the centrifugal forces which guarantees the complete wetting of the substrate surface. Secondly, spin up stage takes place at which the substrate is rotated with a high-speed range between (1000-10000 rpm) for a very short time (5-30 s) using a spin coater machine. Due to the rotational motion, the excess solution is expelled off the rotating substrate edges. The third stage is the stable outflow which starts when the substrate reaches its final spinning speed. Hence, spinning becomes uniform, and consequently, a uniform film thinning takes place under the action of hydrodynamic thinning. Colloidal film thinning stage is characterised by the appearance of distinguishable interference colours that results as the film thickness gradually thins on silicon substrates due to hydrodynamic thinning. Later on, hydrodynamic thinning reaches its minimum and equilibrium occur. Due to the evaporation of the solvent, Viscosity increases initiating the fourth stage at which colloidal film thinning continues under the action of evaporation thinning. During this stage, stepwise film drying causes further shrinkage until the final colloidal thin film forms on the substrate surface [67] [68].

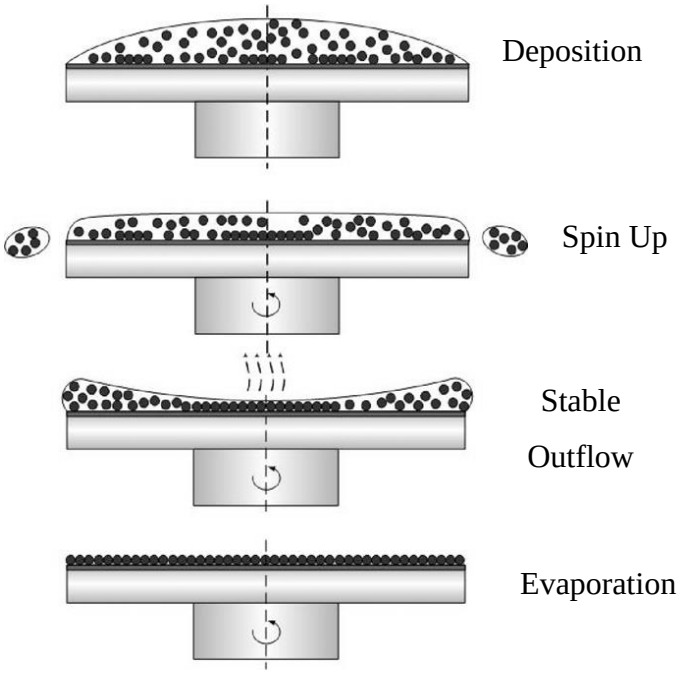

Figure 1.60: Schematic diagram for the stages of spin coating process of colloidal suspensions. Taken and modified from ref. 68.

The realisation of MCCs applications is highly dependent upon the packing quality of colloidal thin films, which is determined by complex self-assembly processes that occur during spin coating. The resultant colloidal thin film morphology is greatly dependent on a number of parameters; nature of colloids, colloidal suspension composition, substrate properties and spin coating parameters. Colloid nature parameters involve Particles diameter, size distribution, surface tension and solubility. Solution composition contains particles concentration, solvent density and evaporation rate. Substrate properties include its hydrophilicity, chemistry, roughness, size and shape. Finally, spin coating parameters are acceleration rate, spinning speed, spinning time, relative humidity and temperature. In order to fabricate well uniform colloidal thin films, all these factors should be considered to optimise the spin coating process fully. Spinning speed and rate of evaporation of the solvent used are among the most important factors affecting the spin coating process. During spinning of the substrate, the solvent evaporates gradually and particles concentration increases which greatly affect the rheology of the solution. Based on the fact that interactions between

substrate and solution layer during the spin coating process are stronger than interactions between solution and air, we can conclude the importance of spinning speed and rate of evaporation in changing the morphology of the produced thin film [45][40].

In 1958, Emslie was the first to initiate research trials to model the spin coating process. Emslie was motivation to solve problems associated with the flow of viscous solutions when being rotated on a flat substrate. In order to do so, Emslie simplified the process by assuming that: (1) the rotating plane is finite and horizontal, (2) the liquid is Newtonian and its layer is thin, (3) in order to eliminate the gravitational force effect, he assumed that liquid layer is symmetric over the whole rotating plate, and finally (4) he assumed that the radial velocity is so small and consequently Coriolis forces, which is responsible for the deflection of moving particles relative to the running frame, have no effect on the flow. These assumptions minimised the applicable factors and simplified the modelling of the spin coating process. This analysis results in a simplified model known as Emslie, Bonner and Peck; commonly referred to as the EBP model as follows; [69]

$$\frac{dh}{dt} = \frac{-2\rho\omega^2 h^3}{3\eta} \tag{1.8}$$

Where h is the film thickness, t is time, ρ is the solution density, ω is the rotation rate in radians per second and η is the solution viscosity in kg s^{-1} m^{-1}.

One major drawback of EBP model is neglecting the effect of solvent evaporation during the process. Meyerhofer was the pioneer to introduce the effect of solvent evaporation to the modelling of the spin coating process. He assumed that spin coating is a two-step process where hydrodynamic thinning is the first step while solvent evaporation acts as the second step of the process. Meyerhofer simply added a term that represents the volatile solvent evaporation to EBP model as shown in the following equation;[70]

$$\frac{dh}{dt} = -2Kh^3 - \mathrm{e} \tag{1.9}$$

Where e is the evaporation rate [ml s^{-1} cm^{-2}]

The impact of the colloidal self-assembly process on the industrial importance of colloidal thin films was the motivation for many researchers to develop further investigations on colloidal self-assembly that takes place during the spin coating process. Monitoring the colloidal self-assembly mechanisms may help to produce better quality MCCs with a minimum defects density.

1.3.3.2 Recent Developments in Studies of Colloidal Self-assembly Taking Place During Spin Coating

In 2004, Jiang *et al.* [1] developed a new method to fabricate 3D large-scale photonic band gap colloidal crystals with a uniform thickness using spin coating technique. Their motivation behind using the spin coating technique was to develop a simple, fast and controllable strategy to fabricate these highly interested structures. In addition, the spin coating process was found to be highly compatible with scale-up to the mass fabrication scale, which is counted as an important advantage over classical techniques, such as self-assembly methods. Herein, monodisperse silica particles with a wide range of diameter sizes from 100 nm to 2 μm were dispersed in non-volatile, viscous ethoxylated trimethylolpropane triacrylate monomer (ETPTA). A Thermdyne Maxi Solution Mixer was used to effectively diffuse silica spheres in ETPTA monomer. Then, colloidal solution was placed on the silicon wafer and spin coated at a specific spin speed. Silica-ETPTA solution was then subjected to ultraviolet radiation to initiate a photopolymerisation process. An oxygen plasma etcher was used to remove ETPTA polymer matrix, producing silica colloidal crystals. 2 % hydrochloric acid solution was used to remove silica spheres producing a macroporous polymer. Effective removal of silica particles and ETPTA polymer matrix without disturbing the structure of the other was guaranteed owing to the high variance in chemical nature of both. UV-vis-NIR spectroscopy was used to characterise optical

properties of the final structures. Scanning electron microscope was used to image final films to characterise their morphology and thickness.

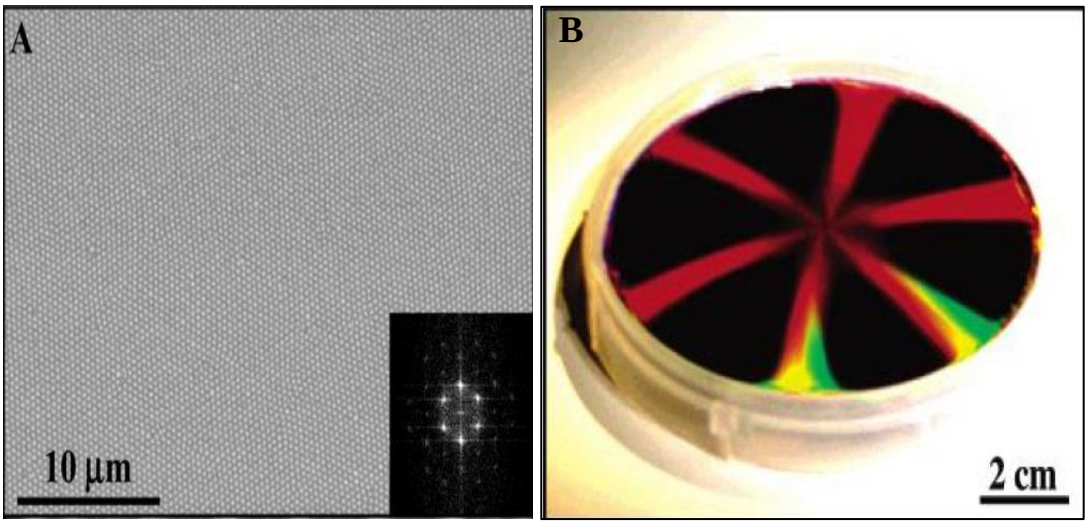

Figure 1.61: A) SEM micrographs with FFT images showing the highly ordered colloidal film formed on the silicon wafer, B) a photographic image for the formed film on silicon wafer during spin coating showing the appearance of six arms regarding to the hexagonal close packing structure. Taken and modified from ref. 1.

Once the substrate rotates, a strong six-arm monochromatic diffraction star appears as shown in Figure 1.61 with a 60° angle between each two adjacent arms. This angle confirmed the formation of a hexagonally close-packed colloidal structure parallel to the silicon substrate. In addition, SEM micrographs together with FFT images confirmed the high ordering of these structures. However, it was found that silica spheres in the top layer were not in close contact with each other. A spacing that coincides with a fraction of the particle diameter (1.41*D) was found to separate each centre-to-centre in the top layer. Jiang claimed that matching between refractive indices of silica spheres (1.42 nm) and ETPTA (1.4689 nm) was the main reason for increasing the stability of films owing to the consecutive decrease in Van der Waals forces between them. In addition, it was found that film layer thickness was highly dependent on both rotational speed and spinning time. As given in Figure 1.62, thickness was found to be inversely proportional to both spinning speed and square root of the spin time. This study provided a step forward in shear-induced crystallisation investigations. However, it still had many drawbacks that limited the possibility of usage of this technique widely in this field. First, the high viscosity of ETPTA monomer solution makes the continuously mechanical mixing essential to avoid any particle aggregation. Photopolymerisation stabilisation of ETPTA monomer

solution through ultraviolet radiation decreases the porosity. As a result, refractive index contrast decreases, which significantly affects the optical properties of the final colloidal structure. Finally, the similar chemical nature of several colloids and matrices in this field inhibits the selective removal step. Consequently, this technique is not compatible in too many cases, which limited its usage and reduced its industrial application.

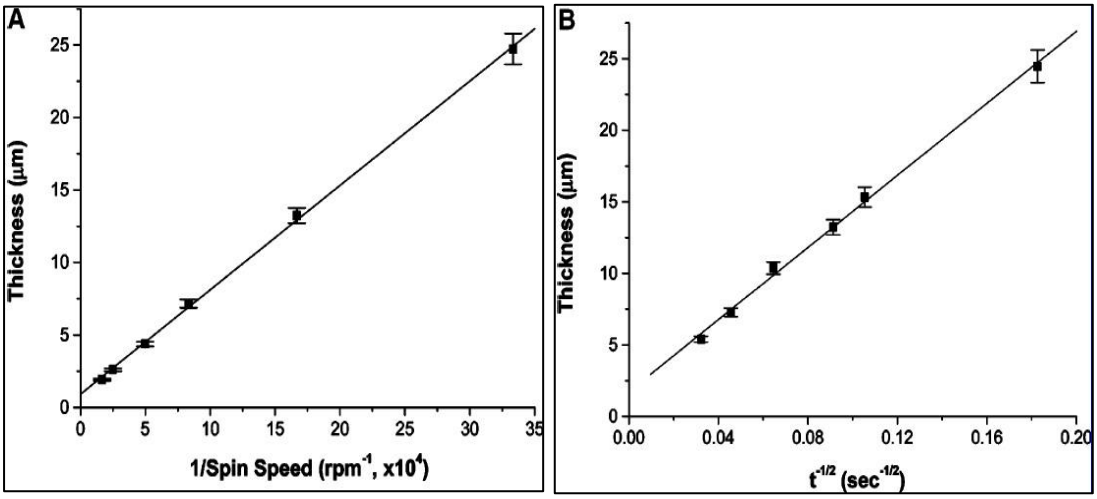

Figure 1.62: Crystal thickness control via spin coating parameters. (A) Linear relationship of the crystal thickness vs the inverse of the spin speed at constant coating time, 120 s. (B) Film thickness vs the inverse of the square root of spin time at constant spin speed, 600 rpm. 325 nm diameter colloids are used for all cases. Taken from ref. 1.

Mihi *et al.* [71] modified the previous technique by utilising volatile solvents instead of the non-volatile, viscous ETPTA monomer as a dispersion medium. The intensions behind that modification were not only to increase the optical quality of the highly ordered close-packed colloidal crystals formed with controllable thickness, but also to determine the crystallisation growth direction regarding the substrate. Their strategy was based on utilising a mixture of water, ethanol and ethylene glycol as a dispersion medium in order to increase the time available for reorganisation of particles under shear forces, and to get rid of that medium easily by complete evaporation without any further processing. In this approach, silica spheres of 400 nm and 600 nm were fabricated by Stöber method. Spheres were suspended in ethanol and left to dry overnight at 50^{o}C. Also, polystyrene particles with a diameter size of 400nm and 500nm were purchased. Glass substrate was subjected to a series of cleaning steps; distilled water, acetone, carbon tetrachloride, isopropyl alcohol, Piranha cleaning.

Then, substrate was washed with a copious amount of distilled water before drying with a nitrogen stream. Colloidal dispersions were prepared by adding particles with different concentrations to water-ethanol-EG mixture with different volume fractions. 200 µL of suspension was placed on the glass substrate for 30s to ensure complete coverage of the substrate size. Sample was then spin coated at different speeds (1500 rpm – 12000 rpm) for different periods (2 - 15 min). SEM was used to characterise the final morphology as well as the growth direction. While, FTIR spectrophotometer together with an optical microscope were used to determine the reflectance spectra.

SEM images, given in Figure 1.63 and Figure 1.64 showed that particle concentration has a significant impact on the colloidal crystal thickness. As the particle concentration increases, the thickness also increases with the favourable formation of [111] oriented crystals with a face-centred cubic close-packing. However, as the particle concentration decreases, thinner films are formed with the favourable orientation of [100] square crystals. In addition, the type of solvent in the dispersion medium had a great effect on the final colloidal crystals. It was found that non-uniform colloidal crystals were formed when using water alone as a dispersion medium. However, utilising ethylene glycol (EG) instead of water favours the formation of a short range of [100] square colloidal crystals. Introducing a mixture of water, ethanol and ethylene glycol not only improves the long-range ordering of [111] oriented crystals, but also improves the thickness uniformity formed. Introducing a mixture of solvents decreases the evaporation rate of the dispersion medium and extends the transition stage in which the possibility of reorganisation of particles increases. These results coincided with Koh's recommendation [59] that increasing the lifetime of transition stage may help to improve colloidal ordering during the self-assembly process. As EG exceeded 30 % by volume fraction, thinner crystals were formed with an improvement in the optical properties. However, decreasing the EG volume fraction led to the formation of thicker layers with bad optical properties. Therefore, optimisation was necessary to compromise the formation of a large scale of highly ordered close-packed colloidal crystal with [111] orientation direction with the desirable thickness. Jiang deduced that the best colloidal crystal among this investigation was formed at 50 vol. % silica particles, 10 vol. % water and 40 vol. % ethylene glycol. This study provided a simple spin coating technique to control both

the colloidal crystal thickness as well as the colloidal crystallisation growth orientation direction. Complete evaporation of dispersant developed the final colloidal structure without any need for further processing. A long domain size was obtained within minutes, which highly facilitates the scaling-up to mass fabrication of these highly uniform colloidal thin films into the industrial field [71].

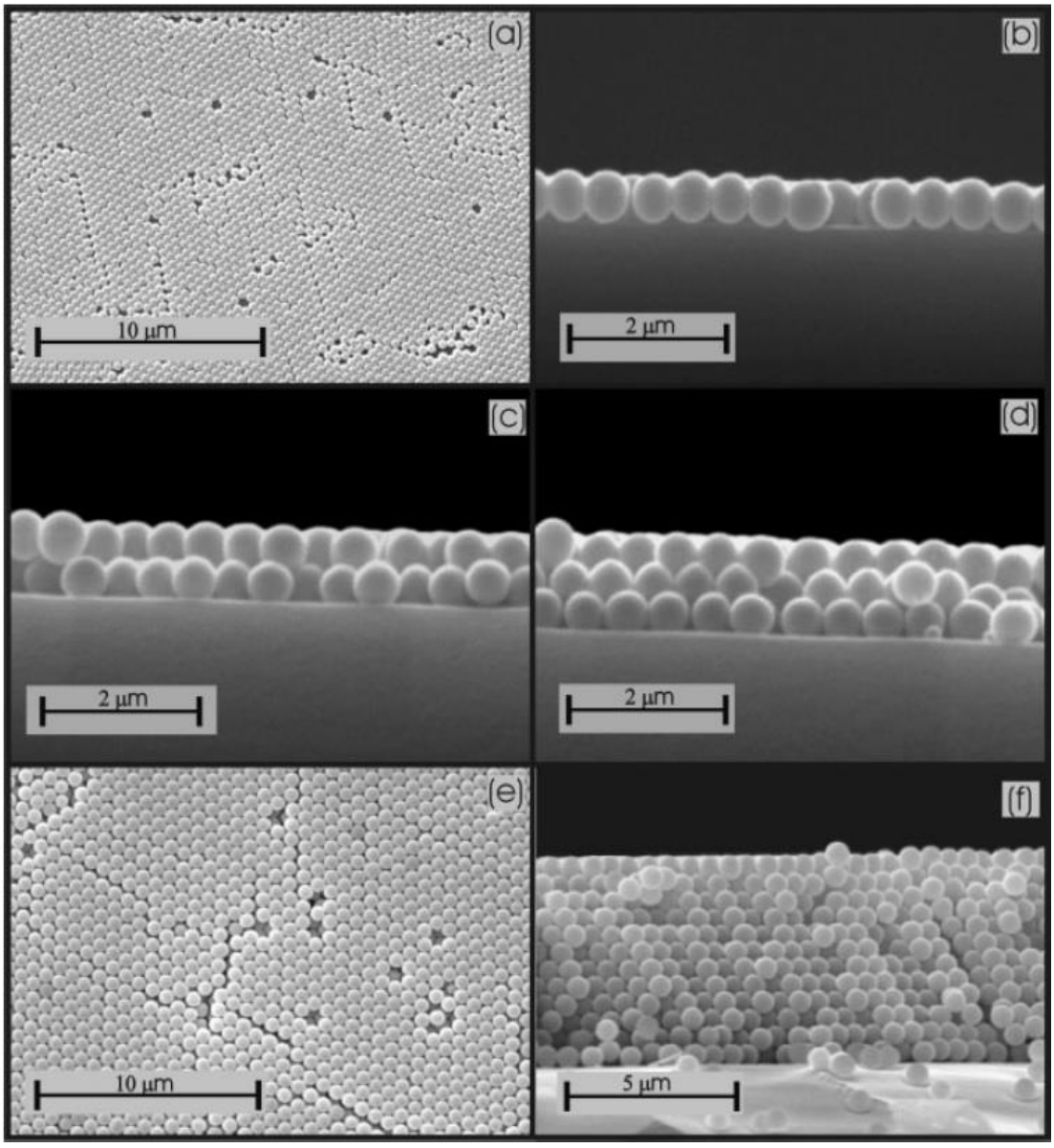

Figure 1.63: SEM images of spin-coated, [111]-oriented colloidal crystals built from dispersions containing a–d) 30% SiO2 particles (440 nm diameter) in a mixture of ethanol and EG (35 vol% each) and e,f) 50% silica spheres (600 nm diameter) in a mixture of water (10 vol %) and EG (40 vol %) at various spinning velocities. a) Top view of a monolayer of silica spheres packed hexagonally, obtained at x= 175 rps. We also show side views of b) the previously mentioned monolayer, c) a bilayer obtained at x= 125 rps, and d) a 3 ML stacking of silica spheres produced at x= 75 rps. Images in (e) and (f) are top and side views of a 12 ML FCC photonic colloidal crystal grown at x= 25 rps. Taken from ref. 71.

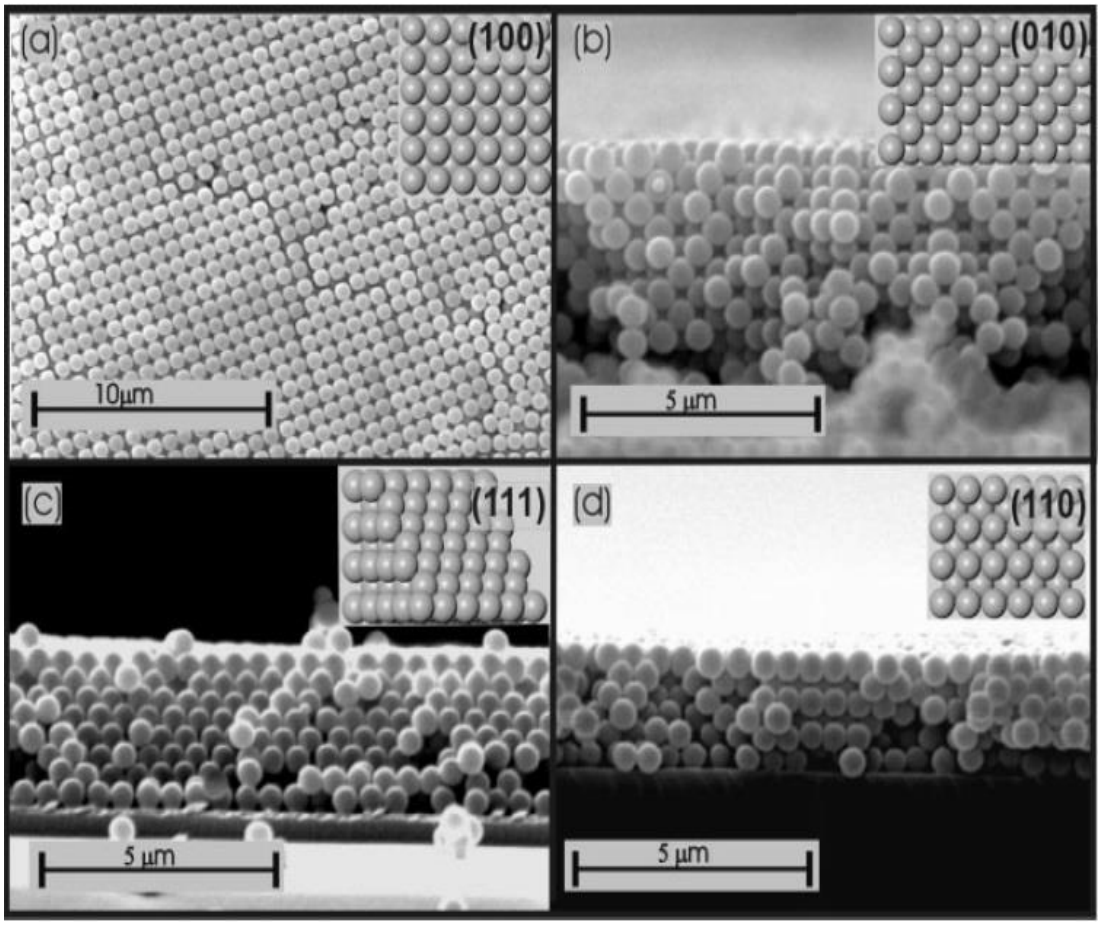

Figure 1.64: SEM images of different crystalline planes found in the top and side views of a [100]-oriented silica colloidal crystal grown by spin-coating, fabricated from a silica dispersion in ethanol containing a 30% particle volume fraction. a) Top view corresponding to (100) planes. b–d) Side views of the structure showing fcc planes differently oriented with respect to the upper surface, namely, b) perpendicular (100) planes, c) inclined (111) planes, and d) perpendicular (110) planes. Spinning speeds are b) x= 25 rps, c) x= 50 rps, and d) x= 100 rps. Insets show the corresponding top and side views of a thin FCC sphere crystal model fabricated by piling seven squarely arranged monolayers. Taken from ref. 71.

Sharma *et al.* [72] demonstrated a simple and fast method to successfully organise oppositely charged PS particles that attain a strong Coulombic attraction into LbL ionic colloidal crystals. In the literature, it was found that strong Coulombic forces limit the length scale of colloidal ordering of oppositely charged colloidal particles into binary superlattices. Consequently, assembly of oppositely charged particles into a three-dimensional colloidal structure with an ordering strong enough to survive during the solvent drying stage was a great challenge. Sharma was motivated to overcome that challenge and achieve an acceptable ordering between

strongly Coulombic oppositely charged particles. The processing method was based on two consecutive steps. Firstly, negatively charged PS particles were deposited on a negatively charged substrate through flow-controlled vertical deposition technique. Secondly, positively charged PS spheres, smaller in diameter, were deposited on the fabricated negatively charged template through spin coating technique at 3000 rpm for 60 s. The developed colloidal structures were found to exhibit only short-range ordering. Lack of long-range ordering was a direct result of the strong electrostatic Coulombic attraction forces between oppositely charged particles. These attraction forces pulled PS particles towards each other. The small interparticle distance restricted the particles mobility and inhibited the long-range colloidal ordering. However, a well ordered colloidal structure with a long domain size was formed on the substrate when Triton X-100 was added as a nonionic surfactant before spin coating. Adsorption of PS spheres to the hydrophobic end of the surfactant induces a steric barrier. This barrier develops a short-range repulsive force that is crucial for colloids to attain mobility during spin coating. Mobility improves particles ordering, forming a long-range of well-ordered LS_2 or LS_6 superlattice structures depending on the rotational speed and spin time.

Initially, 20 µL of 0.025 w/v % and 0.1 w/v % solutions of positively charged 100 nm PS spheres suspended in deionized water were individually grown upon the first layer using spin coating technique. Sample was rotated at 3000 rpm for 60 s. As shown in Figure 1.65; developed colloidal structures were found to exhibit only a short-range ordering. Lack of long-range ordering is a direct result of the strong electrostatic Coulombic attraction forces between oppositely charged particles. These attraction forces pulled PS particles towards each other. Small interparticle distance restricted the particles mobility and prevented the long-range colloidal ordering. Besides the strong Coulombic forces action, Sharma *et al.* claimed that hydrophobic interaction also decreases the particles mobility of positively charged PS spheres during spin coating and minimizes the ordering quality.

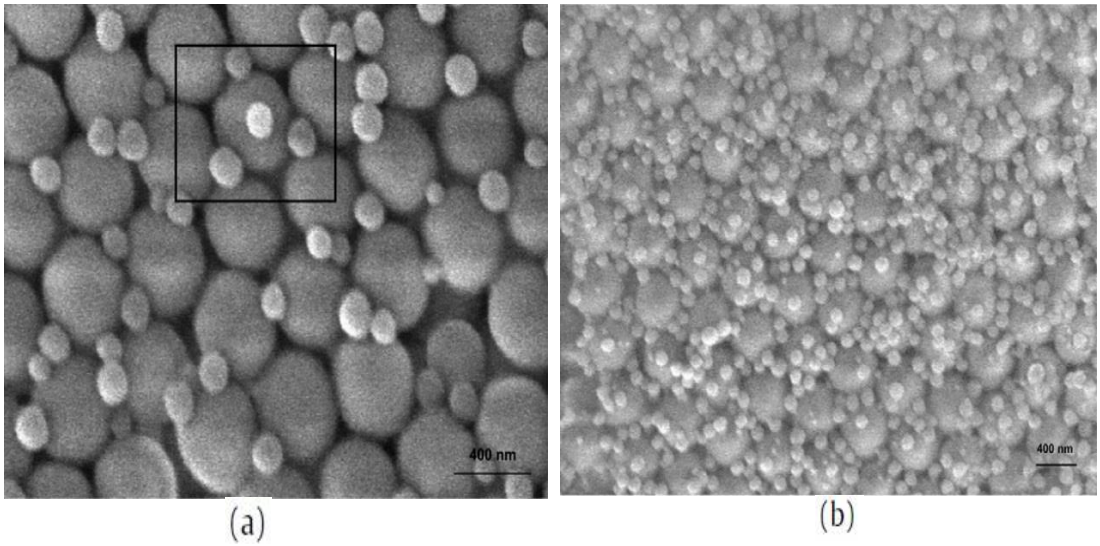

Figure 1.65: (a) 100 nm diameter positively charged PS sphere suspension (0.25%, w/v) spin-coated at 3000 rpm on a substrate made from 420 nm diameter negatively charged PS spheres. (b) 100 nm diameter positively charged PS sphere suspension (1.0%, w/v) spin-coated at 3000 rpm on a substrate made from 420 nm diameter negatively charged PS spheres. Taken from ref. 72.

Deionized water as a solvent in the colloidal suspension was replaced by a mixture of deionized water and isopropanol (IPA) with a volume ratio of 80%: 20% respectively as a trial to improve colloidal ordering by increasing particles mobility during spin coating process. However, SEM micrographs, as given in Figure 1.66, showed that colloidal structures formed in case of DI water-IPA was disordered. It was expected that introducing IPA will reduce capillary forces and then decrease particles coagulation due to its lower surface tension when compared to water. Also, IPA develops a higher ability to wet PS spheres more than water. Increased wettability should increase particles mobility and improve colloidal ordering. However, very low permittivity of IPA (fourth of water permittivity) decreases the Debye screening length to be half of the value exist in case of deionized water. Hence, colloid-colloid interaction increases leading to disordered colloidal arrangement.

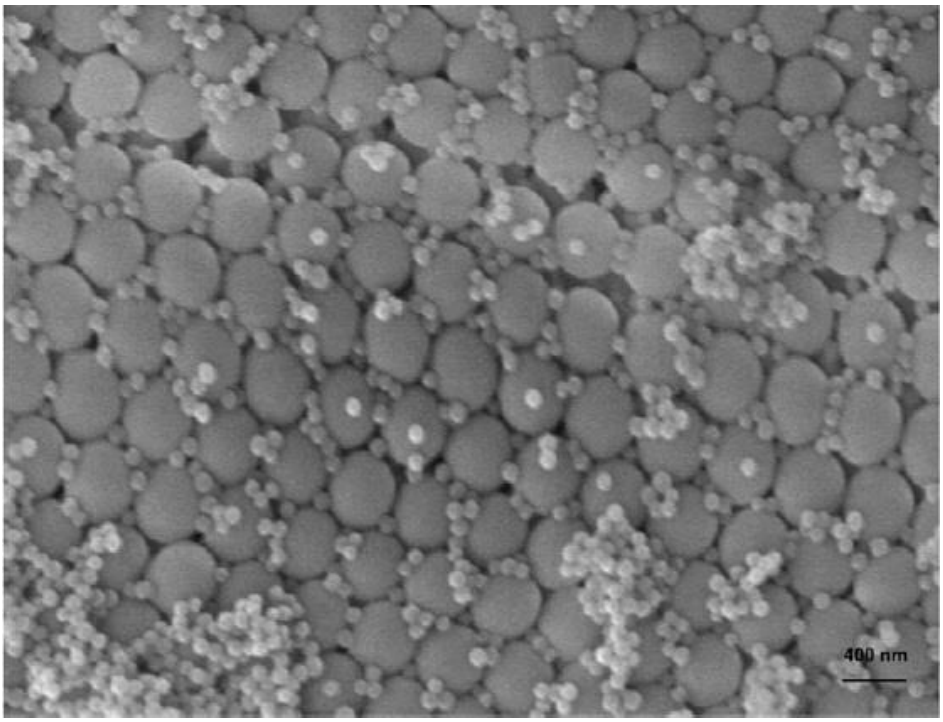

Figure 1.66: SEM micrograph showing disordered structure formed in case of 100 nm diameter positively charged PS sphere suspension (1.0%, w/v) in isopropanol (80%)–DI water (20%) spin-coated at 3000 rpm on a substrate made from 420 nm diameter negatively charged PS spheres. Taken from ref. 72.

Sharma *et al.* then spin coated 0.25 w/v % solution of 100 nm positive PS particles with different salt concentrations. It was found that Debye screening length decreases as concentration of NaCl increases as shown in Table 1.3. As Debye screening length decreases, distance between particles also decreases inducing a limited particles mobility. As a result, limited particles mobility prevents particles from regular ordering. As a result a disordered structure was formed. Also, higher degree of particles coagulation was noticed during spin coating at higher salt concentrations. This may be attributed to the decrease in Coulombic repulsion forces between positively charged PS particles. However, a well ordered colloidal structure with a long domain size was formed on substrate when 1.0 w/v % solution of 100 nm positive PS particles was spin coated with Triton X-100 ($C_{14}H_{22}O$-$(C_2H_4O)_n$ with n = 9–10) as a nonionic surfactant. Adsorption of PS spheres to the hydrophobic end of

the surfactant induces a steric barrier. This barrier develops a short-range repulsive force that is crucial for colloids to attain mobility during spin coating. Mobility improves particles ordering forming a long-range of well-ordered LS_2 superlattice structure as shown in Figure 1.67 a. Spin coating 1.0 w/v % solution of 210 nm positive PS particles in deionized water at 3000 rpm for 60s in the presence of a nonionic surfactant also developed a similar LS_2 ordered structure with a long domain size. However, spin coting 0.25 w/v % solution of 100 nm positive PS particles in water with a nonionic surfactant at 6000 rpm for 60s leads to the formation of LS_6 long-range ordered structure as shown in Figure 1.67 b. In this study, spin coating technique was found to be an effective route to organise particles into ordered arrays. During spin coating, PS spheres were trapped into vacancies which allows capillary attraction forces to drive these colloids to order themselves into large LS_2 and LS_6 ordered structures.

Table 1.3: Variation of Debye length with increasing NaCl concentration in water.

NaCl Concentration [×0.01 mM]	Debye Screening Length [nm]
No added salt (DI water)	250.354
1.635	75.22
9.4672	31.26
87.9	10.256

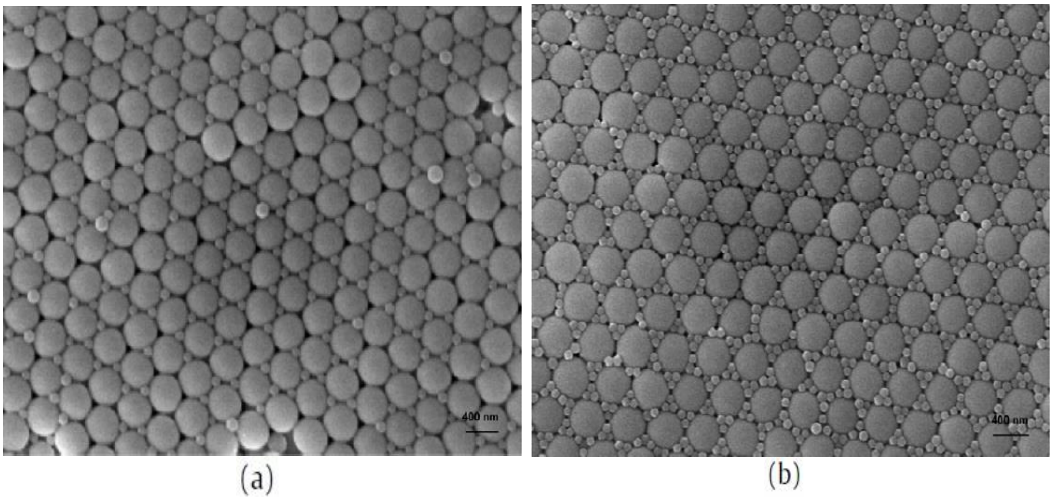

Figure 1.67: (a) 100 nm diameter positively charged PS sphere suspension (0.25%, w/v) in DI water with Triton X-100, spin-coated at 3000 rpm on a substrate made from 420 nm diameter negatively charged PS spheres for 60 s, (b) 100 nm diameter positively charged PS sphere suspension (1.0%, w/v) in DI water, spin-coated at 6000 rpm on a substrate made from 420 nm diameter negatively charged PS spheres for 60 s. Taken from ref. 72.

In 2010, Giuliani *et al.* [73] utilised a combination of high-speed camera, with a rate of 1000 frames per second, together with atomic force microscopy, static photography and scanning electron microscopy in order to investigate the symmetry transitions that took place during spin coating colloidal suspension. In this study, silica particles with a particle diameter of 458 nm and a standard deviation of less than 1.0 % were suspended in acetone or methyl ethyl ketone, as a volatile solvent, with different volume fractions.

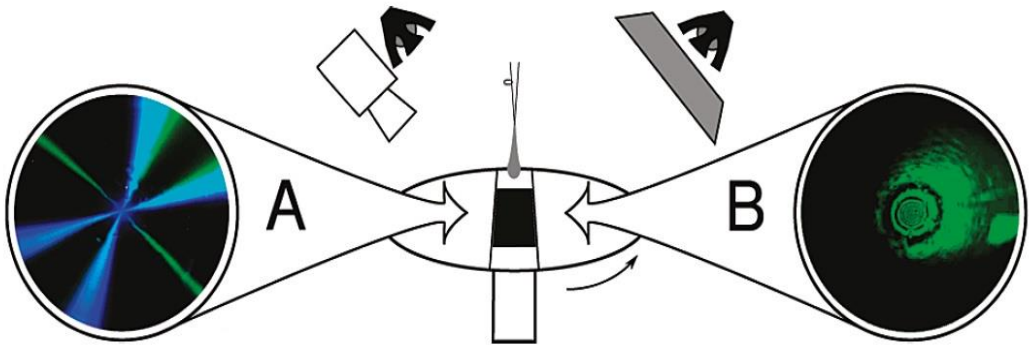

Figure 1.68: Schematic diagram for Giuliani's experimental setup showing different lighting configurations that (A) magnify the contrast of the long-range orientational order and (B) enable the visualization of thickness in the fluid. Taken from ref. 73.

Specular reflections during spin coating were visualised through the imaging setup shown in Figure 1.68. A 300 W tungsten bulb as a light source was used to image the variations in colloidal ordering during the self-assembly process. The light source was adjusted to cover the whole process either in suspension or at the drying colloidal film. Owing to the setup adjustment, any symmetry observed from this set up was attributed to a 2D colloidal structure parallel to the silicon substrate. Patterns of alternating rings observed during spin coating showed that several transitions took place during the colloidal film thinning from six-fold (hexagonal arrangement) to four-fold (square arrangement) and finally back again to six-fold. These transitions indicated that colloidal re-organisation during the spin coating process took place through two consecutive stages: the dynamic stage and the drying stage. These observations showed that thinning dynamics has a key role in colloidal self-assembly during the spin coating process. It not only controls volume fraction and stress profiles,

but also drives the structural transitions. However, these results are still based on reciprocal space. Hence, the real-time colloidal ordering mechanism that takes place during spin coating is not fully understood.

Recently, Toolan *et al.* [74] integrated an "optostrobometer" setup to develop a real-time stroboscopic microscopy insight into colloidal self-assembly mechanisms that take place during the spin coating technique. This study aimed to understand in detail the colloidal ordering mechanisms as well as the forces that govern the self-assembly processes of spin-coated colloidal suspensions. The optostrobometer setup as represented in Figure 1.69 is composed of a small DC motor that acts as the spin coater. The motor shaft was attached to the glass substrate, which contains the colloidal sample, via a transparent Perspex chuck. The motor shaft was used to rotate the substrate at a rotational speed of 1250 rpm for 48 s. An optical microscope with a 40× objective (Nikon CFI S Plan Fluor ELWD 40×) was placed above the glass substrate. Current delivered to the motor develops a sharp pulse. This pulse was used to trigger both illumination and image capture. A high-powered LED was used as a white light source. An Andor iXON (897+) camera with a field of view of 464 × 464 mm was used as a high-sensitivity EMCCD camera. Both LEDs and camera were electronically synchronised with the rotation of the motor in order to capture one static image per revolution, regardless to the rotational speed.

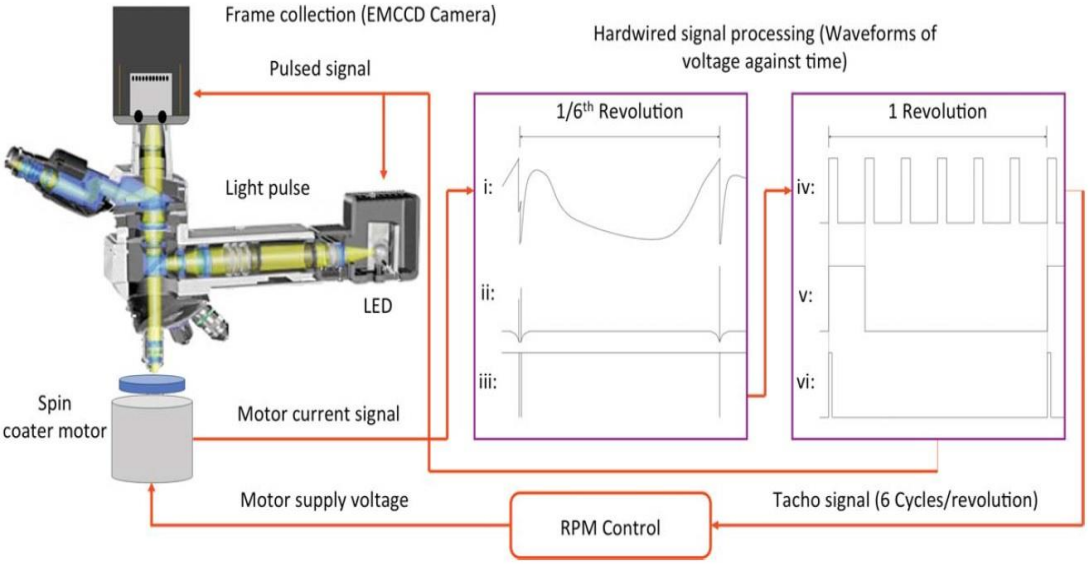

Figure 1.69: Schematic diagram showing the optostrobometer technique. Taken from ref. 74.

In this study, 5.0 µm polystyrene particles with a standard deviation of about 1.0 % were used with different concentrations in water to prepare colloidal suspensions. Ordering changes that took place during the spin coating process in both intermediate and final colloidal structures were visualised and characterised though the stroboscopic microscope setup in combination with the corresponding FFT images.

In situ observations for the 25 wt. % colloidal suspension in water, given in Figure 1.70, showed that initially particles were in random motion. Later on, water evaporation induced shear forces at which point the colloidal suspension film thickness was gradually decreasing. At a certain stage, a transition from shear thinning into evaporation thinning took place. This transition was easily recognised through the real-time observations from the sudden change in the direction of particle motion, since shear force direction should be fixed as it was originally generated as a result of substrate rotation. Hence, any change in particle motion direction is a direct indication for the change in the shear force itself. As water evaporation proceeded, solid content concentration was increased. As a result, a degree of colloidal ordering took place, forming an ordered structure with many voids. Appearance of random voids induced capillary attraction forces that forced particles to reorder themselves along drying fronts. Stroboscopic data for the 35 wt. % dispersion showed similar ordering stages. However, a higher degree of ordering was observed during the evaporation thinning stage owing to the higher particle concentration. Dried colloidal structure morphology was unpleasantly polycrystalline with some holes owing to incomplete coverage. Stroboscopic observations for the 45 wt. % suspension showed an earlier transition followed by a larger degree of colloidal re-organisation owing to higher concentration used in this case. However, multilayers separated by holes and dislocations of particles were formed. This was attributed to the inability of drying fronts to manage dragging the huge number of particles into favourable sites. Stroboscopic data for colloidal suspensions in water revealed that ordering could happen through one of two mechanisms: (1) capillary-induced ordering; and (2) packing constraints initiated by the decrease in interparticle distance owing to the higher particle concentration.[75]

Toolan followed on by trying to investigate the impact of dispersant volatility on the colloidal ordering mechanisms. To do so, water was replaced by pure ethanol as a

solvent in the colloidal suspension. Unlike water suspensions, stroboscopic data for the 25 wt. % colloidal suspension in pure ethanol, given in Figure 1.71, showed the absence of radial flows in the first stage of the spin coating process. This result confirmed the prolonged effect of solvent evaporation even in the early stages of the colloidal spin coating process. However, rapid evaporation of ethanol decreased the time available for the particles to self-assemble. Consequently, particles were unable to explore the favourable sites during the ordering process and became trapped. Hence, non-equilibrium, disordered colloidal structures were observed at the end of the sample rotation. These in situ observations coincided with Routh and Zimmerman's model [76] as well as Reyes and Duda's simulation results [77], which deduced that the fast evaporation of ethanol prevented particles from re-organising into ordered arrays.

These results motivated Toolan to investigate the impact of using different water–ethanol mixtures on the colloidal ordering as a dispersant instead of pure water or pure ethanol. Stroboscopic data for the 25 wt. % dispersant in water–ethanol mixture (6:4) showed the appearance of weak six-fold symmetry containing voids and particle accumulation on both substrate and towards the suspension–air interface. However, as evaporation proceeded, particles were forced to sediment only on the substrate, initiating a shear-induced ordering. Once voids appeared along the growing colloidal structure, ordering was found to be governed by capillary drying fronts. Stroboscopic data for the 25 wt. % dispersant in water-ethanol mixture (1:1), given in Figure 1.72, showed that a regular monolayer structure was completely covering the substrate with the presence of some voids. Then, particles were observed to flow over the initial monolayer. At this stage, colloidal ordering started under the action of shear forces leading to the filling of all holes along the structure. Then, the whole monolayer was moving as a unit until forming a regular ordered close packed colloidal structure under shear-induced crystallisation. However, as volatility was increased in the 25 wt. % dispersant in water–ethanol mixture (4:6), it was found that ordering was greatly distorted owing to excessive shear, leading the reappearance of voids. These voids induced subsequent capillary attraction forces. As a result, capillary-induced ordering took place, forming a highly ordered polycrystalline colloidal structure with the presence of large voids [74]. These real-time observations enabled more

understanding of the finer details of the colloidal self-assembly processes during the spin coating technique. This better understanding shed light on the possibility of developing a controllable industrial strategy to fabricate complete 3D photonic band gap materials with a large domain size, defect-free and highly ordered close packed colloidal structure.

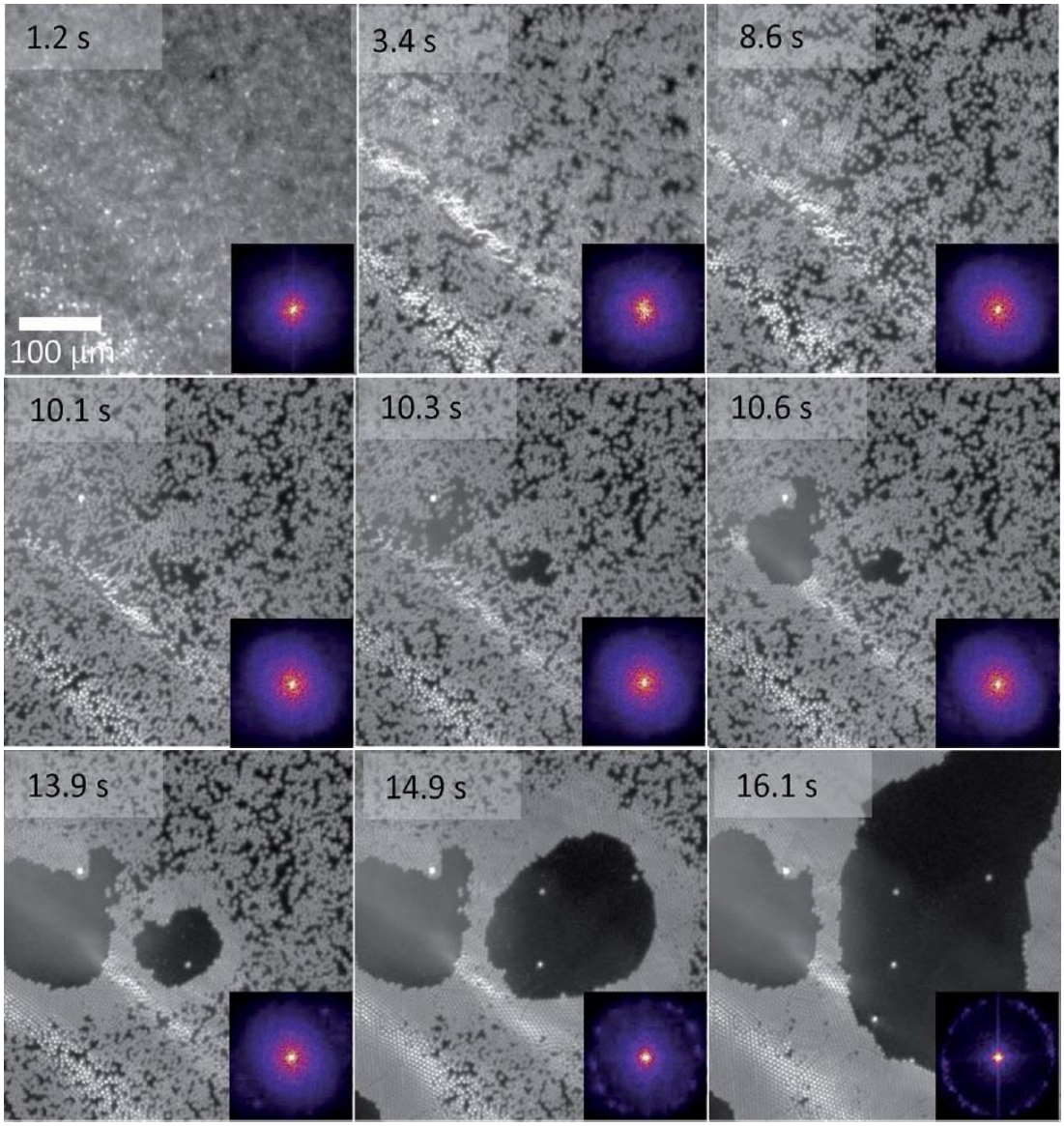

Figure 1.70: Series of stroboscopic microscopy images (with corresponding FFTs) for a 25 wt. % colloidal dispersion in water spun-cast at 1250 rpm. Taken from ref. 75.

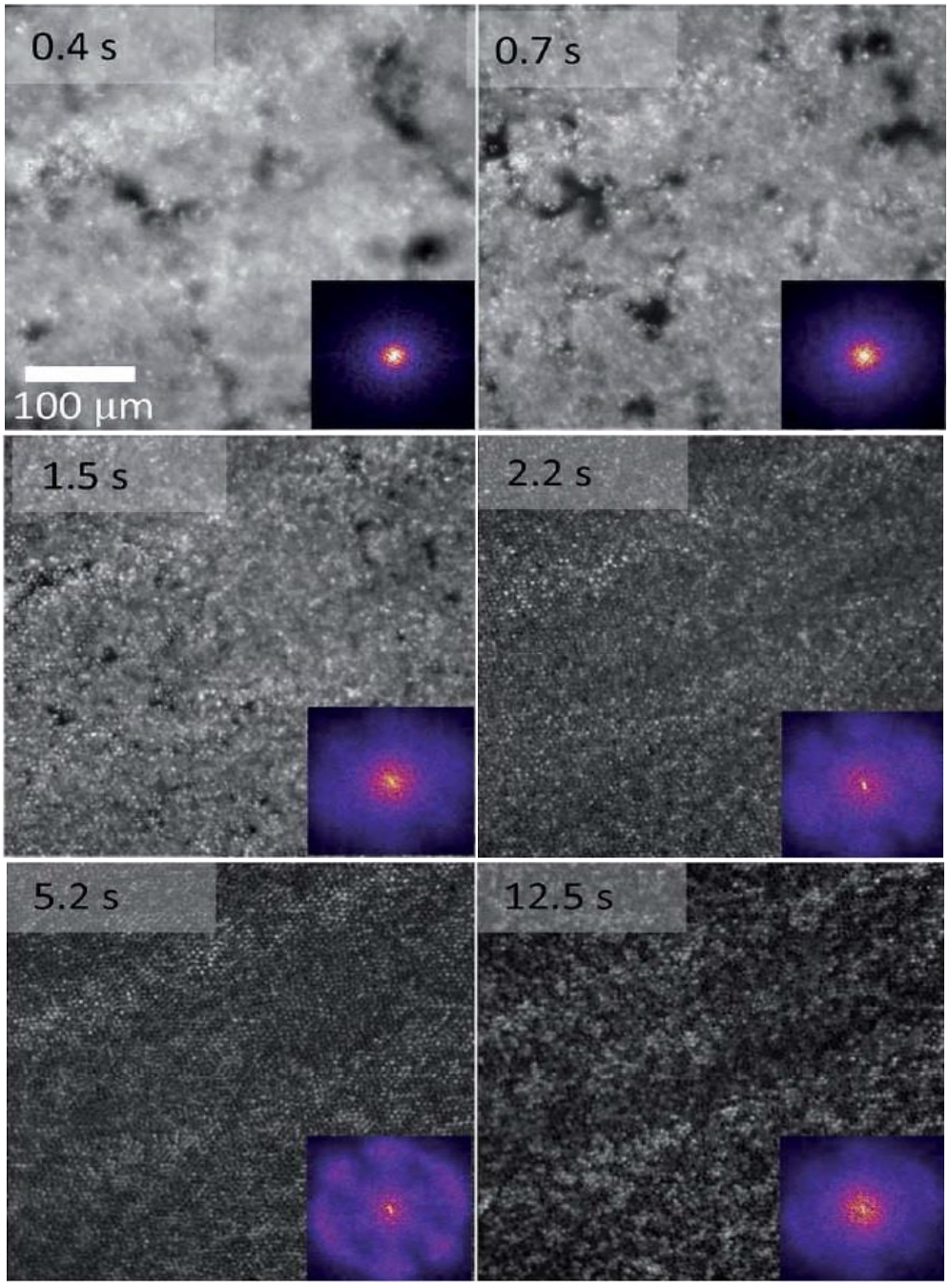

Figure 1.71: Series of stroboscopic microscopy images (with corresponding FFTs) for a 25 wt. % colloidal dispersion in ethanol spun-cast at 1250 rpm. Taken from ref. 75.

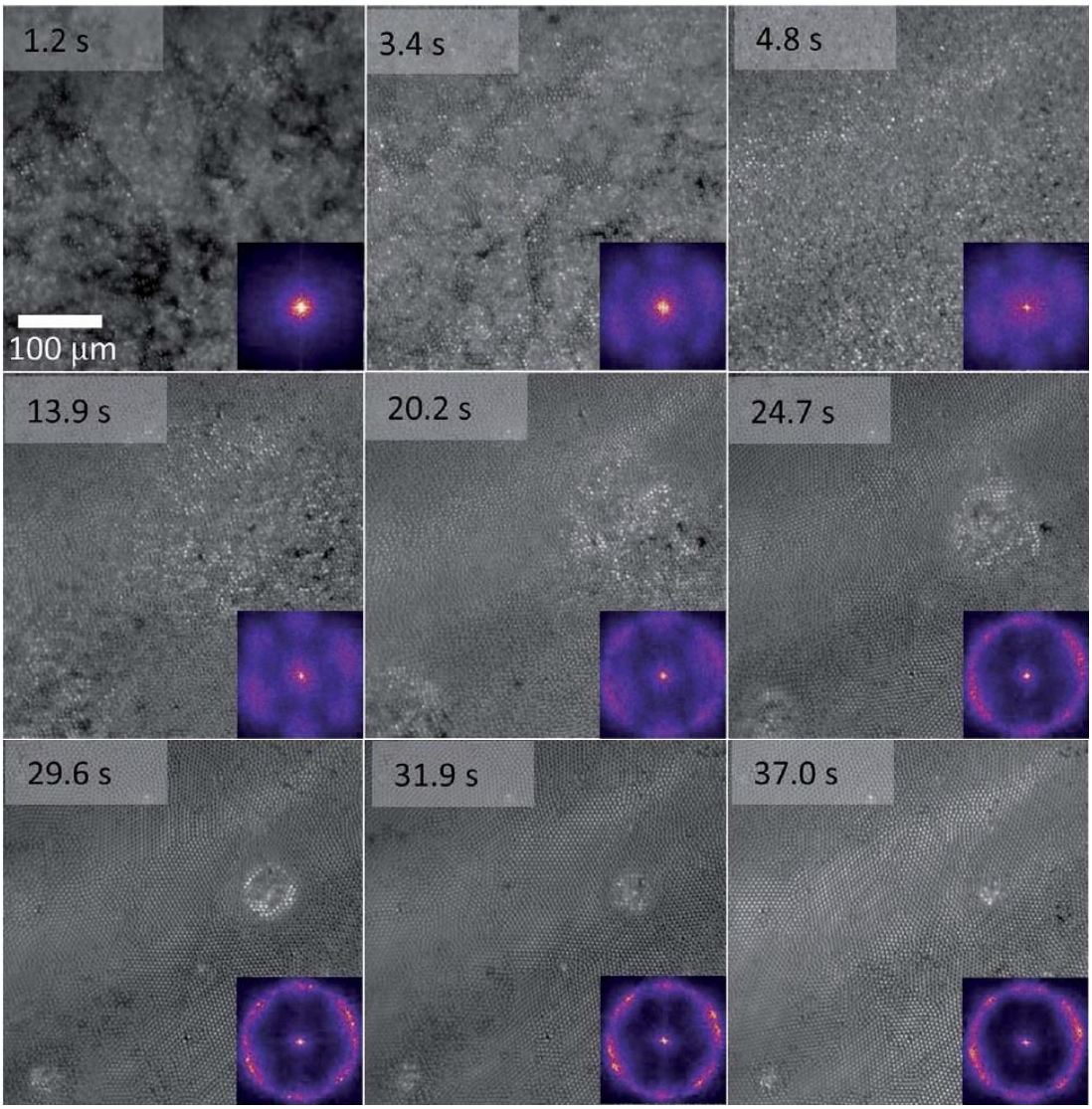

Figure 1.72: Series of stroboscopic microscopy images (with corresponding FFTs) for a 25 wt. % colloidal dispersion in a water–ethanol mixture (1: 1) spun-cast at 1250 rpm. Taken from ref. 75.

1.4 Summary and Scope of This Thesis

Since the discovery of the interesting industrial photonic applications of monolayer colloidal crystals, many researchers have tried to investigate colloidal self-assembly mechanisms in detail, as well as the forces that govern the colloidal ordering. The EBP model together with Meyerhofer's contribution were the first to model the spin coating process. Based on these studies, the spin coating process has been divided into two consecutive stages: the first stage is dominated by flow owing to rotation, whilst the second stage is dominated by solvent evaporation. Later, several techniques based upon reciprocal space were used to characterise the morphology of the final colloidal crystals. This helped in optimising processing parameters and so improving the colloidal reorganisation quality. Real-time studies together with numerical simulations provided further understanding of the whole process. *In situ* investigations, either using direct measurement such as high speed optical microscopy or indirect measurement such as laser scattering, helped to develop assertive information about the development of lateral structure, high-speed dynamics of evaporative spin coating, structural transitions and some crucial forces that significantly affect the colloidal ordering quality. This knowledge acts as a step forward towards the fabrication of long-range, defect-free and highly close-packed monolayer colloidal crystals. However, despite all these studies, we are not yet able to understand the exact mechanism that these nanostructure photonic crystals obey. Furthermore, the huge number of parameters affecting the colloidal ordering process makes full modelling of the spin coating process a serious challenge. Hence, fabrication of complete photonic band gap colloidal crystals is still inaccessible.

This thesis aims to study both the spin coating mechanisms and the crucial factors affecting the colloidal ordering during self-assembly process. This information may lead to optimising the processing conditions and so could lead to fabricate a more uniform colloidal thin films through a simpler and controllable method. To do so, a combination of *in situ* laser scattering investigations and *ex situ* investigations based on reciprocal space took place. My intensions were to study the impact of crucial factors on the degree of colloidal ordering during self-assembly process using optical microscopes together with LabVIEW software for analysis. Results may help to

optimize the spin coating processing parameters in order to develop a controllable technique to fabricate a large domain size of highly ordered, defects free monolayer colloidal crystals. Secondly, through *in situ* investigations using our new laser scattering set up we may be able to provide certain information about what is exactly happening through self-assembly during spin coating process. This setup develops laser scattering patterns that could give instantaneous indication for the colloidal ordering quality and so tracking the structure variations with time could be used to visualise the colloidal self-assembly stages. This information may help to develop further understanding and more control over the whole technique.

Chapter 2.

Methodology

2.0 Introduction

In this chapter, the detailed information of methodology used to study the formation of highly ordered monolayer colloidal crystals (MCCs) during spin coating process at a wide range of processing parameters is described. Moreover, experimental techniques used for either characterisation or analysis are briefly explained.

2.1 Methodology

Experimental work in this thesis is divided into two main stages; (1) *ex-situ* investigations and (2) *in-situ* investigations.

2.1.1 Ex-Situ Investigations Stage

In order to optimise a wide array of different spin-coating parameters, such as colloidal particles concentration, rotational speed, acceleration rate, polydispersity, settling time and solvent volatility and assess their effect on the colloidal ordering quality the final films were assessed *ex situ* using an Eclipse LV100 optical microscope connected to an Andor camera (Zyla 5.5 sCMOS) with a quantum efficiency (QE) of 60 %. An optical microscope was performed in transmission mode, and samples were captured using 20×, 40× and 60× Nikon CFI S Plan Fluor ELWD objectives. Each spin coating processing was repeated five times and fabricated colloidal thin films were captured five times; once from the centre of the substrate and another four times within 1 mm distance from the substrate centre in the four directions. The acquired images of the spun-cast colloidal films were analysed using custom made LabVIEW software that detects each spherical particle in an image and then determines the area coverage percentage occupied by these spherical particles with respect to the total image area. The detailed steps of the *ex-situ* investigations stage are described as follows;

2.1.1.1 Experimental Design

A controllable spin coater regulated within a range of rotational speeds (0 - 5000 rpm) and various acceleration rates (0 - 220 $rev.s^{-2}$) was designed, consisting of a Maxon EC motor with hall sensors (EC 90 flat [Part Number: 323772]), ESCON controller 70/10, NI DAQ USB 6008 and a 420-watt DC power supply. The spin-

coating set-up is shown schematically in Figure 2.1. LabVIEW software was used to control the rotational speed and spin time during spin coating process through NI DAQ module, where input voltage value was calibrated with the motor rotational speed. In addition, ESCON studio software was used to adjust acceleration rate and response of the motor to the applied voltage via DAQ module before spinning starts. This assembly was surrounded by a bowl to remove air flows that might impact on the colloidal ordering quality during the spin coating process.

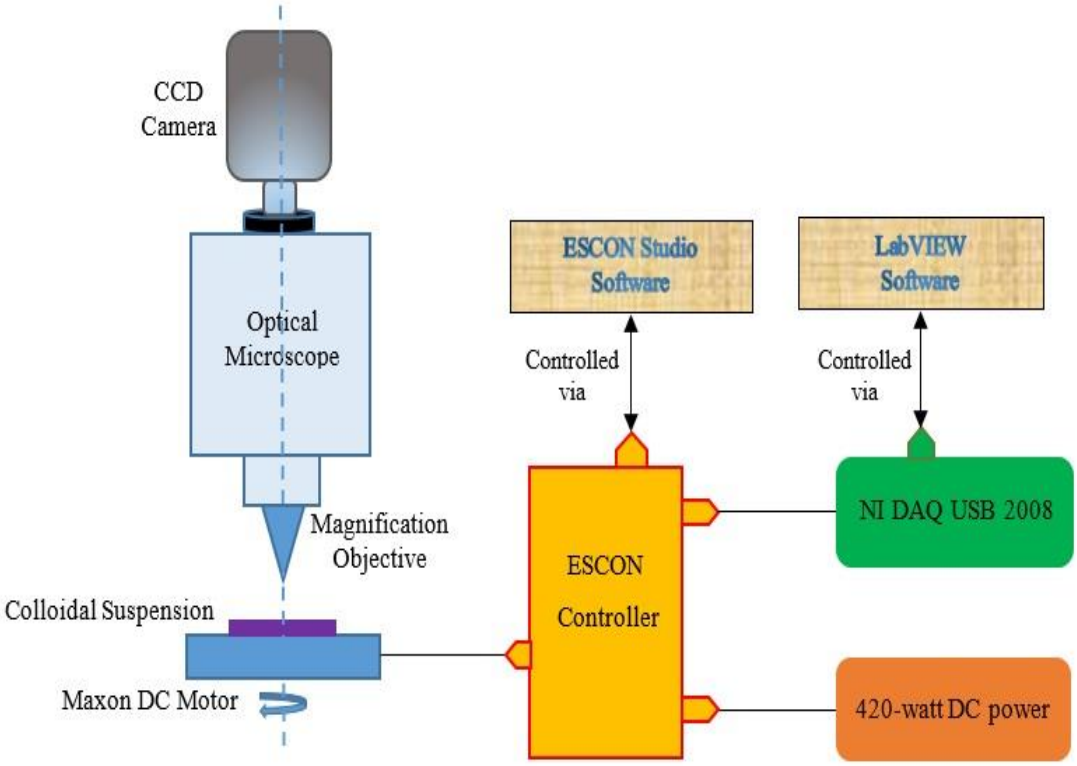

Figure 2.1: Schematic diagram for the designated spin coater used experimentally to prepare colloidal monolayer crystals.

2.1.1.2 Glass substrate surface chemical cleaning

Circular glass coverslips (30 mm diameter No.2, VWR International Ltd) were ultrasonicated in toluene, acetone and then isopropanol for 30 minutes, followed by rinsing with distilled water. Substrates were then submerged carefully in a piranha solution (1:1 v/v, 30% H_2O_2/H_2SO_4) for 2 hours with continuous supervision [*Piranha solution reacts vigorously with organic materials and may cause an explosion*]. Piranha solution is a very strong oxidising agent that removes most of the heavy organic impurities from glass substrates. In addition, Piranha solution adds a hydroxyl group (-OH group) to the substrate surface. The presence of hydroxyl groups on glass substrates increases their hydrophilicity at the end of the treatment process and prior to the spin coating. Therefore, piranha cleaning should improve the colloidal ordering quality on glass substrates forming the desired highly ordered monolayer colloidal crystals. Cleaned glass substrates were then rinsed with a copious amount of deionized water in order to remove any residuals of piranha solution. Glass substrates were kept submerged in distilled water to avoid any reactions with air. Prior to use, the cleaned glass substrates were dried under a stream of nitrogen gas. Nitrogen gas acts as a blanket that isolates air away from the cleaned glass substrates to avoid any contamination.

2.1.1.3 Fabrication of monolayer colloidal crystals

I) Preparation of colloidal suspensions

Firstly, spherical silica particles (1550 nm / Pinfire - Gems & Colloids Company) were suspended as purchased in pure Ethanol and sonicated for 30 minutes. Then, the resultant solution was dried overnight at a temperature of 80^{o}C to ensure the complete evaporation of Ethanol. Previous procedure was repeated three times with using a pestle and mortar in between. Pestle and mortar were used to gently breaking up powder in order to remove any expected physical aggregations between particles. The silica colloids were then suspended in the desired solvent; (distilled water, ethanol, ethylene glycol, water – ethanol mixtures, water – ethylene glycol mixtures and ethanol – ethylene glycol mixtures) with concentrations ranging from 5 wt. % up to 35 wt. %. The colloidal solution was then sonicated continuously for 24 hours using a

water bath sonicator to produce a homogeneous dispersion of colloids and also to reduce particles aggregation.

II) Spin coating colloidal suspensions

100.0 µL of the prepared colloidal solution was deposited on the pre-treated glass substrate (as discussed in section 2.2.1.2), adhered to the DC motor shaft. The motor was rotated at a designated speed (500 – 5000 rpm), acceleration rate (2.2 – 85 rev. s^{-2}) and for a specific spin time (15 – 120 s) under full control via LabVIEW software (as discussed in section 2.2.1.1). Spin coating was repeated five times for each sample to ensure the repeatability of results and the availability of sufficient samples for analysis. Each glass coverslip was marked in its centre of bottom prior to spin coating. Optical microscopy was performed in transmission mode on the resultant colloidal thin films, and colloidal films were captured through Andor camera using 20×, 40× and 60× Nikon CFI S Plan Fluor ELWD objectives.

III) Characterisation of optical microscopy images

LabVIEW software was developed to quantify the area coverage percentage of glass substrate surface occupied by silica colloids in each of the 25 images regarding each sample. The newly developed particle tracking algorithm is described in Figure 2.2 as a flow-chart schematic diagram. As shown in Figure 2.3, each microscopic image was subjected to a sequence of processing steps; firstly, “Colour plane extraction” was applied to produce a grey-scale image. Secondly, “threshold” step was used to produce a binary image to facilitate distinguishing spherical particles in each image. Then, a sequence of steps was performed to remove border objects, fill holes, separate objects from each other, circle detection, shape matching and to perform particle analysis. The image analysis routine described above was performed for all the 25 images taken to determine the mean value of coverage area percentage occupied by spherical particles in each sample.

Samples which have the highest area coverage percentages have been further analysed to quantify the percentage of hexagonal close-packing (HCP %) in each sample as described in Figure 2.4. In an optimally packed HCP colloidal system, each particle should be surrounded by six neighbours. In this LabVIEW code, as shown in Figure 2.5, the image was enlarged to 150 % and then a square from the centre (85 × 85 µm) has been taken as the region of interest to ensure the consistency during the whole investigations. Secondly, spherical particles have been replaced by dots with the removal of the original image background. Then, connectivity between particles in each image was assigned using lines based on Voronoi connectivity diagrams principle at which plane is divided into regions based on distance to points in a specific subset of the plane. Afterwards, any hexagonal polygon found was coloured in pink. While, other polygons have been coloured in blue. Finally, a Vision Assistant script was developed based on "Colour plane extraction", "threshold" and "particle analysis" steps to determine the area percentage occupied by the pink colour that indicates the hexagonal close-packing magnitude in each sample.

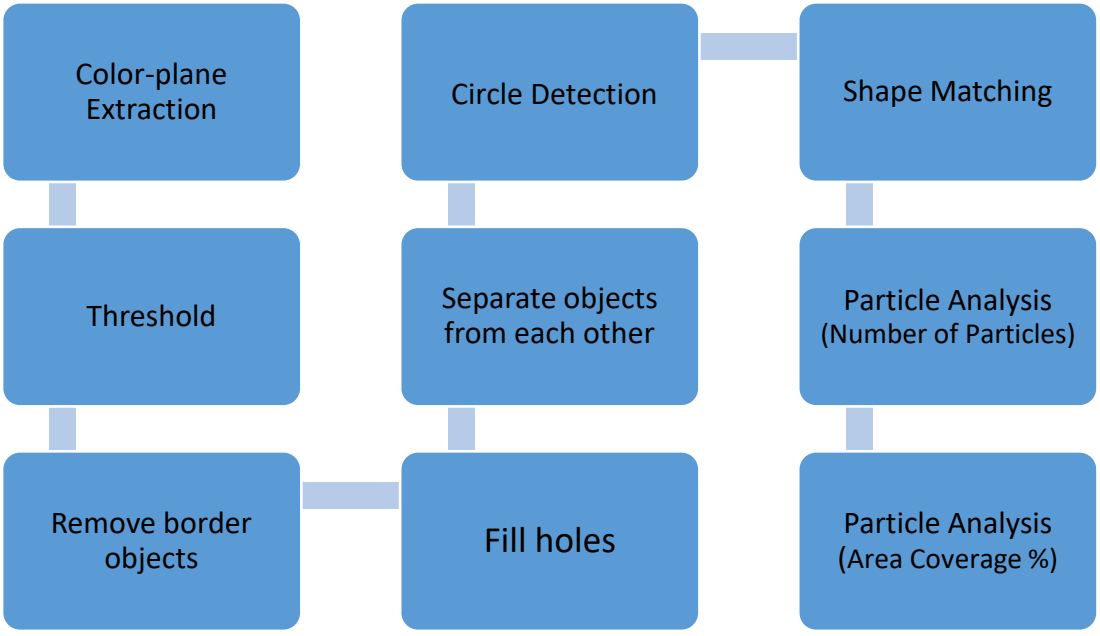

Figure 2.2: Schematic diagram showing the consecutive steps of the newly developed particle tracking algorithm used to either count number of particles in each sample or the area coverage % occupied by particles on substrate.

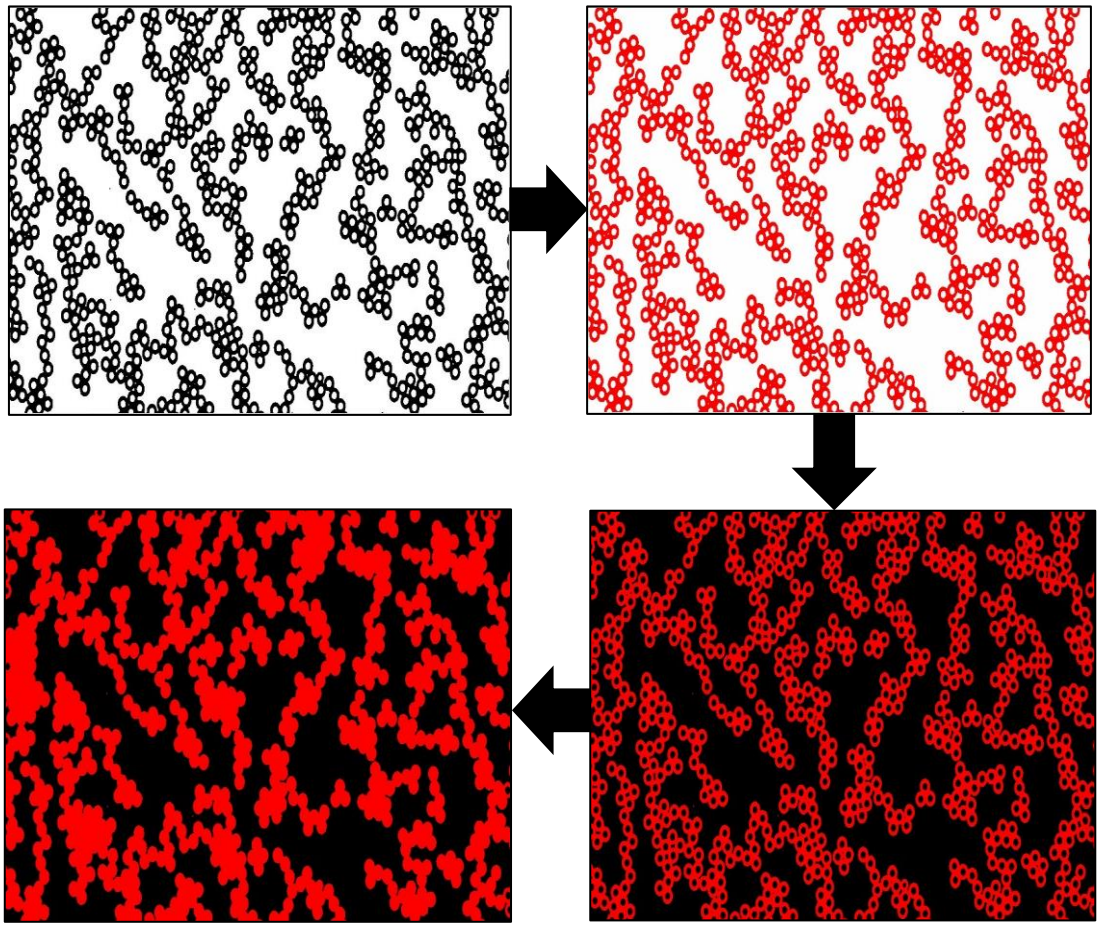

Figure 2.3: Processing of microscopic images through LabVIEW software in order to determine the area coverage % occupied by colloidal particles on the glass substrate surface.

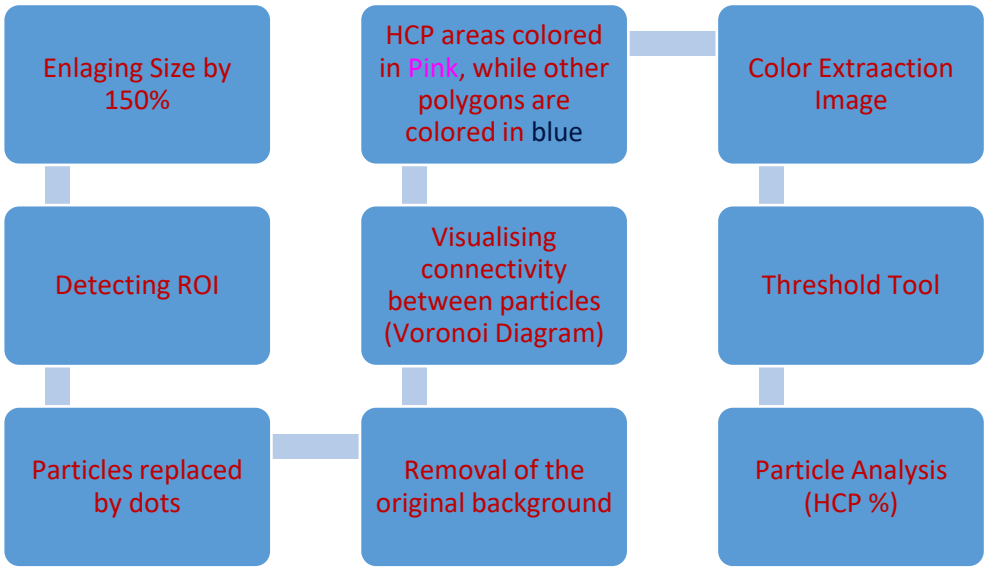

Figure 2.4: Schematic diagram showing the consecutive steps of the newly developed particle tracking algorithm used to evaluate the colloidal ordering quality in the form of HCP %.

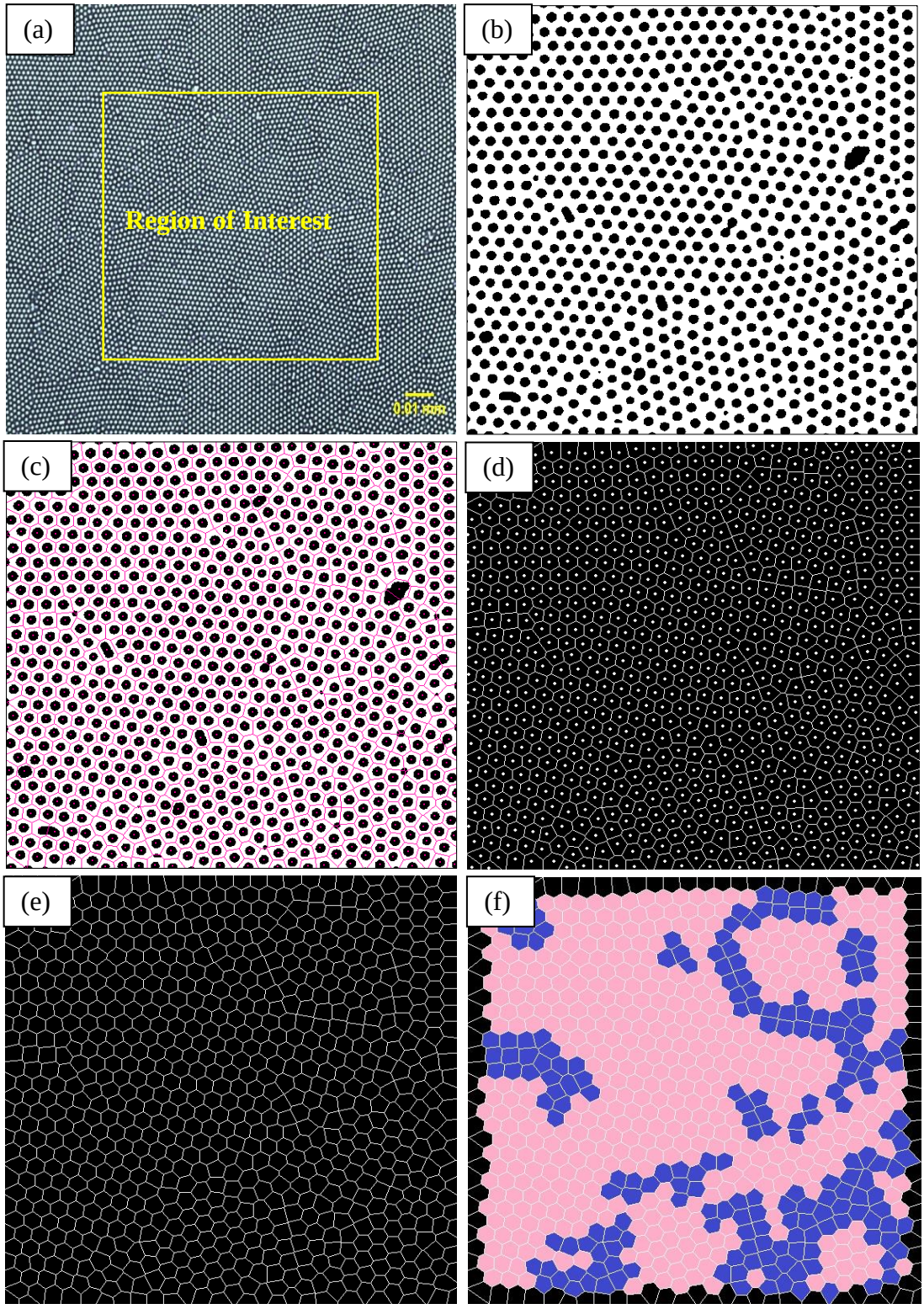

Figure 2.5: Processing of microscopic images through LabVIEW software in order to characterise the ordering quality of the fabricated colloidal crystals in terms of percentage of hexagonal close-packed arrangements; (a) Original microscopic image, (b) Region of interest enlarged to 150 %, (c) Assigning cells for each particle with its surroundings , (d) Correcting particles overlapping, (e) Removal of particles in the centre of each cell and (f) Pink colour indicates hexagonal polygons, while blue areas are for other polygons.

The developed LabVIEW codes helped to characterise the morphology of the fabricated monolayer colloidal crystals with respect to either the coverage density or the hexagonal close-packing structure percentage (HCP %), as an indication of the colloidal ordering quality. However, it was found that HCP % is not enough to fully characterise the packing quality that governs the PBGs applications. As shown in Figure 2.6, static samples, that exhibit high coverage area percentage and relatively high ordering quality, developed unidentical laser scattering patterns. This could be attributed to the distortion of alignment that may be found in different forms such as point defects and line defects. Since the discovery of the significant impact of these dislocations on the colloidal optical properties [9], investigating the degree of alignment of the hexagonal registry over long length scales acquires a great interest to characterise the spatial structure of fabricated colloidal crystals. This could be achievable through tracking the alignment of domain boundaries of silica colloidal crystals in each sample. Tracking the symmetrical alignment of the hexagonal domains could be done through modifying the newly developed LabVIEW software by adding a radial distribution parameter "G (r)" that determines the angle of domains. Alternatively, Studying the Fourier Transforms of the SEM micrographs of the final colloidal crystals could be valuable in the defects analysis.

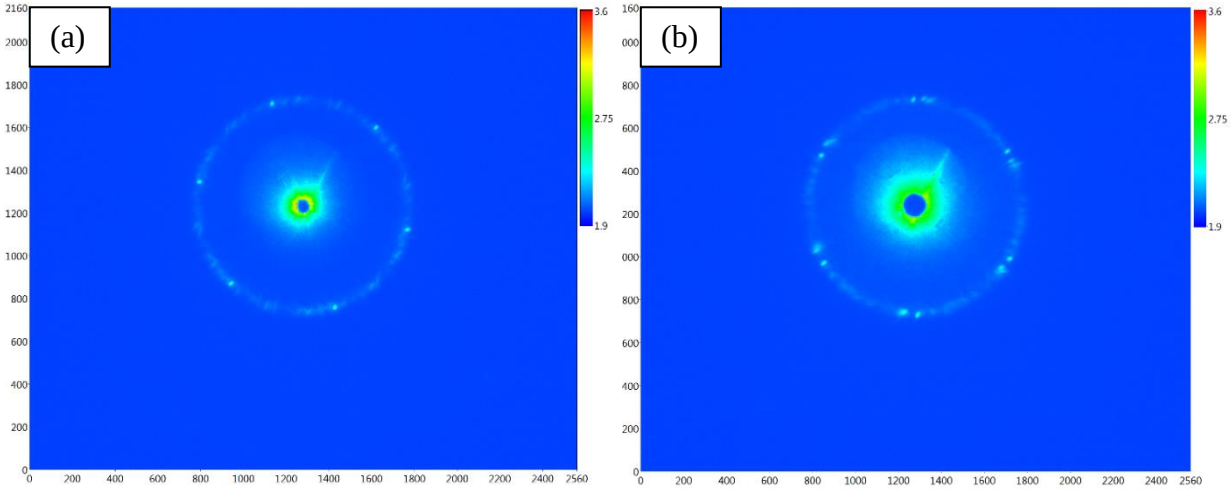

Figure 2.6: LabVIEW processed images for the laser scattering patterns collected from two silica colloidal samples showing the variation in the alignment between hexagonal domains regardless to the HCP % value; (a) hexagonal domains are perfectly aligned developing clear six spots, while in image (b) each single spot splits into 2 adjacent spots showing the difference in domain angles between hexagonal domains

2.1.2 In-Situ Investigations Stage

In-situ investigations stage takes place in order to study the exact mechanisms of colloidal self-assembly that took place during the spin coating process. In this stage, a laser scattering set-up has been developed to enable gathering laser scattering patterns obtained from colloidal suspensions in real-time during the spin coating process. Real-time investigations results develop an assertive information about what is exactly happening during colloidal self-assembly process. This information helps to develop more control over the governing mechanisms that lead to the formation of these highly ordered colloidal structures.

2.1.2.1 Experimental Design of Laser Scattering Set-up

Herein, a laser scattering setup has been developed to enable collecting laser scattering patterns diffracted by colloids in real time during the spin coating process. Tracking the development of these scattering patterns may help to discover in details the stepwise evolution of geometrical arrangements of monolayer colloidal crystals (MCCs) during the self-assembly process. The laser scattering setup, shown in Figure 2.7, composed of a hollow DC motor (U8 pro, KV 170) that acts as the spin coater. Silica colloidal suspensions were deposited on a pre-treated glass substrate (cover glass round 30 mm diameter NO. 2) adhered to the motor shaft. The motor was used to spin coating colloidal suspensions at the designated spinning speed, settling time, acceleration rate and for a specific spin time. The hollow U8 pro motor enables to shine the laser beam through it directly towards colloidal suspension during the spin coating process. Once laser beam hits spherical particles in colloidal suspension a diffraction occurs at a certain scattering angle (Ɵ) as shown in Figure 2.8. Scattering angle is inversely proportional to the particles size. Small particles scatter light at wide angles with low intensity. On the other hand, large particles scatter laser beams at narrow angles but with high intensity as shown in Figure 2.9 [79]. Laser scattering patterns obtained were collected on a screen and captured by a CCD camera.

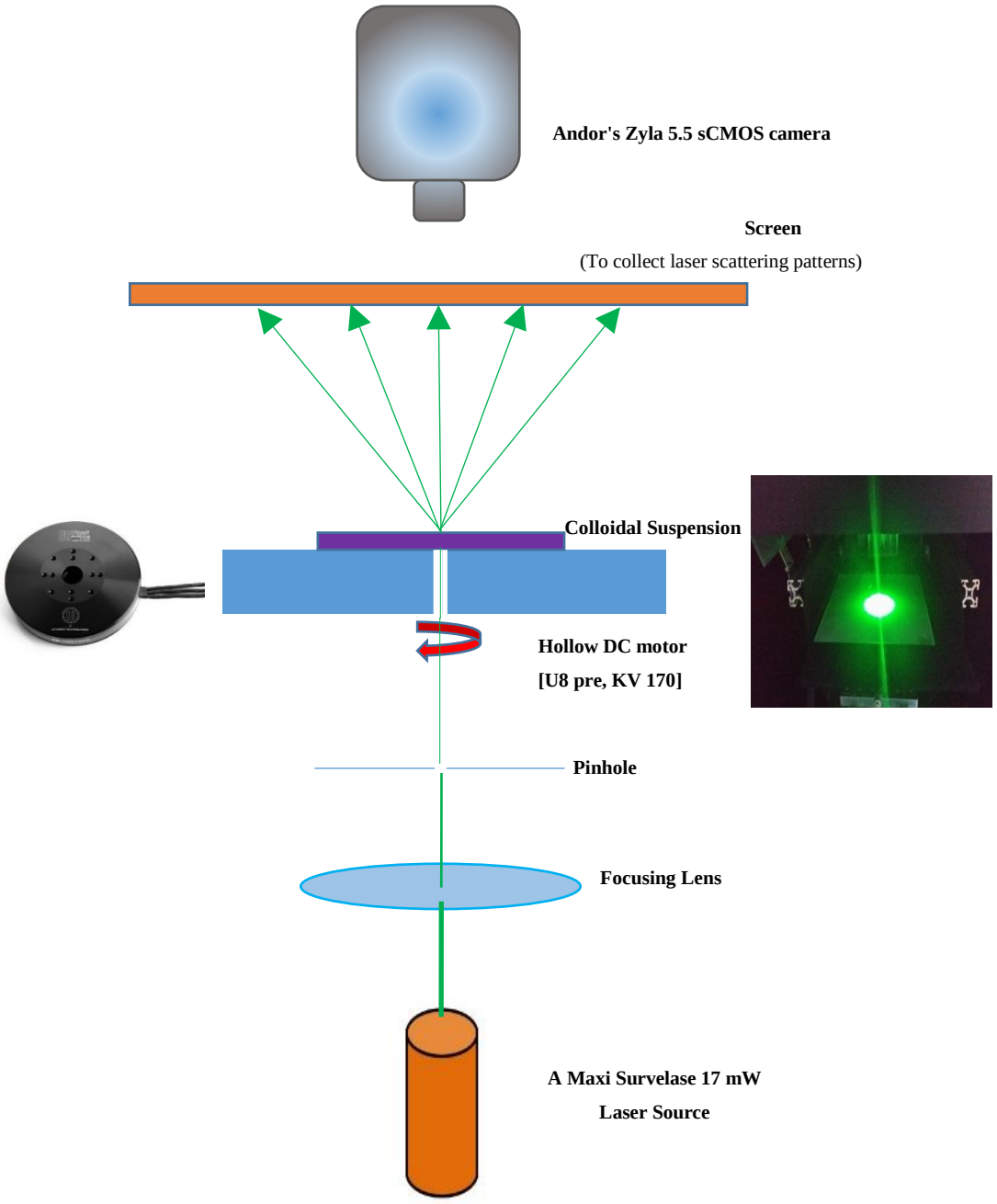

Figure 2.7: Schematic diagram for the laser scattering setup.

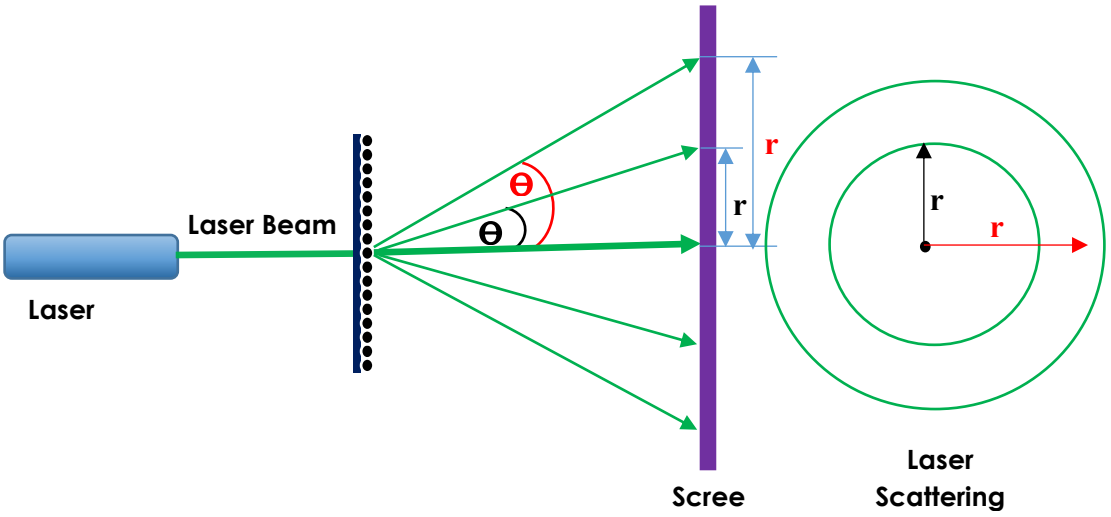

Figure 2.8: Schematic diagram showing the principle of the in-situ laser scattering setup where a laser scattering patterns obtained when the laser beam hits the spherical colloids in the colloidal suspension. The scattering rings obtained due to refraction induced by particles have different scattering angles and different radii.

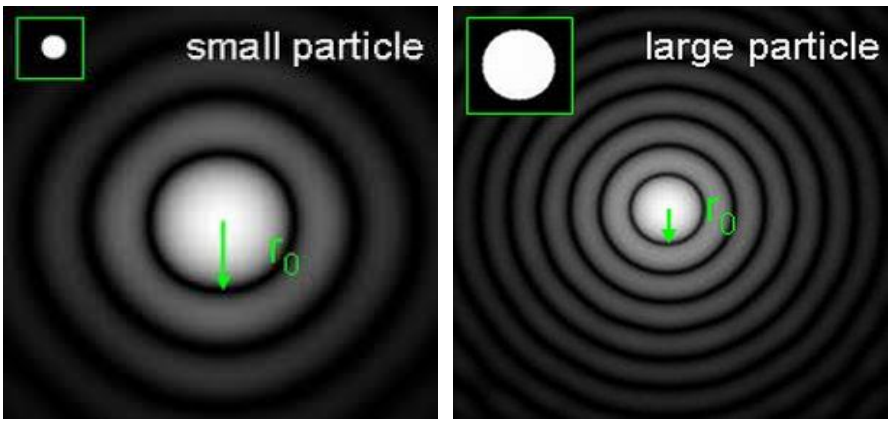

Figure 2.9: Schematic diagram showing that small particles develop scattering rings with large angles, while spherical particles with bigger sizes refract laser beams at smaller scattering angles. Taken from ref. [79].

The motor was connected to a 420-watt DC power supply via an electronic speed controller (UAS 75 HVC+) in order to electronically control the motor spinning speed. Actual motor rotational speed was calibrated using a photodetector connected to NI DAQ USB 2008 module. A Maxi Survelase 17 mW laser pointer (purchased from Global Laser Ltd Company) was used as a light source to shine a 520 nm green laser beam. A switch was used to adjust the stop/start positions and the transition time for the spin coating process. As laser beam passes through colloidal suspension, the resultant scattering patterns were collected on a projecting screen placed in front of the camera at a 5.1 cm away from the sample. Andor's Zyla 5.5 sCMOS camera, that offers a high frame rate performance of up to 100 fps at a 1.2 e^- rms read noise, with a high resolution of 5.5 Megapixels and a maximum quantum efficiency of 60 % was used for recording the real-time changes that took place in colloidal ordering during spin coating process. Camera, screen and laser source were assembled on a 1.5 m rail, which is attached vertically to an optical breadboard, to ensure proper lining and flexibility in changing distance between the sample and either screen or laser source. The whole laser scattering setup was surrounded by a box made of black correx sheets with a 6.0 mm thickness. Correx box helps to isolate the setup from the surrounding area and avoiding any interfering stray lights. Finally, correx box door was connected to the laser interlock through a magnetic interlock. So, laser source is on if and only if the box setup door was closed to ensure safety for the user.

2.1.2.2 Safety of using Laser beam in laboratory experiment

Lasers produce electromagnetic radiation at wavelengths extending from 100 nm in the ultra-violet, through the visible (400-700 nm), and the near infrared (700 - 1400 nm), to the far infrared (1400 nm - 1 mm). Thus, the light emitted can be either visible or invisible. Lasers can be operated in a number of different modes. Some lasers produce a continuous output and are known as continuous wave or CW lasers. The power outputs of CW lasers are usually expressed in terms of watts (W). Others operate in a pulsed mode producing short bursts of radiation. The power of the laser output can vary from less than 1 mW to many watts in some CW devices. Laser sources can be classified regarding their power as follows; (1) Class 1 and 1M 0.39 mW, (2) Class 2 and 2M 1 mW, (3) Class 3R 5 mW and (4) Class 3B 500 mW.

A Maxi Survelase laser pointer (purchased from Global Laser Ltd Company) was used as a light source to shine a 520 nm green laser beam. This laser pointer has a power of 17 mW, so it is classified as class 3B. This class is normally hazardous when direct exposure occurs. Also, working with class 3B lasers has a high possibility of being exposed to stray laser beams that could damage the eyesight. Hence, following the safety regulations during the experimental work are crucial to ensure laser users safety. These safety regulations include using the proper laser eyewear, risk assessment must be done prior to work to minimise hazards levels and strictly following the Policy/Guidance and Schemes of Work applicable to the lasers.

2.1.2.3 Analysis of *in-situ* laser scattering patterns

Once laser beam hits silica colloids placed on the glass substrate, a scattering was collected on the screen. Geometrical structure of laser scattering patterns is dependent on the ordering quality (length scale) of colloidal crystals at that moment. Formation of monolayer colloidal crystals at the end of the spin coating can be easily recognised through the emergence of a persistent ring. The diameter of this ring is dependent on the size of colloids and spacing of adjacent colloids in the final packing. *In-situ* tracking of the stepwise evolution of final ring through Andor's Zyla 5.5 sCMOS camera, that offers a high frame rate up to 100 fps develops valuable information about colloidal self-assembly during the spin coating process.

Images for scattering patterns observed at each frame was processed through LabVIEW software to determine the radius of the scattering ring in pixels. Then, unwrapped images were then analysed to measure the variation in intensity with respect to distance from the centre (pixel number). Monitoring the intensity fluctuations enables *in situ* tracking for the stepwise evolution of the laser scattering patterns in each colloidal suspension sample over time.

Figure 2.10, shows that the collected laser scattering patterns on the screen are functions of both radius (r) and scattering angle (θ). Hence, converting the distance from the centre (pixels) into scattering vector (Q) becomes a must. In order to calibrate the laser setup, several diffraction gratings with different spacings were used. Each grating adhered to the motor shaft and rotated at a designated speed using our

developed laser setup. Laser scattering patterns obtained were collected on the screen and captured through Andor Camera. Images were then processed to determine the radius of each scattering ring in pixel numbers. Since laser scattering patterns observed follow Bragg's law: d sin (θ) = n λ, so θ can be easily determined. Then, Q value for each ring was calculated manually where Q = 2π / d. Plotting Q values against rings radius (pixels) developed a trigonometric relationship between Q and Pixels. Fitting that curve develops a simple equation that converts radius in pixels into Q. Finally, the stepwise evolution of scattering rings was shown through plotting Q values via frame time as shown in Figure 2.11.

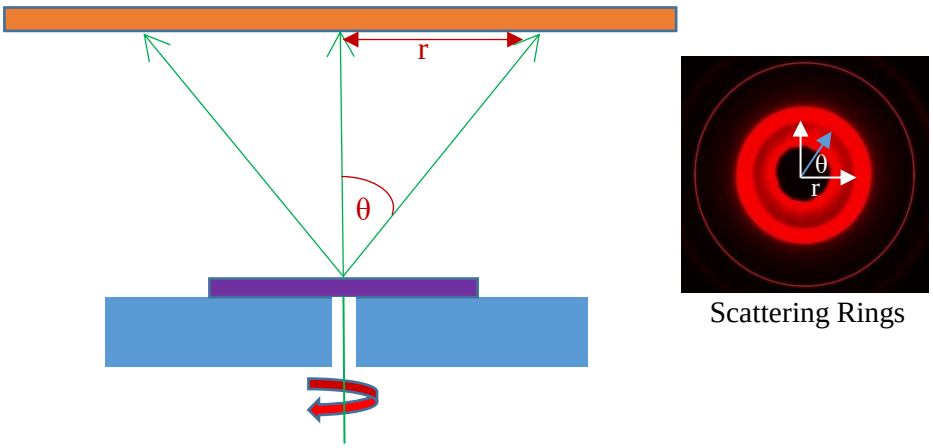

Figure 2.10: Schematic diagram showing that each laser scattering ring is function of both scattering angle and radius.

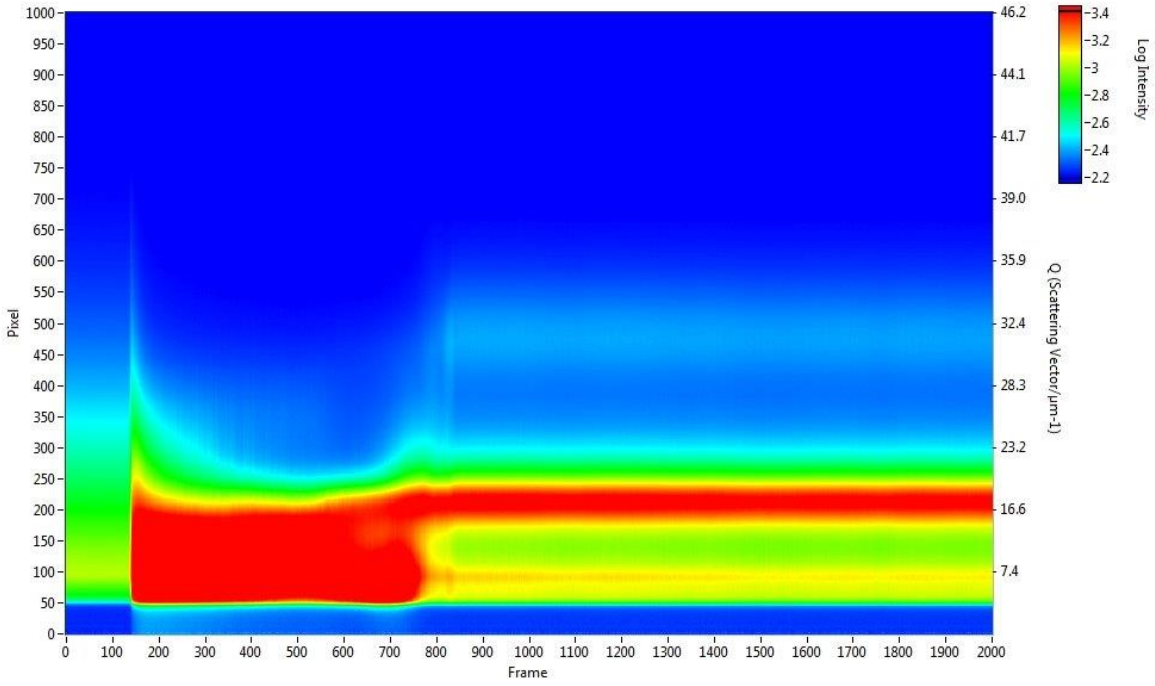

Figure 2.8: A sample for the in situ laser scattering charts obtained when spin coating colloidal suspensions using the developed in situ laser scattering setup. Intensity at each frame is plotted against both radii in pixels and Q (the scattering vector).

2.2 Experimental Techniques

2.2.1 Scanning electron microscope (SEM)

Scanning electron microscopy (SEM, JOEL JSM-6010LA) was used to image monolayer colloidal crystals fabricated on glass substrates. Scanning electron microscopy (SEM) is a tool that enables a high-resolution imaging for solid surfaces. SEM uses electrons in imaging, instead of visible light in optical microscopy, which enables a higher magnification (>100,000×) and 100 times the greater depth of field when compared to light microscopy. Further, the energy of the backscattered electrons can be measured to obtain an energy dispersive X-ray spectrum (EDS) that enables qualitative and quantitative chemical analysis of the investigated sample. Firstly, an electron beam is produced by the electron gun over the sample chamber. The energy of incident beam ranges between few hundreds and tens of thousands of electron volts. The electron beam is dedicated into a narrow beam through a series of the

electromagnetic condensing lens. Then, the focused electron beam is accelerated down towards the target using scanning coils placed at the near end of the column. As the beam plays over the sample, secondary electrons are scattered. Scattered electrons are collected by a detector, then magnified and displayed as a visible signal. Two types of detectors are used in SEM; (1) solid-state detectors and (2) scintillator type detectors [Evenhart - Thornley] at which detector is positively charged to attract electrons and improve image to noise ratio that enables the system to explore the sample point by point and develops a high-quality three-dimensional image. SEM electron column and sample chamber are always under moderate vacuum to ensure that electrons can travel freely from electron gun to the investigated sample. High magnified SEM Images give valuable information about the nanostructure sample size, shape, and morphology [80][81][82].

Scattered electrons can be classified into two categories; (1) secondary electrons (SE) and (2) backscattered electrons (BSE). SE are formed from inelastic scattering due to the ejection of loosely unbounded electrons from the sample atoms. They give images with a high resolution where the contrast between SE comes from the variations in sample morphology. SE are low-energy electrons with a maximum energy of 50 eV. On the other hand, BSE is high-energy electrons which scattered back from the sample surface by elastic scattering due to collisions between incident electron beam and nuclei of sample atoms. In this case, the contrast in the backscattered images comes from the inequality in atomic number among different points in the sample surface. Higher intensity of backscattered electron beam indicates a higher atomic number point characterised by a more brightness. Images formed from BSE can be used effectively in qualitative and quantitative analysis to find the chemical composition of the sample. Fabricated monolayer colloidal crystals based on silica colloids are non-conductive samples which distort the imaging resolution. For that reason, samples are coated with a thin layer of gold using a gold sputter coater (AGAR B7340, Serial No. A5947) prior to SEM imaging. Gold coating together with SEM working at high pressures, high vacuum (2.3×10^{-5} torr) and at high energy electron beam (25 keV) was found to improve the imaging resolution of these samples [80][81].

2.2.2 Nano-Sight Size Analyser

Nano-Sight size analyser [Nano Sight nanoparticle tracking analysis (NTA) version 2.1, Build 0325] was used to determine particles size distribution of spherical silica particles which have particle diameters greater than 1000 nm. Nano Sight analysis technique offers a simple, fast and cheap method to track moving particles in a liquid medium. Consequently, size and particle size distribution of samples can be easily obtained utilising both laser scattering and Brownian motion of these colloids. In this technique, a small volume of diluted colloidal suspension sample is injected into the sample chamber. A laser beam passes through this sample chamber. As laser beam hits particles in the colloidal suspension, a light scattering takes place. An optical microscope with a 20× magnification objective connected to a CCD camera operating at 30 to 60 frames per seconds (fps) enables the system to dynamically analyse the paths the moving colloids take under Brownian motion in a specific period of time (e.g. 30 seconds). Nano Sight instrument generates a video for each sample visualising nanoparticles as very small points of light moving fast under Brownian motion. The intensity of light is directly proportional to the particles size. So, larger particles were found to be visualised as brighter points. While smaller particles are visualised as faster, darker points. Videos are then analysed through the Nano Sight NTA 2.2 analytical software program that determines each particle separately. Nanoparticle Tracking Analytical (NTA) software program utilises the Stokes-Einstein equation, given as equation 2.1, in order to determine the hydrodynamic radius (r_h) of sample particles. Then, the software produces accurate particle size distribution profiles for the colloidal sample. NTA software offers a range of image adjustment settings that enables the user to select the optimum conditions to visualise individual type of particles [83][84].

$$D_t = \frac{k_B\, T}{6\, \pi\, \eta\, r_h} \tag{2.1}$$

Where D_t is the particle diffusion coefficient, k_B is Boltzmann's constant, T is temperature, η is solvent viscosity and r_h is the sphere-equivalent hydrodynamic radius.

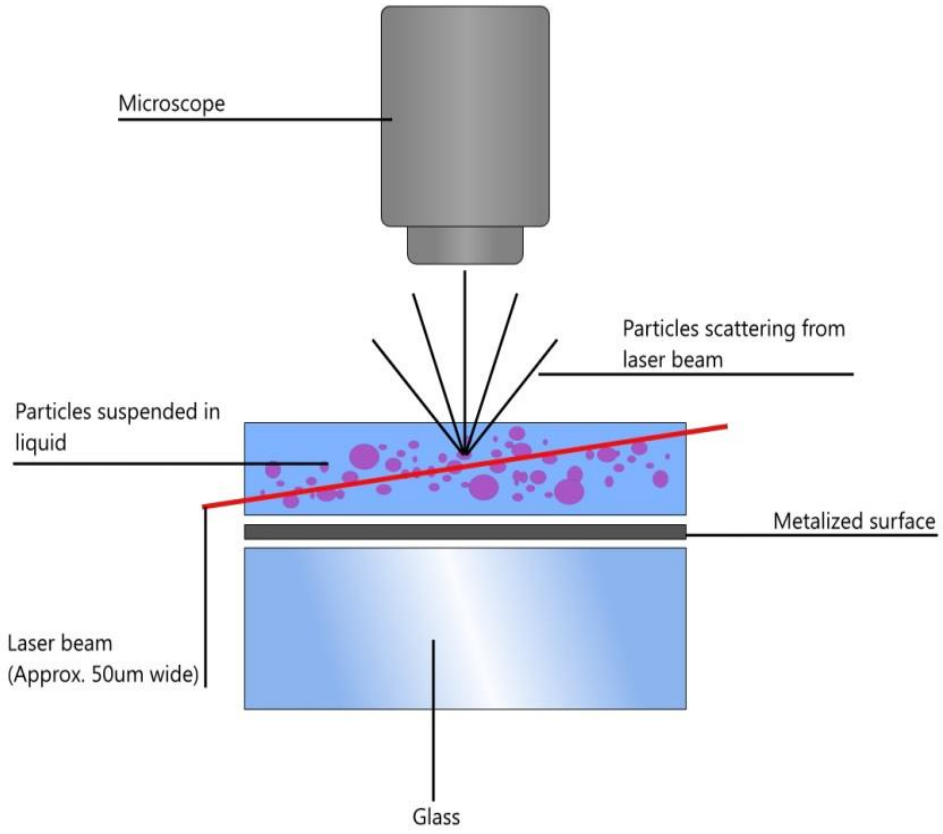

Figure 2.9: Schematic of Nano Sight nanoparticle tracking analysis (NTA) instrument. Taken from ref. 6.

2.2.3 Laser Diffraction Particles Size Analyser

Laser Diffraction Particles Size Analyser (Malvern Mastersizer 3000) has been used to determine the particle size distribution of silica particles with particle diameters lower than 1000 nm. Laser Diffraction Mastersizer 3000 is a common technique that is widely used as a particle sizing technique for particle sizes between 10 nm to 3.5 mm. It offers a wide dynamic range, fast measurements within seconds, repeatability and simple method for particle sizing where calibration is not required before initiating the measurements. The process is easily displayed on a screen as an instant feedback. Also, it enables the user to control the particle dispersion process if necessary.

In this technique, a laser beam shines through the investigated sample. Particles in sample scatter the laser beam with different angular angles with respect to their sizes. Large particles scatter light at small angles, while smaller particles scatter light at large angles. Laser diffraction utilises the angular variation in the intensity of

scattered light in the determination of particle size distribution in terms of a volume equivalent sphere diameter using the Mie theory of light scattering. In order to do so, refractive indices of both the dispersant as well as the sample should be known. Data of dispersant usually exists in the instrument database that includes common dispersants. Optical properties of the sample should be either experimentally measured or estimated. Fraunhofer approximation is a simplified approach that is commonly used especially for large particles. However, this approximation approach should be used with caution either in the case of samples which have particles below 50 µm or if sample particles are relatively transparent [85].

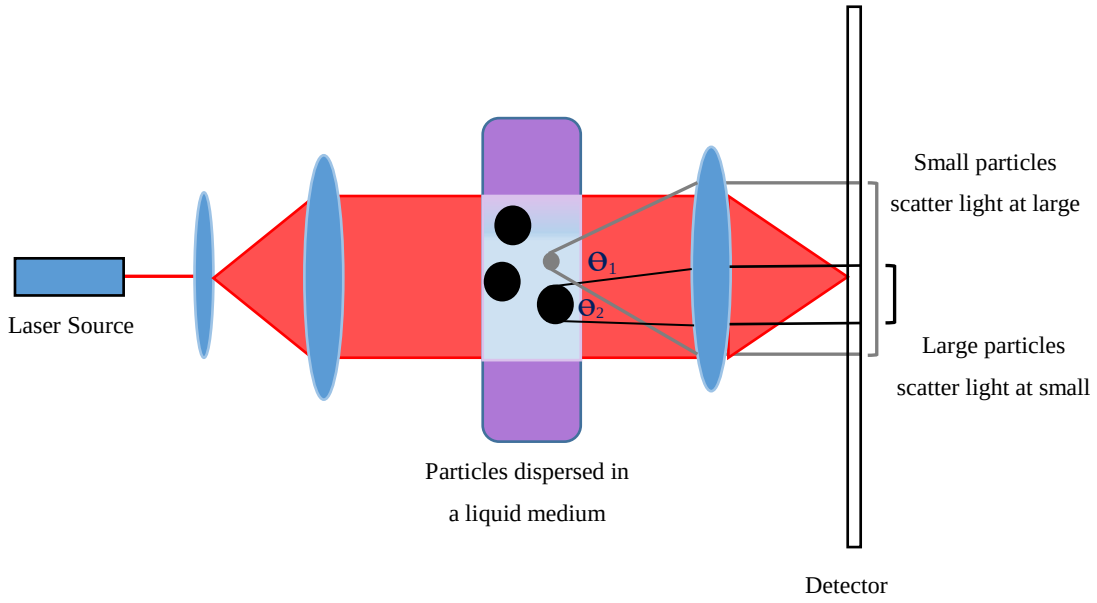

Figure 2.10: Schematic of laser diffraction particles size analysis technique.

Chapter 3.

Fine-tuning Laser Scattering Setup

3.0 Introduction

As explained in section 2.1.2.1 laser scattering patterns obtained during spin coating colloidal suspensions were captured in real-time. However, obtaining high-quality images/movies for the stepwise evolution of these colloidal structures was not straightforward. So, the *in situ* laser scattering setup was subjected to a series of precise modifications. This chapter explains the detailed methodology used to regulate our laser setup to reduce the direct laser beam spot size and improve the quality of scattering patterns signals.

3.1 Focusing the direct laser beam

Once the direct laser beam hits the screen, a high-intensity halo is formed. The very high bright circle of light makes recording of the real-time structural evolution of colloidal crystals a series challenging. For that reason, the first adjustment step to the laser setup was tuning the laser beam to obtain the smallest possible laser direct beam size. As the laser primary beam size decreases, its intensity significantly decreases which helps to visualise the laser scattering patterns with better quality. In addition, reducing the laser direct beam spot size facilitates tracking the stepwise structural evolution of these scattering rings. It was observed that laser beam with a relatively big size could combine with the final scattering ring, as shown in Figure 3.1. So, hindering the ability to observe the stepwise evolution of these scattering rings. The stepwise formation of laser scattering rings can develop valuable information on the structural formation of monolayer colloidal crystals during the spin coating process.

Maxi Survelase 17 mW laser pointer, that develops a collimated green-laser beam with a wavelength of 520 nm, was used as a light source. According to Braggs Law, diffraction angle is directly proportional to the wavelength of the laser beam used as a light source. Lower wavelength of the green-laser with respect to the wavelengths the red, yellow and orange lasers develops diffraction with a relatively narrower angle. Narrow angles facilitate collecting laser scattering patterns on the screen. The green laser has another advantage over other types that its wavelength is closer to the visible spectrum,

this allows it to be easier and clearer for the human eye to recognize the colour as opposed to red lasers. Better visibility facilitates the laser calibration and alignment in the early stages of building up the laser scattering setup. In addition, the green-laser source developed a primary laser beam with a smaller spot size and a relatively less intensity when compared to the red laser source. This facilitates collecting laser signals with a better quality. The area of investigation developed by the green-laser source was investigated by studying the intensity profile along the primary laser spot on the screen. As shown in Figure 3.2, the laser source develops approximately 97 % of its intensity within 9 pixels ≈ 1.05 mm.

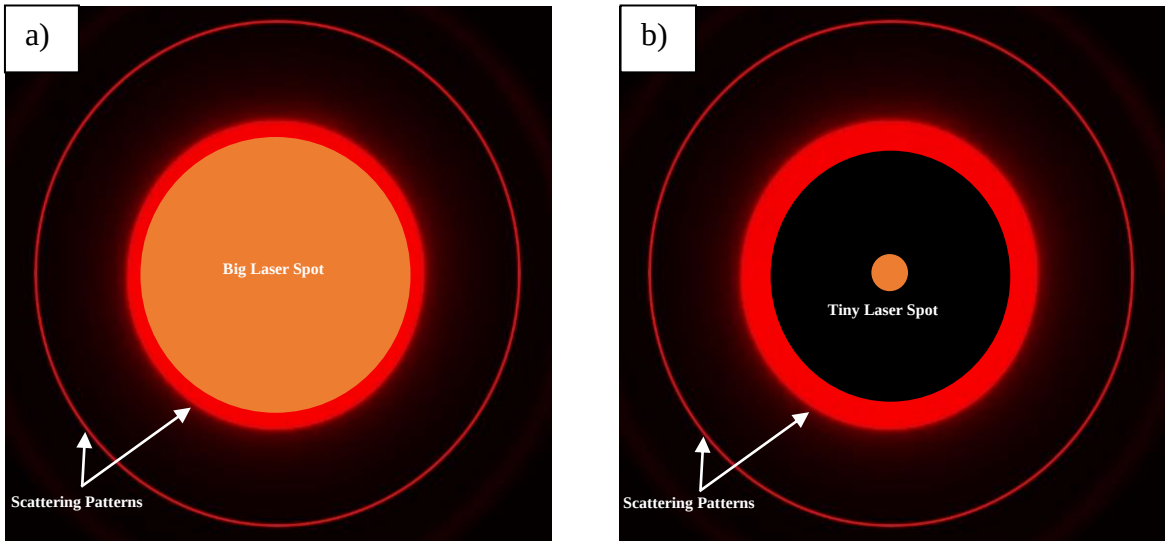

Figure 3.1: Schematic diagram for the same scattering ring observed in two cases; a) Big laser direct beam spot size that clearly combines with scattering rings, b) Laser scattering patterns observed after focusing the laser direct beam.

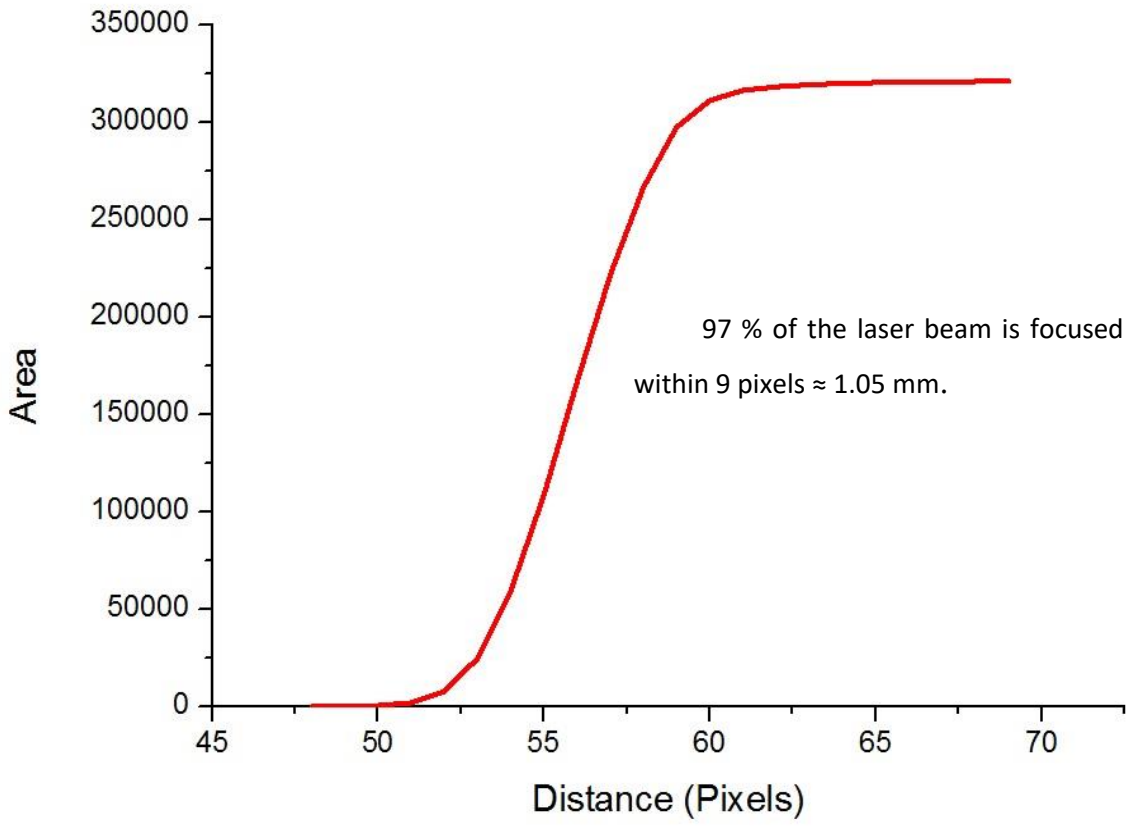

Figure 3.2: Studying the intensity profile developed by the green-laser source on the screen shows that 97% of the intensity of laser primary beam is collected within 1.05 mm which acts as the actual area under investigation using this laser source.

Firstly, we have placed laser source at different distances with respect to the sample to investigate the proper distance at which laser beam has the smallest spot size. Then, we have used a series of pin holes with different hole diameters until we developed the sharpest laser beam spot. Afterwards, different camera lenses have been used in order to both increase the region of interest area and also developing the lowest laser primary beam density. The 18 mm DOUBLE GAUSS 54857 lens, purchased from EDMUND INDUSTRAIL OPTICS, was found to be the optimum camera lens to be used in our setup. Finally, a series of beam stoppers, also known as beam blockers, with different inner diameters have been used at different distances with the sample to block the primary laser beam.

Laser scattering patterns collected in the presence of beam stoppers were captured individually. Captured images were then processed using LabVIEW software in order to measure the effect of each stopper on the resulted line intensity profile. Also, an image for laser scattering patterns collected on screen was captured in the absence of any beam stoppers. Signals collected at both without any beam stoppers and for laser only without a colloidal suspension sample were saved as the initial background images. Comparing these results together showed that using a beam stopper with an inner diameter of 12 mm was able to effectively block most of the primary laser beam showing the whole scattering signal as shown in Figure 3.3. Blocking the primary laser beam significantly inhibits the formation of the very bright halo around the centre which significantly increases the density of laser scattering patterns and so maximises the signal quality collected on the screen. Hence, recording the stepwise structure evolution of scattering rings in real time becomes easier to achieve.

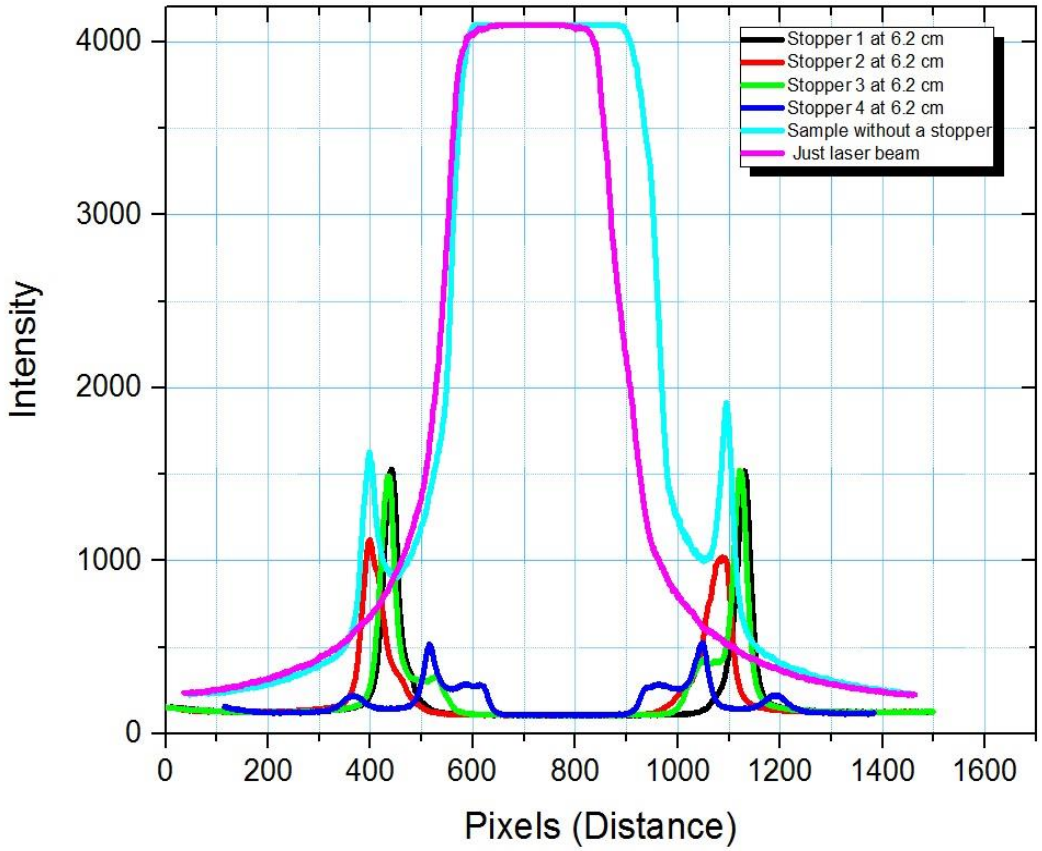

Figure 3.3: Impact of using beam stoppers with different diameters on signal quality collected on the screen.

3.2 Screen Analysis

As laser beam shines through the motor hitting colloidal spheres, laser scattering patterns are collecting on the screen. These patterns are captured in real time by a CCD camera. The quality of these images is significantly affected by the type of the screen used. For that reason, the impact of using different types of screens; sand-blasted, chemically etched, a Perspex screen and a projecting screen, on the quality of captured images, have been studied. To do so, a line laser module (LYTE-MV-EXCEL-660-50-45-A Laser Module, 660 nm 50 mW, Modulating Line pattern, Linear control +3.5 → +5.5 V) was used to shine a laser line directly towards each screen individually at different distances; 10, 20, 30, 40, 50, 60 and 70 cm. Laser line collected at each distance on each individual screen was captured using Andor's Zyla 5.5 sCMOS camera. Images were then processed using LabVIEW software, as shown in Figure 3.4, in order to measure the light intensity distribution along each line.

Line profile results shown in Figure 3.5 clarified that either sand-blasted screen, chemically-itched screen or the Perspex screen were acted as a diffuser where laser line intensity was unevenly distributed following a Gaussian distribution-like behaviour. The irregular distribution of laser intensity along the screen lead to the appearance of a very high-intensity spot at the centre regarding the primary laser beam. This bright spot hinders the ability to detect the evolution of laser scattering rings obtained at these screens. On the other hand, the projecting screen was able to evenly distribute light intensity along the screen from centre to edges. As light intensity more evenly distributed along laser line, the screen becomes better to be used to collect laser scattering patterns.

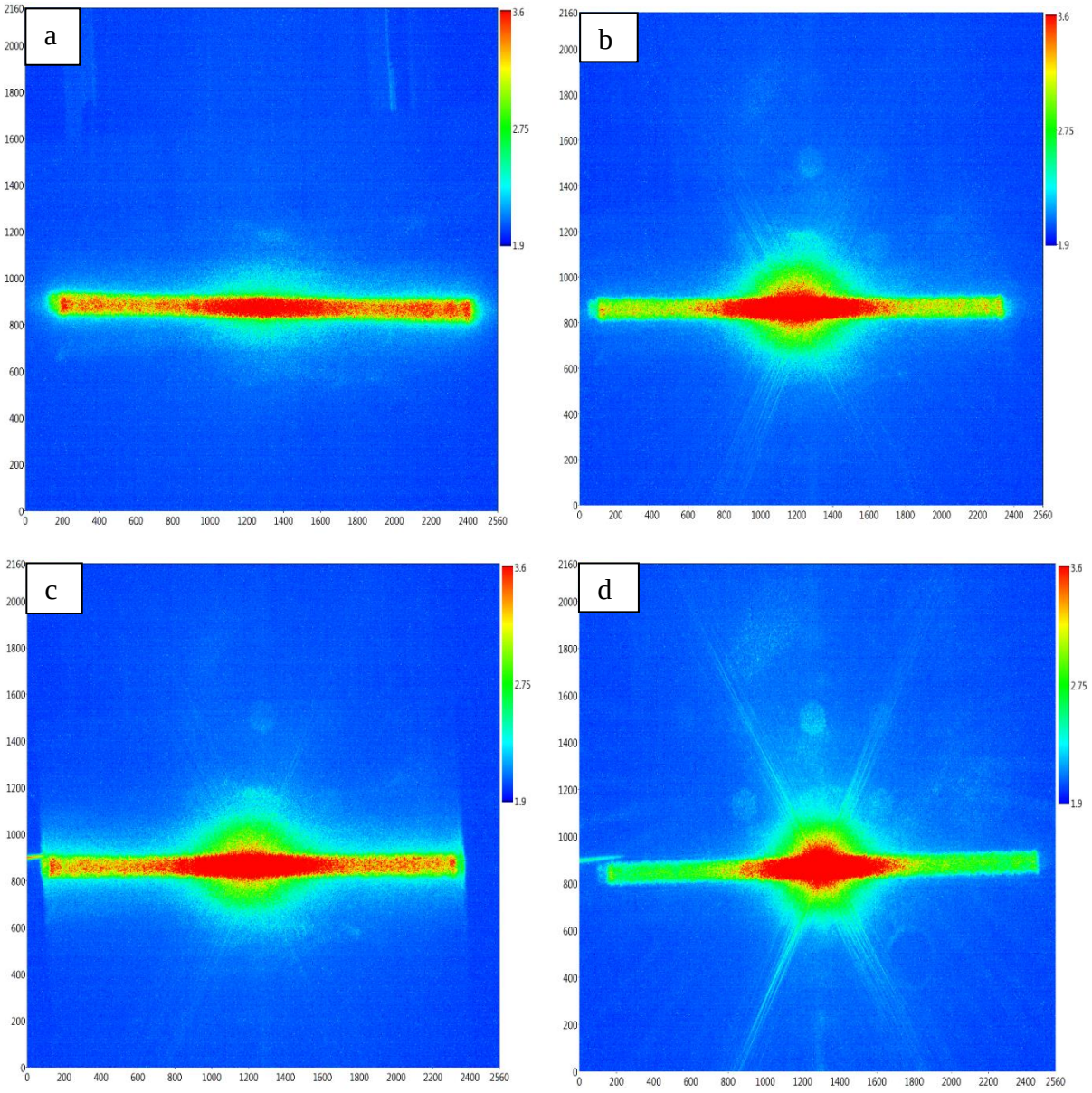

Figure 3.4: LabVIEW processed images for the laser line collected using different types of screens; a) projecting screen, b) sand blasted diffuser grit, c) AR-coated diffuser grit and d) Perspex screen, placed at the same distance (10 cm). Image (a) shows a normal distribution of laser line intensity along the whole line in case of using a projecting screen, while a Gaussian distribution appeared in the other screen types.

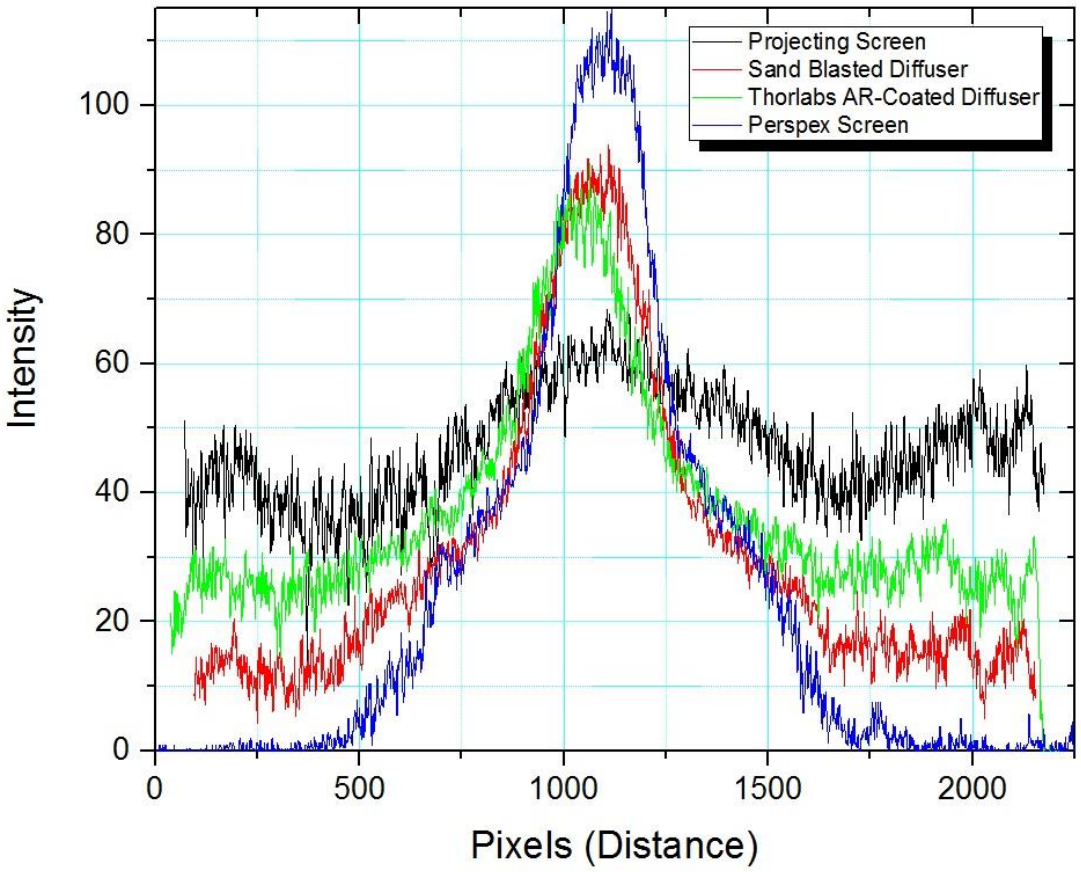

Figure 3.5: Intensity line profiles for laser line intensity collected at a distance of 10 cm away from different types of screens; sand-blasted screen, chemically-itched screen, Perspex screen and a projecting screen.

3.3 Elimination of unnecessary light scattering interference

As laser beam hits the sample, it was expected to collect only their laser scattering patterns on the screen. However, it was found that interference light coming from a scattered laser beam from the surrounding environment were included in captured images as shown in Figure 3.6 (a). To exclude these undesirable interferences, we covered the whole space between sample and screen with a black self-adhesive Velour film. Elimination of light interferences from other sources except sample helped to significantly

increase the signal quality as shown in Figure 3.6 (b). The whole setup was surrounded by the a thick black correx sheet (6.0 mm) to isolate the setup from its surroundings.

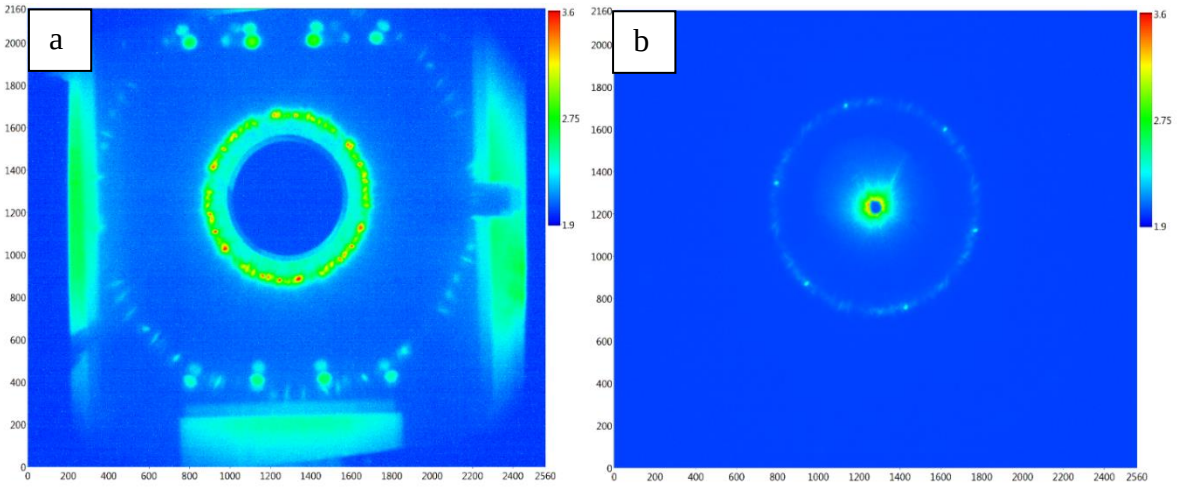

Figure 3.6: LabVIEW processed images for a standard colloidal monolayer thin film sample with a high ordering quality collected at different conditions; (a) image captures before fixing the black self-adhesive Velour sheet and (b) image obtained after fixing the Velour sheet shows a clear laser scattering ring without any light interferences from the surroundings.

3.4 Modifying camera sensitivity / dynamic range

Andor's Zyla 5.5 sCMOS camera offers three different sensitivity modes; 12-bit high well capacity mode, 12-bit low noise mode and 16-bit low noise & high capacity mode. Different sensitivity modes develop different response degrees of the camera towards the laser scattering patterns collected on the screen. For that reason, the effect of camera sensitivity modes on the collected signal quality was studied. Herein, the same sample was captured at a series of exposure times individually at the three sensitivity modes. The captured images were then processed using LabVIEW software to unwrap images around the centre. The intensity line profile in each case was measured individually in each unwrapped image.

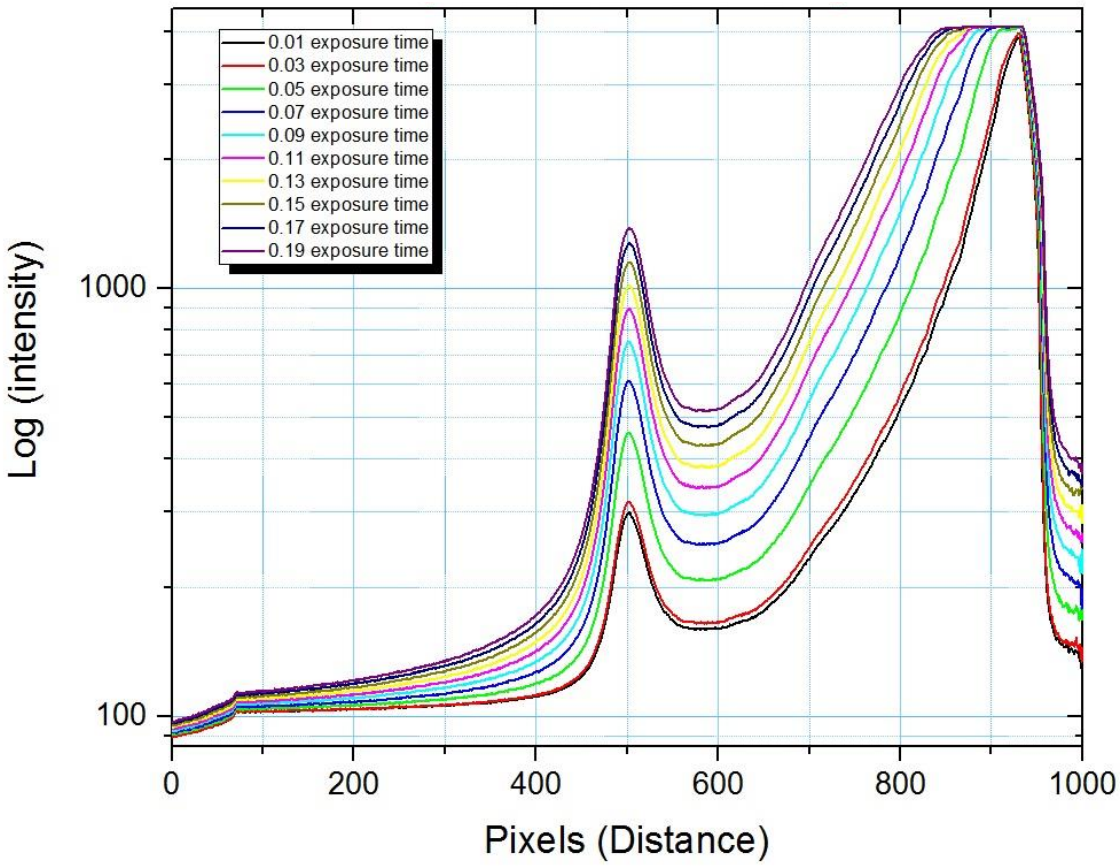

Figure 3.7: Plotting log (intensity) values for signals collected at 12-bit low noise sensitivity mode at different exposure times shows the direct proportional between signal intensity and exposure time.

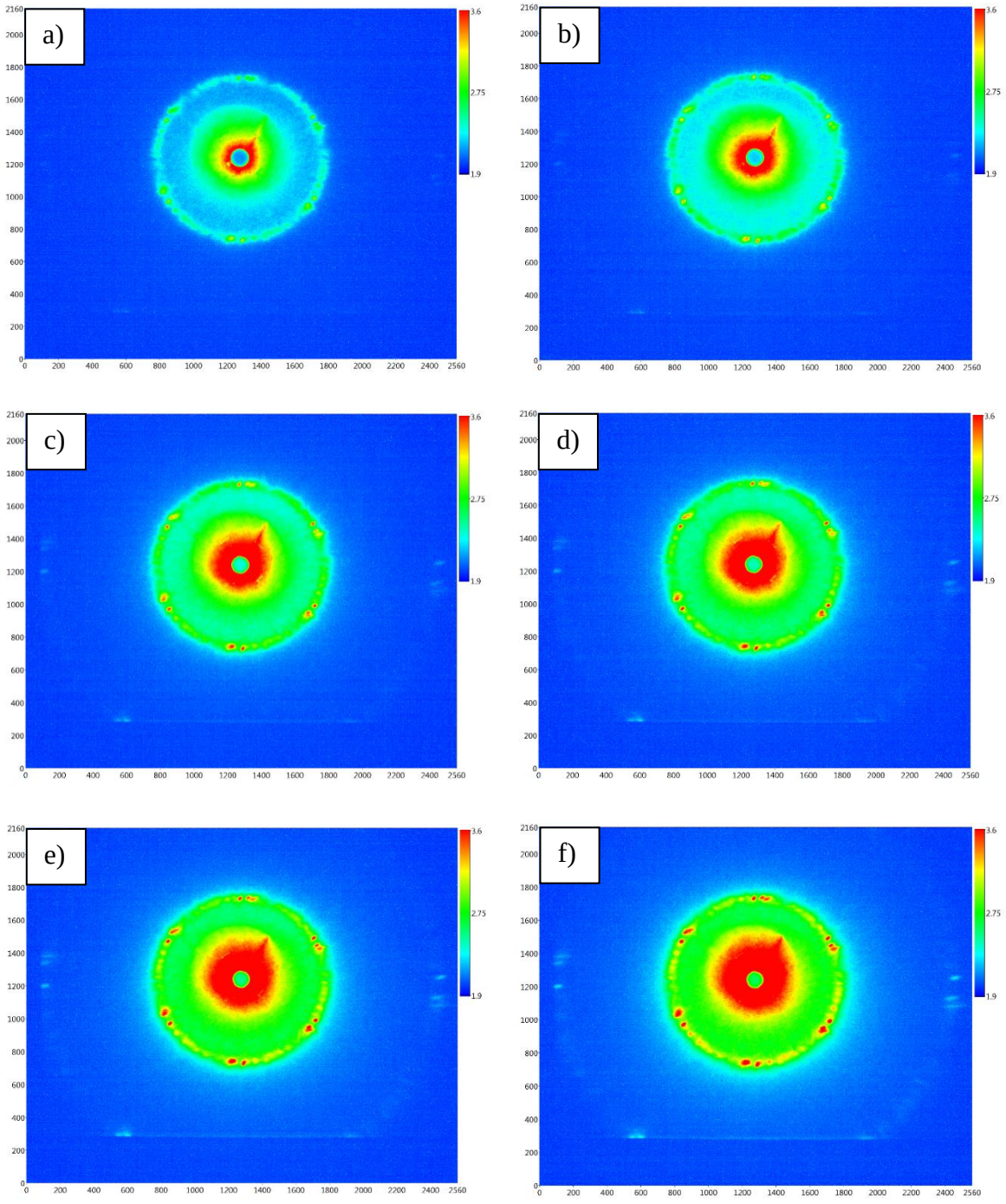

Figure 3.8: LabVIEW processed images for a standard colloidal crystal sample captured using Andor Zyla 5.5 camera set at the 12-bit low noise sensitivity mode at different exposure times; a) 0.01 s, b) 0.05 s, c) 0.09 s. d) 0.11 s, e) 0.15 s and f) 0.19 s. Images confirm the direct proportional between signal intensity and exposure time.

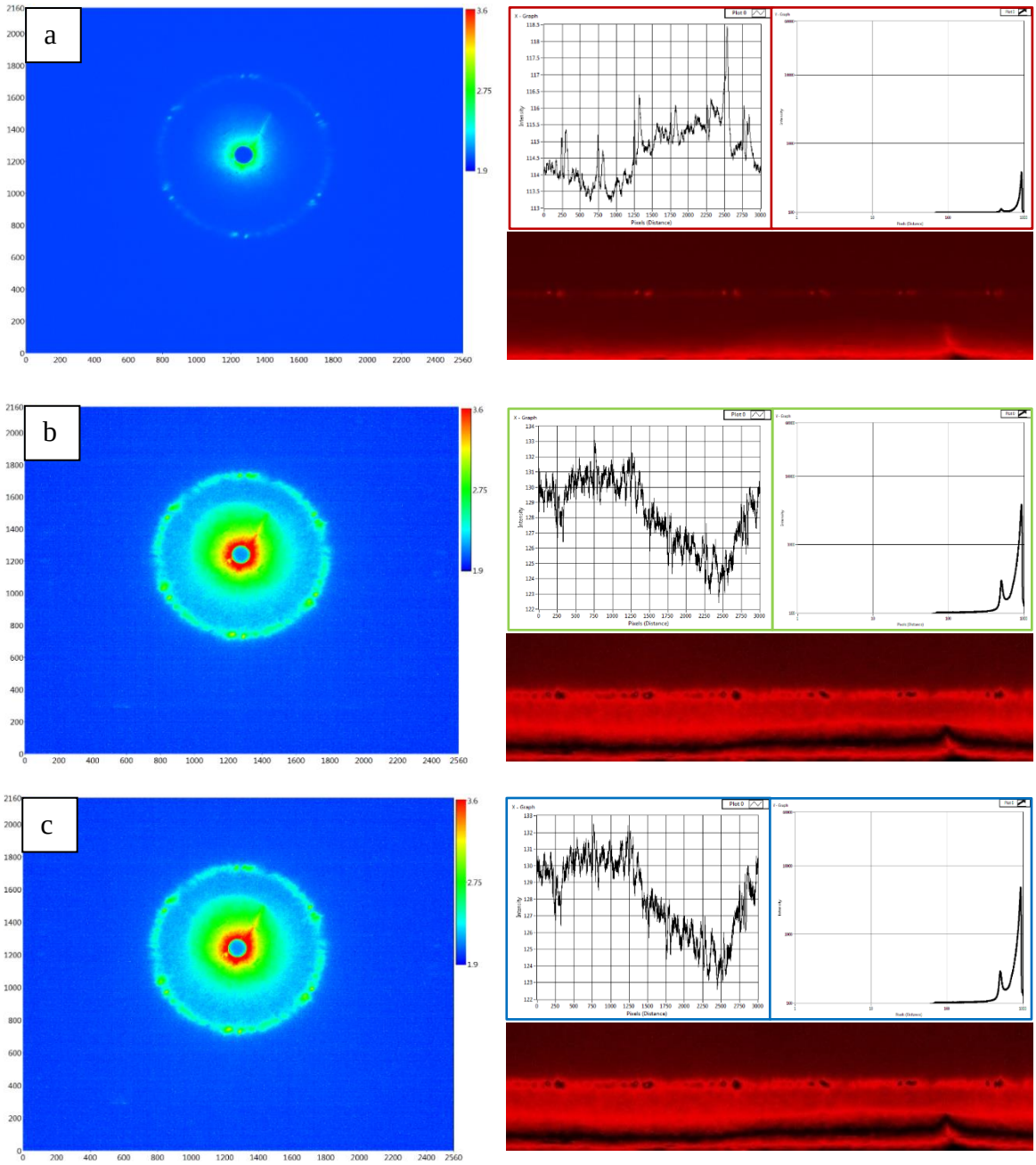

Figure 3.9: LabVIEW processed images together with the unwrapped data for a standard monolayer colloidal sample captured using Andor Zyla 5.5 camera at an exposure time of 0.01 s at different camera sensitivity modes; a) 12-bit high well capacity mode, b) 12-bit low noise sensitivity mode and c) 16-bit low noise & high well capacity mode. Images show that the camera sensitivity mode greatly governs the signal quality.

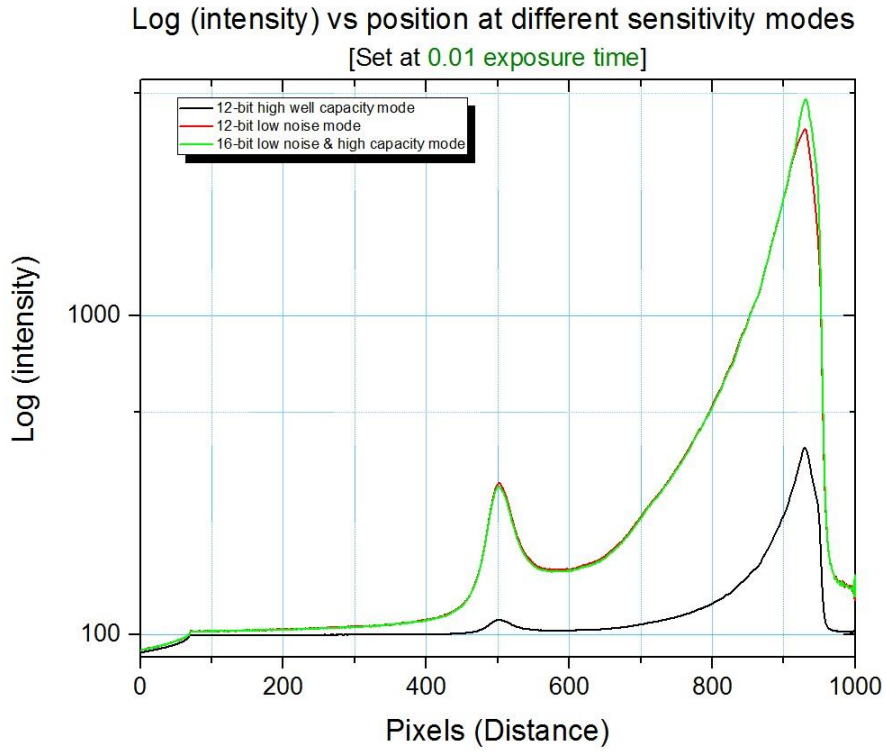

Figure 3.10: Plotting log (intensity) values for signals collected at 0.01 s exposure time but at different sensitivity modes. Images show that the camera sensitivity mode greatly governs the signal quality.

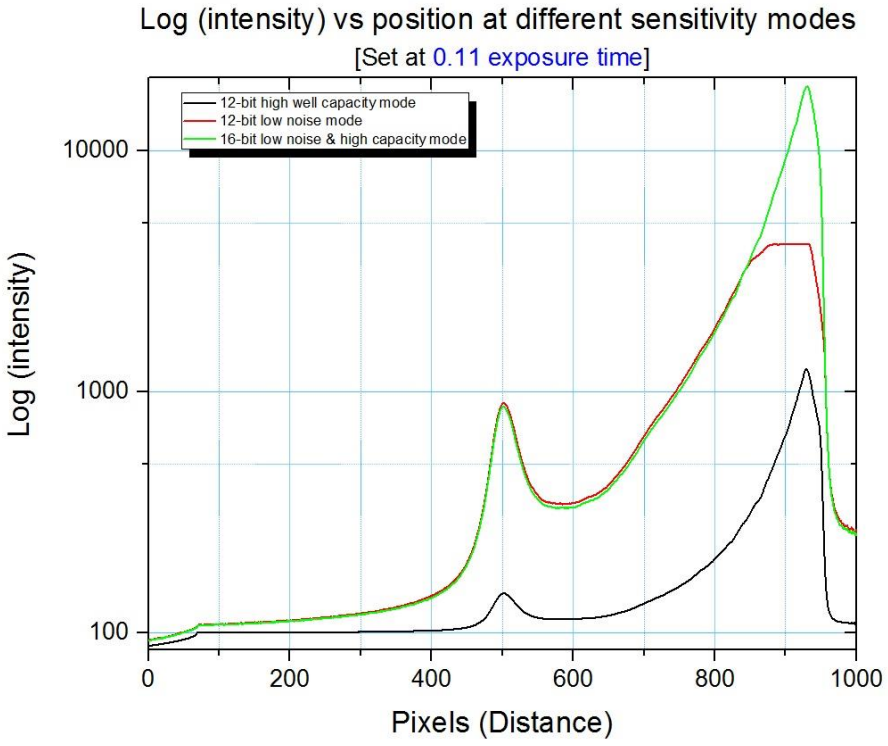

Figure 3.11: Plotting log (intensity) values for signals collected at 0.11 s exposure time but at different sensitivity modes.

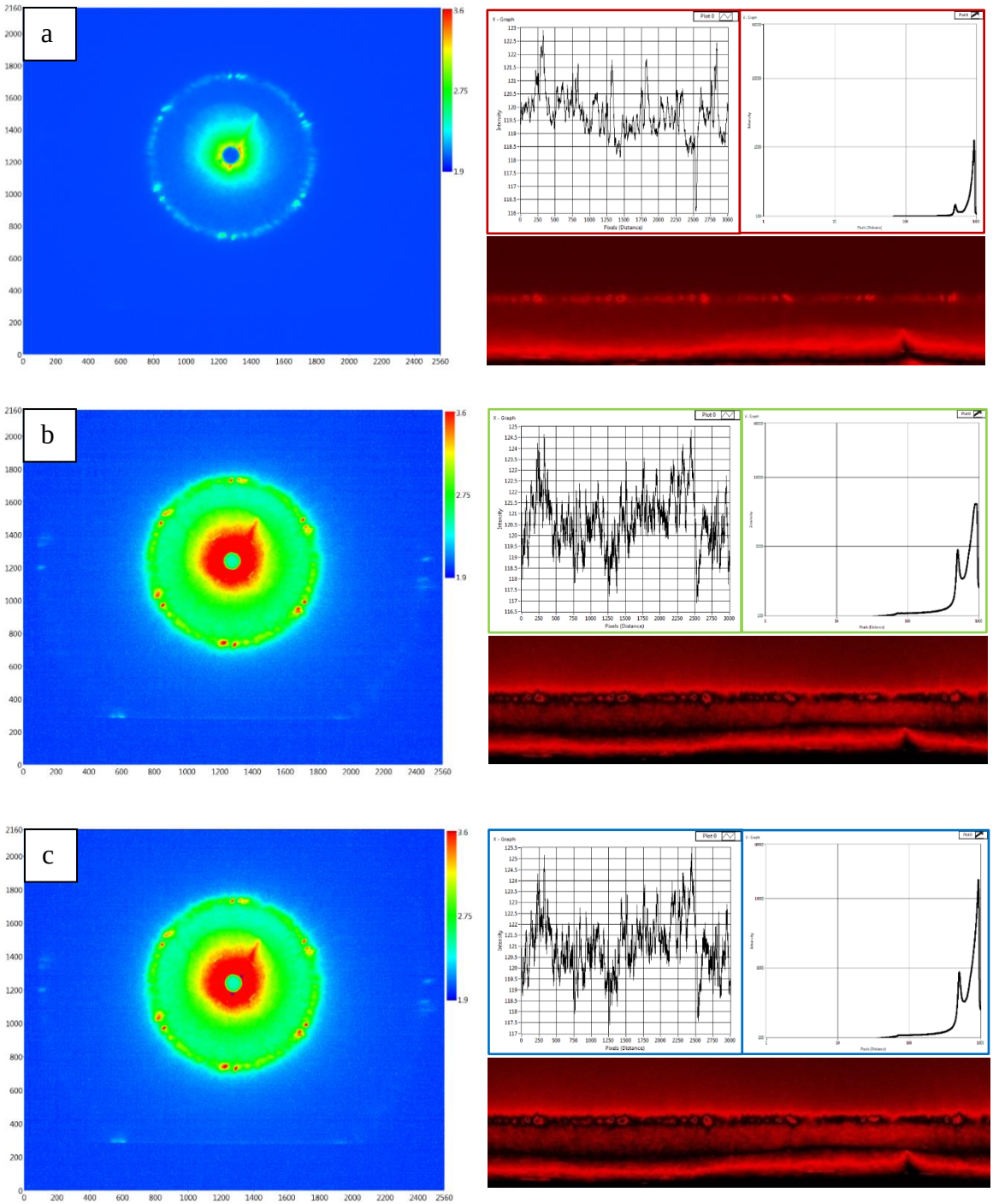

Figure 3.12: LabVIEW processed images together with the unwrapped data for a standard monolayer colloidal sample captured using Andor Zyla 5.5 camera at an exposure time of 0.11 s at different camera sensitivity modes; a) 12-bit high well capacity mode, b) 12-bit low noise sensitivity mode and c) 16-bit low noise & high well capacity mode.

Figures 3.7 shows the direct proportional between signal intensity and the exposure time used at the same sensitivity mode. In addition, Figures 3.8 – 3.12 show that signal intensity is significantly affected by changing the sensitivity mode at the same exposure time. These results recommend an optimisation between the camera sensitivity mode and the exposure time in order to reach the optimum conditions that develop signal with the maximum possible quality. Comparing intensity profiles measured at different sensitivity modes and at a variety of exposure times showed that 12-bit high well capacity sensitivity mode set at 0.01 s exposure time develops high signal intensity with relatively low noise. However, these camera settings are compatible with only very slow frame rates. On the other hand, the 16-bit low noise & high well capacity sensitivity mode at a very short exposure time of 0.034 s developed the optimum setting conditions to capture signal with high quality, low noise and at a very fast frame rate of 29.0 fps. Fast frame rates enable to track every single change in the signal intensity during the very fast spin coating process. This should facilitate collecting valuable real-time information about the colloidal self-assembly that took place during the spin coating of colloidal suspensions from volatile solvents.

Chapter 4.
Results and Discussions for *Ex-Situ* Investigations Stage

4.0 Introduction

In this chapter, silica colloids with a variety of particle size distributions were suspended in different volatile solvents; pure water, pure ethanol, water – ethanol mixtures, ethylene glycol, water – ethylene glycol mixtures and ethanol – ethylene glycol mixtures. Colloidal suspensions with a range of concentrations (5 wt. % - 35 wt. %) were spin coated at different rotational speeds, acceleration rates and settling times. Monolayer colloidal thin films fabricated on glass substrates at the end of the spin coating process have been characterised in reciprocal space (*ex-situ*). Images of the fabricated colloidal thin films were captured through an Eclipse LV100 Polarizing optical microscope with a 40× objective (Nikon CFI S Plan Fluor ELWD 40×) connected to an Andor camera (Zyla 5.5 sCMOS) with a quantum efficiency of 55% and a field of view of 464 × 464 µm.

As discussed in Chapter 2, these microscopic images have been processed through a series of LabVIEW codes in order to determine both coverage area percentage occupied by colloids on a glass substrate and the hexagonal close-packing percentage (HCP %). Samples can be classified based on the colloidal area coverage % into three categories; (1) monolayers, that have a relatively highly coverage area, (2) sub-monolayers, where area coverage decreases regarding the formation of large empty voids between ordered areas and (3) multilayers, where overlapping took place and a series of consecutive layers are formed instead of monolayer thin films. HCP % in each sample acts as an indication of the colloidal ordering quality of the final thin film. A sample that exhibits a HCP% equals 100% is the single crystal which represents the ideal structure without any defects. As HCP% decreases, either point or line defects increase forming a less ordered colloidal structure. Finally, scanning electron microscope (SEM) has been used to develop a higher resolution power needed to characterise the morphology of fabricated colloidal thin films effectively. Intension behind performing *ex-situ* investigations stage was to compare results collected at different factors in order to investigate the impact of these operating parameters on the ordering quality of colloidal crystals during the spin coating process. This may help to optimise the spin coating processing parameters and so facilitates the fabrication of highly ordered, defects free monolayer colloidal crystals with a long domain size.

4.1 Effect of rotational speed on quality of colloidal ordering

In order to study the effect of rotational speed on the area coverage % occupied by silica colloids on a glass substrate, silica colloids with an average particle size of 1550 nm were suspended in distilled water with a concentration of 5, 15 and 25 wt. %. Then, 100 µL drops of each colloidal suspension were deposited on a pre-treated glass substrate. Finally, colloidal deposition was spin coated at a range of rotational speeds between 500 and 4000 rpm, while acceleration rate and spin time were kept constant at 2.2 $rev.s^{-2}$ and 30 s respectively. The detailed parameters and corresponding area coverage % occupied by silica colloids in the resultant colloidal thin films are listed in Table 4.1.

Table 4.1: Effect of rotational speed on the area coverage % occupied by colloids in the final colloidal thin film fabricated using spin coating technique.

Rotational Speed (rpm)	5 % wt. silica	15 % wt. silica	25 % wt. silica
	Area Coverage % (Mean Value)		
500 rpm	43.5	84.2	99.6
1000 rpm	41.9	73.1	98.5
2000 rpm	32.8	49.1	70.5
3000 rpm	30.9	43.9	59
4000 rpm	27.6	41.0	50

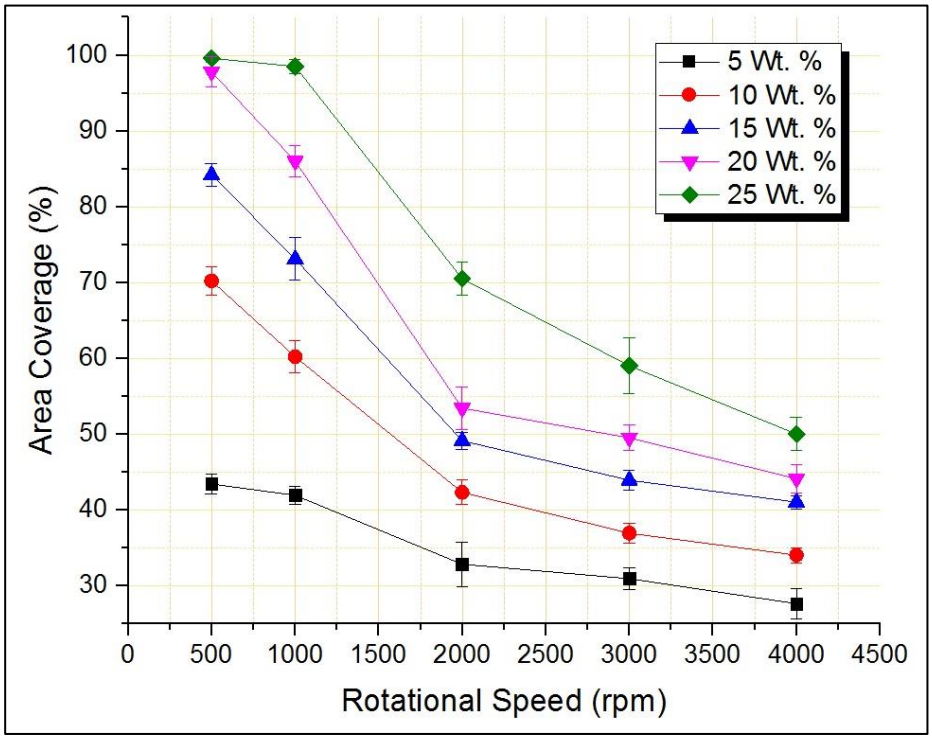

Figure 4.1: Effect of rotational rate on area coverage % occupied by silica colloids after spin coating process.

It is clearly noticed from results given in Table 4.1 that magnitude of rotational speed has a significant impact on the colloidal area coverage % during the spin coating process. As described in Figure 4.1, rotational speed was found to be in inversely proportional to the area coverage % occupied by colloids. For the 5 wt. % colloidal suspension, shown in Figure 4.2, area coverage % increases from 27.6 % up to 43.5% as rotational speed decreases from 4000 rpm to 500 rpm. Similarly, maximum area coverage % in case of either 15 wt. % (Figure 4.3) or 25 wt. % (Figure 4.4) colloidal suspensions were found to be at the minimum used the rotational speed of 500 rpm. These results confirm the inverse relationship between rotational speed and colloidal area coverage %. The relationship between rotational speed and area coverage % of colloids can be explained by the direct connection between speed and evaporation rate of the used solvent. As the rotational speed of the motor increases, the rate of evaporation of water also increases. This provides a shorter period of time for particles to be arranged before complete evaporation of water. As a result, opportunity for particles to explore optimum sites to occupy in the colloidal structure during the colloidal ordering process dramatically decreases which distorts the structure uniformity. Consequently, ordering quality of the final colloidal films decreases as rotational speed increases.

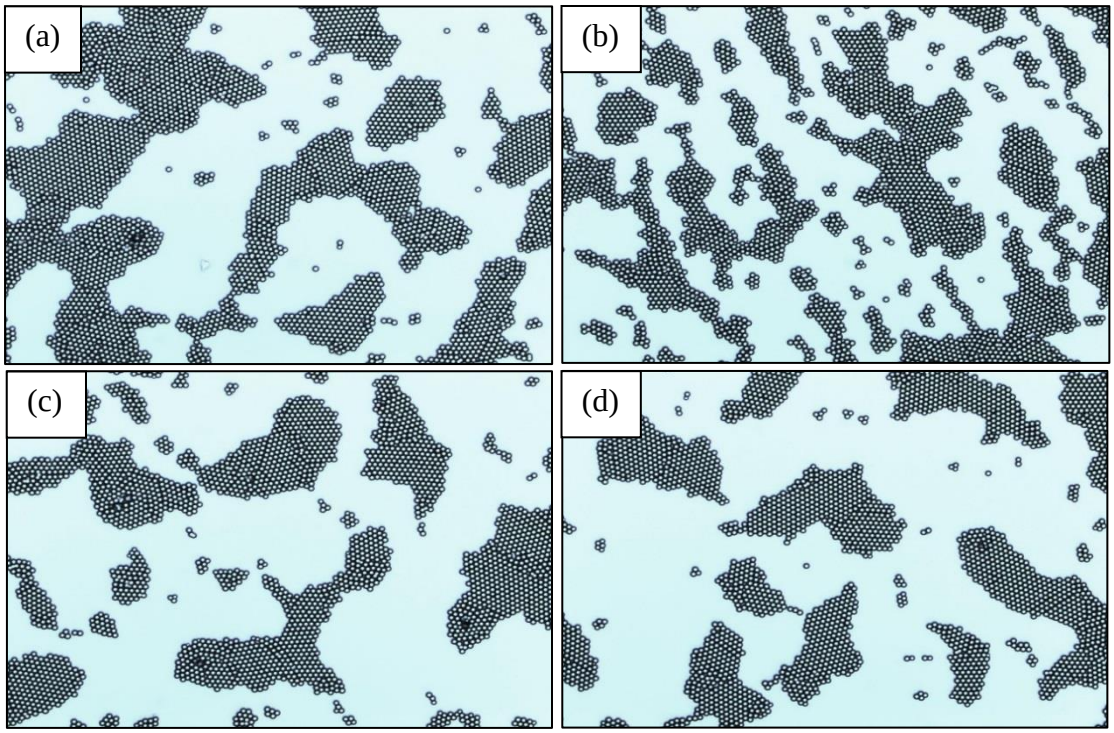

Figure 4.2: Microscopic images for colloidal thin films fabricated from spin coating of 5 wt. % silica colloidal suspensions in water at different rotational speeds; (a) 500 rpm, (b) 1000 rpm, (c) 2000 rpm and (d) 3000 rpm.

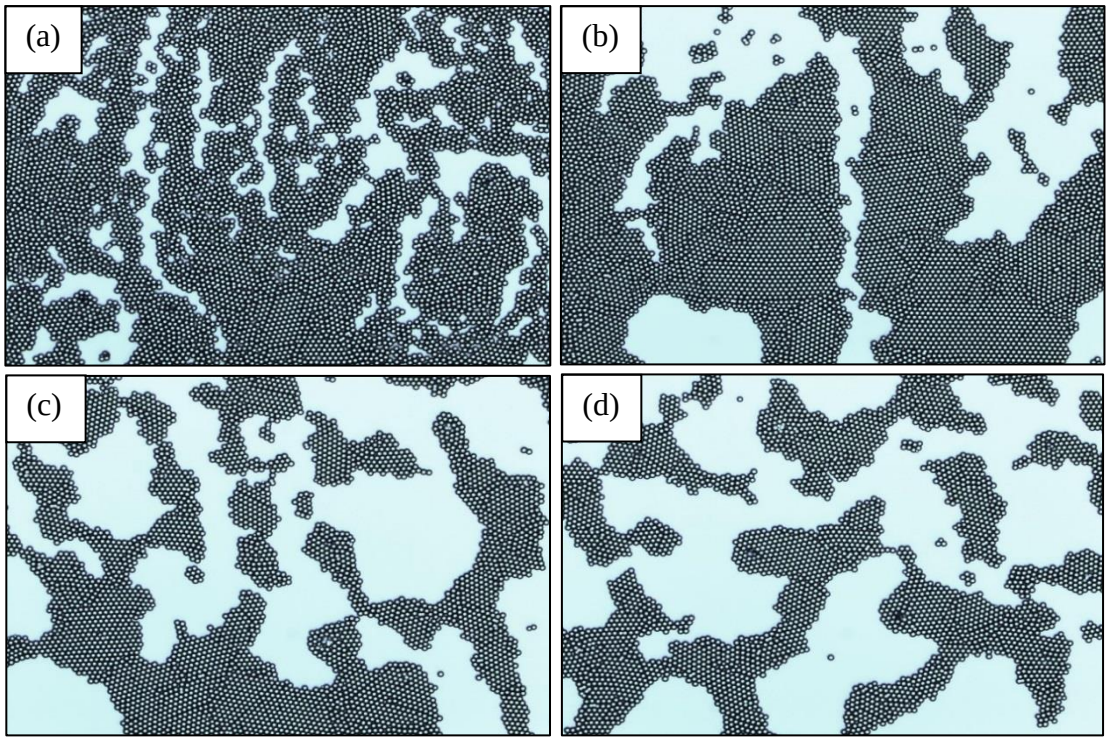

Figure 4.3: Microscopic images for colloidal thin films fabricated from spin coating of 10 wt. % silica colloidal suspensions in water at different rotational speeds; (a) 500 rpm, (b) 1000 rpm, (c) 2000 rpm and (d) 3000 rpm.

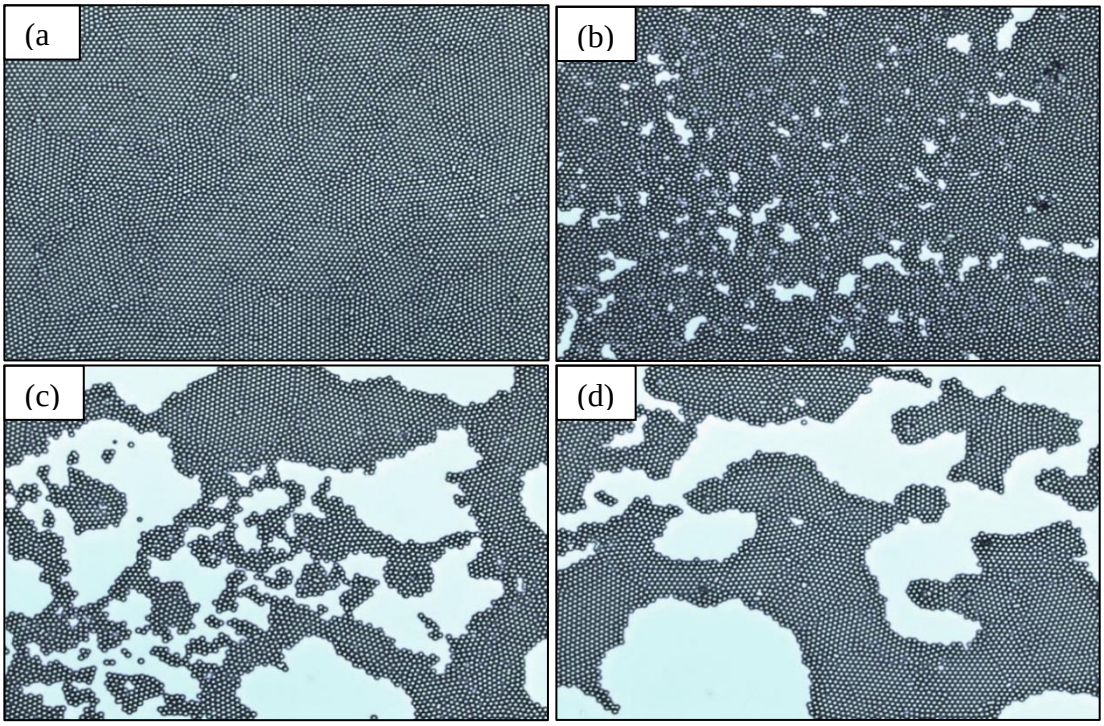

Figure 4.4: Microscopic images for colloidal thin films fabricated from spin coating of 25 wt. % silica colloidal suspensions in water at different rotational speeds; (a) 500 rpm, (b) 1000 rpm, (c) 2000 rpm and (d) 3000 rpm.

4.2 Effect of Solid content on quality of colloidal ordering

In this part, the effect of silica particles concentration on the magnitude of colloidal area coverage percentage has been investigated as an indication of the colloidal ordering quality of fabricated monolayer colloidal crystals. To do so, silica colloids were suspended in distilled water with different concentrations of 5%, 10%, 15%, 20% and 25% (weight fraction). Colloidal suspensions were then spin coated at a designated rotational speed ranges between 500 rpm - 4000 rpm. Acceleration rate and spin time have been kept constant at 2.2 rev.s^{-2} and 30 s respectively. Area coverage % results against the corresponding rotational speed and solute concentration for each sample are summarised in Table 4.2.

Table 4.2: Effect of particles concentration on the area coverage % occupied by colloids in the final colloidal thin film fabricated using spin coating technique.

Rotational Speed (rpm)	5 wt. % Silica	10 wt. % Silica	15 wt. % Silica	20 wt. % Silica	25 wt. % Silica
	Area Coverage % (Mean Value)				
500 rpm	**43.4**	**70.2**	**84.2**	**97.8**	**99.6**
1000 rpm	41.9	60.2	73.1	86.0	98.5
2000 rpm	32.8	42.3	49.1	53.4	70.5
3000 rpm	30.9	36.9	43.9	49.5	59.0
4000 rpm	27.6	34.0	41.0	44.1	50.0

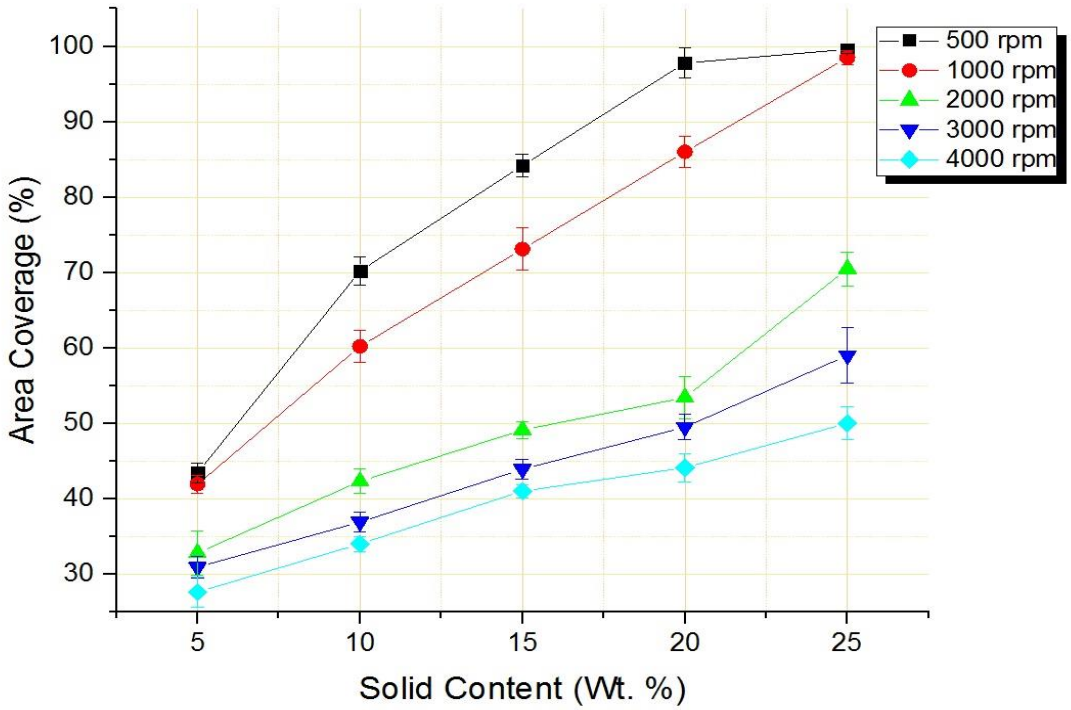

Figure 4.5: Effect of solute concentration on the area coverage % of silica colloids after spin coating process.

As noticed in results given in Table 4.2 and Figure 4.5, area coverage % is directly proportional to the solute concentration suspended in the colloidal suspension. As particles weight percentage increases from 5 wt. % to 25 wt. %, area coverage % was also found to increase with respect to the value of rotational speed. Highest area coverage % of 99.6 % was found when a solute concentration of 25 wt. % spin coated at a rotational speed of 500 rpm. Similarly, lowest area coverage % of 27.6 % was found at 5 wt. % suspension spin coated at 4000 rpm. These results confirmed that solids concentration in the colloidal suspension plays an important role in the colloidal ordering quality that took place during the self-assembly process.

Interestingly, these results coincide with literature survey as discussed in Chapter 1. Higher concentrations of colloidal particles increase the volume fraction of colloidal suspension system during the self-assembly process. Consequently, the inter-particle distance between colloids in the colloidal suspension decreases. This helps particles to reorder themselves more uniformly during the spin coating process. Better organisation of colloids governed by the packing constraints leads to the fabrication of regular structures of highly ordered particles. In addition, this investigation also confirms our former conclusion that area coverage % is inversely proportional to the rotational speed. As a result, an optimisation was required to manage the combination effect of both rotational speed and solute concentration, while both acceleration rate and spinning time were kept constant at 2.2 $rev.s^{-2}$ and 30 s respectively. In addition, SEM micrograph given in Figure 4.6 confirms the fabrication of highly ordered close-packed colloidal structure after optimisation of the impact of both rotational speed and solids content. This sample was obtained from a 25 wt. % silica colloidal suspension in pure water spin coated at 500 rpm and 2.2 $rev.s^{-2}$ for 30 s. Hexagonal close-packing percentage (HCP %) for this sample, measured using LabVIEW software as described in details in Chapter 2, was found to be 68.9 % as given in Figure 4.7. Full collage for the microscopic images together with their Fourier Transforms (FFTs) obtained after spin coating colloidal suspensions with different concentrations at different rotational speeds is shown in Figure 4.8.

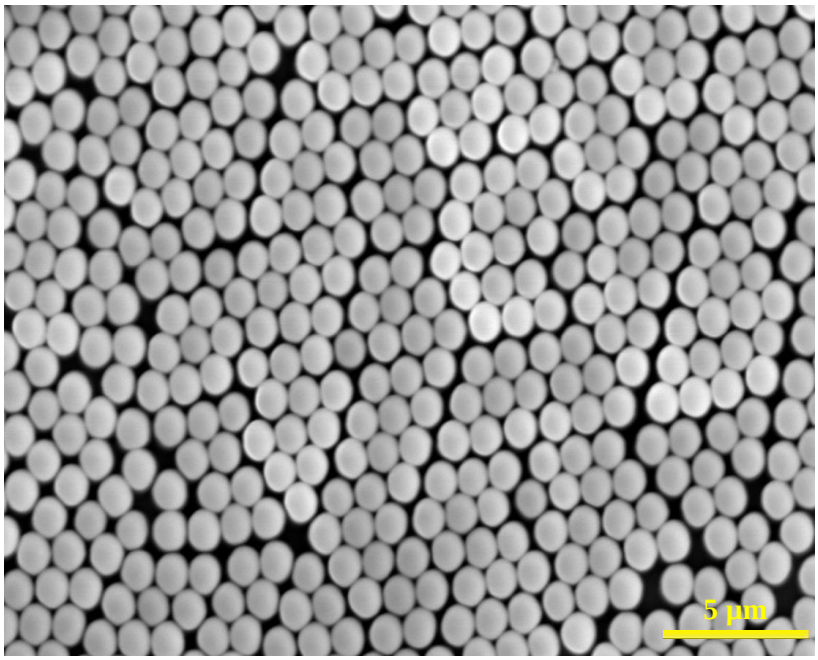

*Figure 4.6: SEM image for monolayer colloidal thin film with a HCP percentage of **68.9 %** obtained from spin coating of 25 wt. % silica colloidal suspension in water at 500 rpm, 2.2 rev.s^{-2} for 30s. Magnification is 4300x.*

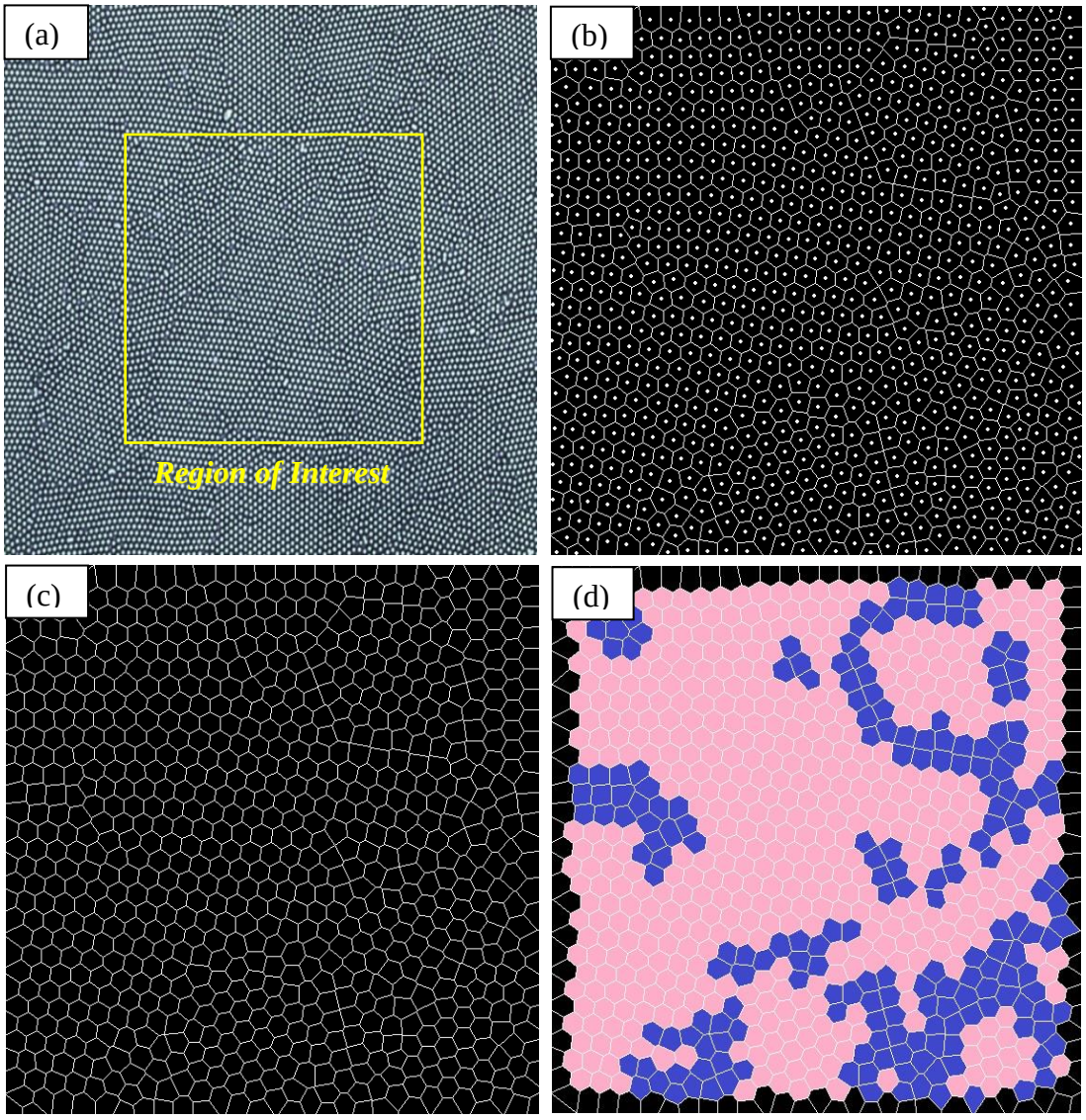

Figure 4.7: Processing of microscopic images through LabVIEW software in order to characterise the ordering quality of the fabricated colloidal crystals in terms of percentage of hexagonal close-packed arrangements; (a) original microscopic image of monolayer colloidal crystal fabricated through spin coating of 25 wt. % silica colloidal suspension in water at 500 rpm, 2.2 rev.s^{-2} for 30 s. Square indicates region of interest in analysis, (b) Output of connectivity of each particle with the neighbouring in the sample, (c) Connectivity after removal of dots that represent the presence of spherical colloidal particles, (d) Quantifying of hexagonal patterns in the image shows a ***HCP % = 68.9 %*** *[pink areas indicate the hexagonal polygons, while blue areas are for other polygons].*

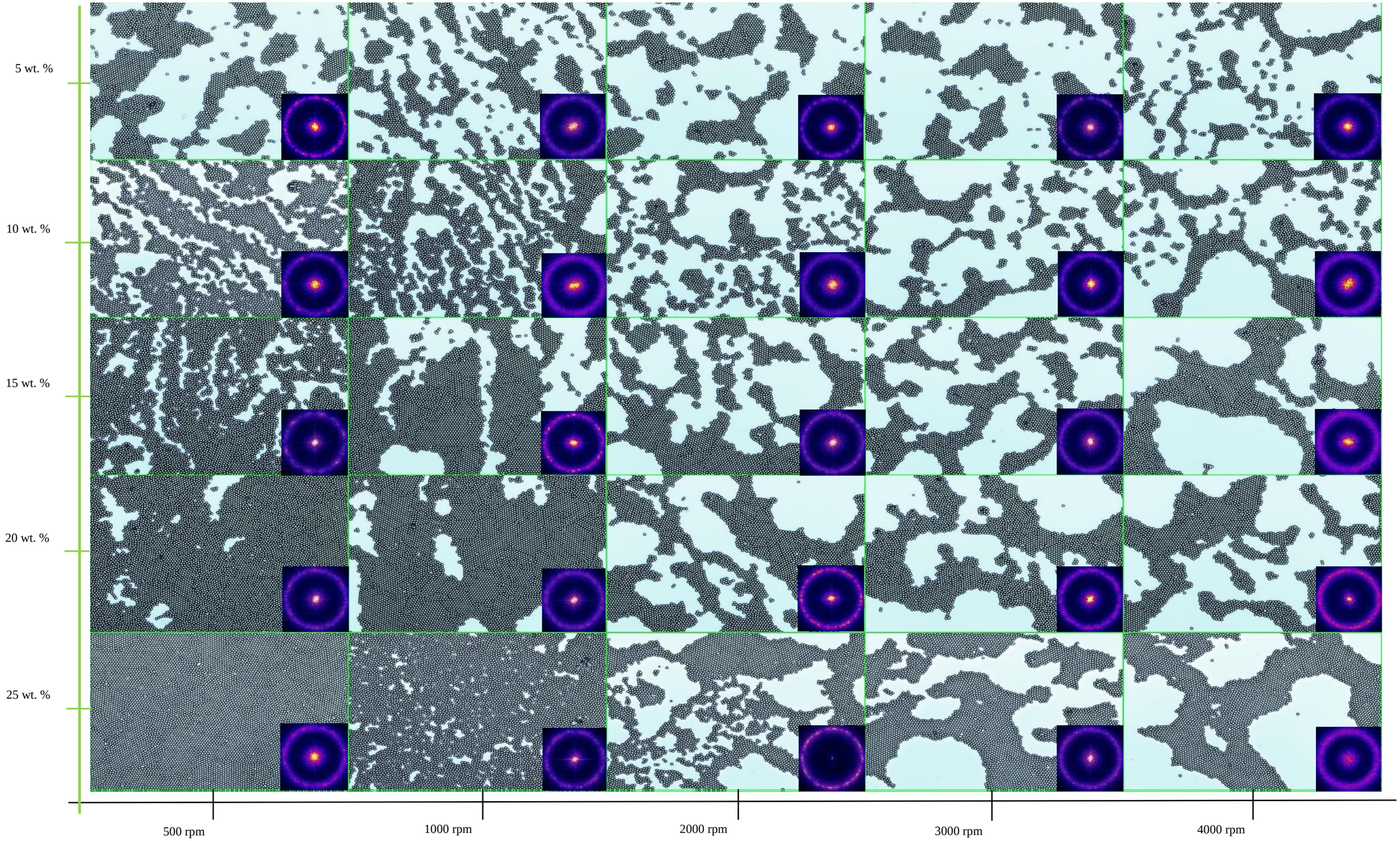

Figure 4.8: Collage includes images for samples spun cast at different spinning speeds and various solid weight % in the presence of water as a solvent.

4.3 Effect of Speed ramp (acceleration rate)

Herein, a series of experiments have been performed in order to investigate the impact of acceleration rate value, as one of the processing parameters during the spin coating process, on the fabricated colloidal crystals morphology. To do so, 1550 nm silica colloids were suspended in distilled water at a concentration of 30 wt. % and 35 wt. % individually. Colloidal suspensions were then sonicated continuously for 24 hours to remove any physical aggregations between colloids. Then, 100 µL were deposited on a pre-treated glass substrate which is attached to the DC motor shaft. The motor was then rotated at 3000 rpm for 30 s spin time. However, acceleration rate has been changed in each set of experiments as follows; 2.2 rev.s^{-2}, 55 rev.s^{-2}, 110 rev.s^{-2} and 220 rev.s^{-2}. Each sample has been repeated for five times to confirm consistency of results. Fabricated colloidal crystals were imaged once from the centre and another four times from the four directions surrounding the substrate centre within 1 mm^2 using an Andor CCD camera with a 55 % quantum energy together with a 40× microscopic objective with a field of view of 464 × 464 µm. Images were then processed using LabVIEW software to determine the average area coverage % for each sample. Results of coverage area percentage of colloids against acceleration rates are summarised in Table 4.3.

As listed in Table 4.3, area coverage % in samples spun cast from 35 wt. % colloidal suspensions increased from 94.6 % to 99.8 % as the acceleration rate decreases from 220 rev.s^{-2} to 2.2 rev.s^{-2} respectively. Ordered colloidal structure with the highest area coverage % of 99.8% was obtained at the slowest speed ramp of 2.2 rev.s^{-2}. Similarly, area coverage % in samples spun cast from 30 wt. % colloidal suspensions was increased from 91.4 % to 99.7 % as the acceleration rate decreases from 220 rev.s^{-2} to 2.2 rev.s^{-2} respectively. Herein, the highest area coverage % of 99.7% obtained also at the lowest rate of acceleration of 2.2 rev.s^{-2}. These results show that acceleration rate is inversely proportional to the colloidal ordering quality obtained at the centre of pre-treated glass substrates as represented in Figure 4.9. Increasing the acceleration rate may increase the shear forces during the spin coating process. This significantly affects the opportunity for colloids to settle down and

rearrange themselves in a regular manner. Consequently, colloids area coverage percentage decreases as the acceleration rate increases as shown in Figures 4.10 and 4.12.

Table 4.3: Effect of rate of acceleration on area coverage% occupied by colloids on glass substrates.

Sample Number	Acceleration (rev/s^2)	Spinning Speed (rpm)	Solute Concentration, (wt. %)	Area Coverage % (Mean Values)
1	**2.2**	3000 rpm	**35 wt. %**	**99.8**
2	**55**			**98.2**
3	**110**			**95.2**
4	**220**			**94.6**
5	2.2		30 wt. %	99.7
6	55			95.7
7	110			92.5
8	220			91.4

Hexagonal close-packing percentage (HCP %) has been calculated for microscopic images regarding samples that have the highest area coverage percentage either in 30 wt. % or 35 wt. % suspensions. As shown in Figure 4.11, hexagonal close-packing percentage (HCP %) of monolayer colloidal crystals obtained from spin coating 30 wt. % silica colloidal suspension at 3000 rpm, 30 s and at an acceleration rate of 2.2 rev.s^{-2} was found to be 72.2%. While the hexagonal close-packing percentage (HCP %) of monolayer colloidal crystals obtained from spin coating 35 wt. % silica colloidal suspension at the same conditions was found to be 78.1% as shown in Figure 4.13. Interestingly, HCP % results for both 30 wt. % and 35 wt. % colloidal

suspensions together with HCP % previously determined for 25 wt. % colloidal suspension, shown in Figure 4.7, reveal that not only the colloidal area coverage percentage is directly proportional to the solid content, but also colloidal ordering quality, in terms of HCP %, improves as the solids content increases in the colloidal suspension introduced to spin coating process.

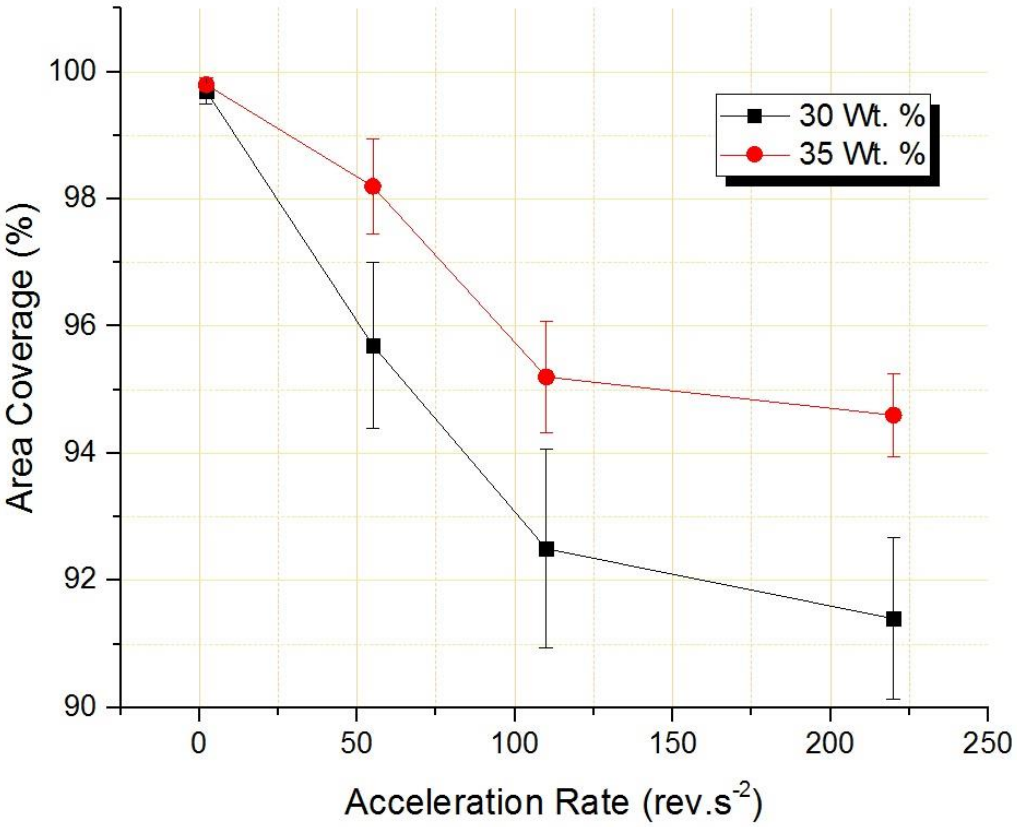

Figure 4.9: Effect of acceleration rate on the area coverage % of silica colloids after spin coating process.

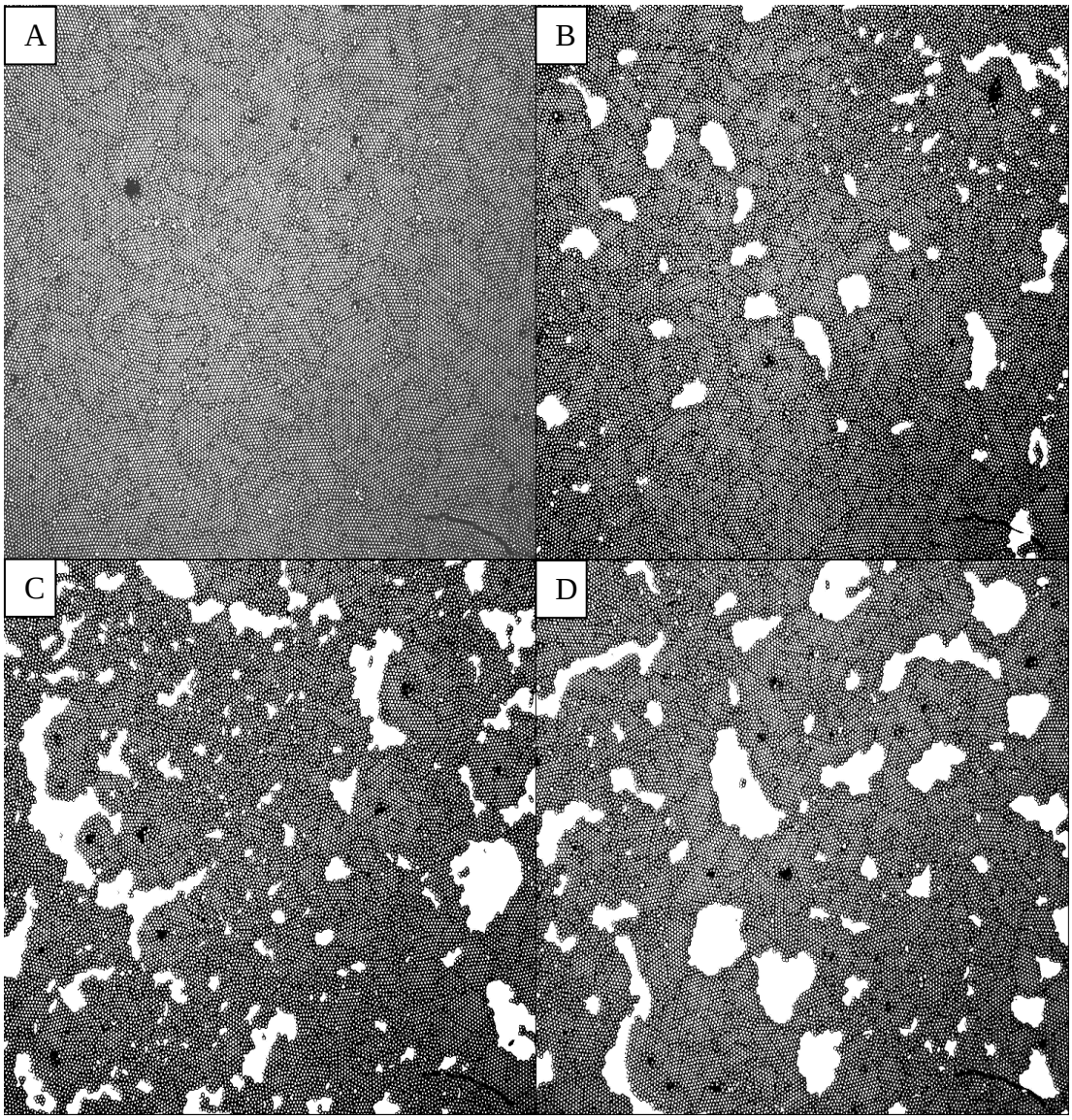

Figure 4.10: Images for the final colloidal crystals formed from 30 wt. % colloidal suspensions in water spun cast at 3000 rpm for 30 s at different accelerations; A) 2.2 rev.s^{-2}, B) 55 rev.s^{-2}, C) 110 rev.s^{-2} and D) 220 rev.s^{-2}. As acceleration decreases the ordering of colloids at the centre of the glass substrate improves.

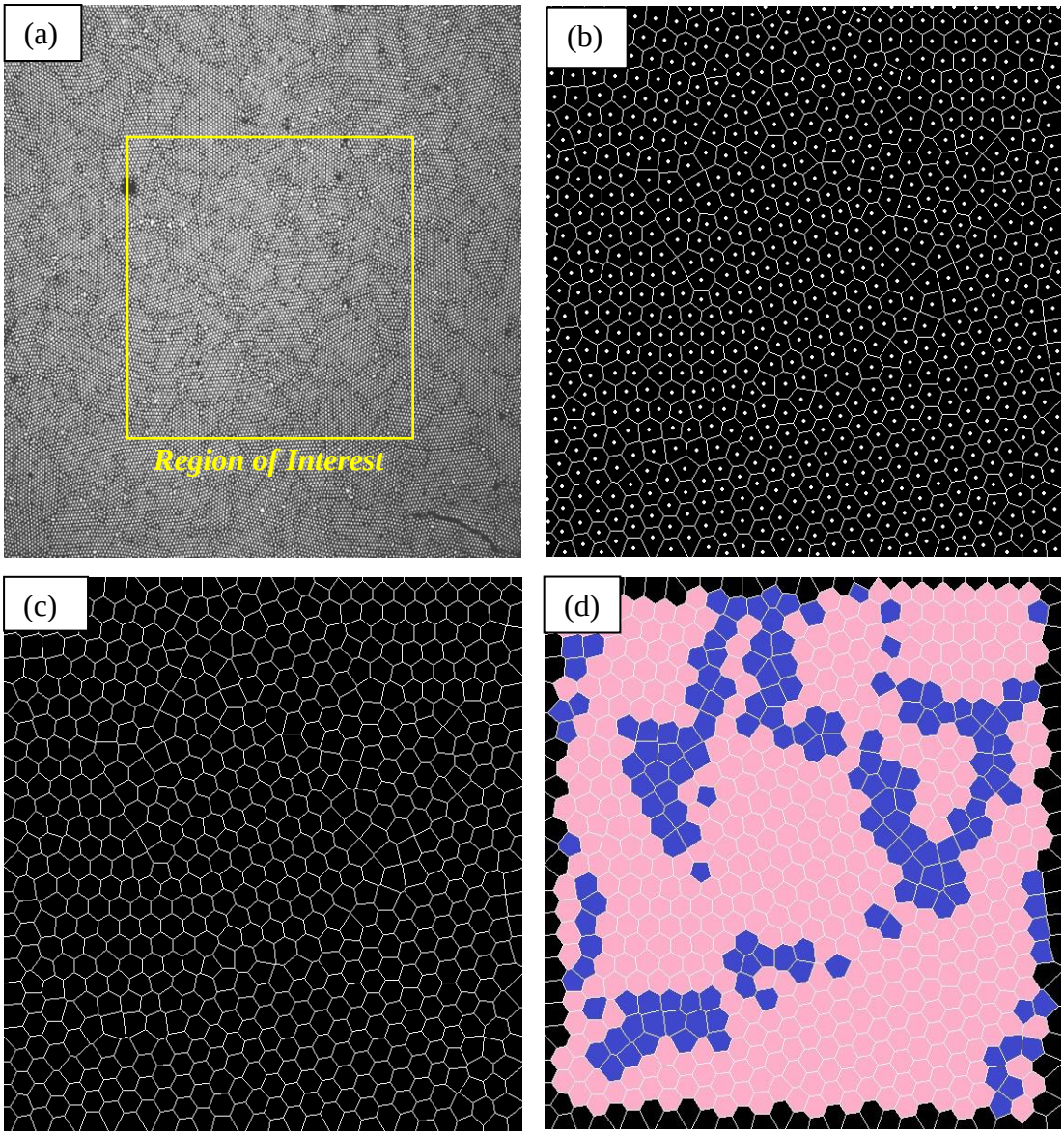

Figure 4.11: Processing of microscopic images through LabVIEW software in order to characterise the ordering quality of the fabricated colloidal crystals in terms of percentage of hexagonal close-packed arrangements; (a) original microscopic image of monolayer colloidal crystal fabricated through spin coating of 30 wt. % colloidal suspension in water spun cast at 3000 rpm, 2.2 rev.s^{-2} and for 30s spin time, (b) Output of connectivity of each particle with the neighbouring in the sample, (c) Connectivity after removal of dots that represent the presence of spherical colloidal particles and (d) Quantifying of hexagonal patterns in the image shows a ***HCP % = 72.2 %*** *[pink areas indicate the hexagonal polygons, while blue areas are for other polygons].*

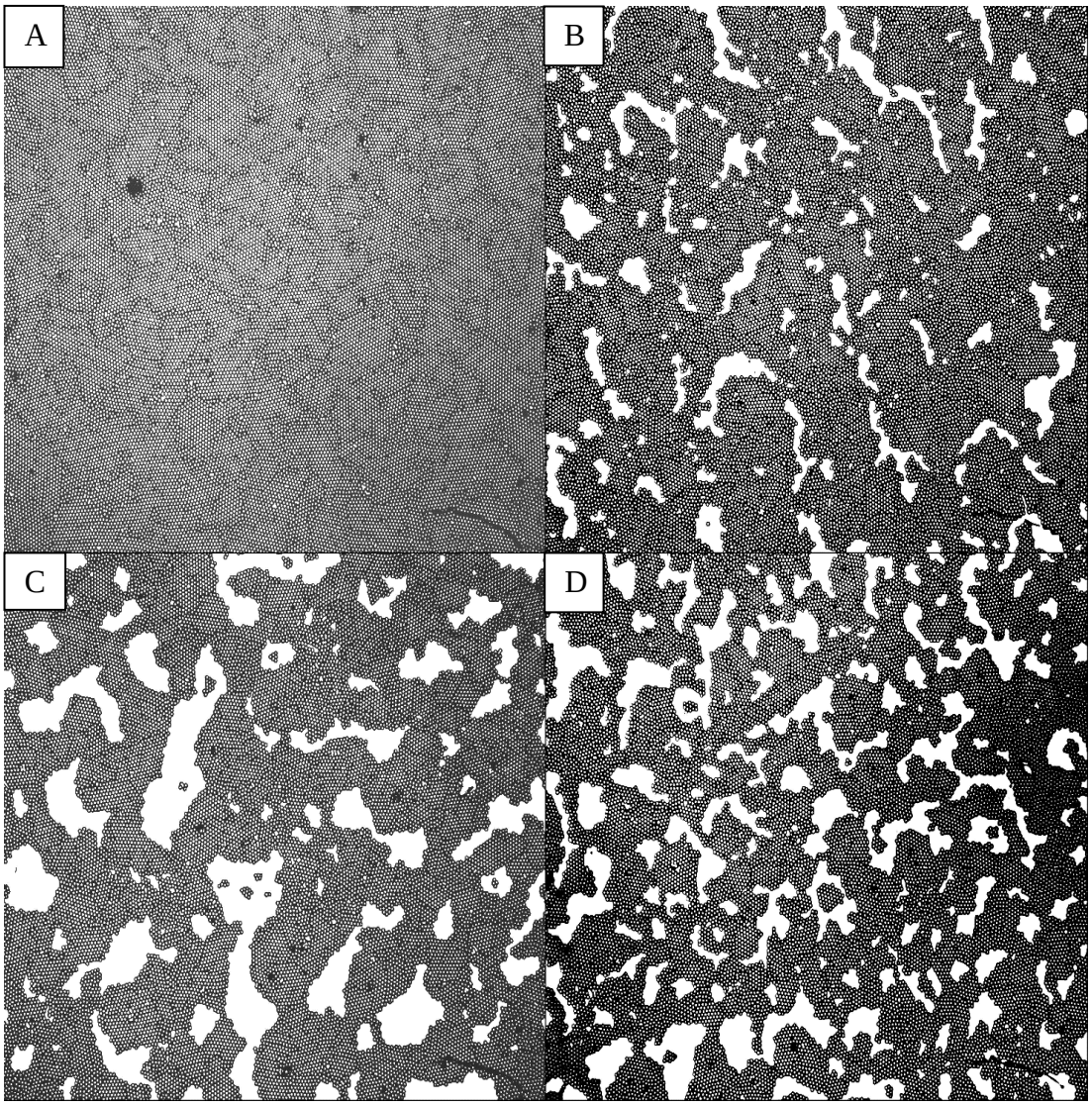

Figure 4.12: Images for the final colloidal crystals formed from 35 wt. % colloidal suspensions in water spun cast at 3000 rpm for 30 s at different accelerations; A) 2.2 rev.s^{-2}, B) 55 rev.s^{-2}, C) 110 rev.s^{-2} and D) 220 rev.s^{-2}. As acceleration decreases the ordering of colloids at the centre of the glass substrate improves.

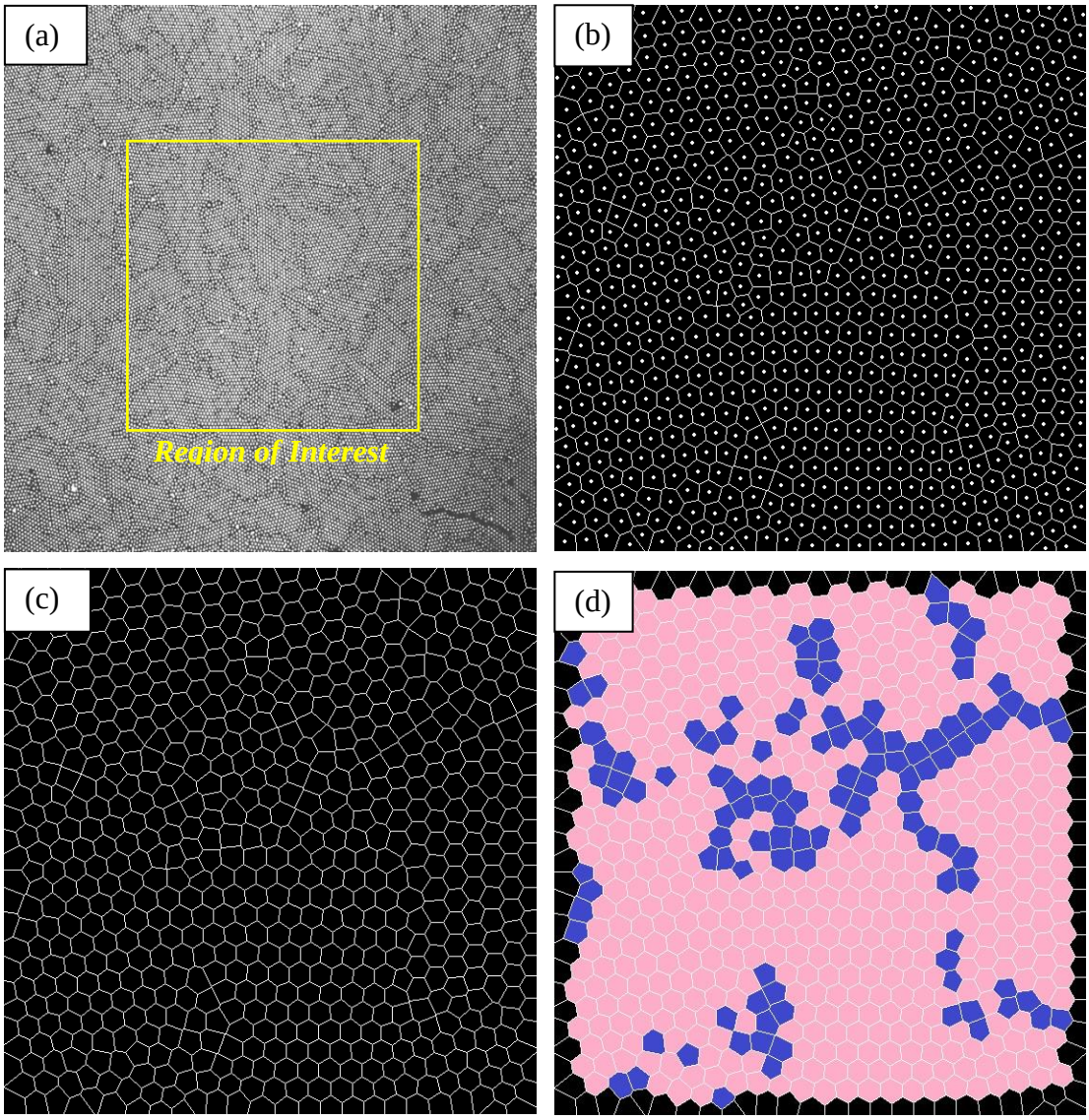

Figure 4.13: Processing of microscopic images through LabVIEW software in order to characterise the ordering quality of the fabricated colloidal crystals in terms of percentage of hexagonal close-packed arrangements; (a) original microscopic image of monolayer colloidal crystal fabricated through spin coating of 35 wt. % colloidal suspension in water spun cast at 3000 rpm, 2.2 rev.s^{-2} and for 30 s spin time, (b) Output of connectivity of each particle with the neighbouring in the sample, (c) Connectivity after removal of dots that represent the presence of spherical colloidal particles and (d) Quantifying of hexagonal patterns in the image shows a ***HCP % = 78.1 %*** *[pink areas indicate the hexagonal polygons, while blue areas are for other polygons].*

4.4 Effect of settling time on colloidal ordering quality

As discussed before, spin coating of colloidal suspensions starts by solution deposition on the substrate. Afterwards, the substrate is rotated at a designated speed inducing shear forces that lead to the solution layer thinning. The volatile solvent evaporates gradually leaving a colloidal thin film in its wake after complete evaporation of the solvent. In the following set of experiments, a specific period of time, as a settling time, was given to the colloidal sample after deposition on a substrate and before spinning. Settling time apparently helps to increase the solvent dispersion on glass substrate surface. Settling time governs the sedimentation rate of colloids through the colloidal suspension. Hence, settling time could have a significant impact on the stability of colloidal suspensions, so governing the colloidal ordering quality of the final thin film obtained at the end of the spin coating.

Different settling times have been used in this study. The effect of settling time on the colloidal ordering quality has been investigated in terms of hexagonal close-packing percentage (HCP %) in each sample. Herein, 1550 nm silica colloids were suspended in distilled water with concentrations of 30 wt. % and 35 wt. %. Then, 100 µL drops of each colloidal suspension were deposited on glass substrate. Colloidal solution was left to distribute freely on the substrate surface for different settling times; 0 s, 15 s, 30 s, 60 s, 120 s and 200 s. Afterwards, the sample was rotated at a fixed rotational speed of 3000 rpm for 30 s spinning time with a fixed rate of acceleration of 2.2 $rev.s^{-2}$. Each sample was repeated five times to ensure consistency of results. Images for fabricated colloidal crystals on glass substrates have been captured through optical microscopy with a 40× objective together with an Andor camera with a quantum energy of 55 % and a field of view of 464 × 464 µm. Each sample has been captured five times; once at the centre and four times around the substrate glass centre within 1 mm^2 in the four directions. Finally, images were analysed using the pre-coded LabVIEW script in order to determine the percentage of hexagonal close-packing (HCP %) in each sample.

Results for the colloidal films obtained from spin coating the 30 wt. % silica suspensions showed that the length of settling time significantly affects the quality of colloidal ordering in the final films. At 0 s settling time, given in Figure 4.14 A, area coverage % was found to be 96.7 %. As settling time increases from 0 s up to 30 s, area coverage % increases gradually to be 99.6% at 15 s (Figure 4.14 B) and 99.8 % at 30 s settling time (Figure 4.14 C). At 60 s settling time, given in Figure 4.14 D, particles start to sediment on the substrate surface. As a result, undesirable spots of irreversible aggregation of particles. These aggregations distort the colloidal ordering quality and decrease the area coverage % to be 96.6 %. As settling time increases to 120 s and 200 s, as shown in Figure 4.14 E and F respectively, multilayer spots expand due to the increased rate of particles sedimentation on the substrate surface. Both samples of colloidal thin films fabricated at 120 s and 200 s are not acceptable as monolayer colloidal crystals. Therefore, a 30 s settling time was found to be the optimum settling time when a 30 wt. % silica colloidal suspension in distilled water was spun cast at 3000 rpm, 2.2 rev.s^{-2} and for 30 s spin time. Hexagonal close-packing percentage (HCP %) in this sample was found to be 72.2 % as shown in Figure 4.15.

Similarly, colloidal suspensions of 35 wt. % in distilled water showed the same criteria with settling time. As settling time increases from 0 s (Figure 4.16 A) to 15 s (Figure 4.16 B) area coverage % was also increased from 98.6 % with an HCP % of 69.5 %, as describe in Figure 4.17, to an area coverage % of 99.7 % with an HCP % of 78.1 % as describe in Figure 4.18. Samples at a settling time of 30 s, shown in Figure 4.16 C, exhibited an area coverage % of 99.7 % with the highest HCP % of 79.6 % as describe in Figure 4.19. At settling times longer than 30 s, as shown in Figure 4.16 D - F, irreversible particles aggregations appeared due to the sedimentation of particles on the glass substrate surface. Sedimentation significantly decreases the ordering quality of final colloidal thin films fabricated by the spin coating process. This leads to the formation of multi-layered colloidal structures instead of monolayer colloidal crystals (MCCs).

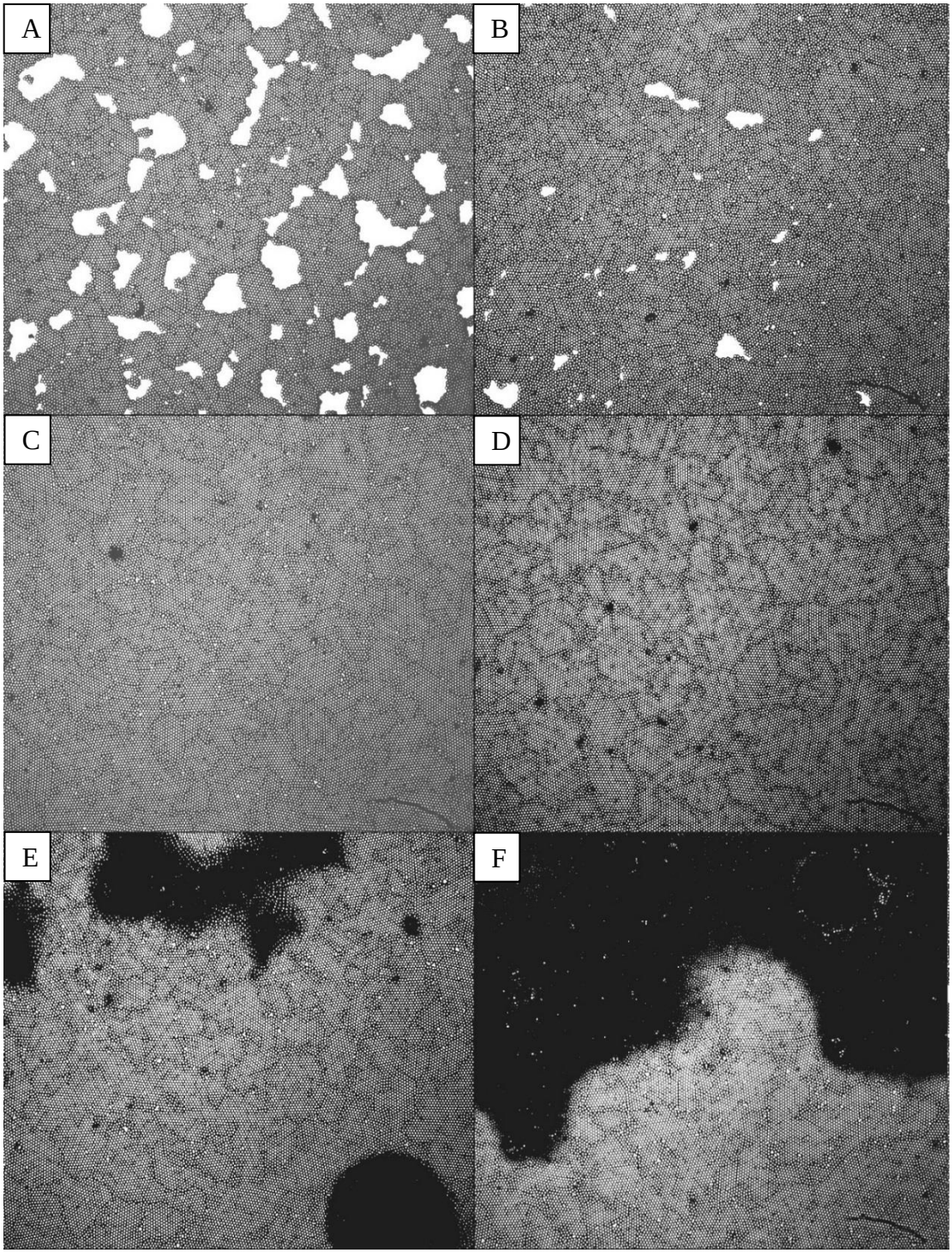

Figure 4.14: Microscopic images for final colloidal crystals formed through spin coating of 30 wt. % silica colloidal suspension in water at 3000 rpm, 2.2 rev.s^{-2}, 30 s spin time and at different settling times; A) 0 s, B)15 s, C) 30 s, D) 60 s, E) 120 s and F) 200 s.

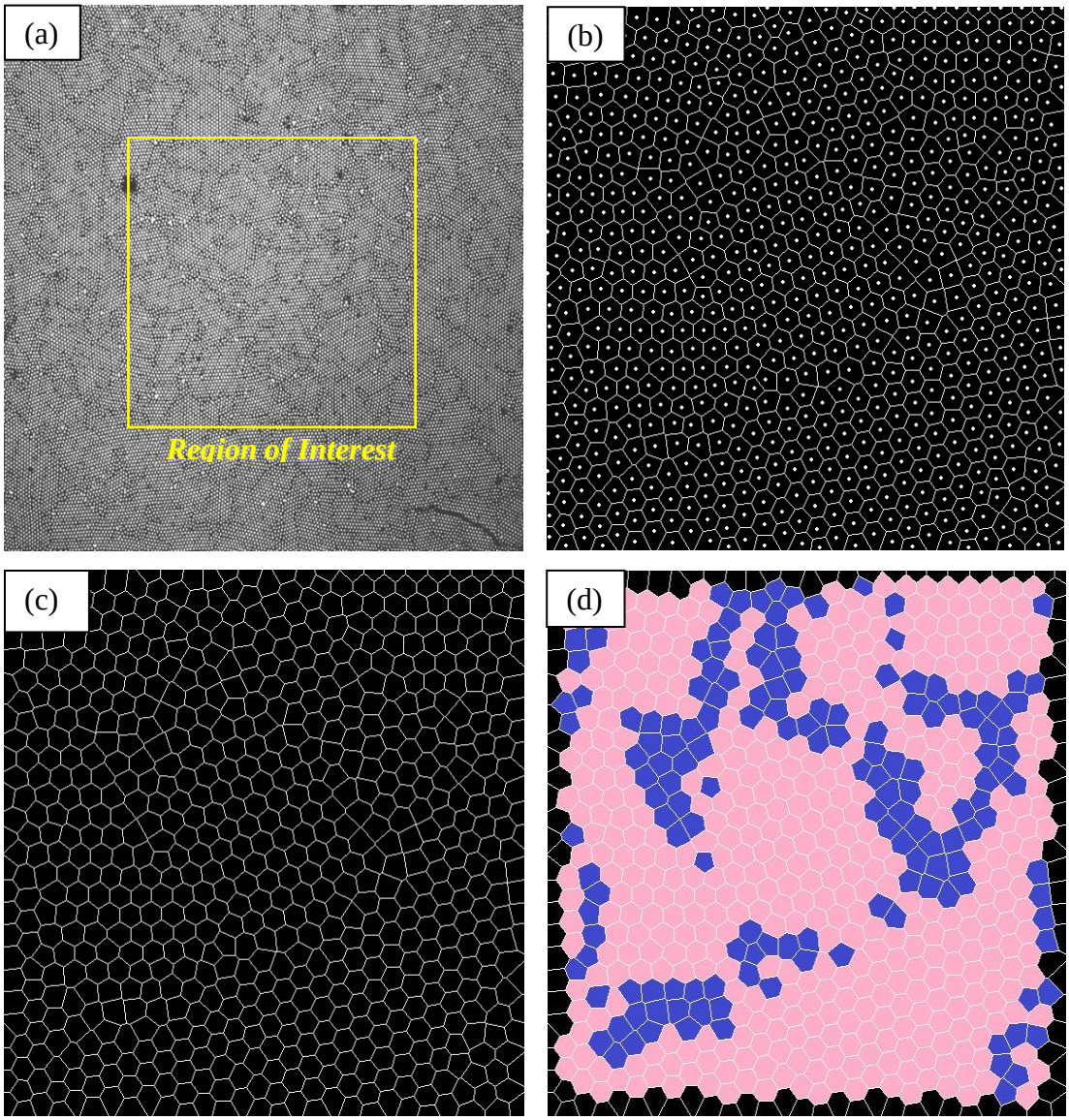

Figure 4.15: Processing of microscopic images through LabVIEW software in order to characterise the ordering quality of the fabricated colloidal crystals in terms of percentage of hexagonal close-packed arrangements; (a) original microscopic image of monolayer colloidal crystal fabricated through spin coating of 30 wt. % colloidal suspension in water spun cast at 3000 rpm, 2.2 rev.s^{-2}, 30 s spin time and after 30 s settling time, (b) Output of connectivity of each particle with the neighbouring in the sample, (c) Connectivity after removal of dots that represent the presence of spherical colloidal particles and (d) Quantifying of hexagonal patterns in the image shows a ***HCP % = 72.2 %*** *[pink areas indicate the hexagonal polygons, while blue areas are for other polygons].*

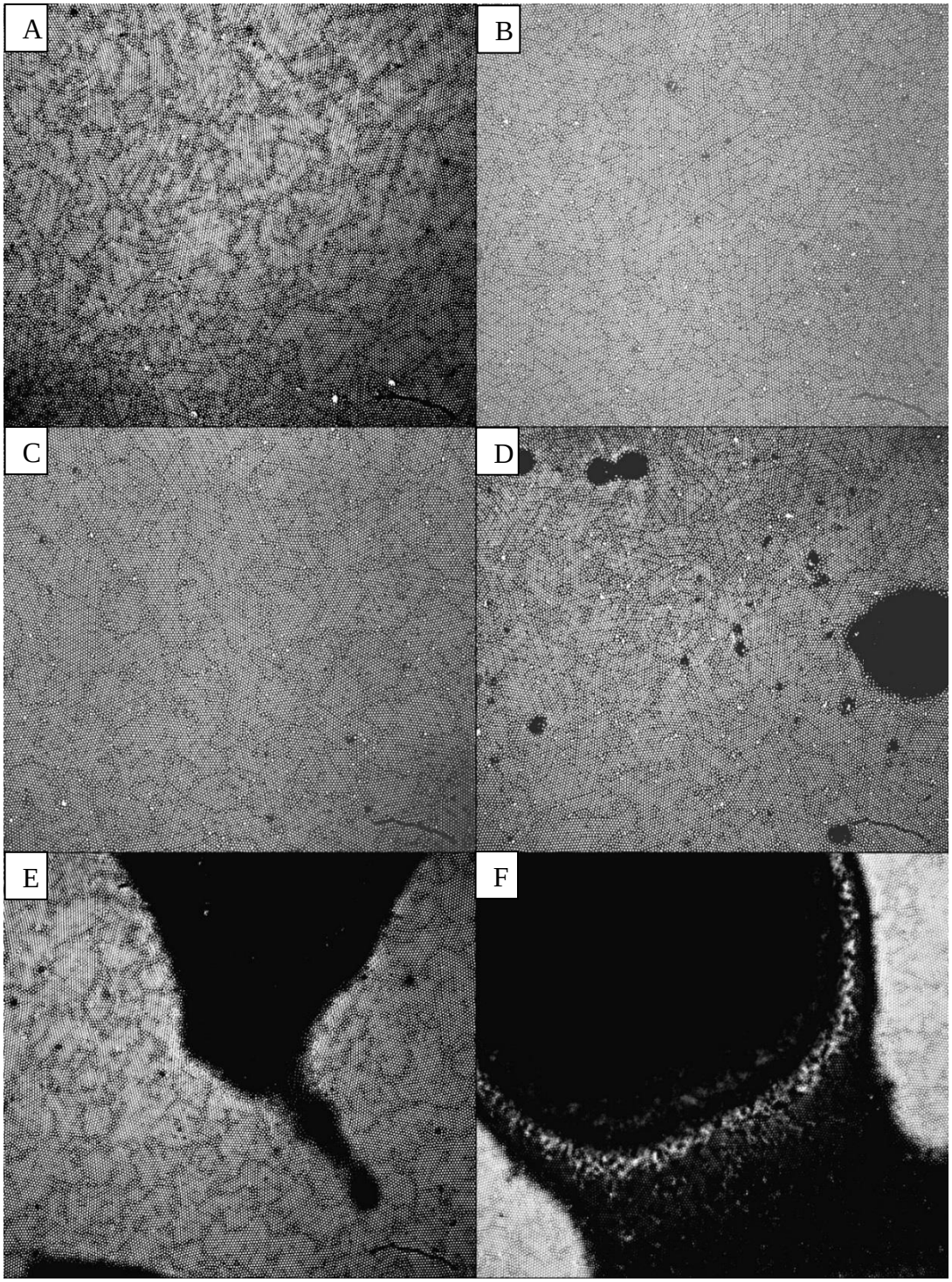

Figure 4.16: Microscopic images for final colloidal crystals formed through spin coating of 35 wt. % silica colloidal suspension in water at 3000 rpm, 2.2 rev/s², 30 s spin time and different settling times; A) 0 s, B)15 s, C) 30 s, D) 60 s, E) 120 s and F) 200 s.

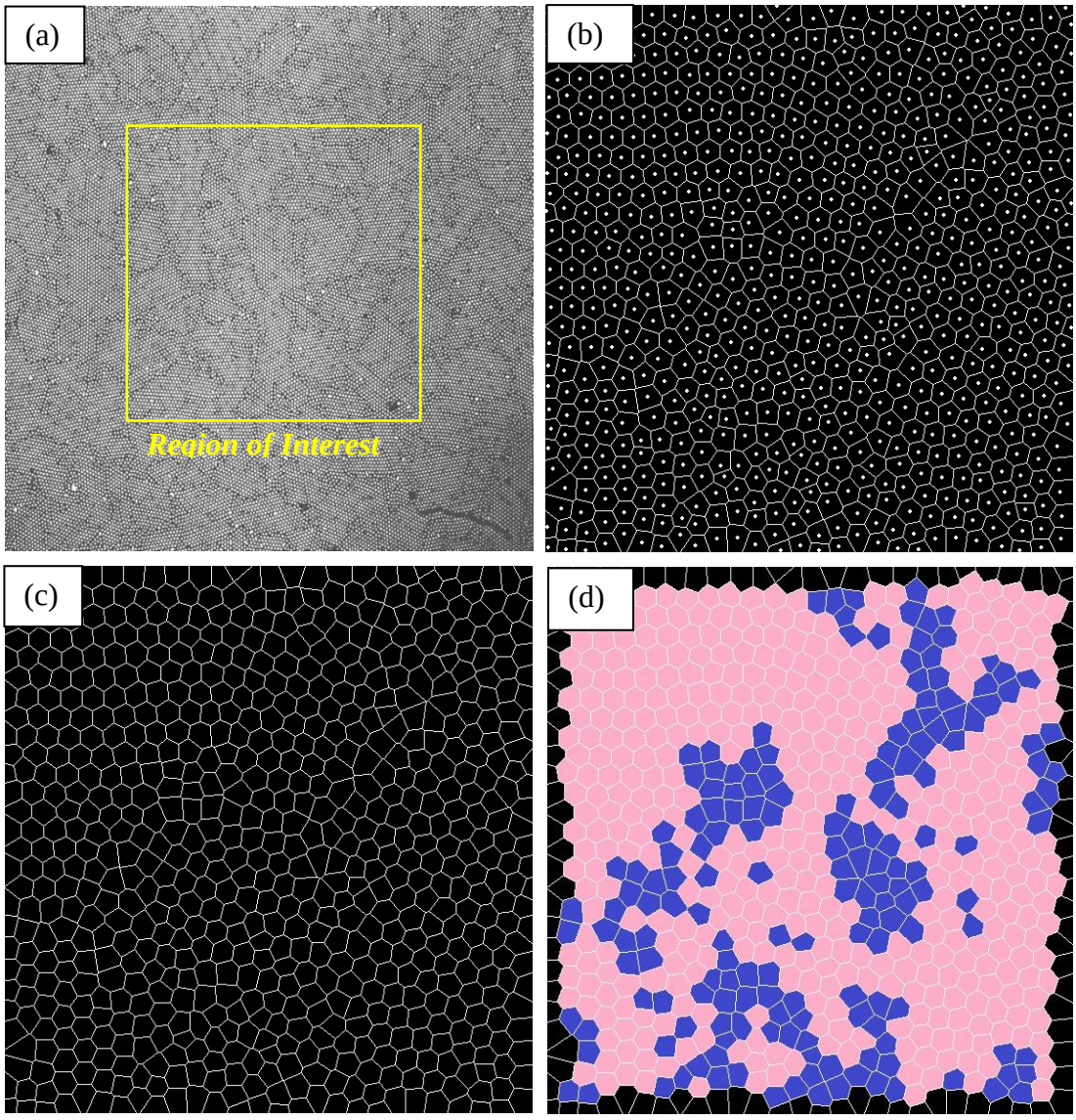

Figure 4.17: Processing of microscopic images through LabVIEW software in order to characterise the ordering quality of the fabricated colloidal crystals in terms of percentage of hexagonal close-packed arrangements; (a) original microscopic image of monolayer colloidal crystal fabricated through spin coating of 35 wt. % colloidal suspension in water spun cast at 3000 rpm, 2.2 rev.s^{-2}, 30 s spin time and after 0 s settling time, (b) Output of connectivity of each particle with the neighbouring in the sample, (c) Connectivity after removal of dots that represent the presence of spherical colloidal particles and (d) Quantifying of hexagonal patterns in the image shows a ***HCP % = 69.5 %*** *[pink areas indicate the hexagonal polygons, while blue areas are for other polygons].*

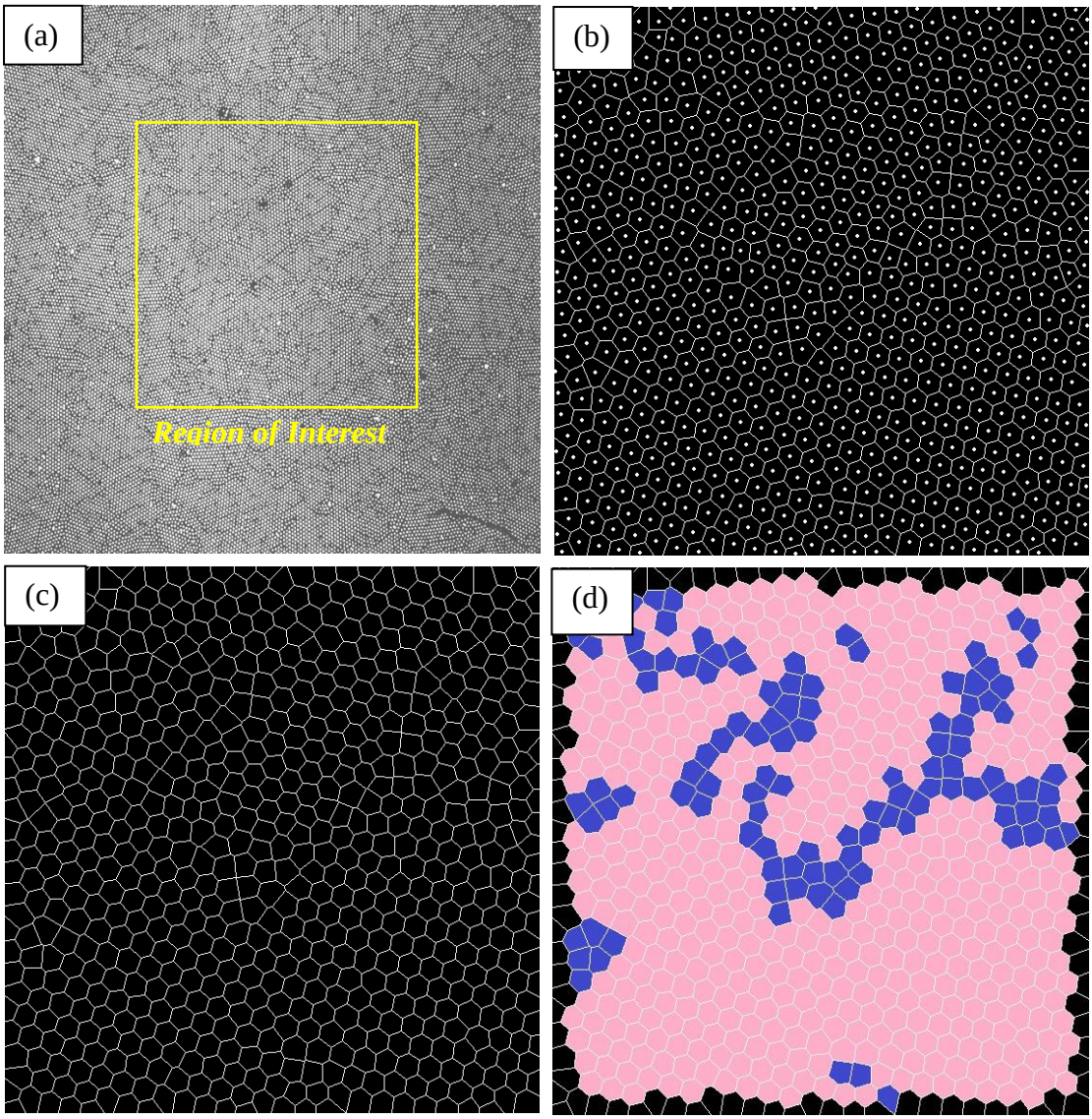

Figure 4.18: Processing of microscopic images through LabVIEW software in order to characterise the ordering quality of the fabricated colloidal crystals in terms of percentage of hexagonal close-packed arrangements; (a) original microscopic image of monolayer colloidal crystal fabricated through spin coating of 35 wt. % colloidal suspension in water spun cast at 3000 rpm, 2.2 rev.s^{-2}, 30 s spin time and after 15 s settling time, (b) Output of connectivity of each particle with the neighbouring in the sample, (c) Connectivity after removal of dots that represent the presence of spherical colloidal particles and (d) Quantifying of hexagonal patterns in the image shows a ***HCP % = 78.1 %*** *[pink areas indicate the hexagonal polygons, while blue areas are for other polygons].*

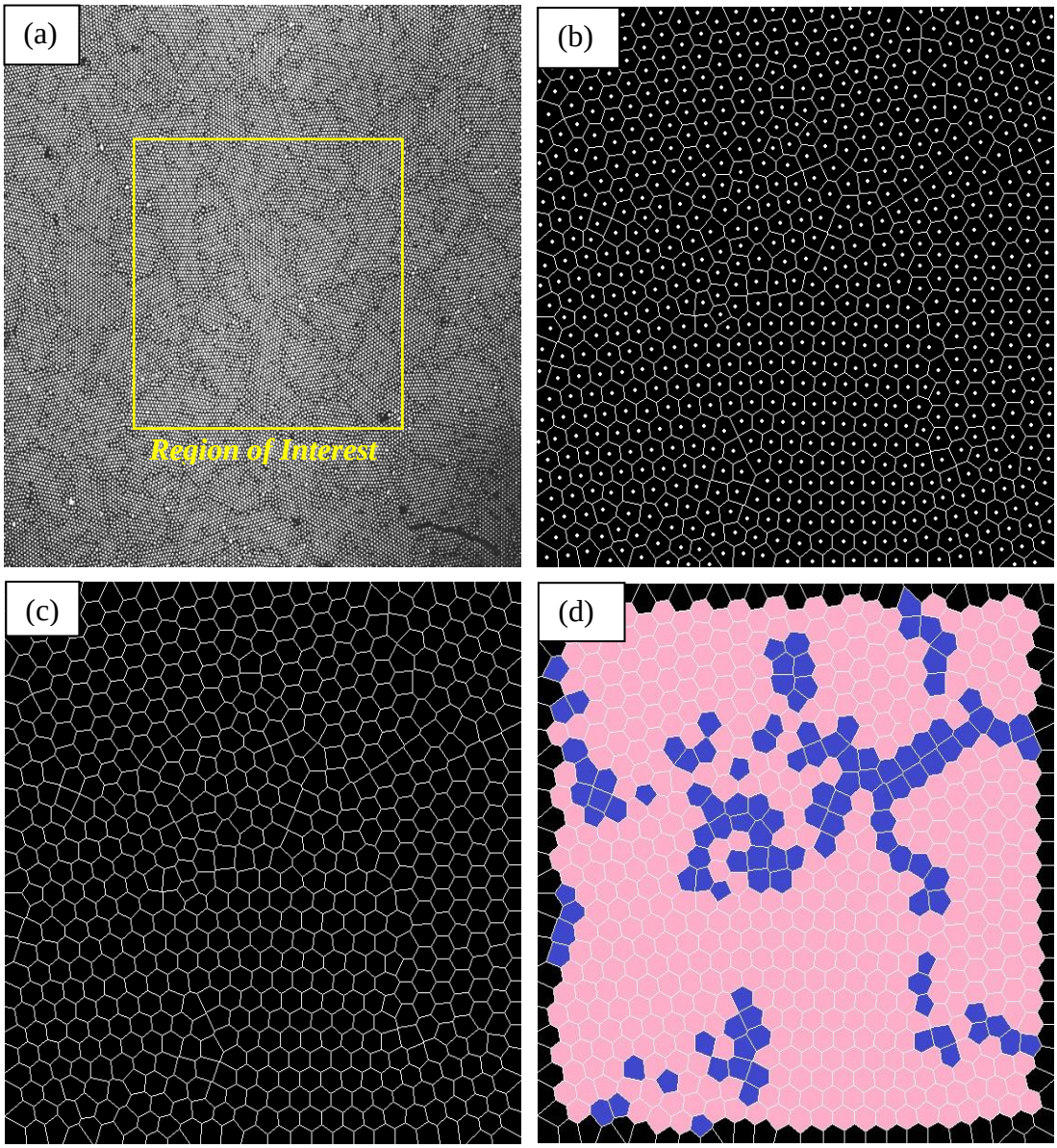

Figure 4.19: Processing of microscopic images through LabVIEW software in order to characterise the ordering quality of the fabricated colloidal crystals in terms of percentage of hexagonal close-packed arrangements; (a) original microscopic image of monolayer colloidal crystal fabricated through spin coating of 35 wt. % colloidal suspension in water spun cast at 3000 rpm, 2.2 rev.s^{-2}, 30 s spin time and after 30 s settling time, (b) Output of connectivity of each particle with the neighbouring in the sample, (c) Connectivity after removal of dots that represent the presence of spherical colloidal particles and (d) Quantifying of hexagonal patterns in the image shows a ***HCP % = 79.6 %*** *[pink areas indicate the hexagonal polygons, while blue areas are for other polygons].*

4.5 Effect of volatile solvent type

Colloidal self-assembly that took place during solvent evaporation from colloidal suspensions may develop either non-uniform coffee ring-like colloidal structures or highly ordered monolayer colloidal structures, known as photonic colloidal crystals. Morphology of the final colloidal thin films obtained from spin coating process is highly dependent on several parameters such as rotational speed, solute concentration, spin time, acceleration rate, settling time, particle size and particle size distribution. Solvent volatility is highly coherent with the solvent viscosity, colloidal suspension stability as well as the magnitude of shear forces induced during the spinning process. So, volatility may act as one of the most important factors among the solution properties that may affect the colloidal ordering quality of the spin coated colloidal films.

In the following series of experiments, the impact of solvent volatility on the colloidal ordering quality has been studied. Silica spherical particles with an average particle size of 1550 nm were suspended with a concentration of 35 wt. % in different solvents; pure water, water-ethanol mixtures, water-ethylene glycol mixtures and ethanol-ethylene glycol mixtures. Then, after a settling time of 30 s, each colloidal suspension was spin coated for 120 s at a rotational speed of 3000 rpm and an acceleration rate of 2.2 $rev.s^{-2}$. Each sample was experimentally repeated five times. Fabricated colloidal thin films were imaged through optical microscopy with a 40× objective connected to Andor CCD camera with a quantum energy of 60 % and a field of view of 464 × 464 µm. Each sample was imaged once at the substrate centre and four times in the four directions around the substrate centre within a 1 mm^2. Images were then processed using LabVIEW software in order to determine the percentage of hexagonal close-packing connections in each image.

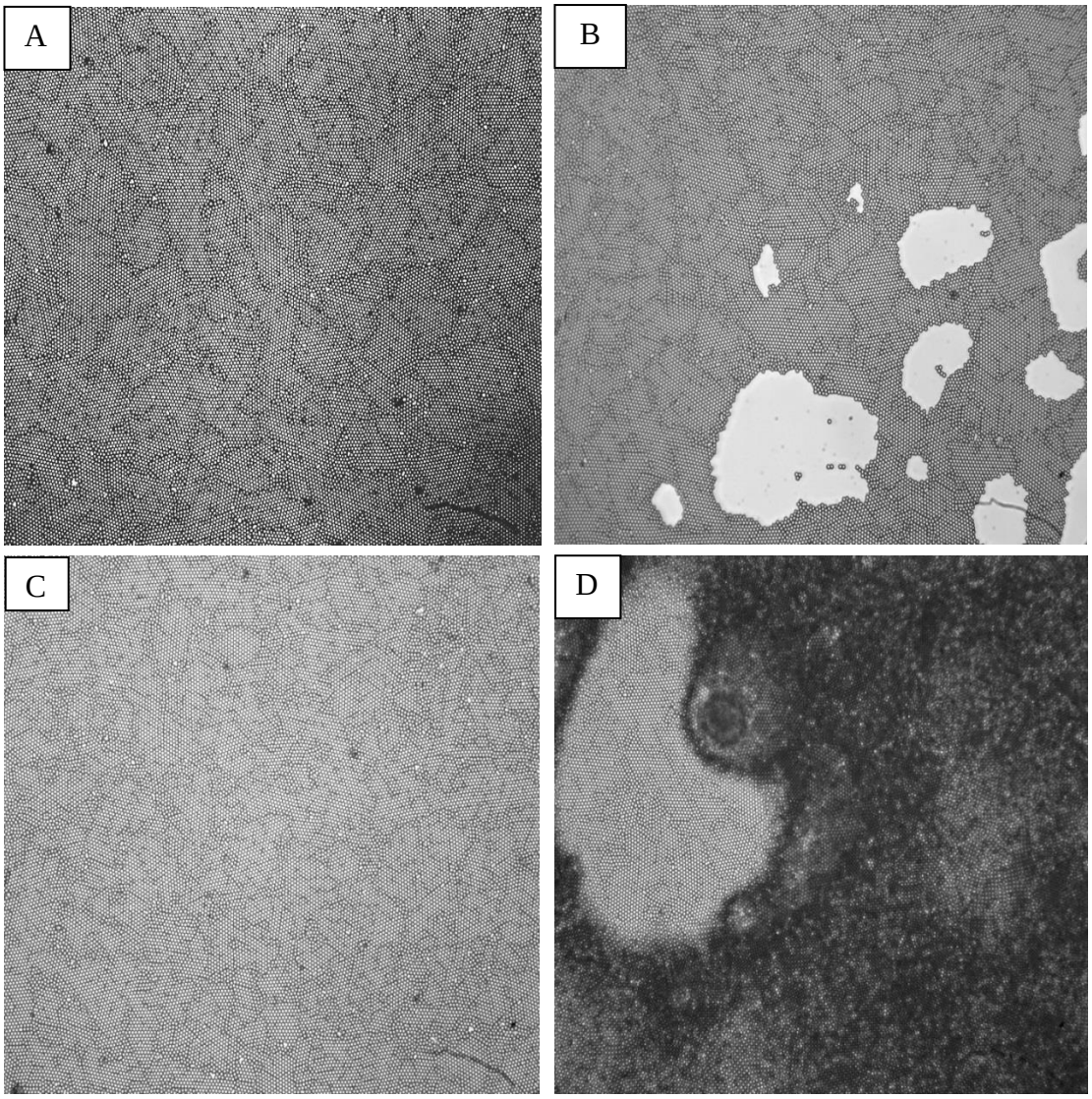

Figure 4.20: Microscopic images for final colloidal crystals obtained from a 35 wt. % silica colloidal suspension in different liquid solutions; A) pure water, B) water : Ethanol = 3:1, C) water : Ethanol = 1:1 and D) water : Ethanol = 1:3 (weight fraction) after 30 s settling time spun cast at 3000 rpm, 2.2 rev.s^{-2} and 120 s spin time.

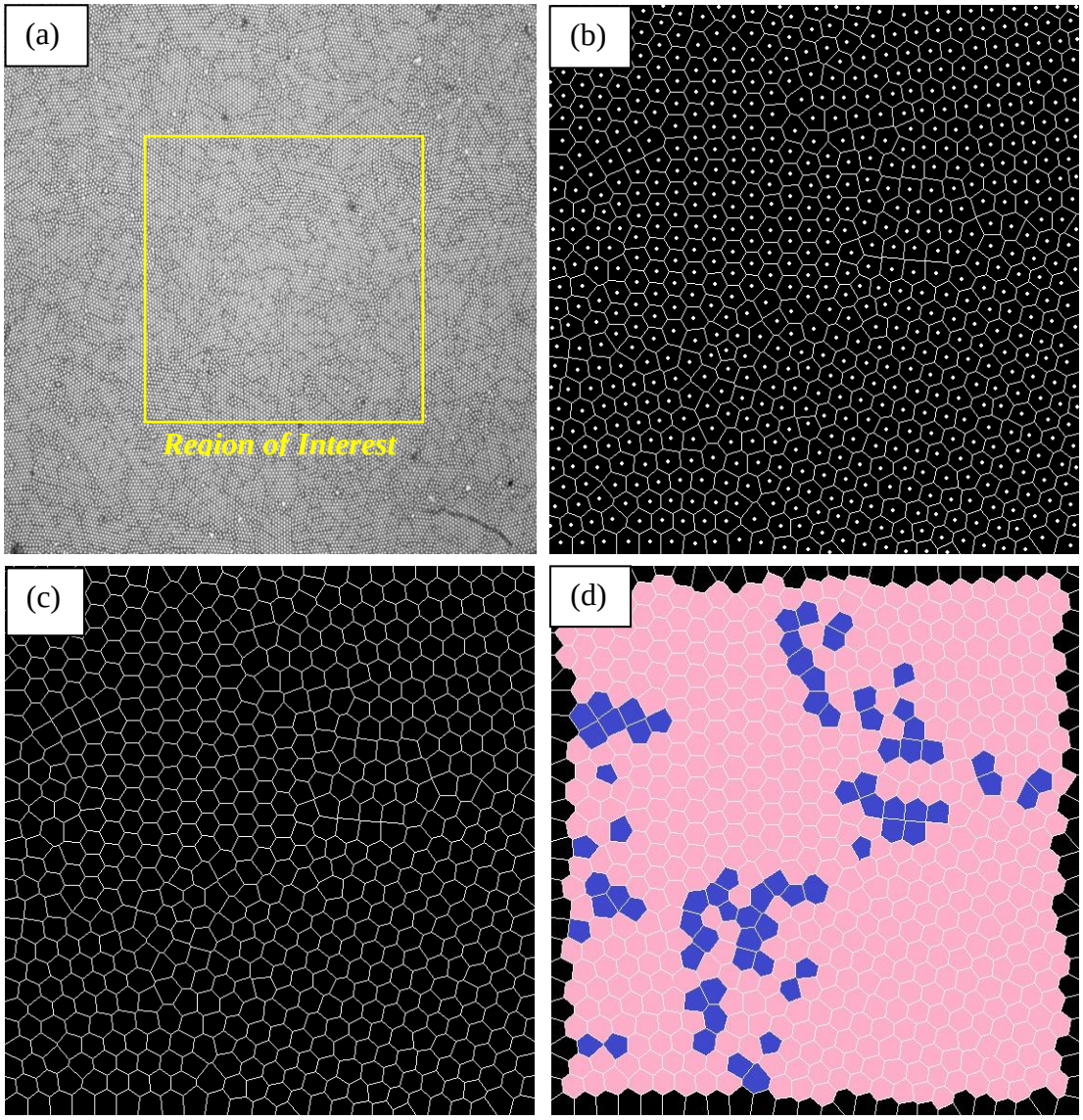

Figure 4.21: Processing of microscopic images through LabVIEW software in order to characterise the ordering quality of the fabricated colloidal crystals in terms of percentage of hexagonal close-packed arrangements; (a) original microscopic image of monolayer colloidal crystal fabricated through spin coating of 35 wt. % colloidal suspension in water: Ethanol = 1:1 mixture (weight fraction) spun cast at 3000 rpm, 2.2 rev.s^{-2}, 120 s spin time and after 30 s settling time, (b) Output of connectivity of each particle with the neighbouring in the sample, (c) Connectivity after removal of dots that represent the presence of spherical colloidal particles and (d) Quantifying of hexagonal patterns in the image shows a ***HCP % = 84.5 %*** *[pink areas indicate the hexagonal polygons, while blue areas are for other polygons]*

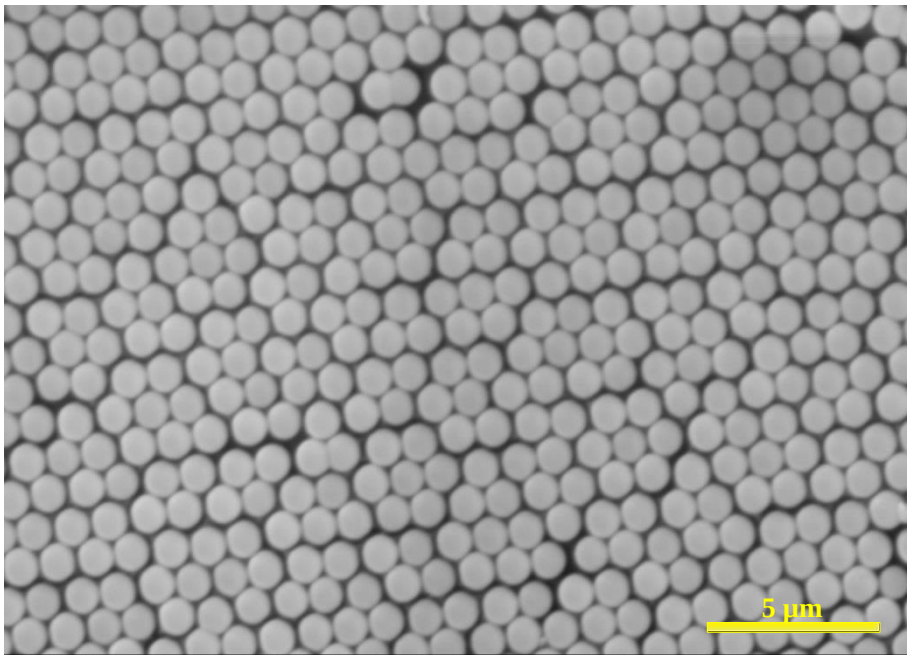

*Figure 4.22: SEM image for monolayer colloidal thin film with a HCP percentage of **84.5 %** obtained from spin coating of 35 wt. % silica colloidal suspension in water-ethanol mixture (1:1) (weight fraction) at 3000 rpm, 2.2 rev.s^{-2} ,120 s spinning and 30 s settling time. Magnification is 4300x.*

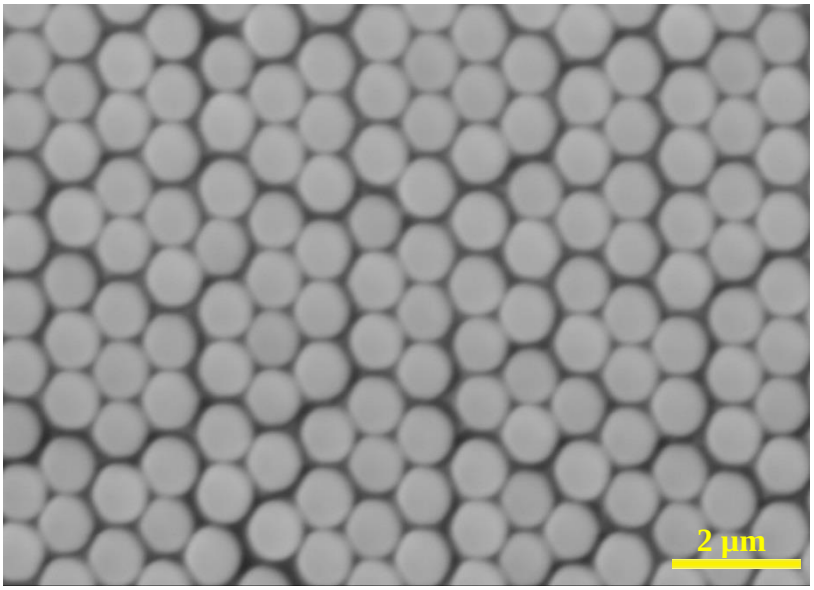

*Figure 4.23: SEM image for monolayer colloidal thin film with a HCP percentage of **84.5 %** obtained from spin coating of 35 wt. % silica colloidal suspension in water-ethanol mixture (1:1) (weight fraction) at 3000 rpm, 2.2 rev.s^{-2},120 s spinning and 30 s settling time. Magnification is 7500x.*

For water – ethanol mixture (3:1), shown in Figure 4.20 (b), it is clearly noticed that introducing ethanol to water leads to the formation of ordered colloidal islands separated by empty holes. This may be attributed to the faster evaporation rate of that mixture with respect to pure water as a solvent, shown in Figure 4.20 (a), where highly ordered colloidal structures formed without the appearance of any air voids. Images for water – ethanol mixture (1:1) given in Figure 4.20 (c) showed the formation of the regular colloidal structure without any empty holes. This colloidal thin film looks similar to that obtained in the case of pure water shown in Figure 4.20 (a). However, LabVIEW analysis, as described in Figure 4.21, showed that monolayer colloidal crystals formed in case of water – ethanol mixture (1:1) (weight fraction) exhibits a hexagonal close-packing percentage of 84.5 % which is significantly higher than that obtained in case of pure water as a solvent (HCP % = 79.6 % as described in Figure 4.19). Hence, water – ethanol mixture (1:1) (weight fraction) developed a liquid medium with an average volatility that helped spherical silica particles to explore the optimum sites to occupy and reorganise themselves properly before complete evaporation of the solvent. As a result, a relatively better colloidal ordering quality obtained at the end of the spin coating process when compared to monolayer colloidal crystals obtained in the case of pure water as a solvent. When ethanol weight fraction was increased in the water – ethanol mixture (1:3) (weight fraction) multilayer colloidal crystal structure was formed as shown in Figure 4.20 (d). Formation of multi-layered colloidal structure in case of water – ethanol mixture (1:3) (weight fraction) as a liquid medium may be attributed to the higher volatility of the mixture developed due to the increased weight fraction of ethanol. As the volatile solvent rate of evaporation increases, solvent layer evaporative thinning takes place faster. This may increase the shear forces induced during rotation of sample at the spin coating process. Excessive shear forces distort the particles reordering forming irregular colloidal structures.

SEM images at a magnification power of 4300 × and 7500 ×, as shown in Figures 4.22 and 4.23 respectively, clarified the formation of highly ordered monolayer colloidal crystals at the end of the spin coating process when using water – ethanol

(1:1) (weight fraction) as a volatile liquid medium. SEM micrographs together with hexagonal close-packing percentages (HCP %) obtained from LabVIEW analysis confirmed that introducing ethanol to water as a liquid medium in the spin coating process significantly affect the colloidal ordering quality of the fabricated colloidal crystals. Hence, volatility of the solvent used in the spin coating process plays an important role in the colloidal self-assembly process that leads to the formation of ordered colloidal crystals.

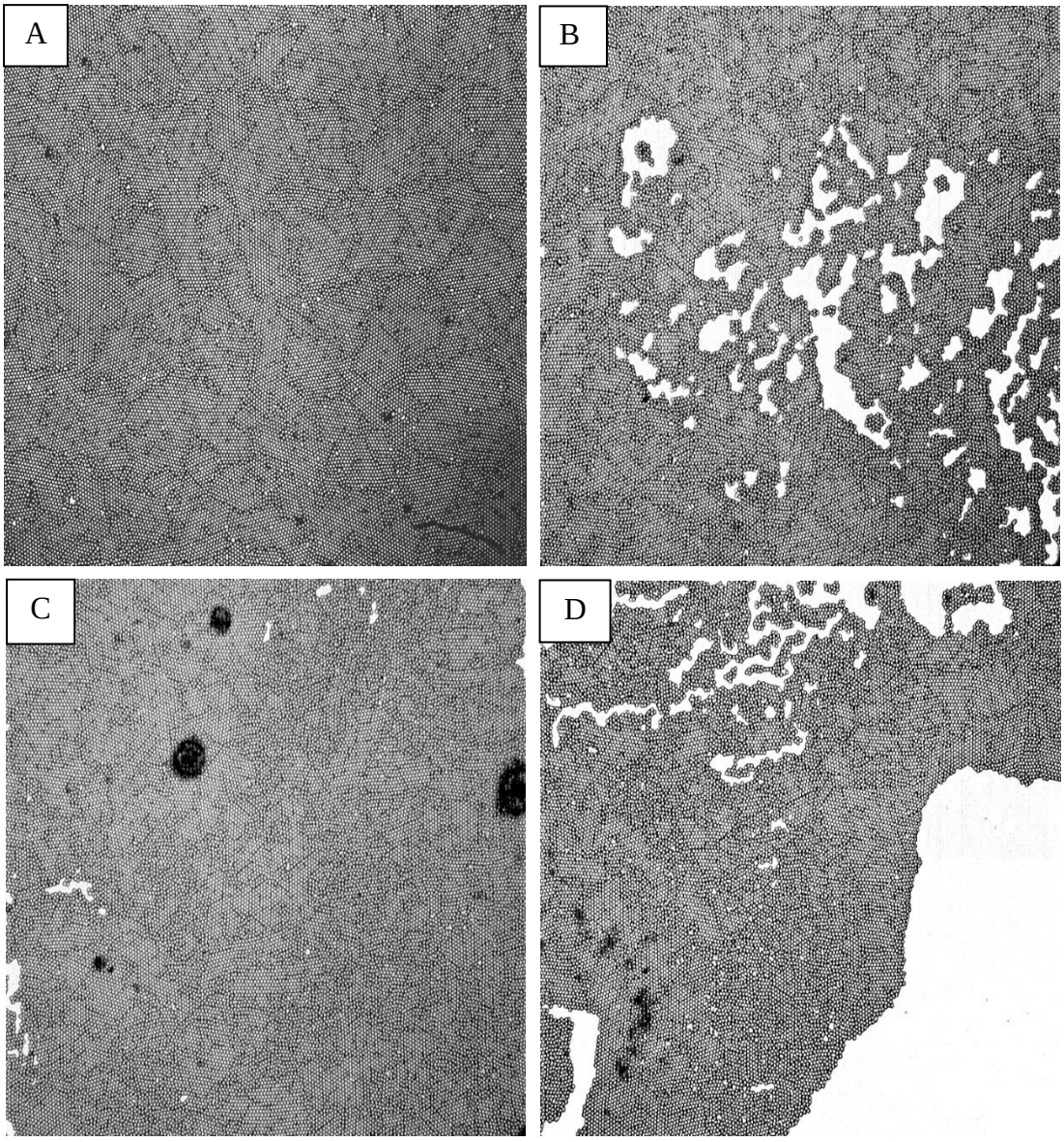

Figure 4.24: Microscopic images for final colloidal crystals of 35 wt. % silica colloidal suspension spun cast at 3000 rpm, 2.2 rev.s^{-2}, 120 s spin time in different liquid solutions; A) pure water, B) water : EG = 3:1, C) water : EG = 1:1, D) water : EG = 1:3.

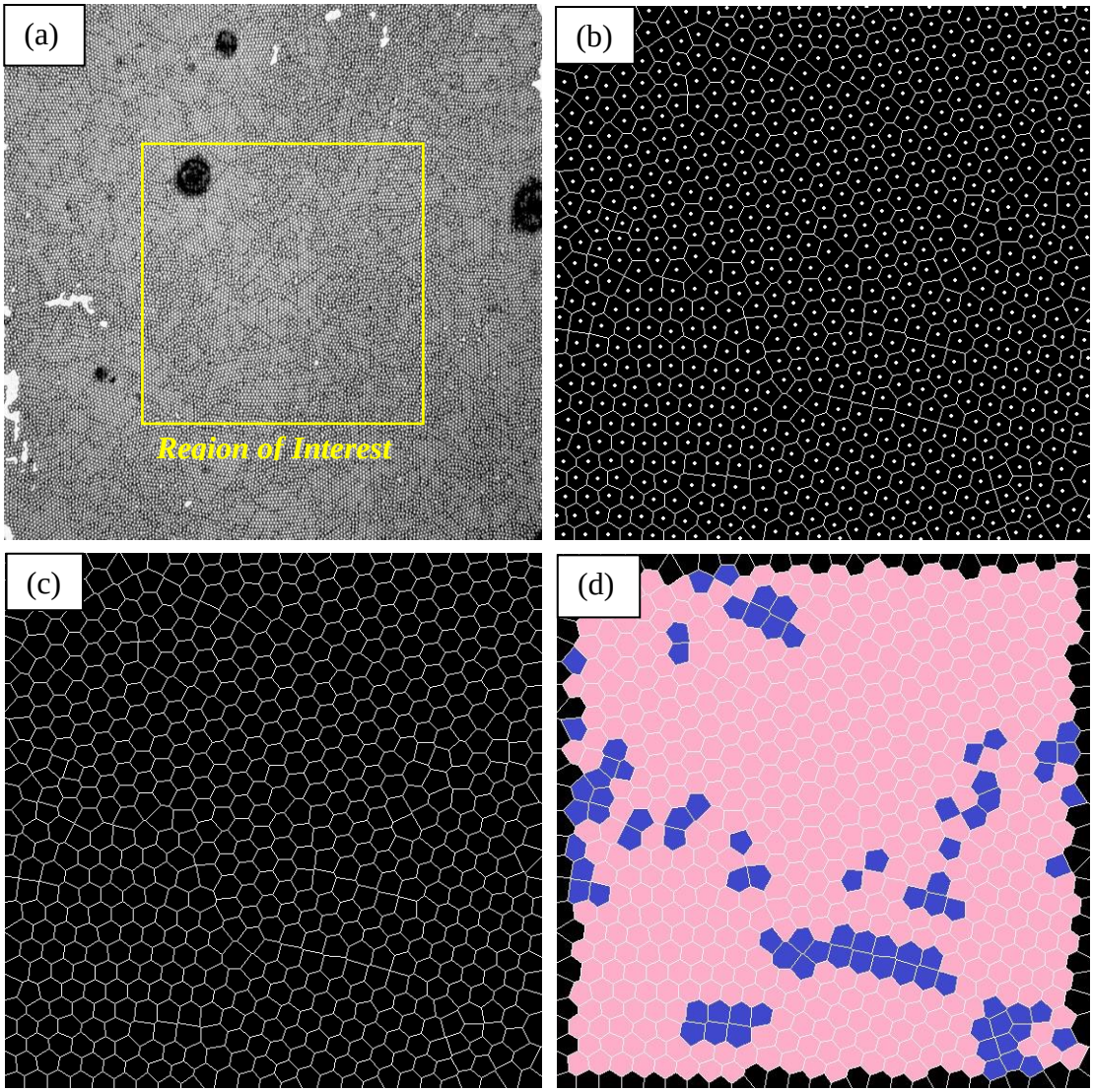

Figure 4.25: Processing of microscopic images through LabVIEW software in order to characterise the ordering quality of the fabricated colloidal crystals in terms of percentage of hexagonal close-packed arrangements; (a) original microscopic image of monolayer colloidal crystal fabricated through spin coating of 35 wt. % colloidal suspension in water: EG = 1:1 mixture spun cast at 3000 rpm, 2.2 rev.s^{-2}, 30 s spin time and after 30 s settling time, (b) Output of connectivity of each particle with the neighbouring in the sample, (c) Connectivity after removal of dots that represent the presence of spherical colloidal particles and (d) Quantifying of hexagonal patterns in the image shows a ***HCP % = 83.8 %*** *[pink areas indicate the hexagonal polygons, while blue areas are for other polygons].*

Microscopic images, shown in Figure 4.24 B, for the fabricated monolayer colloidal crystals formed when water – ethylene glycol mixture (3:1) (weight fraction) was used as a volatile solvent medium showed the formation of ordered structures with the appearance of some empty holes between colloidal aggregates. Area coverage percentage of this colloidal structure was found to be 98.1 %. This high area coverage percentage occupied by colloids on glass substrates may be attributed to the lower evaporation rate of liquid medium induced by the high boiling point of ethylene glycol [b.p = 197.3 ^{o}C]. Unexpectedly, increasing ethylene glycol weight fraction in water – ethylene glycol mixture (1:3), as shown in Figure 4.24 D, lead to the fabrication of a colloidal structure with a relatively low area coverage percentage of 72.9 %. This colloidal structure was characterised by the large empty holes between spherical particles. For water – ethylene glycol mixture (1:1) (weight fraction), shown in Figure 4.24 C, highly ordered monolayer colloidal crystals were observed with an area coverage percentage of 99.3 % and a hexagonal close-packing percentage (HCP %) of 83.8 %. HCP % obtained in this case is relatively higher than the HCP % of 79.6 % which was obtained in the case of pure water only. However, hexagonal close-packing percentage obtained in the case of water – ethylene glycol mixture (1:1) (weight fraction) was found to be less than the percentage of 84.5 % that obtained in the case of water – ethanol mixture (1:1) (weight fraction). These results confirmed that the type of liquid medium used in the spin coating process of colloidal suspensions significantly affects the self-assembly process efficiency and governs the colloidal ordering quality obtained.

Former results were the motivation to investigate the impact of ethanol – ethylene glycol mixture on the colloidal ordering quality through the spin coating process. For ethanol – ethylene glycol mixture (3:1) (weight fraction), shown in Figure 4.26 B, colloidal structure with a low area coverage percentage of 50.6 % was obtained. Interestingly, increasing the ethylene glycol ratio in ethanol – ethylene glycol mixture (1:1) (weight fraction), as shown in Figure 4.26 C, lead to the formation of a colloidal structure with a relatively higher area coverage percentage occupied by colloids of 80.4 %. This may be attributed to the lower rate of evaporation of the second mixture

induced by the high boiling point of ethylene glycol when compared to the boiling point of ethanol [b.p of ethanol = 78 ^{o}C]. For ethanol – ethylene glycol mixture (1:3) (weight fraction), as shown in Figure 4.26 D, a highly ordered colloidal structure was obtained with an area coverage percentage of 99.6 %. LabVIEW analysis, shown in Figure 4.27, showed that colloidal crystals fabricated in the case of using ethanol – ethylene glycol mixture (1:3) (weight fraction) as a solvent exhibited a hexagonal close-packing percentage of 83.8 %. HCP % obtained in the case of ethanol – ethylene glycol mixture (1:3) is the same as that obtained in the case of water – ethylene glycol mixture (1:1). However, HCP % value obtained in case of water – ethanol mixture (1:1) (weight fraction) is still the highest, as shown in Table 4.4, which implies that it is the optimum liquid medium to be used in colloidal suspensions in order to fabricate highly ordered monolayer colloidal crystals with a good ordering quality via spin coating process.

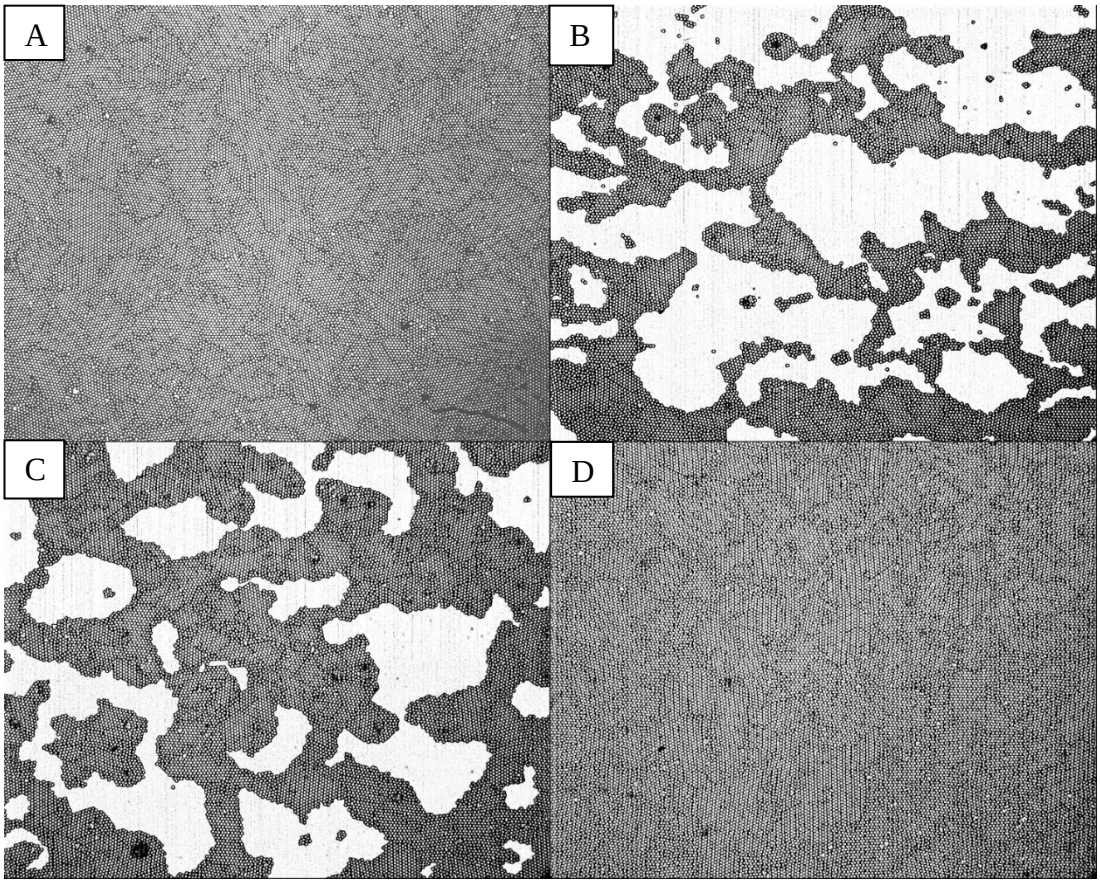

Figure 4.26: Microscopic images for final colloidal crystals of 35 wt. % silica colloidal suspension spun cast at 3000 rpm, 2.2 rev.s^{-2}, 30 s spin time in different liquid solutions; A) pure water, B) Ethanol : EG = 3:1, C) Ethanol: EG = 1:1, D) Ethanol: EG = 1:3.

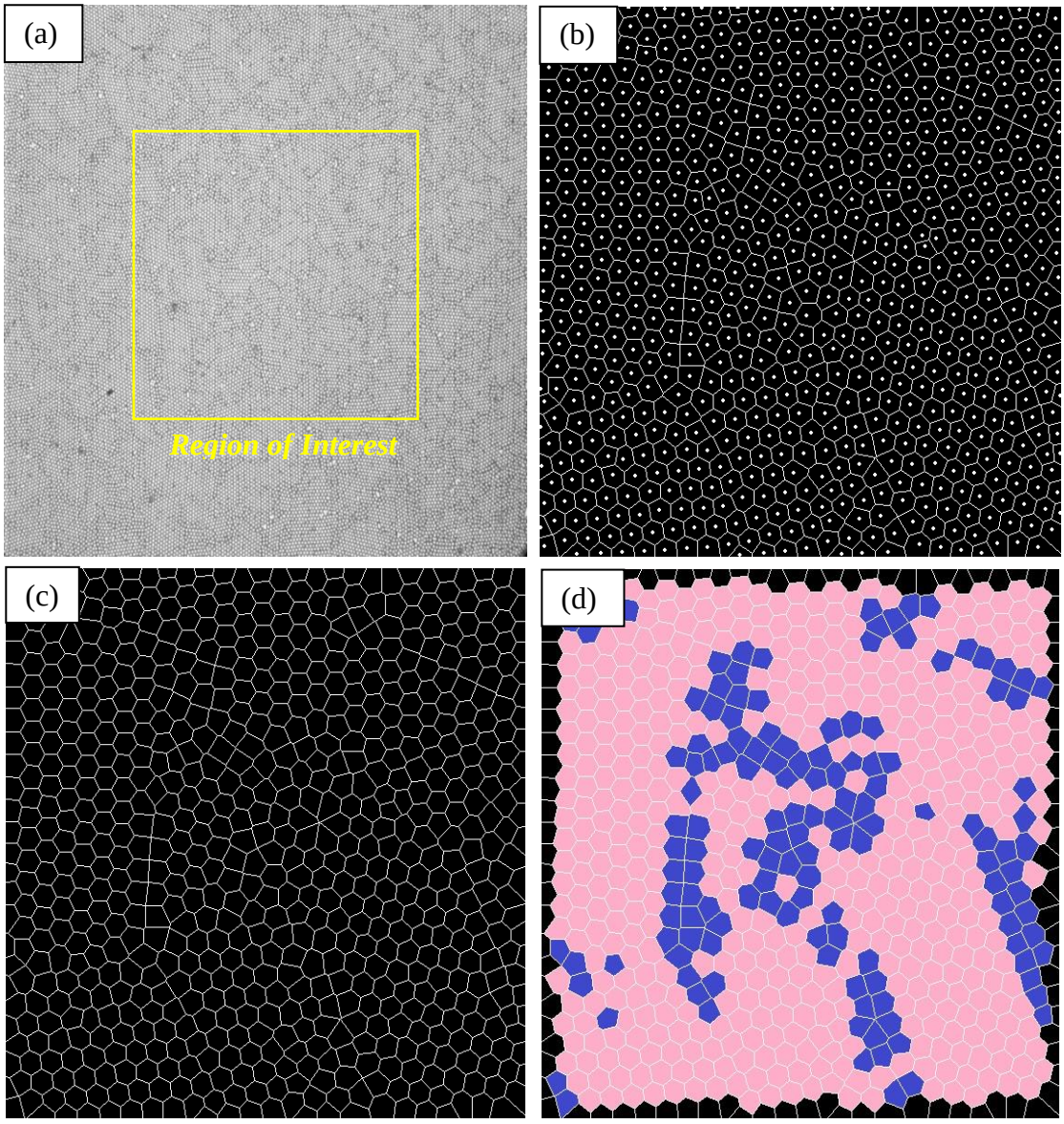

Figure 4.27: Processing of microscopic images through LabVIEW software in order to characterise the ordering quality of the fabricated colloidal crystals in terms of percentage of hexagonal close-packed arrangements; (a) original microscopic image of monolayer colloidal crystal fabricated through spin coating of 35 wt. % colloidal suspension in Ethanol: EG = 1:3 mixture spun cast at 3000 rpm, 2.2 rev.s^{-2}, 30s spin time and after 30 s settling time, (b) Output of connectivity of each particle with the neighbouring in the sample, (c) Connectivity after removal of dots that represent the presence of spherical colloidal particles and (d) Quantifying of hexagonal patterns in the image shows a **HCP % = 83.8 %** *[pink areas indicate the hexagonal polygons, while blue areas are for other polygons].*

Table 4.4: Impact of liquid medium type on the colloidal ordering quality.

Sample No.	Liquid Medium Type	Rotational Speed (rpm)	Acceleration Rate (rev.s-2)	Solid Content, (Wt. %)	HCP %
1	Pure Water	3000	2.2	35 %	79.6
2	Water – Ethanol (1:1)				84.5
3	Water – EG (1:1)				83.8
4	Ethanol – EG (1:1)				83.8

4.6 Effect of polydispersity

The standard deviation of particles size distribution or polydispersity of colloids is an important factor to be considered in the fabrication of monolayer colloidal crystals. As discussed in chapter 1 polydispersity of colloids was found to significantly affect either ordering quality or the domain size of fabricated colloidal thin films. It was reported by Jiang et al. [9] that the standard deviation of colloids is a crucial factor in the ordering quality of the fabricated arrays. They showed that the standard deviation of particle size distribution should be less than 8 % in order to form ordered colloidal crystals with a long domain size. Samples fabricated using colloids with a polydispersity higher than 8 % exhibited a diffuse ring in the Fourier transform. These thin films fabricated using the higher standard deviation particles were white and opaque. On the other hand, samples with a narrow size distribution exhibited sharp peaks in the Fourier transform due to the formation of well-ordered arrays over a long length scale. These colloidal crystals gave brilliant colours when being illuminated with white light due to the highly ordered structure.

In the next series of experiments, the effect of polydispersity of silica colloids on the hexagonal close-packing percentage (HCP %) was studied. To do so, spherical

silica colloids with a particle size of 1275 nm were suspended in pure water at a concentration of 35 wt. %. The prepared solution was used as the original suspension. Six equal portions were taken from that original suspension where different weight fractions of 1550 nm and 1000 nm silica particles were added, as listed in Table 4.5, to change the particle size distribution of the colloidal suspensions before starting the spin coating process. Each colloidal suspension was sonicated continuously for 24 hours to remove any physical aggregations between particles. Then, 100 µL was deposited on a glass substrate. The substrate surface was then rotated at 3000 rpm for 30 s with a fixed acceleration rate of 2.2 rev.s^{-2}. Fabricated colloidal thin films were imaged using a 40× microscopic objective together with an Andor camera with a field of view of 464 × 464 µm and a quantum energy of 60 %. Finally, microscopic images have been processed using LabVIEW software in order to quantify the connectivity between particles in terms of hexagonal close-packing percentage (HCP %) as summarised in Table 4.5.

Table 4.5: Effect of polydispersity of particles on the hexagonal close-packing arrangement.

Sample Number	**Wt. % of 1275 nm silica colloids**	**Wt. % of 1550 nm silica colloids**	**Wt. % of 1000 nm silica colloids**	**HCP %**
1	35 %	---	---	**73.2 %**
2	33.25 %	1.75 %	---	**70.6 %**
3	31.5 %	1.75 %	1.75 %	**66.6 %**
4	29.75 %	3.5 %	1.75 %	**56.0 %**
5	28.0 %	3.5 %	3.5 %	**47.6 %**
6	24.5 %	7.0 %	3.5 %	**47.0 %**
7	21.0 %	7.0 %	7.0 %	**37.7 %**

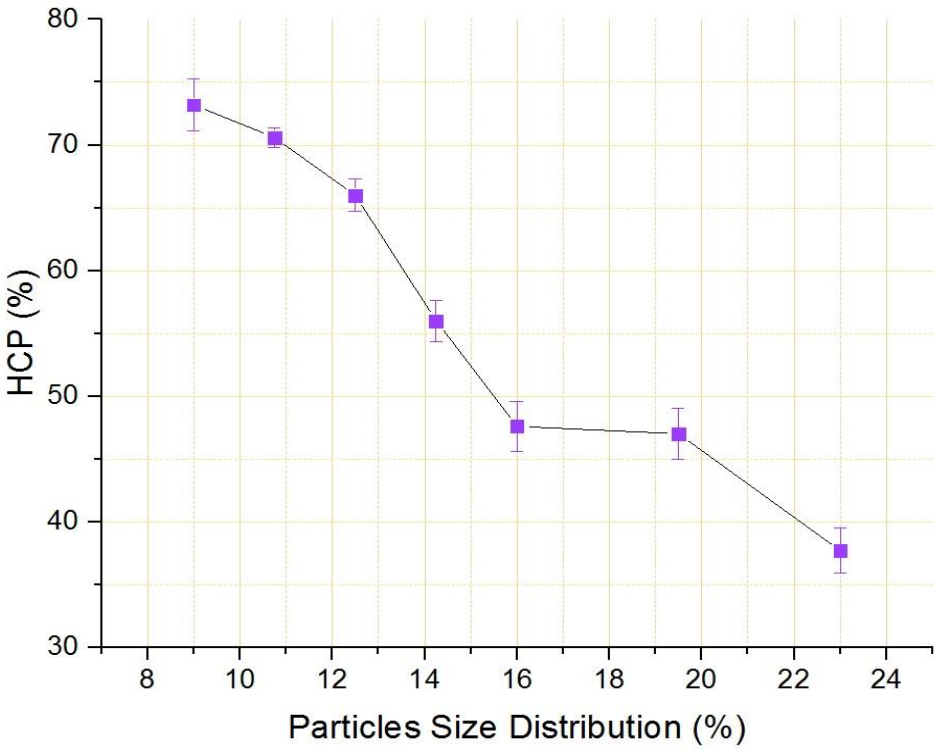

Fig. 4.28: Effect of polydispersity of particles on the hexagonal close-packing arrangement.

As shown in Figure 4.28, it was found that hexagonal close-packing percentages are inversely proportional to the polydispersity of particles. As given in Table 4.5, Hexagonal close-packing percentage value for the original suspension (1275 nm only) was 73.2 %, as shown in Figure 4.29, which is the highest value in this investigation. Once silica particles (1550 nm) with a concentration of 1.75 wt. % were added, colloidal ordering quality decreases forming a colloidal structure with a hexagonal close-packing percentage of 70.6 % as shown in Figure 4.30. The addition of equal concentration of 1.75 wt. % from both 1550 nm and 1000 nm silica particles to the original suspension lead to the formation of colloidal thin films with a hexagonal close-packing percentage of 66.6 % as given in Figure 4.31. Then, as the concentration of 1550 nm and 1000 nm particles added to original suspension increases up to 5.25 %, 7.0 % and 10.5 %, as given in Figures 4.32, 4.33 and 4.34 respectively, hexagonal close-packing percentage was decreased from 56.0 %, 47.6 and 47.0 %. Finally, when the concentration of added silica particles (1550 nm and 1000 nm) reaches 14.0 wt. %, as given in Figure 4.35, hexagonal close-packing percentage becomes 37.7 % which

is the lowest determined value. SEM micrograph showed that presence of particles with a different average size distorts the colloidal ordering, as indicated by yellow circles in Figure 4.36, forming a colloidal structure with a lower colloidal ordering quality.

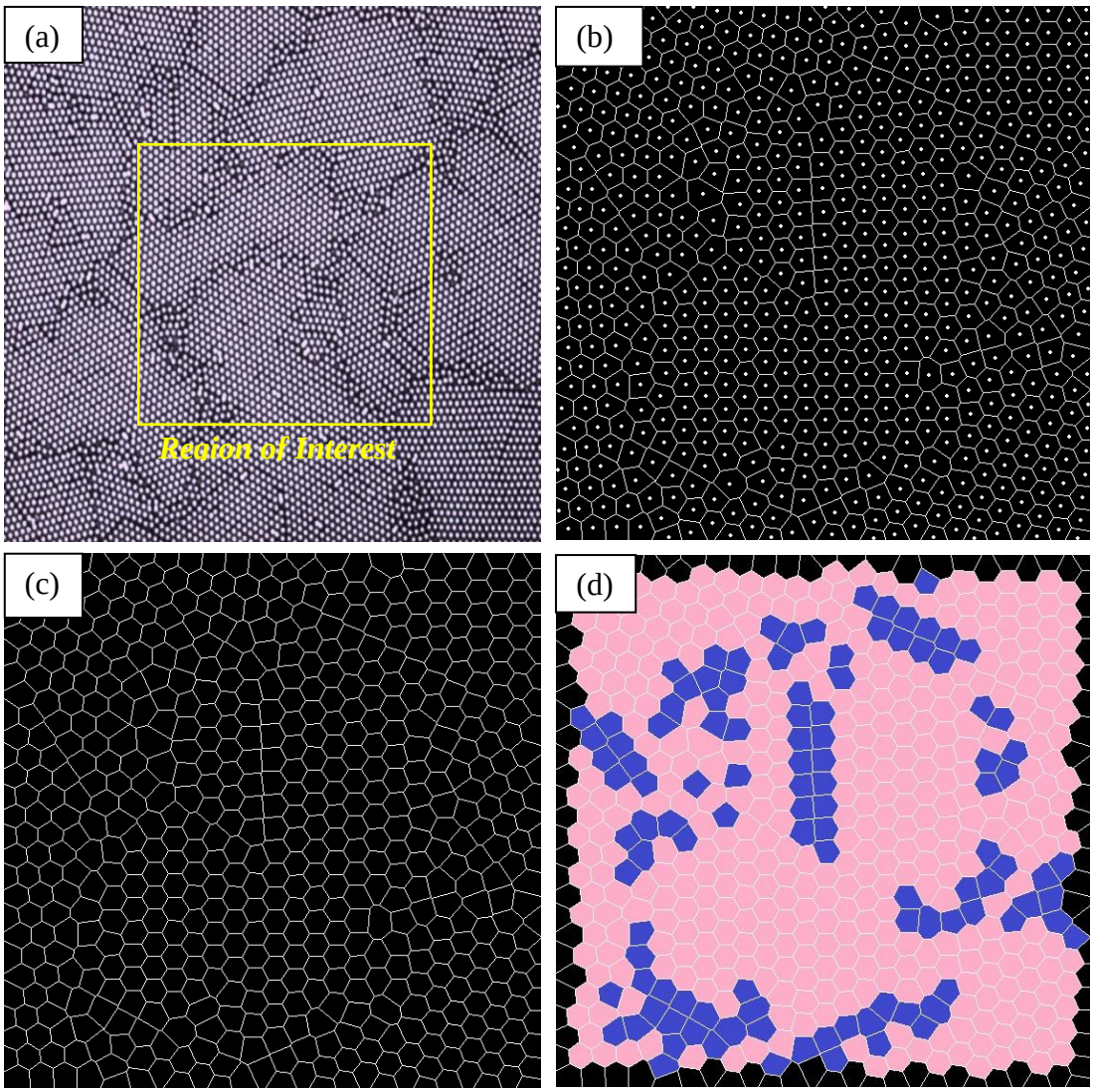

Figure 4.29: Processing of microscopic images through LabVIEW software in order to characterise the ordering quality of the fabricated colloidal crystals in terms of percentage of hexagonal close-packed arrangements; (a) original microscopic image of monolayer colloidal crystal fabricated through spin coating of 1275 nm silica colloids with a 35 wt. % colloidal suspension in water spun cast at 3000 rpm, 2.2 rev.s^{-2}, 30 s spin time and after 30 s settling time, (b) Output of connectivity of each particle with the neighbouring in the sample, (c) Connectivity after removal of dots that represent the presence of spherical colloidal particles and (d) Quantifying of hexagonal patterns in the image shows a **HCP % = 73.2 %** *[pink areas indicate the hexagonal polygons, while blue areas are for other polygons].*

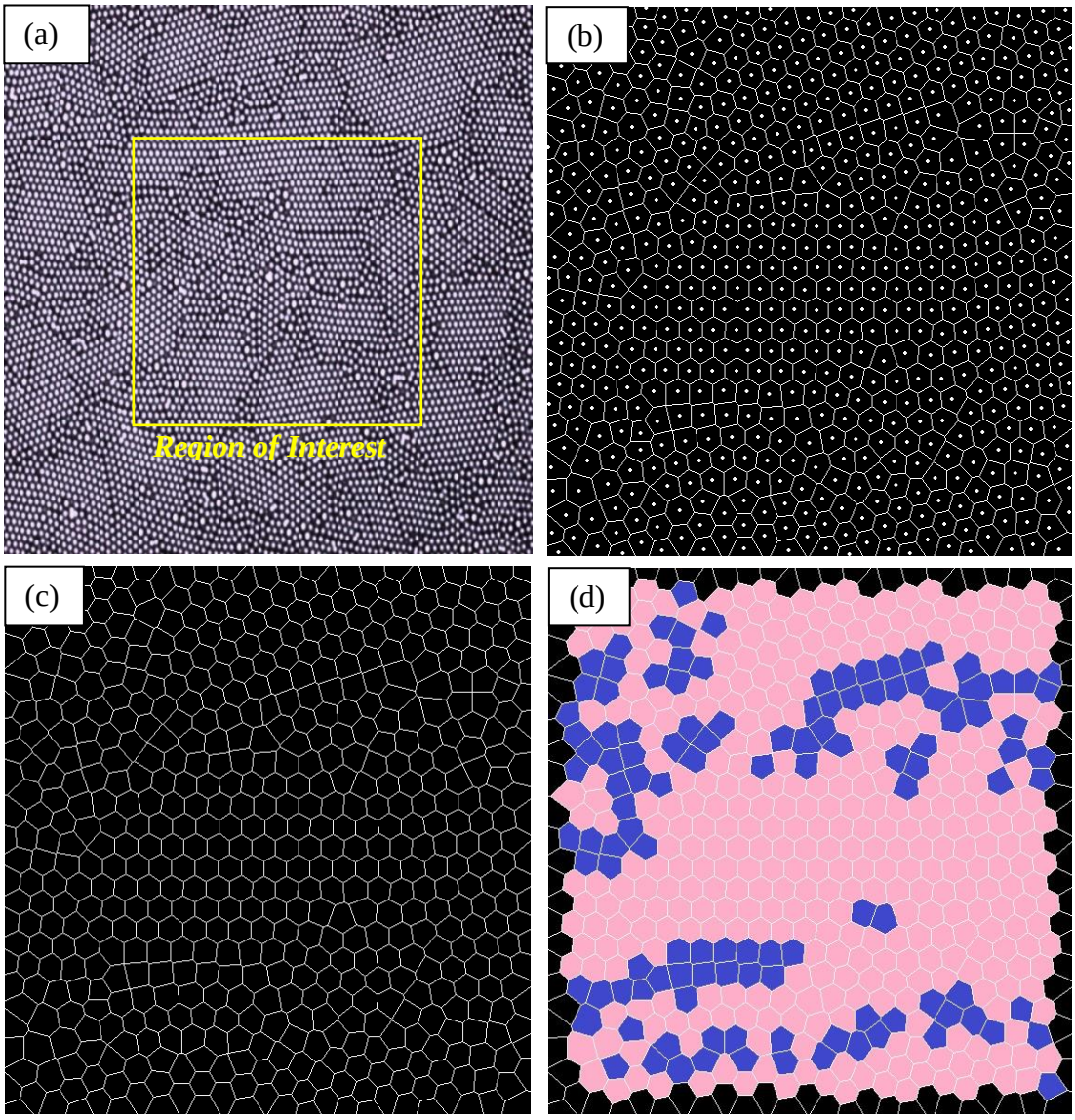

Figure 4.30: Processing of microscopic images through LabVIEW software in order to characterise the ordering quality of the fabricated colloidal crystals in terms of percentage of hexagonal close-packed arrangements; (a) original microscopic image of monolayer colloidal crystal fabricated through spin coating of a 35 wt. % colloidal suspension [33.25 % 0f 1275 nm + 1.75 % of 1550 nm silica colloids] in water spun cast at 3000 rpm, 2.2 rev.s^{-2}, 30 s spin time and after 30 s settling time, (b) Output of connectivity of each particle with the neighbouring in the sample, (c) Connectivity after removal of dots that represent the presence of spherical colloidal particles and (d) Quantifying of hexagonal patterns in the image shows a **HCP % = 70.6 %** *[pink areas indicate the hexagonal polygons, while blue areas are for other polygons].*

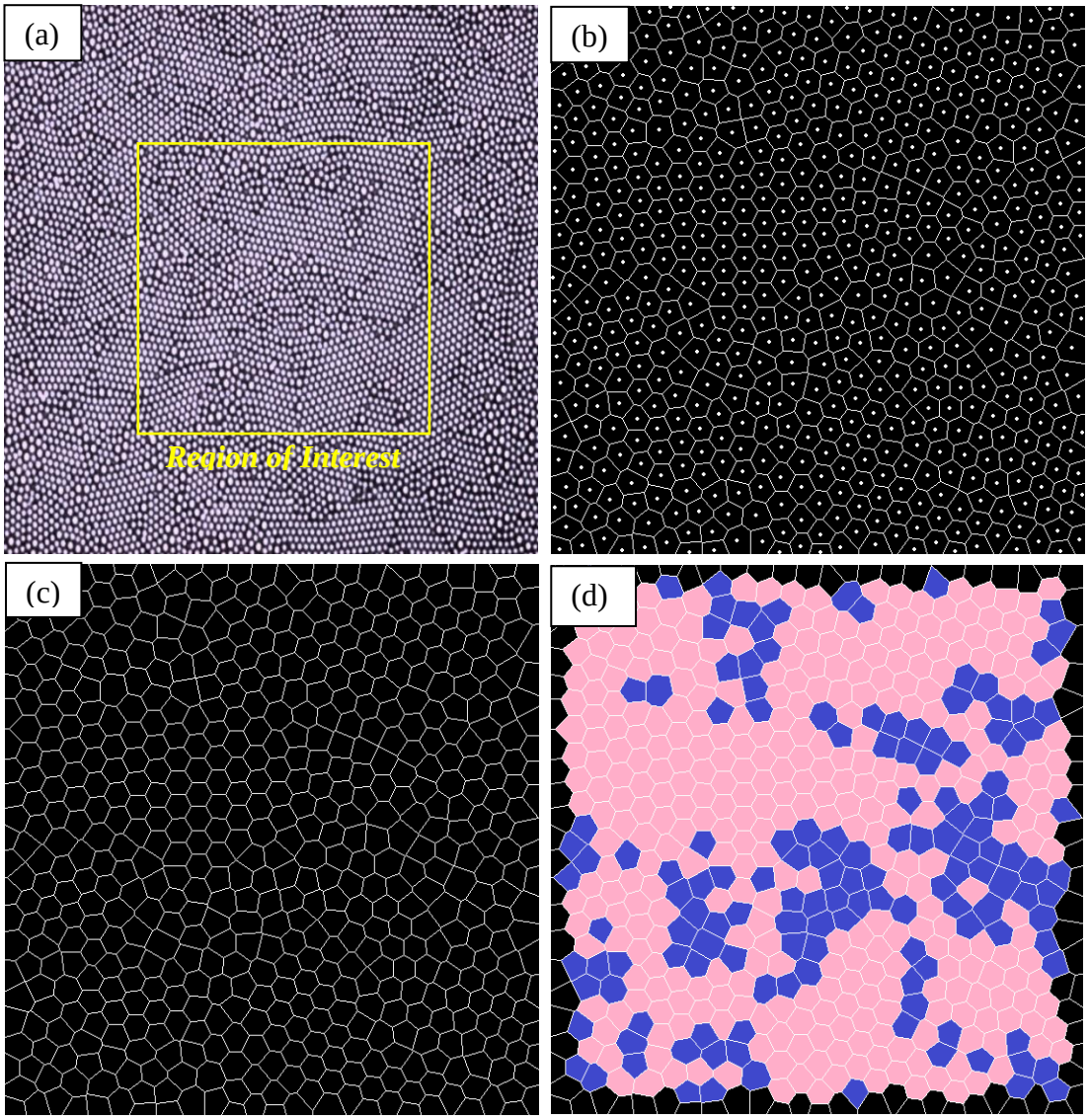

Figure 4.31: Processing of microscopic images through LabVIEW software in order to characterise the ordering quality of the fabricated colloidal crystals in terms of percentage of hexagonal close-packed arrangements; (a) original microscopic image of monolayer colloidal crystal fabricated through spin coating of a 35 wt. % colloidal suspension [31.5 % 0f 1275 nm + 1.75 % of 1550 nm + 1.75 % of 1000 nm silica colloids] in water spun cast at 3000 rpm, 2.2 rev.s^{-2}, 30 s spin time and after 30 s settling time, (b) Output of connectivity of each particle with the neighbouring in the sample, (c) Connectivity after removal of dots that represent the presence of spherical colloidal particles and (d) Quantifying of hexagonal patterns in the image shows a **HCP % = 66.6 %** *[pink areas indicate the hexagonal polygons, while blue areas are for other polygons].*

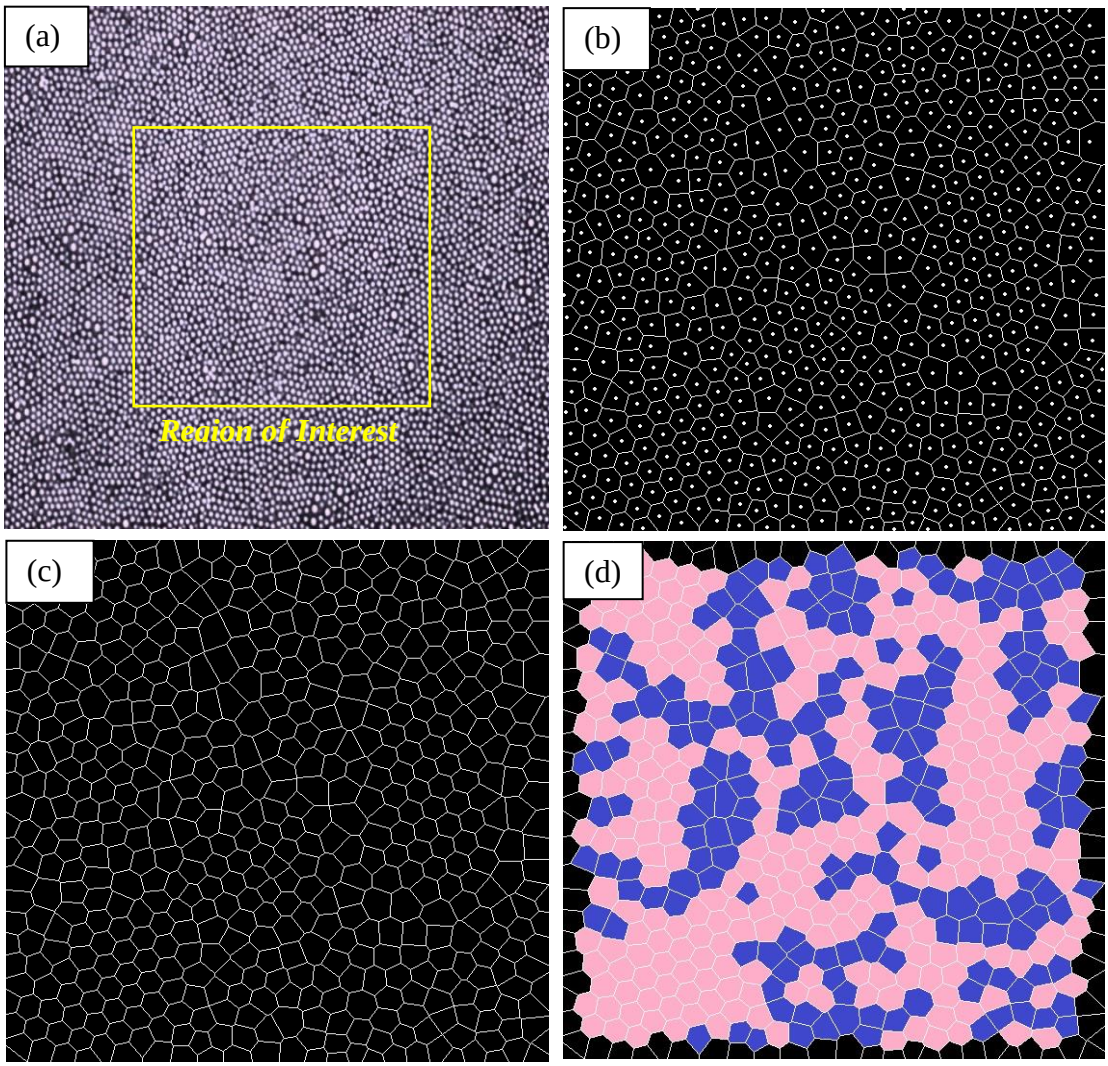

Figure 4.32: Processing of microscopic images through LabVIEW software in order to characterise the ordering quality of the fabricated colloidal crystals in terms of percentage of hexagonal close-packed arrangements; (a) original microscopic image of monolayer colloidal crystal fabricated through spin coating of a 35 wt. % colloidal suspension [29.75 % 0f 1275 nm + 3.5 % of 1550 nm + 1.75% of 1000 nm silica colloids] in water spun cast at 3000 rpm, 2.2 rev.s^{-2}, 30 s spin time and after 30 s settling time, (b) Output of connectivity of each particle with the neighbouring in the sample, (c) Connectivity after removal of dots that represent the presence of spherical colloidal particles and (d) Quantifying of hexagonal patterns in the image shows a **HCP % = 56.0 %** *[pink areas indicate the hexagonal polygons, while blue areas are for other polygons].*

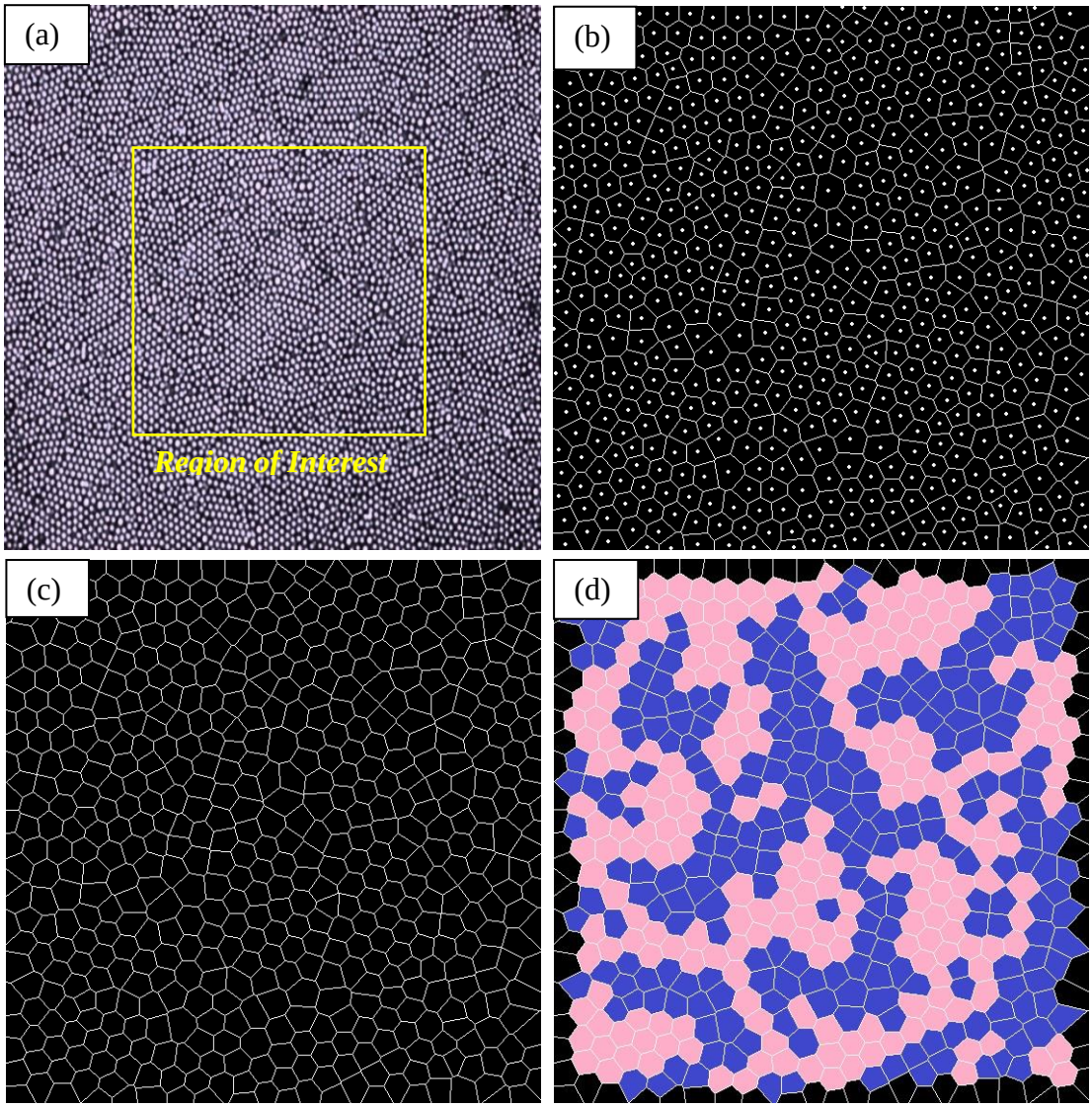

Figure 4.33: Processing of microscopic images through LabVIEW software in order to characterise the ordering quality of the fabricated colloidal crystals in terms of percentage of hexagonal close-packed arrangements; (a) original microscopic image of monolayer colloidal crystal fabricated through spin coating of a 35 wt. % colloidal suspension [28.0 % 0f 1275 nm + 3.5 % of 1550 nm + 3.5 % of 1000 nm silica colloids] in water spun cast at 3000 rpm, 2.2 rev.s^{-2}, 30 s spin time and after 30 s settling time, (b) Output of connectivity of each particle with the neighbouring in the sample, (c) Connectivity after removal of dots that represent the presence of spherical colloidal particles and (d) Quantifying of hexagonal patterns in the image shows a **HCP % = 47.6 %** *[pink areas indicate the hexagonal polygons, while blue areas are for other polygons].*

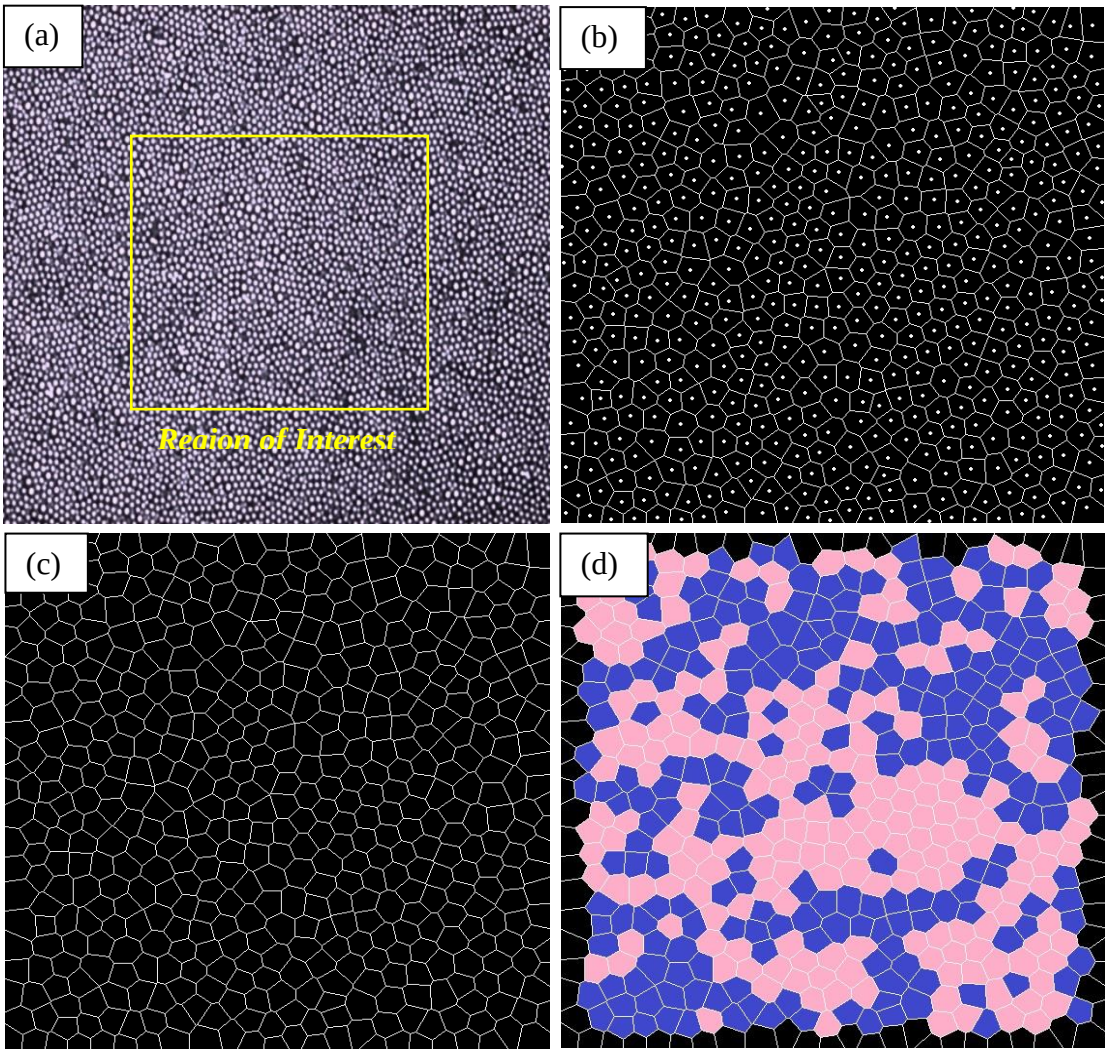

Figure 4.34: Processing of microscopic images through LabVIEW software in order to characterise the ordering quality of the fabricated colloidal crystals in terms of percentage of hexagonal close-packed arrangements; (a) original microscopic image of monolayer colloidal crystal fabricated through spin coating of a 35 wt. % colloidal suspension [24.5 % 0f 1275 nm + 7.0 % of 1550 nm + 3.5 % of 1000 nm silica colloids] in water spun cast at 3000 rpm, 2.2 rev.s^{-2}, 30 s spin time and after 30 s settling time, (b) Output of connectivity of each particle with the neighbouring in the sample, (c) Connectivity after removal of dots that represent the presence of spherical colloidal particles and (d) Quantifying of hexagonal patterns in the image shows a **HCP % = 47.0 %** *[pink areas indicate the hexagonal polygons, while blue areas are for other polygons].*

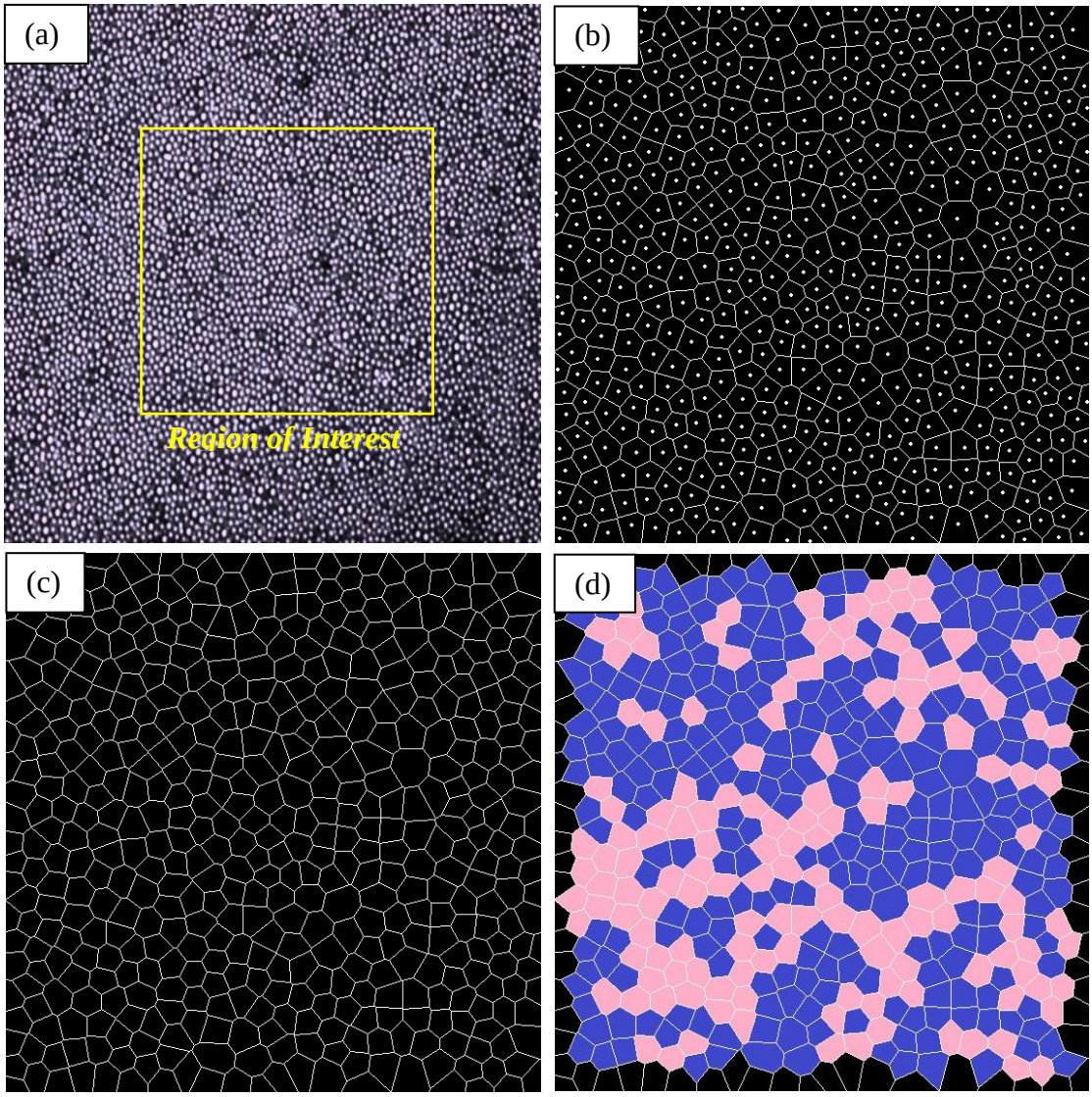

Figure 4.35: Processing of microscopic images through LabVIEW software in order to characterise the ordering quality of the fabricated colloidal crystals in terms of percentage of hexagonal close-packed arrangements; (a) original microscopic image of monolayer colloidal crystal fabricated through spin coating of a 35 wt. % colloidal suspension [21.0 % 0f 1275 nm + 7.0 % of 1550 nm + 7.0 % of 1000 nm silica colloids] in water spun cast at 3000 rpm, 2.2 rev.s^{-2}, 30 s spin time and after 30 s settling time, (b) Output of connectivity of each particle with the neighbouring in the sample, (c) Connectivity after removal of dots that represent the presence of spherical colloidal particles and (d) Quantifying of hexagonal patterns in the image shows a **HCP % = 37.7 %** *[pink areas indicate the hexagonal polygons, while blue areas are for other polygons].*

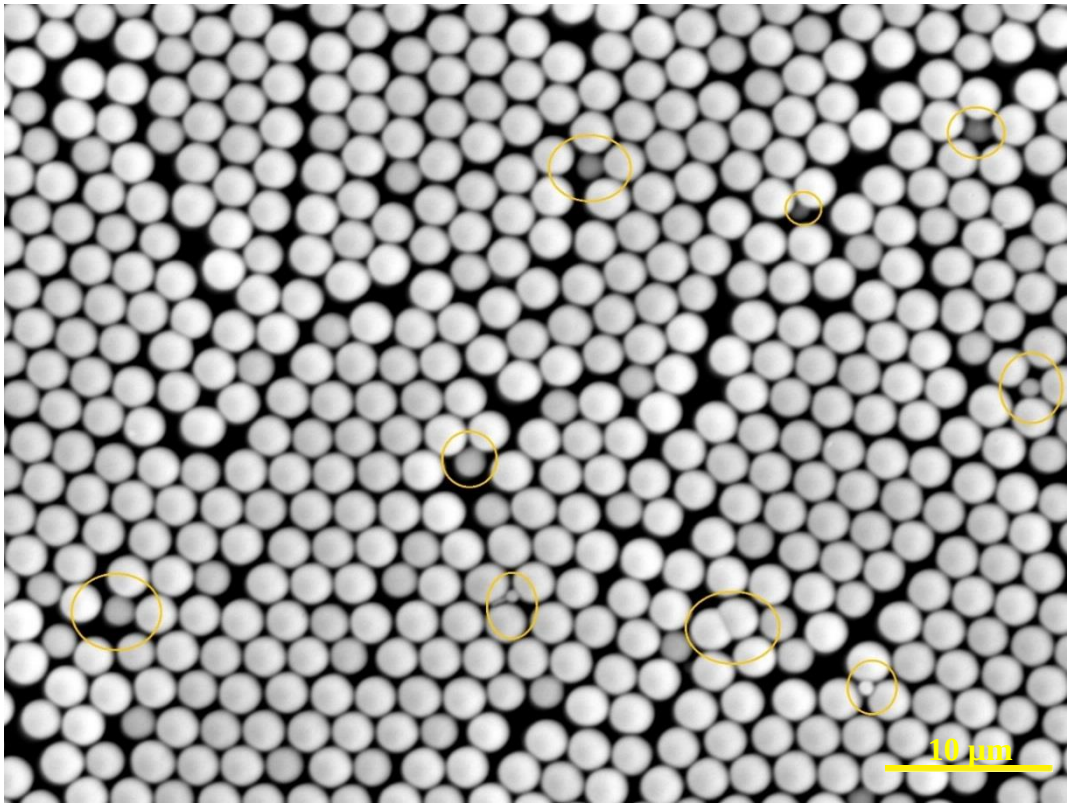

Figure 4.36: SEM image for colloidal thin film fabricated from spin coating a 35 wt. % colloidal suspension [33.25 % 0f 1275 nm + 1.75 % of 1550 nm silica colloids] in water spun cast at 3000 rpm, 2.2 rev.s^{-2}, 30 s spin time and after 30 s settling time showing the distorting effect of smaller particles that leads to the appearance of cracks and dislocations in the final colloidal crystals.

4.7 Optimisation of spin coating process parameters

Based upon the results concluded from studying the impact of rotation speed, acceleration rate, settling time, solute concentration, solvent type and polydispersity of particles on the quality of colloidal ordering in fabricated colloidal thin films obtained from spin coating process, it was able to optimise all these crucial factors in order to develop a simple and controllable spin coating process to fabricate highly ordered, defects-free monolayer colloidal crystals. Spin coating silica colloids suspended in water – ethanol mixture (1:1) (weight fraction) after 30 s settling time at 3000 rpm, 2.2 rev.s^{-2} and 30 s spin time leads to the formation of highly ordered

colloidal structure, as shown in Fig. 4.29, with a hexagonal close-packing percentage of 84.5 %.

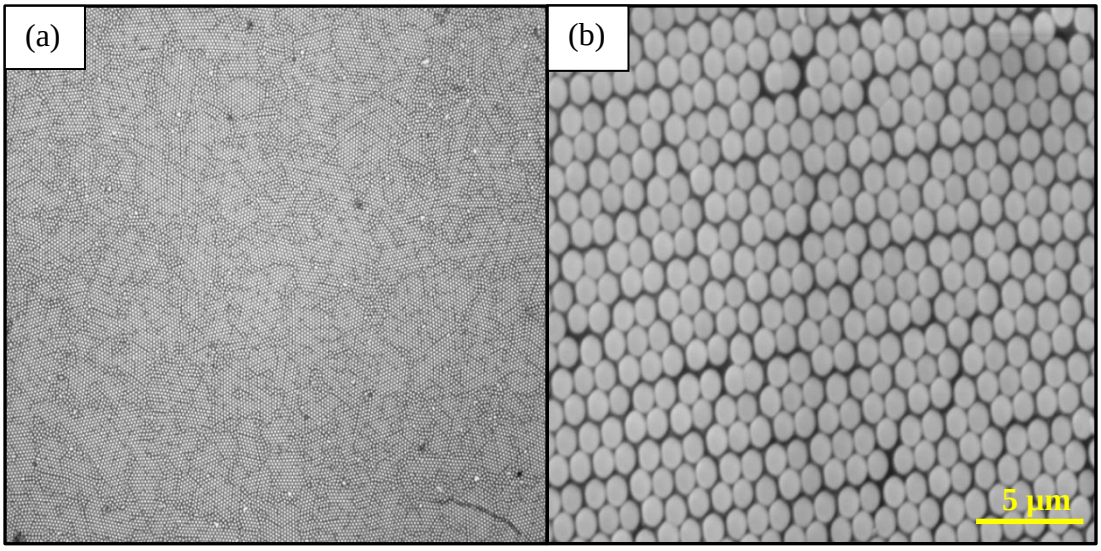

Figure 4.37: Monolayer colloidal crystals fabricated after optimisation of spin coating process at 3000 rpm, 2.2 rev.s^{-2} and 30 s spin time for 35 wt. % 1550 nm silica spherical particles suspended in water – ethanol mixture (1:1) (weight fraction), (a) microscopic image captured through a 40 × objective and (b) SEM micrograph for the same sample with a magnification of 4300 ×.

Chapter 5.
In-Situ Studies of the Rotational Speed Effect in Spin Coating

5.0 Introduction

As shown in section 3.1, changing the rotational speed had a significant effect on the morphology of the final colloidal crystals fabricated at the end of the spin coating process. Rotational speed is significantly affecting the solvent evaporation rate and hence controlling the time available for colloidal particles to explore the optimum sites to occupy during spinning. Optimising the designated rotational speed helped to minimise the dislocations and defects density forming highly ordered monolayer colloidal crystals. However, these investigations were unable to explain what was exactly happening in real-time and how changing the spinning speed affects the mechanism of colloidal ordering during the spin coating process.

In this chapter, I have used the *in-situ* laser scattering set-up (as described in section 2.1.2) to record and analyse the laser scattering patterns collected in real-time during spin coating of 1.5 µm silica colloidal suspensions in pure water. These *in-situ* patterns enabled to track the colloidal self-assembly that took place during spin coating process starting from the deposition of the colloidal suspension on a substrate until the formation of the final thin film. This achievement provides a deep insight into the sophisticated spin coating process of colloidal suspensions. This insight significantly helps to develop a better understanding of how these ordered colloidal structures form during spin coating.

5.1 Experimental Work

Silica spherical particles with an average particle diameter of 1550 nm and 1.228 particle size distribution (measured by Nano-Sight) were purchased from Pinfire - Gems & Colloids Company, Germany. Silica spherical particles as purchased were suspended in pure Ethanol and sonicated for 30 minutes. Sonicated solution was dried overnight at a temperature of 80^{o}C. Dried colloids were then smashed gently using a pestle and mortar. This procedure was repeated three times to ensure the complete removal of any physical aggregations between particles. The silica colloids were then suspended in pure water to prepare a 25 wt. % silica colloidal suspension. The colloidal

solution was then sonicated continuously for 24 hours to ensure uniform distribution of particles in water.

Round glass coverslips, (30 mm diameter No.2) were purchased from VWR International Ltd, have been used as the substrate. Glass coverslips were chemically cleaned followed by Piranha cleaning (as described in section 2.1.1.2) to remove any impurities and to increase their hydrophilicity prior to spin coating. Cleaned glass substrate then adhered to the top of the hollow U8 pro motor shaft; that acts as the spin coater. 100 µL of the colloidal suspension was deposited on the glass substrate, and the setup door was then closed. Once door closes, the laser beam shines towards the colloidal suspension sample through the hollow DC motor (as described in section 2.1.2). Then, the motor was used to drive the substrate to move at a designated speed. Simultaneously, Andor's Zyla 5.5 sCMOS camera starts to record the laser scattering patterns collected on the screen once laser beam becomes on. Data gathered during the spin coating process using Andor camera took place at 2000 exposures at a fast frame rate of 29.0 fps, corresponds to 68.96 s. Recorded movies obtained from the *in situ* laser scattering setup were then processed using LabVIEW software as previously discussed in section 2.2.3 in order to enable tracking of the real-time impact of changing rotational speed on the colloidal self-assembly mechanisms during the spin coating process.

An example of the resultant *in-situ* charts during spin coating of silica colloidal suspensions is given in Figure 5.1. Combining both Unwrapping data, shown in figure 5.1 (b), together with the 2D - average radial integrations, shown in figure 5.1 (c), enabled us to develop the final chart, illustrated in figure 5.1 (a). These pictures enable to distinguish each main stage along the spin coating process clearly. As showed in Figure 5.1 (a), no structure is obtained for the static fluid at the early stage before spinning starts. This confirms the random distribution of spherical silica particles in the solution. The onset of the motor spinning is easily recognised which is followed by a decrease in the intensity regarding the shear thinning stage. The shear thinning stage is governed by the shear forces induced by the rotational motion of the colloidal suspension. Evaporative thinning stage dominates afterwards due to the strong action

of water evaporation that exceeds the shear forces action at this point. The evaporative thinning stage continues until a sudden increase in intensity observes. This sudden increase in intensity indicates the onset of the structure formation of the final colloidal monolayer thin film. Afterwards, intensity remains constant due to the formation of the final scattering ring. This indicates the end of the spin coating of the colloidal suspension. An Eclipse LV100 optical microscope connected to an Andor camera (Zyla 5.5 sCMOS) was used to capture an image for the final monolayer colloidal thin film after the end of the spin coating process. Microscopic images were taken using 40 × Nikon CFI S Plan Fluor ELWD objective. Scanning electron microscopy (SEM, JOEL JSM-6010LA) was used to develop a higher-resolution imaging for solid surfaces needed to effectively characterise the packing quality of colloidal crystals at the end of the spin coating process. Figures 5.1 (d) and Figure 5.1 (e) show the microscopic image together with its Fourier Transform (FFT) and the SEM micrograph of the final colloidal thin film respectively.

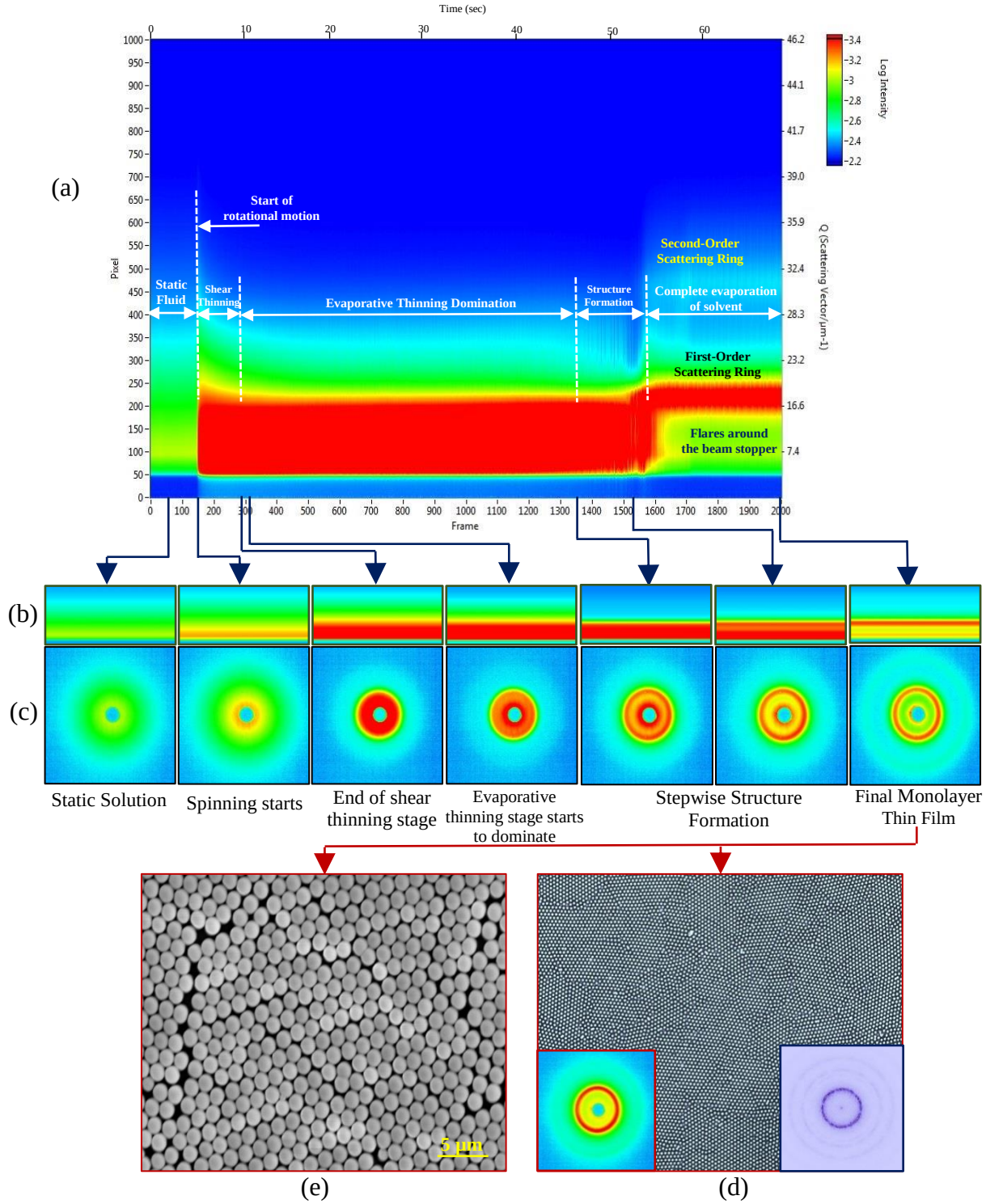

Figure 5.1: a) Combined laser scattering chart collected from the laser scattering setup for silica colloidal suspension during spin coating process at 500 rpm, b) Unwrapped data, c) 2D-radial intergration patterns, d) Microscopic image for final thin film together with its FFT (on the right) and in-situ laser scattering patttern (on the left) and e) SEM micrograph for the same

5.2 Results and discussions

In-situ data for the 25 wt. % silica colloidal suspension in water spun cast at 500 rpm (given in Figure 5.2 and Figure 5.3 accompanying movie https://youtu.be/jQ6nsXig1KU) shows that initially, after deposition of colloidal suspension on the substrate, no conventional laser scattering patterns appear. This is an indication of the random distribution of silica colloids in the solution. Once spinning starts, a very bright diffuse circle appears at 0.03 s regarding the emergence of shear forces due to rotational motion. The bright circle continues to expand in size accompanied by an increase in intensity until 0.24 s. At 0.24 s, the diameter of the diffuse ring becomes fixed. Between 0.24 – 4.55 s, no changes observed where shear forces were in the balance with gravitational force and solvent was still in the liquid form. Once solvent evaporation starts to dominate at 4.55 s, the diffuse ring shrinks gradually towards the centre governed by evaporative thinning. Between 45.31 – 50.24 s, a stepwise evolution of the final scattering ring can be clearly observed. Finally, at 50.24 s a sharp laser scattering ring forms after complete evaporation of the solvent. The sharp ring is an indication of the complete self-assembly of colloids at the end of the spin coating forming the final monolayer colloidal crystals. Figure 5.12 (a) shows the microscopic image captured for the final thin film after the end of spin coating. The similarity between the *in situ* laser scattering ring, obtained from our laser setup, and The Fourier Transform (FFT) shows the accuracy of the setup. Figure 5.1 (e) shows the SEM micrograph of the same sample at a magnification power of 4300×. SEM image confirms the highly ordering quality of the monolayer thin film fabricated at these conditions. These results coincide with our *ex-situ* stage results shown in chapter 4.1.

The 25 wt. % silica colloidal suspension spun cast at 1000 rpm (shown in Figure 5.4 and Figure 5.5 accompanying movie https://youtu.be/qAraaB8LSeE) initially, behaves in a similar manner to the 25 wt. % silica colloidal suspension spun cast at 500 rpm at the early stages. However, the shift from shear thinning to the evaporative thinning starts earlier at 0.76 s. Earlier domination of the evaporative thinning indicates that water evaporates at a higher rate regarding the faster-spinning speed. This induces

an excessive wetting power that limits the time available for the colloidal self-assembly process. In addition, evaporative thinning stage took 22.0 s while it took 45.69 s in case of spin coating at 500 rpm, which confirms the faster evaporation rate at 1000 rpm. Structure formation stage started at 19.31 s and took 3.45 s, and the final scattering rings were formed at 22.76 s. The microscopic image given in Figure 5.12 together with its FFT confirms the lower colloidal ordering quality of this sample when compared to that fabricated when spin coating the same sample at 500 rpm.

Figures 5.6 - 5.9 accompanying movies https://youtu.be/kb2N79Hf0XU and https://youtu.be/kc4UrmezF9A show the stepwise evolution of laser scattering patterns obtained when spin coating a 25 wt. % silica colloidal suspension in water at 2000 rpm and 3000 rpm respectively. *In situ* laser scattering charts showed an earlier shift from shear thinning to the evaporative thinning at 0.62 s and 0.59 s at 2000 rpm and 3000 rpm respectively. Duration of the evaporative thinning stage in case of spinning at 2000 rpm was 12.45 s while it was found to be 8.69 s in case of spinning at 3000 rpm. Structure formation stage starts at 11.0 s, and its duration was found to be 2.31 s when spinning at 2000 rpm, while it was observed that structure formation in the case of spinning at 3000 rpm started at 8.14 s and took only 1.03 s until the formation of the final stable scattering ring. These results confirmed that increasing rotational speed increases the rate of evaporation of water. As the rate of evaporation increases, the evaporative thinning stage took place in a shorter duration. As water layer thickness thins, particles become closer to each other. Smaller particle-particle distances limit the particles manoeuvre and decrease the colloidal ordering quality during self-assembly process. Microscopic images given in Figure 5.12 show the difference in coverage area regarding the rotational speed used during the spin coating process.

In situ data for the 25 wt. % silica colloidal suspension spun cast at 4000 rpm (shown in Figures 5.10 and 5.11, accompanying movie https://youtu.be/MhQNg5vh9Vc) shows that similarly shear thinning stage starts at 0.03 s. The shift from shear to evaporative thinning starts at 0.48 s earlier than all the previous samples spun cast at lower rotational speeds. Evaporative thinning stage

dominates for 5.97 s between 0.48 – 6.55 s. The structure formation observed between 6.28 – 6.55 s. As expected, spin coating the colloidal suspension sample at 4000 rpm, the fastest spinning speed in this set of experiments, developed the shortest evaporative thinning stage. Consequently, water evaporated very quickly in comparison with other samples. This explains the formation of a monolayer colloidal thin film with the lowest area coverage percentage of 50 % as explained in section 4.1.

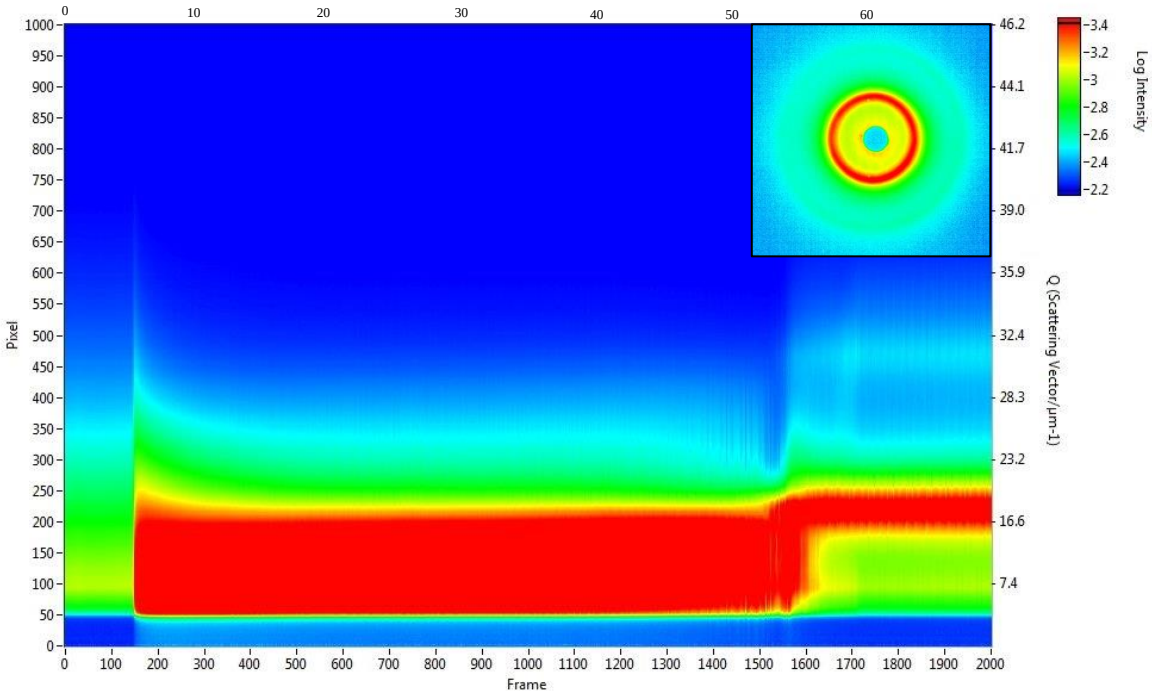

Figure 5.2: In Situ laser scattering charts collected during spin coating of 25 wt. % silica colloidal suspension at 500 rpm.

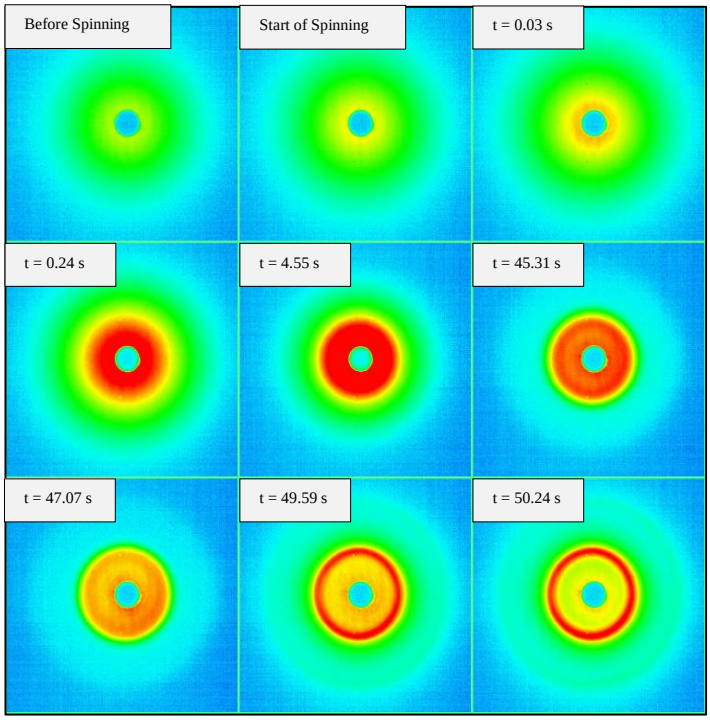

Figure 5.3: In Situ laser scattering patterns collected during the spin coating of the 25 wt.% silica colloidal suspension at 500 rpm.

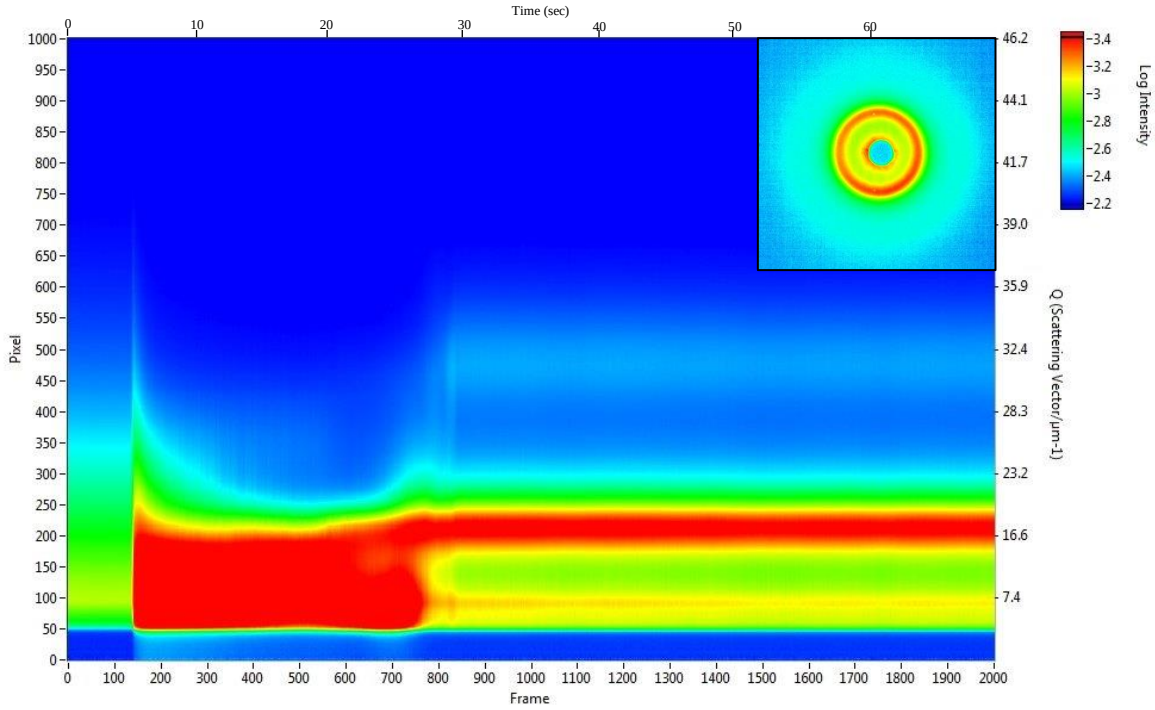

Figure 5.4: In Situ laser scattering charts collected during spin coating of 25 wt. % silica colloidal suspension at 1000 rpm.

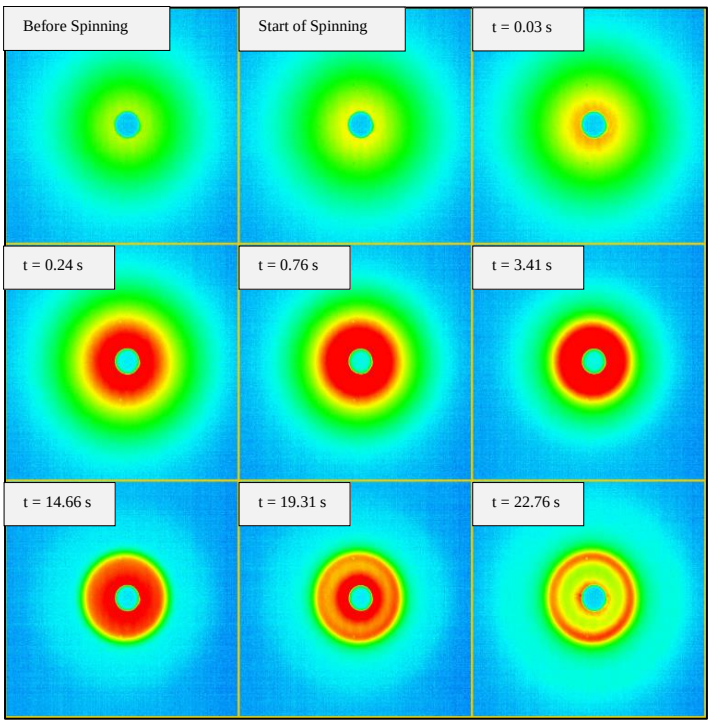

Figure 5.5: In Situ laser scattering patterns collected during the spin coating of the 25 wt. % silica colloidal suspension at 1000 rpm.

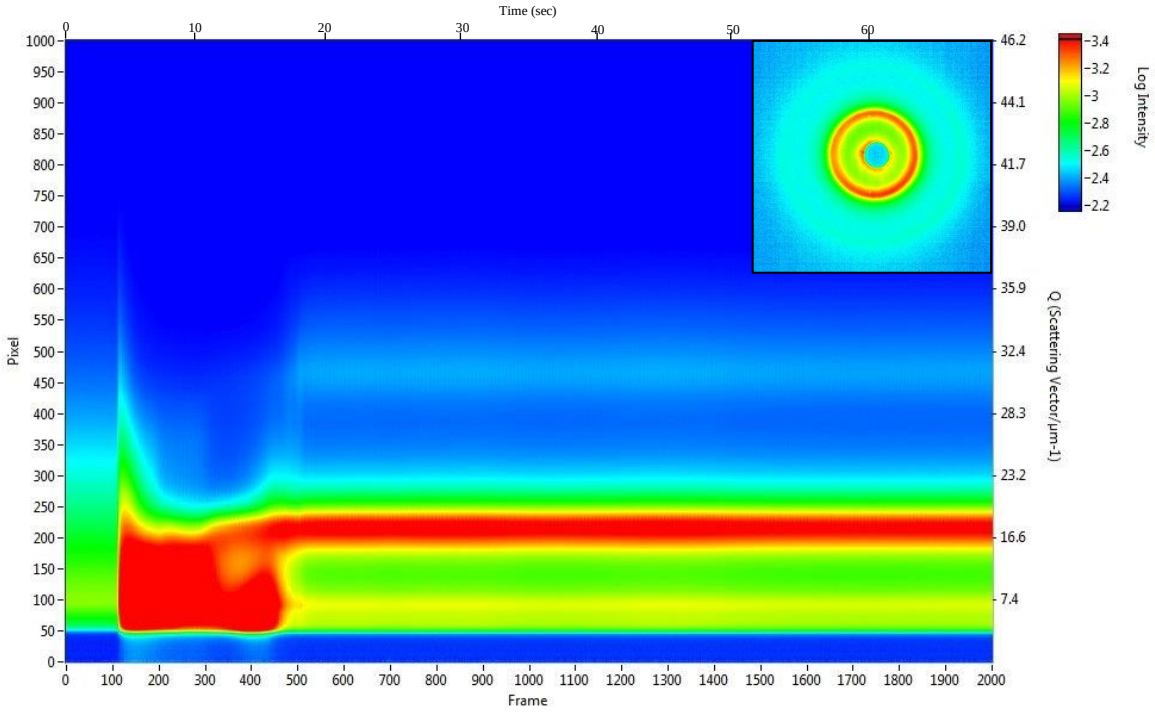

Figure 5.6: In Situ laser scattering charts collected during spin coating of 25 wt. % silica colloidal suspension at 2000 rpm.

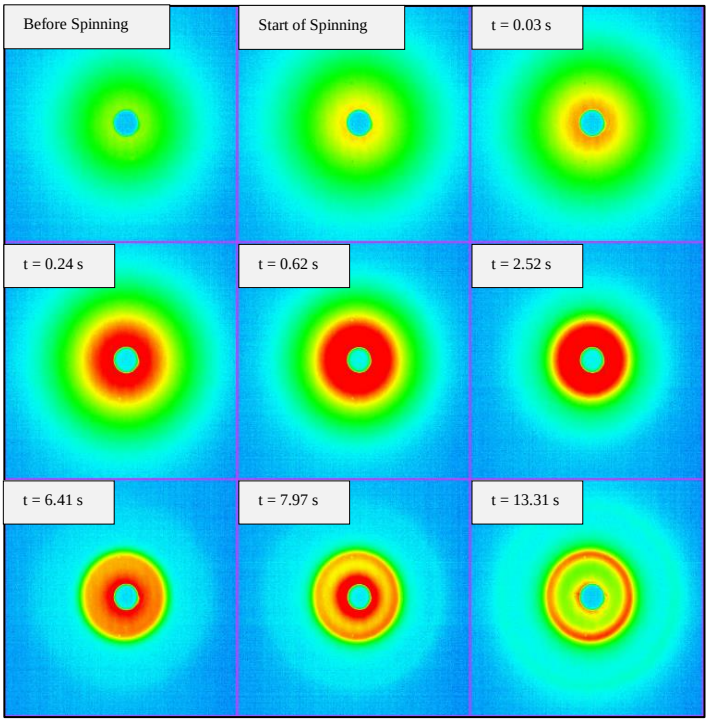

Figure 5.7: In Situ laser scattering patterns collected during the spin coating of the 25 wt.% silica colloidal suspension at 2000 rpm.

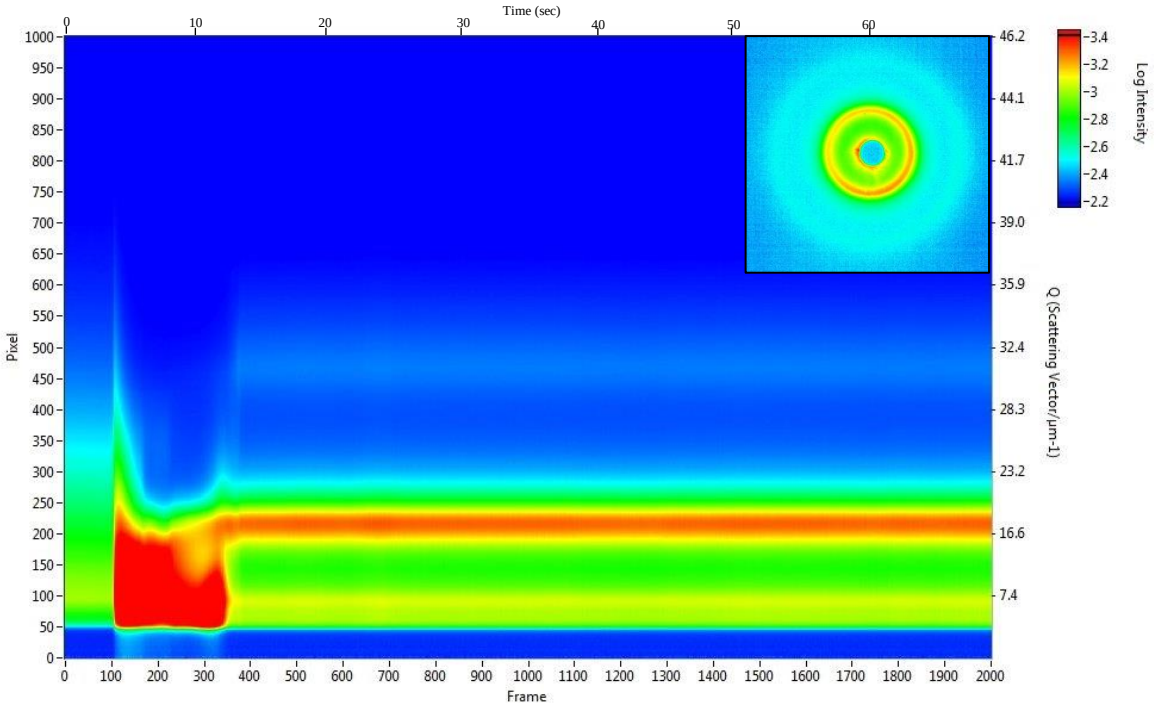

Figure 5.8: In Situ laser scattering charts collected during spin coating of 25 wt. % silica colloidal suspension at 3000 rpm.

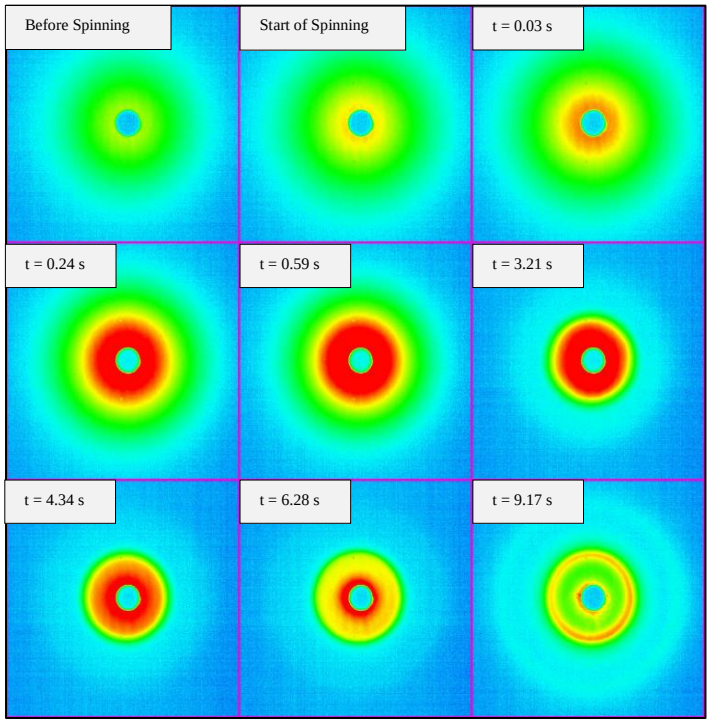

Figure 5.9: In Situ laser scattering patterns collected during the spin coating of the 25 wt.% silica colloidal suspension at 3000 rpm.

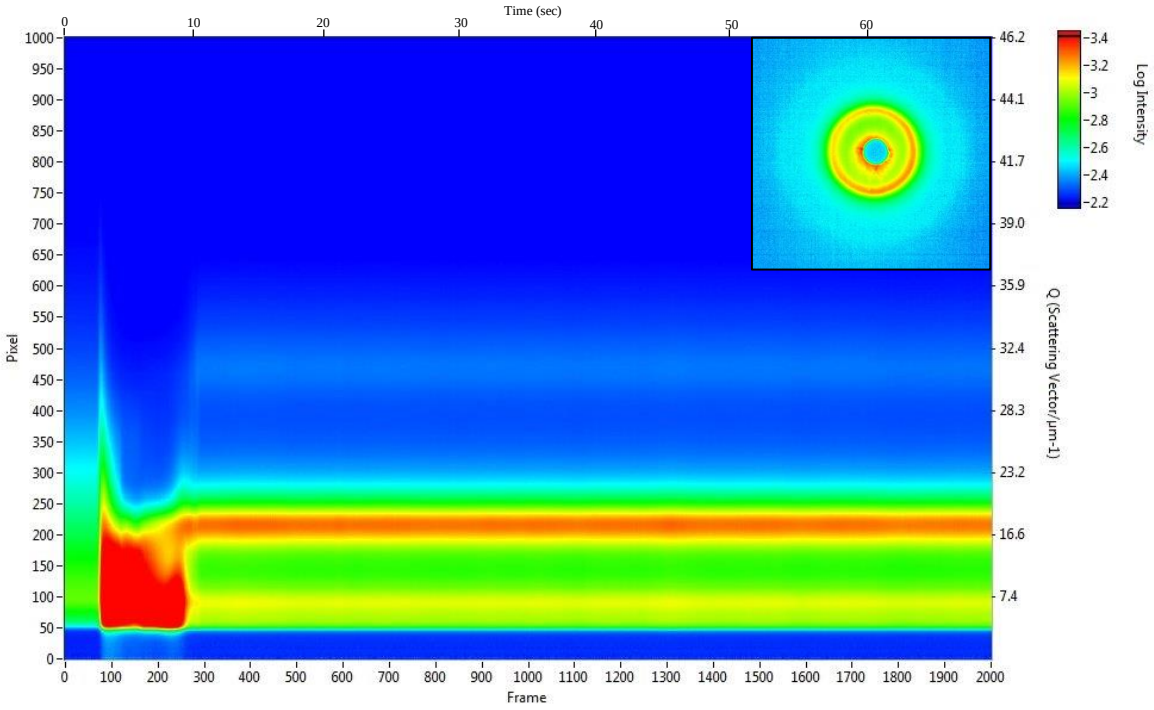

Figure 5.10: In Situ laser scattering charts collected during spin coating of 25 wt. % silica colloidal suspension at 4000 rpm.

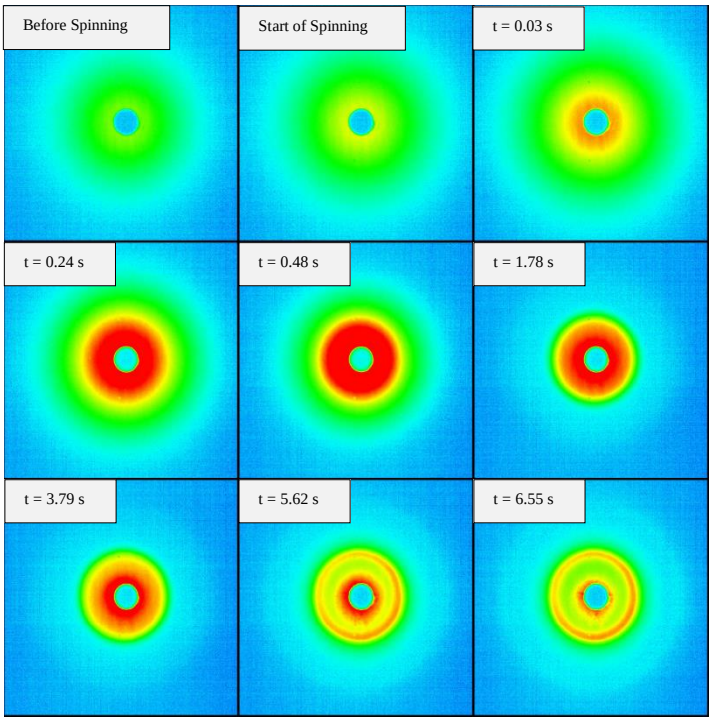

Figure 5.11: In Situ laser scattering patterns collected during the spin coating of the 25 wt.% silica colloidal suspension at 4000 rpm.

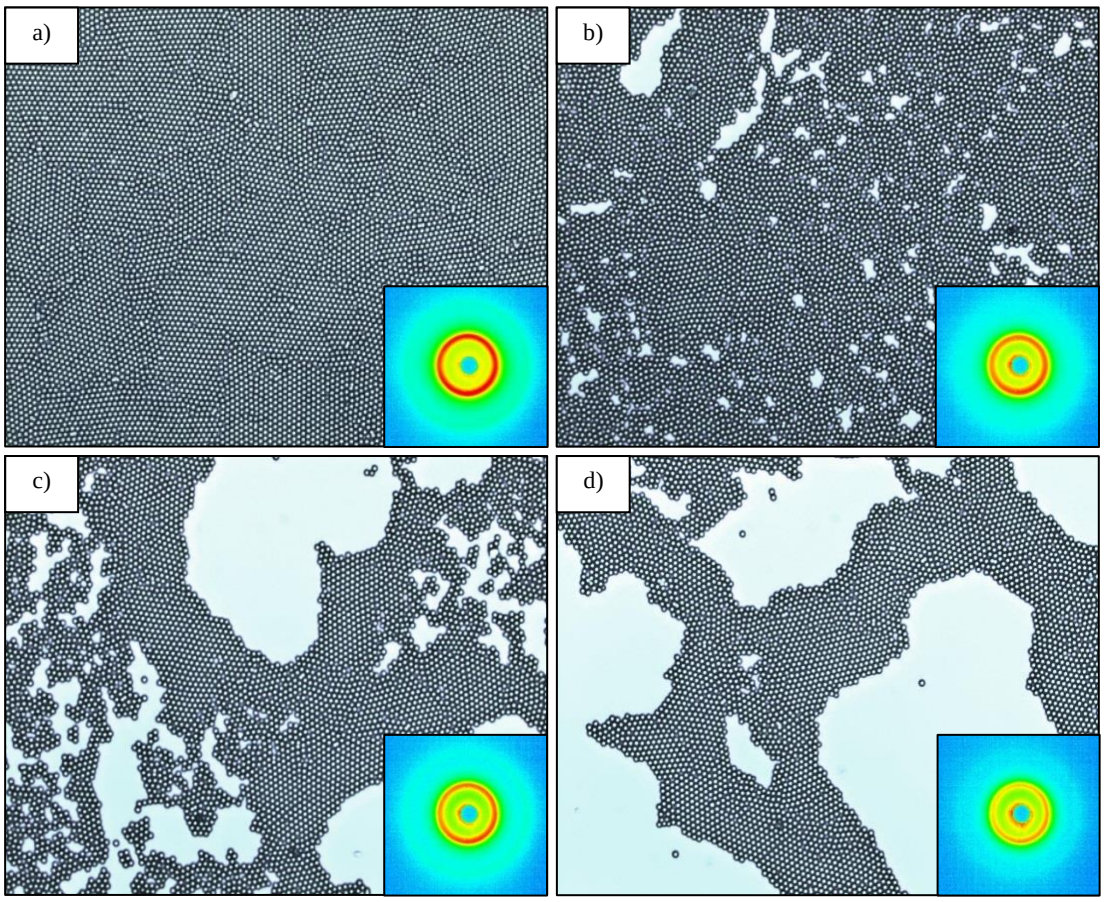

Figure 5.12: Microscopic images together with their laser scattering patterns for the final monolayer colloidal crystal fabricated when spin coating a 25 wt. % silica suspension in water at different rotational speeds; a) 500 rpm, b) 1000 rpm, c) 2000 rpm and d) 3000 rpm.

5.3 Discussions and Conclusions

The developed *in situ* laser scattering setup enables to visualise the different stages of the colloidal self-assembly that took place during the spin coating of colloidal silica suspensions from volatile solvents. The resultant real-time data shows the capability to track the colloidal self-assembly process starting from the deposition of the colloidal suspension on the glass substrate prior to rotation and ending by the formation of the final monolayer colloidal structure. The fast frame rate of 29 fps used in these experiments enables to identify clearly each stage among the shear thinning, evaporative thinning and the stepwise structure formation stage.

Figure 5.13 shows the development with respect to time in the stepwise evolution of laser scattering patterns collected when the 25 wt.% silica colloidal suspension was spin coated at different rotational speeds. It is clear that the development of final colloidal scattering patterns occurs faster at higher rotational speeds. The detailed durations of each stage; shear thinning, evaporative thinning and structure formation stage, when spin coating either the 25 wt. % or the 5 wt.% silica colloidal suspensions at different speeds are given in Tables 5.1 and 5.2 respectively. As shown in Figures 5.14 and 5.15, the duration of each stage during the spin coating process is inversely proportional to the designated rotational speed. Faster speeds induce shorter durations for the evaporative thinning stage. As a result, particles spin coated at faster speeds have a shorter time to be self-organised and so lower packing quality obtains.

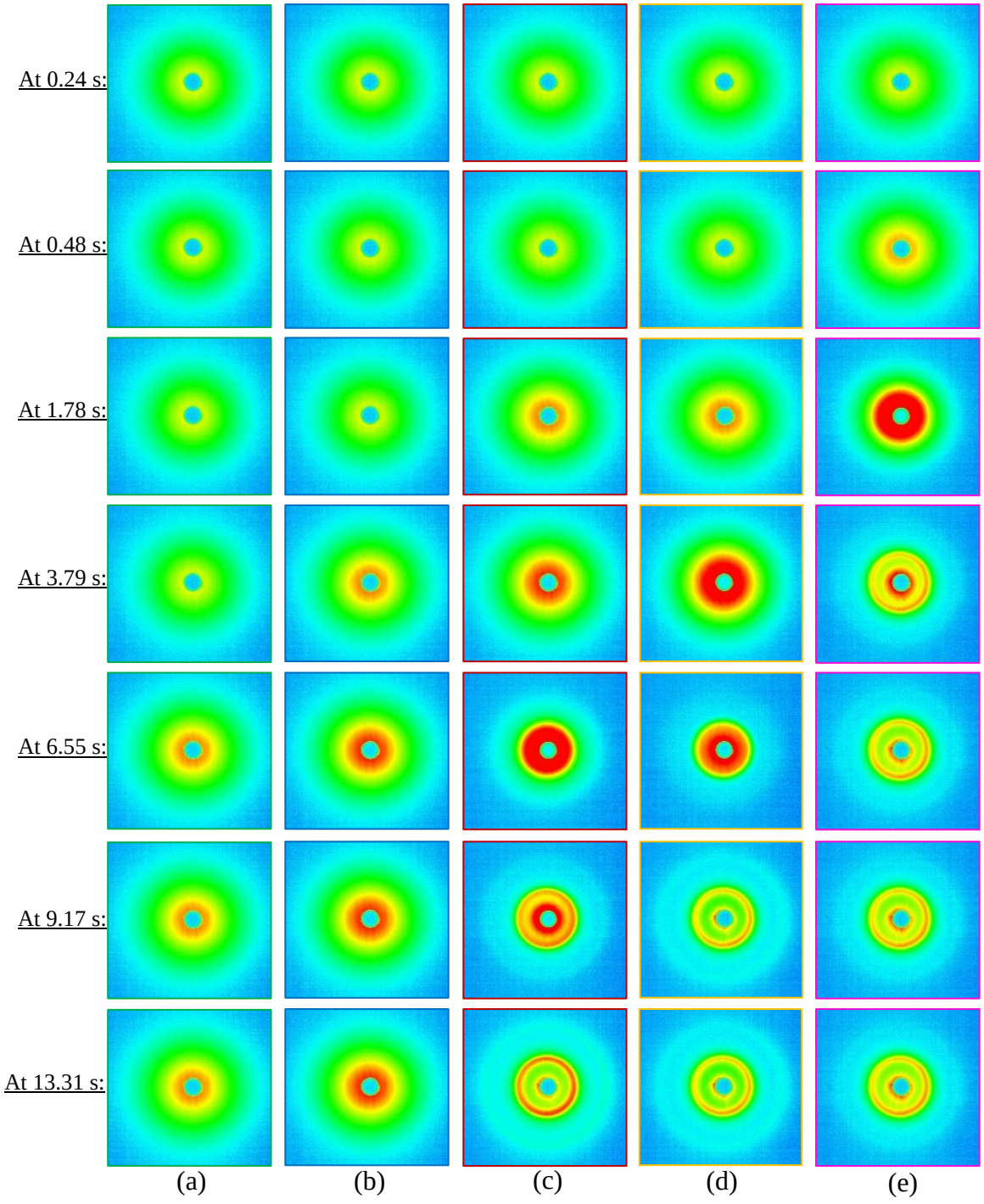

Figure 5.13: In Situ laser scattering patterns for the 25 wt. % silica colloidal suspensions in water spun cast at different rotational speeds; (a) 500 rpm, (b) 1000 rpm, (c) 2000 rpm, (d) 3000 rpm and (e) 4000 rpm.

Table 5.1: The duration of shear thinning, evaporative thinning and structure formation stages took place during spin coating of 25 wt.% silica colloidal suspension in water at different rotational speeds.

Sample no.	Spin Speed (rpm)	Duration, s (Shear Thinning)	Duration, s (Evaporative Thinning)	Duration, s (Structure Formation)
1	500	0.21	45.69	4.93
2	1000	0.21	22.00	3.45
3	2000	0.21	12.45	2.31
4	3000	0.21	8.69	1.03
5	4000	0.21	5.97	0.28

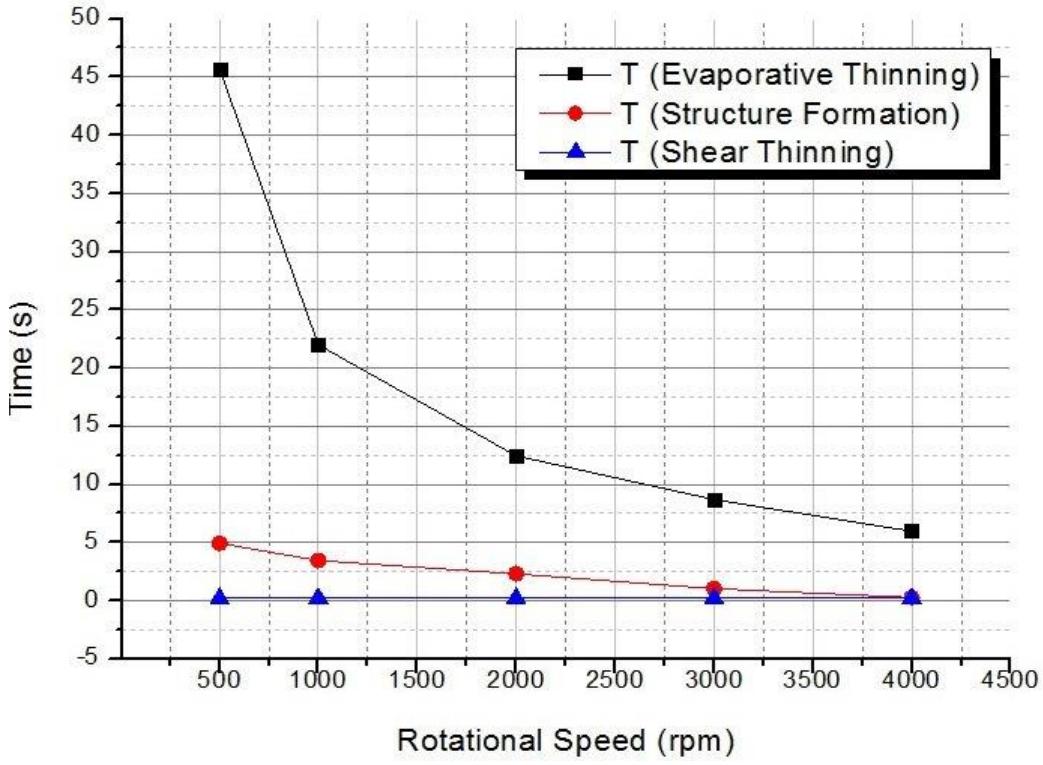

Figure 5.14: Effect of the rotational speed on the duration of the colloidal self-assembly stages that took place during spin coating of 25 wt.% silica colloidal suspensions in water at different speeds.

Table 5.2: The duration of shear thinning, evaporative thinning and structure formation stages took place during spin coating of 25 wt.% silica colloidal suspension in water at different rotational speeds.

Sample no.	Spin Speed (rpm)	Duration, s (Shear Thinning)	Duration, s (Evaporative Thinning)	Duration, s (Structure Formation)
1	1000	4.12	38.99	10.62
2	2000	2.66	18.24	5.48
3	3000	1.85	11.35	4.31
4	4000	1.07	8.31	3.52

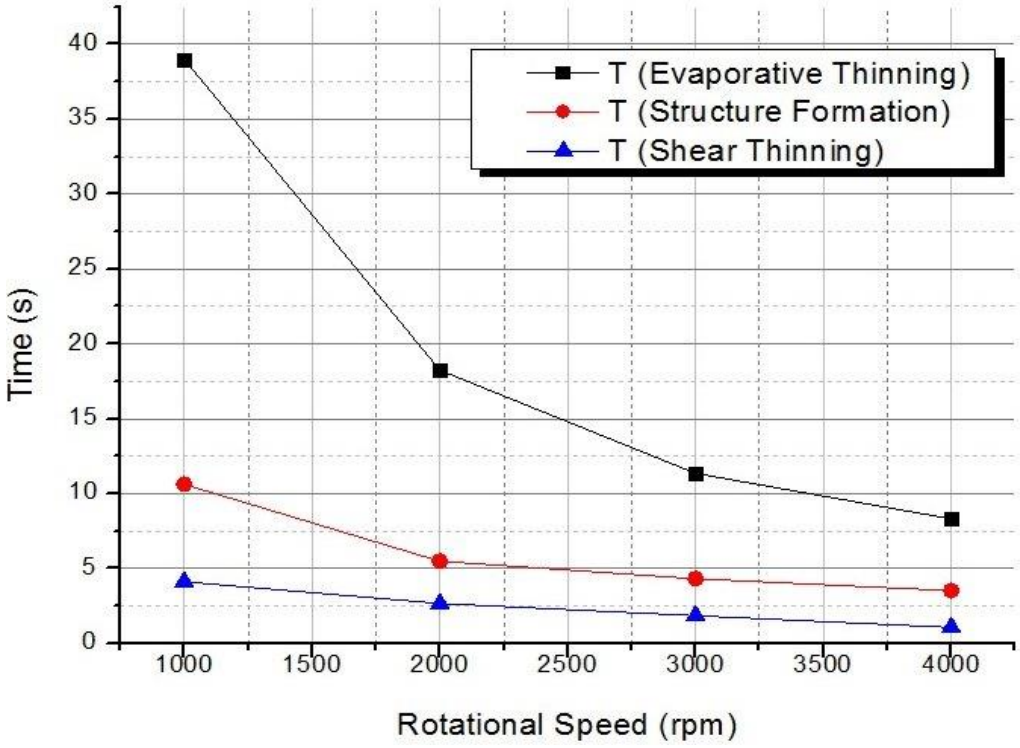

Figure 5.15: Effect of the rotational speed on the duration of the colloidal self-assembly stages that took place during spin coating of 5 wt.% silica colloidal suspensions in water at different speeds.

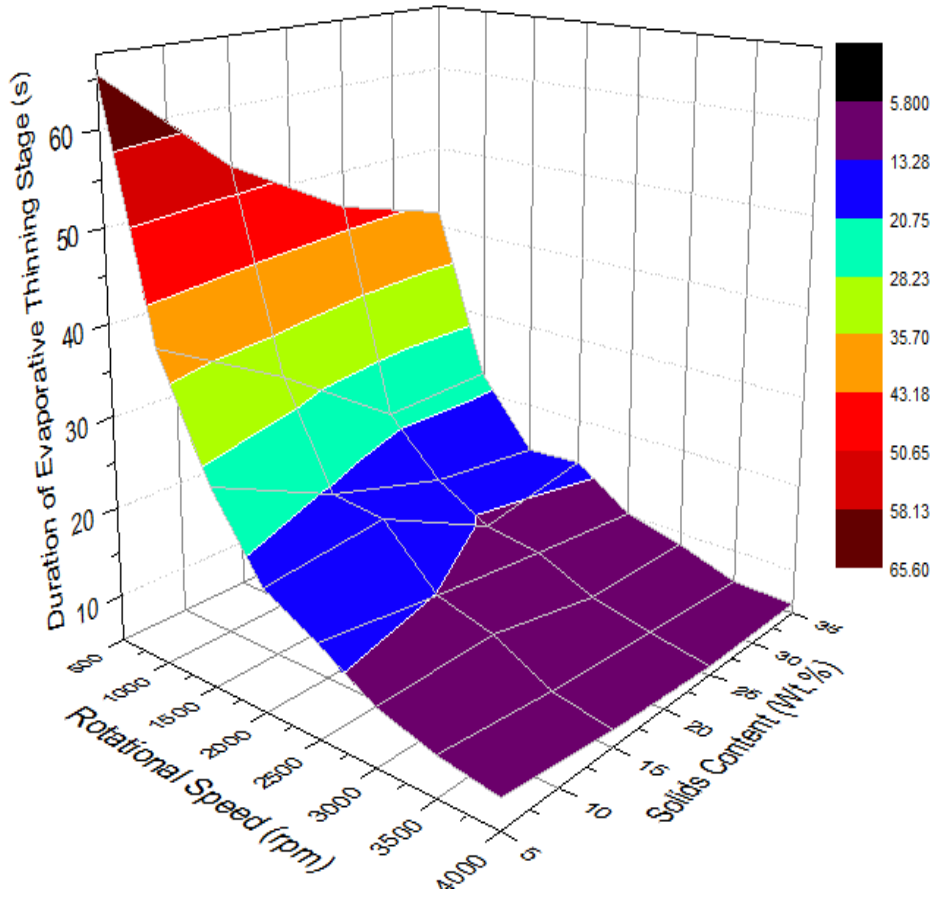

Figure 5.16: 3-D schematic diagram for the impact of both rotational speed and solids content on the duration of the evaporative thinning stage during spin coating of silica colloidal suspensions.

The 3-D schematic diagram, shown in Figure 5.16, confirms that spin coating the same colloidal suspension at a faster rotational speed dramatically decreases the duration of the evaporative thinning stage. Increasing the rotational speed increases the evaporation rate of the water, which can be easily deduced by the gradual shrinkage of the evaporative thinning duration as speed increases. In addition, it was able to visualise, for the first time, the stepwise evolution of the final scattering rings at the end of the spin coating process. We imagine that at the last stage of water evaporation, the attractive capillary forces dominate the process. Capillary forces induce an additional ordering power that pushes spherical particles towards each other. This helps to enhance the colloidal ordering quality just before the complete evaporation of the solvent.

Chapter 6.

In-Situ Studies of the Solids Content Effect in Spin Coating

6.0 Introduction

As shown in section 3.2, colloids weight percentage in the colloidal suspension was found to have a significant impact on both the ordering quality of colloids in the final thin films and on the coverage area percentage. However, these investigations were carried out in reciprocal space, and so real-time information was unachievable.

In this chapter, I have used the new developed laser scattering set-up (as explained in section 2.2.1) to investigate the effect of solids content on the colloidal self-assembly during spin coating in real time. Silica spherical particles with an average particle size diameter of 1550 nm and a polydispersity of 1.228 (determined by Nano Sight) were used as the raw material. Silica spherical particles were suspended with different weight percentages, 5, 15, 25 and 35 wt. %, in pure water, to prepare a series of colloidal suspensions. Suspensions were sonicated for 24 h continuously to remove any physical aggregations. Then, 100 µL of each suspension were deposited on glass coverslips, pre-treated as explained in section 2.1.2, adhered to the motor shaft. The sample was then rotated at 1000 rpm to fabricate monolayer colloidal crystals. The laser beam was shining through motor shaft directly towards sample once the colloidal suspension was deposited on the substrate. Laser scattering patterns were collected in real-time on a projecting screen. The whole process was recorded *in-situ* through Andor's Zyla 5.5 sCMOS camera at a high frame rate of 29.0 fps and 2000 exposures, corresponds to 68.96 s. Images were then processed using LabVIEW software as explained in section 2.2.3 and section 5.1 in order to develop a tracking chart for the whole process in real time. An Eclipse LV100 optical microscope connected to an Andor camera (Zyla 5.5 sCMOS) was used to capture an image for the final monolayer colloidal thin film after the end of the spin coating process. Microscopic images were taken using 40 × Nikon CFI S Plan Fluor ELWD objective. Scanning electron microscopy (SEM, JOEL JSM-6010LA) was used to develop a higher-resolution imaging for solid surfaces needed to effectively characterise the packing quality of colloidal crystals at the end of the spin coating process.

6.1 Results and discussion

Figures 6.1, 6.2, 6.3 and 6.4 show the laser scattering charts for the spin coating of colloidal suspensions of 1550 nm silica spherical particles in pure water at 1000 rpm, at a series of different colloids weight percentages of 5, 15, 25 and 35 wt. %, respectively.

In-situ data for the 5 wt. % silica suspension (Figure 6.1 accompanying movie https://youtu.be/tj9Ci6dUKGA) shows that initially, after deposition of the colloidal suspension on the substrate, no regular laser scattering patterns appear. This is an indication of the random distribution of silica colloids in the solution. Once spinning starts, a very bright diffuse circle appears at 0.03 s regarding the advent of shear forces due to rotational motion. Between 0.03 – 4.12 s, the diameter of that diffuse circle increases gradually regarding film thinning on the substrate which is governed by shear forces. At 4.12 s, the diameter of the diffuse ring becomes fixed due to the balance occurred between shear forces and gravitational forces. Between 4.12 – 9.22 s, no changes observed where shear forces were in balance with gravitational force and solvent was still in the liquid form. Once solvent starts to evaporate at 9.22 s, diffuse ring shrinks gradually towards the centre governed by evaporative thinning. Evaporative thinning action continues until 26.47 s at which laser scattering pattern becomes fixed. Stepwise evolution of the final scattering ring can be clearly observed between 37.59 – 48.21 s. Finally, at 48.21 s, the laser scattering pattern became fixed. This indicates the complete evaporation of the water leaving a monolayer colloidal crystal in its wake.

Figure 6.2 accompanying movie https://youtu.be/LjKX3_03X4Q shows the *in situ* laser scattering data for the spin coating of 15 wt. % silica colloidal suspension at 1000 rpm, which initially behaves similarly to the 5 wt. % colloidal suspension, forming irregular scattering patterns once spinning starts. This confirms the random distribution of particles in a solvent with the absence of any crystalline structure. At 0.03 s shear thinning takes place once rotational starts which is characterised by the appearance of a bright scattering circle. However, it took 2.14 s until the bright circle

expands to its maximum which is significantly shorter when compared to the period it takes in the case of 5 wt. % suspension (4.12 s). This could be attributed to the higher solids content which favours colloidal ordering through packing constraints. At 3.79 s, a transition from shear thinning into evaporative thinning took place which is characterised by shrinkage in ring size. This transition was observed earlier than the transition observed in the case of 5 wt. suspension. This confirms that higher particles concentrations induce packing constraints that favours colloidal ordering. At 16.59 s, ring size becomes fixed which is attributed to balance occurs between shear forces and gravity. Stepwise evolution of final scattering ring regarding the fabricated colloidal crystals takes place between 22.07 – 30.03 s. At 30.03 s a laser scattering ring appears with more intensity than that resulted in case of the 5 wt. colloidal suspension.

Figures 6.3 accompanying movie https://youtu.be/pgeF3HUzNa4 shows the stepwise evolution of the final laser scattering ring obtained during the spin coating of 25 wt. % silica colloidal suspensions at 1000 rpm. Stepwise evolution of colloidal structure was similar to that of either 5 wt. % or 15 wt. % colloidal suspensions in the early stage. However, the shear thinning stage was significantly shorter (0.21 s). This indicates the effect of more concentration in ordering mechanisms. In addition, evaporative thinning stage dominates for 22.0 s between 0.76 – 22.76 s. This shows that the duration of the evaporative thinning stage in the case of 25 wt. % is less than that observed in the case of either the 15 wt.% suspension (31.34 s) or the 5 wt.% suspension (38.99 s). As a result, it was expected that the ordering quality and colloidal coverage area percentage in this sample should be less than the ordering quality observed in the case of the 15 wt. % sample. However, the microscopic images given in Figure 6.5 showed the formation of a highly ordered crystalline structure with the maximum coverage area in case of 25 wt. %, while colloidal crystals formed in case of 5 wt.% and 15 wt.% had less coverage area percentage and large voids. Formation of a highly ordered structure occurred in case of the 25 wt.% suspension, unless the shorter duration of the evaporative thinning, could be attributed to the packing constraints induced due to the higher solid content ratio that decreases the inter-particles distances and favours colloidal self-organisation.

Figure 6.4 accompanying movie https://youtu.be/tNkYC3AHQQ0 shows the real-time chart for the laser scattering patterns collected during the spin coating of 35 wt. % silica colloidal suspension in water at 1000 rpm. Structural evolution resulted for the 35 wt.% suspension behaves in a similar manner to the 25 wt.% sample. Shear thinning dominates between 0.03 – 0.24 s for a 0.21 s duration, which exactly coincides with data for the 25 wt.% sample. However, the shift from the shear to the evaporative thinning stage observed at 0.55 s, which is earlier than that observed in the case of 25 wt.% (0.76 s). The reason behind that could be the higher concentration of particles exist in case of the 35 wt.% suspension. Unexpectedly, *in situ* data showed a long evaporative thinning stage domination between 0.55 – 23.07 s for 22.52 s until forming a fixed, stable final scattering ring. This duration is longer than the duration observed for the 25 wt.% suspension (22.52 s). It was expected that the evaporative thinning stage duration in the case of the 35 wt.% sample should be less than that of the 25 wt.% suspension regarding the higher concentration and so the packing constraints impact on colloidal ordering. However, the higher concentration in the case of the 35 wt.% suspension develops a huge number of particles that exceeds the concentration needed for full coverage of the substrate. As a result, particles took more time to occupy a position in the colloidal array forming a multi-layered colloidal crystal as shown in Figure 6.5 (d).

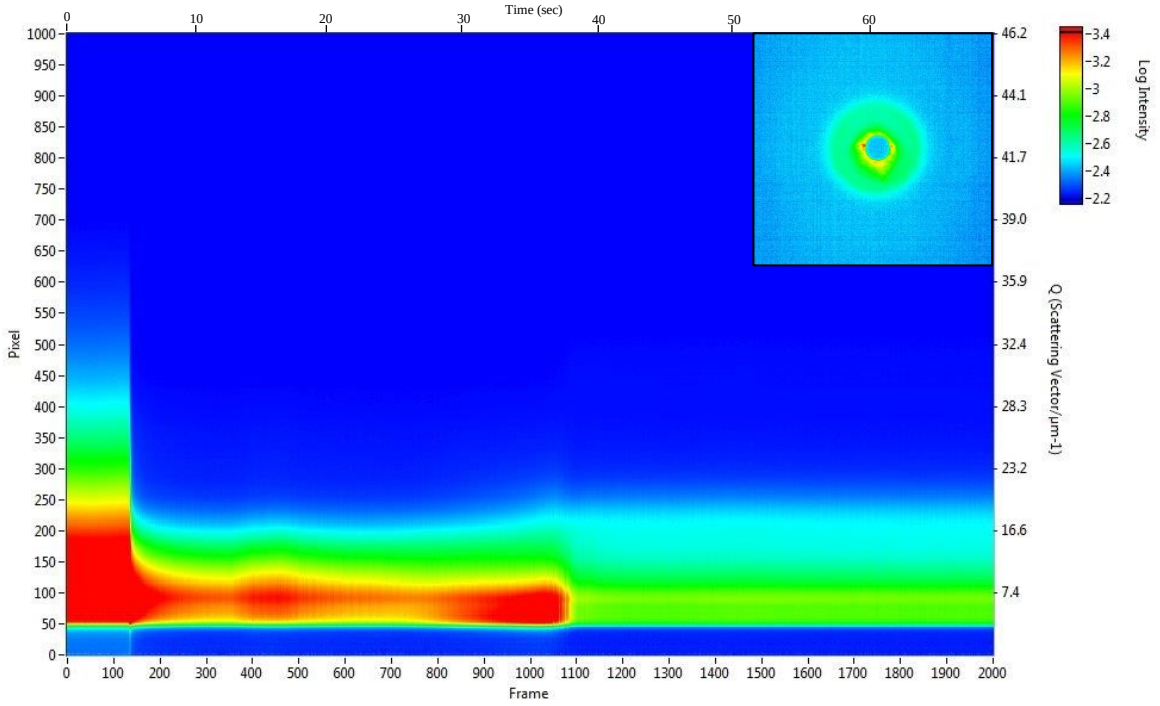

Figure 6.1: In Situ laser scattering charts collected during spin coating of 5 wt. % silica colloidal suspension at 1000 rpm.

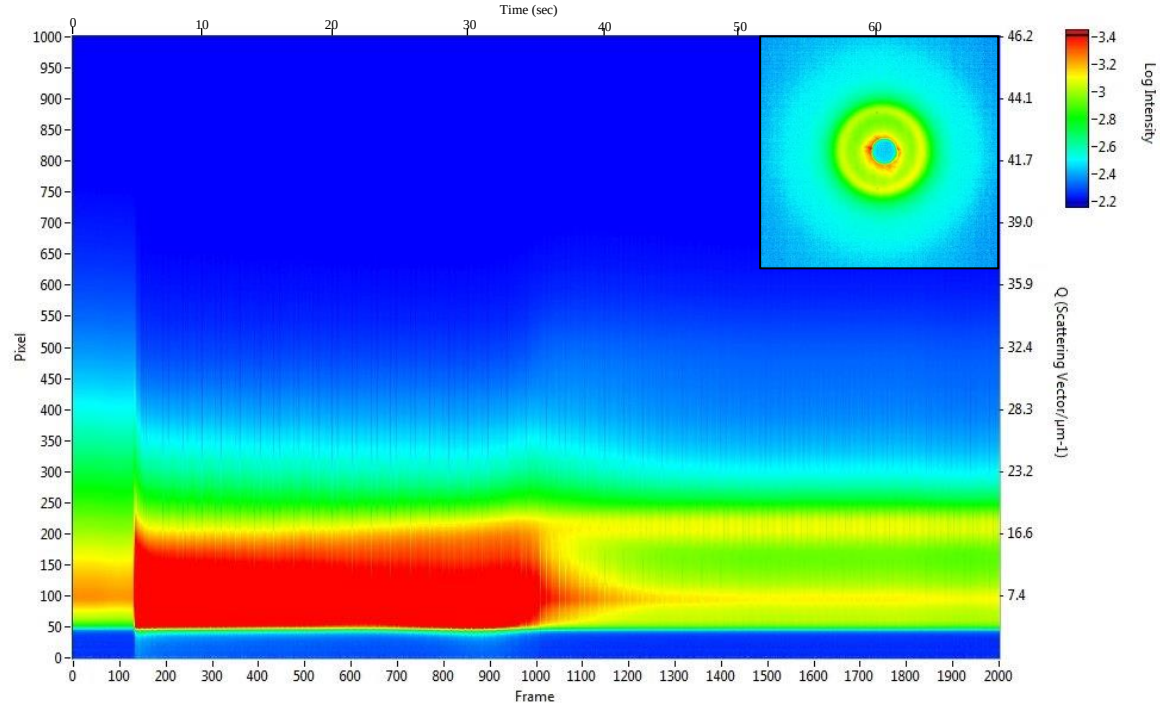

Figure 6.2: In Situ laser scattering charts collected during spin coating of 15 wt. % silica colloidal suspension at 1000 rpm.

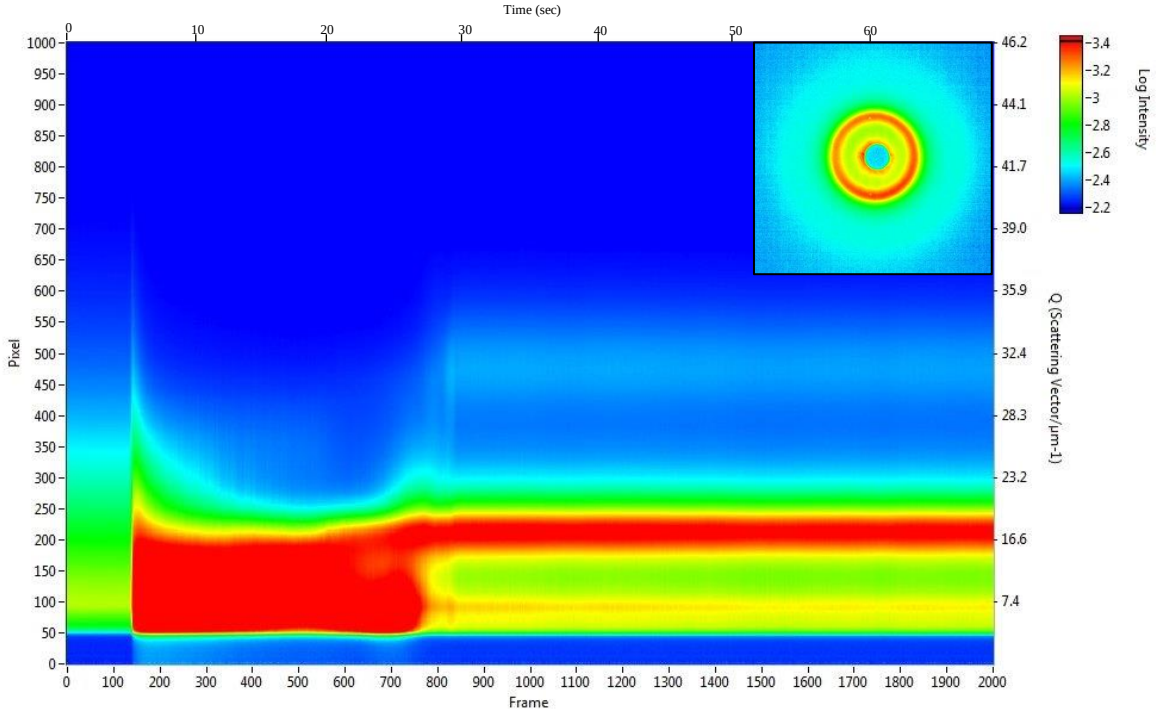

Figure 6.3: In Situ laser scattering charts collected during spin coating of 25 wt. % silica colloidal suspension at 1000 rpm.

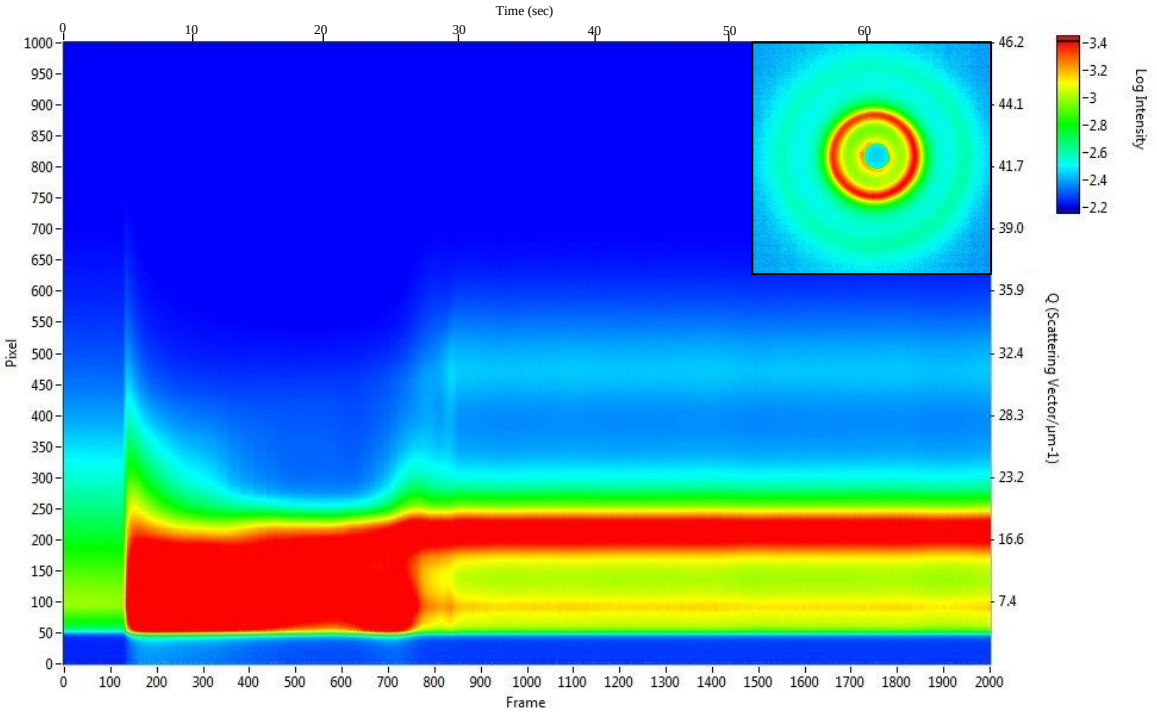

Figure 6.4: In Situ laser scattering charts collected during spin coating of 35 wt. % silica colloidal suspension at 1000 rpm.

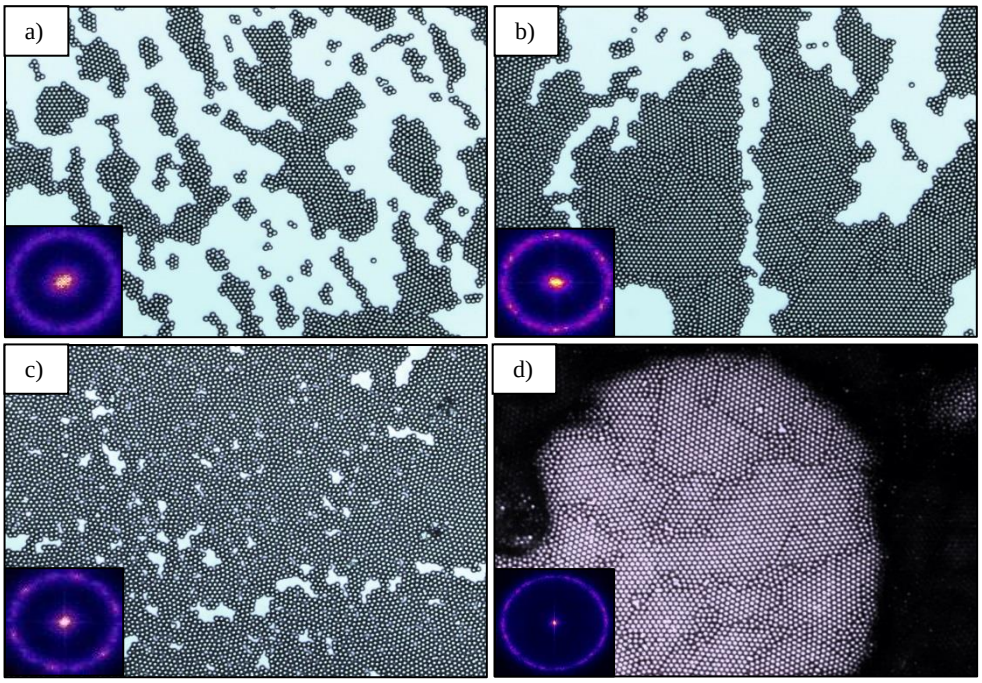

Figure 6.5: Microscopic images together with their FFTs for the final monolayer colloidal crystal fabricated when spin coating of silica colloidal suspensions in water with different concentrations; a) 5 wt. %, b) 15 wt. %, c) 25 wt. % and d) 35 wt. % at 1000 rpm.

6.2 Discussions and Conclusions

In this chapter, I have used the *in-situ* laser scattering setup to visualise and analyse the colloidal self-assembly that took place during spin coating colloidal suspension from volatile solvents. As shown in Figure 6.6, the development of the laser scattering patterns was greatly affected by the colloidal particles concentration in the colloidal suspension. Solute concentration governs the averaged particle distance between spherical particles through the colloidal suspension. Higher concentrations develop shorter relative interparticle distance inducing packing constraints that favours the ordering mechanism through the concentration-induced self-assembly. Lower concentrations of particles increase the distance between particles forming large voids among particles aggregation islands. So, colloidal suspensions with relatively lower concentrations form colloidal structure governed by the capillary-induced self-assembly mechanism. Evaporation of solvent occupying these voids induced capillary

attraction forces that pushes particles towards each other in the same aggregation. This leads to the formation of highly ordered colloidal islands separated by large voids occupied by air. However, increasing the concentration of particles decreases the inter-particle distances. This induces packing constraints that favours the colloidal reorganisation mechanism forming a higher ordering quality. If the particles concentration exceeds the optimum number of particles needed for a full coverage, this leads to the formation of a multi-layered colloidal structure.

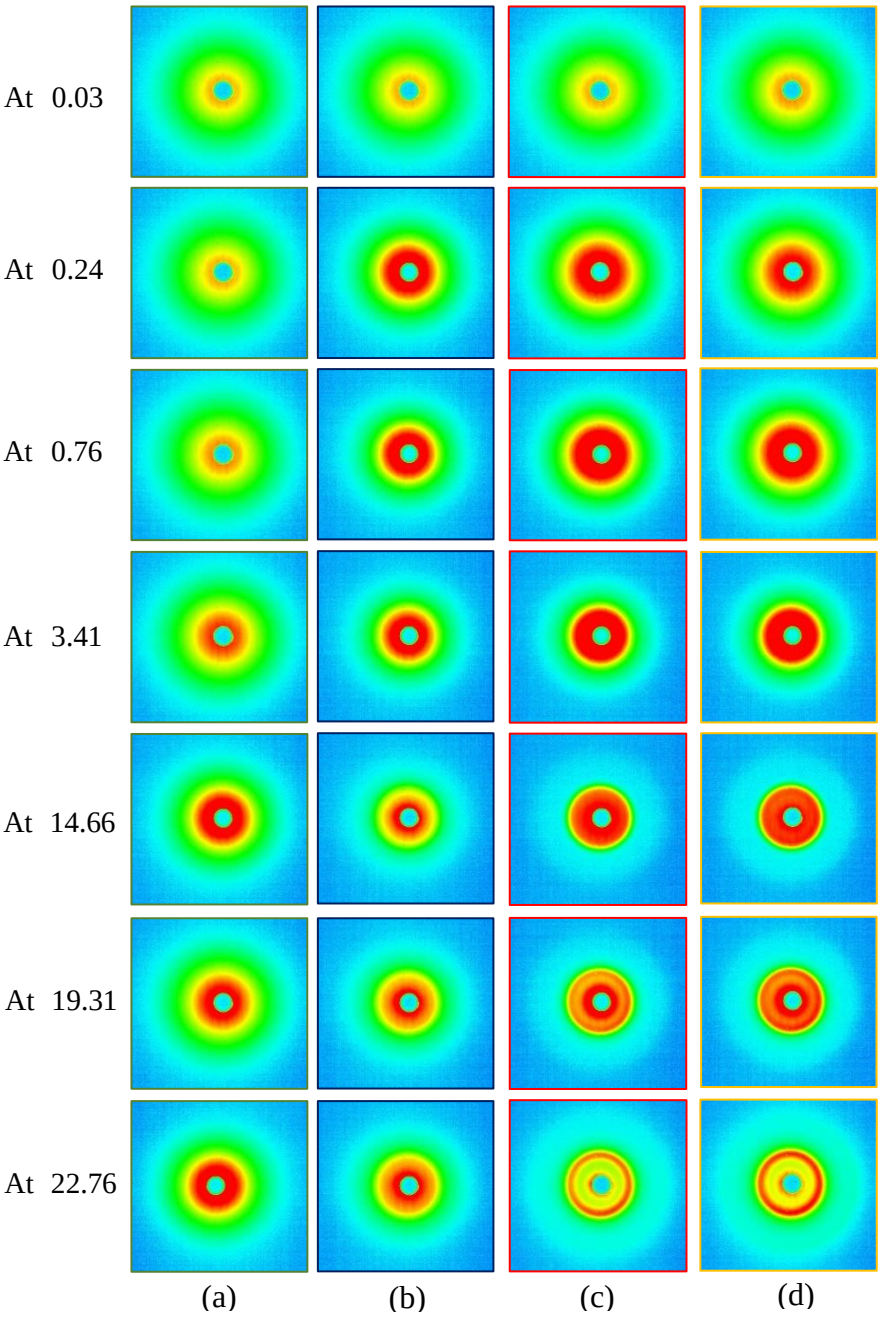

Figure 6.6: In Situ laser scattering patterns for silica colloidal suspensions of different concentrations in water; (a) 5 wt.%, (b) 15 wt.%, (c) 25 wt.% and (d) 35 wt.% spun cast at 1000 rpm.

Table 6.1: The duration of shear thinning, evaporative thinning and structure formation stages took place during spin coating of different concentrations of silica colloidal suspensions in water at 1000 rpm rotational speeds.

Sample no.	Solids Content (Wt. %)	Duration, s (Shear Thinning)	Duration, s (Evaporative Thinning)	Duration, s (Structure Formation)
1	5	4.12	38.99	10.62
2	15	2.14	31.34	7.45
3	25	0.21	22.00	3.45
4	35	1.87	22.52	6.35

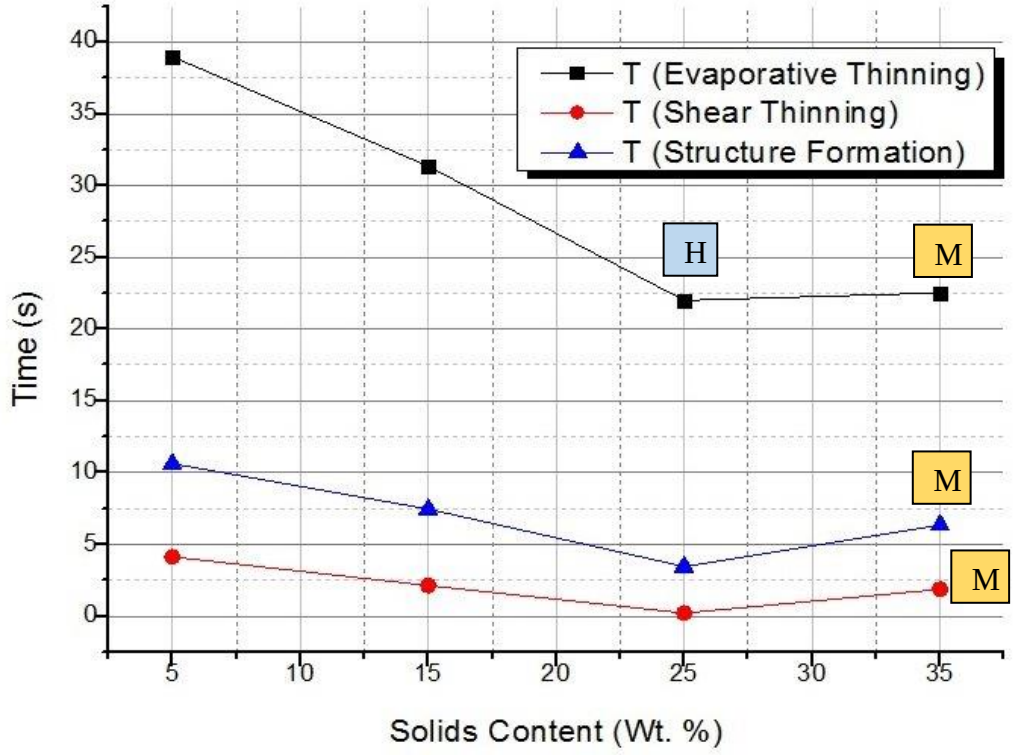

Figure 6.7: Effect of concentration on the duration of the colloidal self-assembly stages that took place during the spin coating of different concentrations of silica colloidal suspensions in water at 1000 rpm. [H] refers to the colloidal monolayer structure with the highest HCP% and [M] refers to the formation of a multi-layered colloidal structure.

Table 6.2: The duration of shear thinning, evaporative thinning and structure formation stages took place during spin coating of different concentrations of silica colloidal suspensions in water at 4000 rpm.

Sample no.	Solids Content (Wt. %)	Duration, s (Shear Thinning)	Duration, s (Evaporative Thinning)	Duration, s (Structure Formation)
1	5	1.07	8.31	3.52
2	15	0.83	6.72	1.78
3	25	0.21	5.97	0.28
4	35	1.59	6.01	2.21

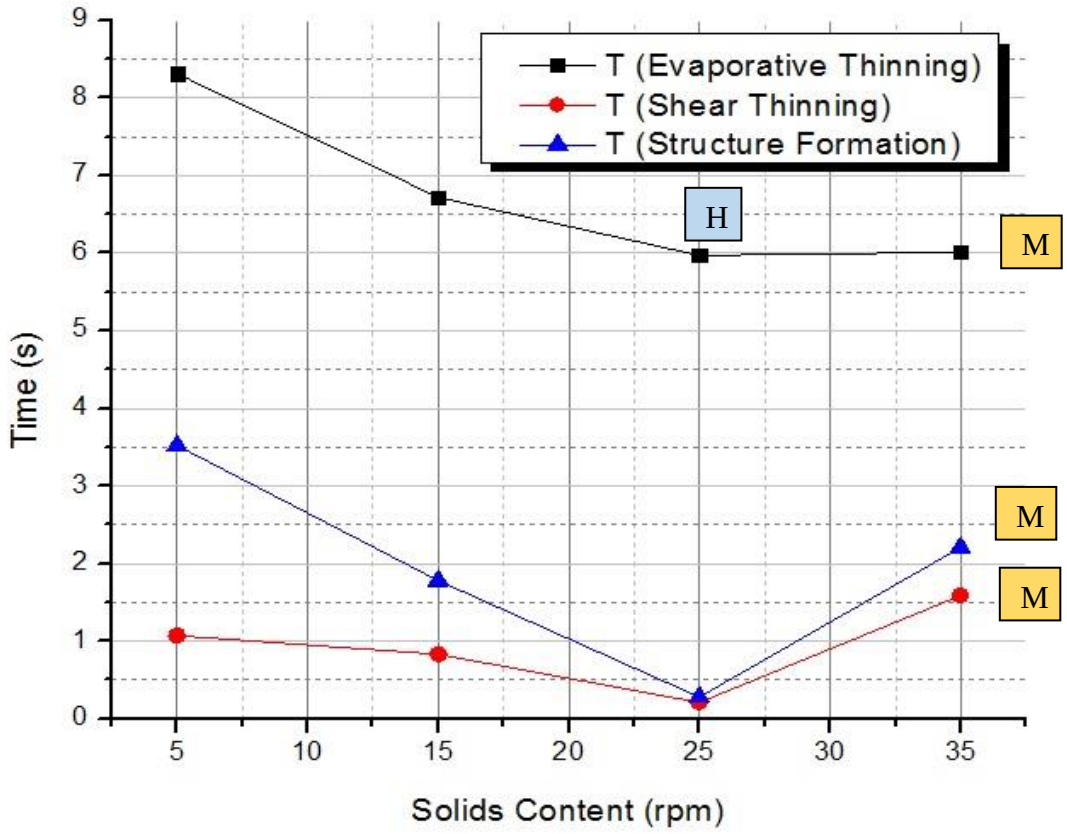

Figure 6.8: Effect of concentration on the duration of the colloidal self-assembly stages that took place during the spin coating of different concentrations of silica colloidal suspensions in water at 4000 rpm. [H] refers to the colloidal monolayer structure with the highest HCP% and [M] refers to the formation of a multi-layered colloidal structure.

The detailed durations for each stage during the spin coating of different concentrations of silica colloidal suspensions are given in Tables 6.1 and 6.2 and represented in Figures 6.7 and 6.8. These results showed that increasing the solids content from 5 – 25 wt. %, either at 1000 or 4000 rpm, directly decreases the duration of self-assembly stages; shear thinning, evaporative thinning and final structure formation stage. This could be attributed to the packing constraints accompanying the increased load of colloids. The packing constraints favours colloidal ordering and decreases the time needed for particles re-organisation. The solids content of 25 wt. % represents the optimum concentration of colloidal particles producing colloidal thin films with the highest ordering quality. However, when the particles concentration exceeds the optimum value (25 wt. %) a sudden increase in the duration of the colloidal self-assembly stages was noticed. This odd behaviour is attributed to formation of multi-layered colloidal crystals regarding the huge amount of colloids.

Chapter 7.
In-Situ Studies of the Solvent Volatility Effect in Spin Coating

7.0 Introduction

As explained in Chapter 1, Meyerhofer [70] was the first to introduce the effect of solvent evaporation into EBP model. Meyerhofer assumed that spin coating process could be divided into two main stages. Firstly, the film thinning is governed by shear forces and once solvent starts to evaporate the whole process becomes governed by evaporative thinning. Based on that assumption, solvent evaporation rate becomes a very important parameter in controlling the packing quality in the colloidal self-assembly during spin coating. Since, changing the solvent type will not change the rate of evaporation only but also many parameters will be affected such as vapour pressure, mixture viscosity, colloidal suspension stability and solvent volatility. So, it was easier for simplicity to link changing the solvent type directly to the solvent volatility.

In this chapter, water and ethanol were mixed together with different concentrations to produce a set of solvent mixtures. Intensions behind that was to study the impact of different volatilities on laser scattering patterns during the stepwise formation of the final scattering structure. However, as it is well-known, mixing a 95.63% ethanol and 4.37% water (by weight) forms a positive azeotrope. In the azeotrope mixtures, vapour has the same proportions of constituents as the unboiled mixture, so the whole mixture boils as a single component at 78.2 °C which is lower than either of its constituents. Based on that fact, water and ethanol were mixed carefully with weight percentages; (50:50 %), (25:75 %) and (40:60 %) to avoid the formation of that azeotrope. Hence, each component evaporates individually giving the colloidal suspension a multi-step evaporation mechanism. This develops more time for particles to reorder themselves properly during the colloidal self-assembly before the complete evaporation of the solvent. Extending the evaporation period should help to improve the colloidal ordering quality of the final colloidal crystals.

7.1 Experimental Work

As discussed in *ex-situ* investigations stage, given in section 4.5, solvent volatility had a significant effect on the ordering quality of final colloidal crystals. It was found that the hexagonal close-packing percentage (HCP %) was clearly increased from 78.1 % to 84.5 % when the solvent type was changed from pure water into Water – ethanol (1:1) mixture. However, *ex-situ* measurements were unable to develop assertive information about the real-time consequences accompanied by changing the solvent used. In this chapter, we trace the colloidal self-assembly changes that took place in real-time during spin coating of colloidal silica suspensions in different solvents. *In-situ* laser scattering set-up has been used here to record the stepwise evolution of colloidal crystals during the spin coating process in the presence of different solvents. In this stage, rotational speed, acceleration rate and solids content were kept constant at 1000 rpm, 2.2 rev.s^{-2} and 25 wt. % respectively. However, the only variable in this set was set to be the solvent type; pure water, pure ethanol and water – ethanol mixtures.

7.2 Results and discussions

Figure 7.1 accompanying movie https://youtu.be/iGjCA6d-g64 shows the *in situ* stepwise evolution of laser scattering patterns obtained during the spin coating of a 25 wt. % silica colloidal suspension in pure ethanol at 1000 rpm. Interestingly, a diffuse ring appeared even before the rotational motion starts. This indicates the early action of evaporative thinning induced by the fast evaporation of ethanol. At 1.17 s, a sharp scattering ring starts to appear regarding the particles organisation. Between 1.17 – 2.93 s, the intensity of that ring increases gradually. This could be attributed to the self-assembly of particles forming a regular crystalline structure. However, particles self-organisation was disrupted suddenly at 4.89 s and no more scattering rings appeared. This could be attributed to the formation of some randomly ordered islands on the top of the primarily monolayer colloidal crystals, as shown in the microscopic image given in Figure 7.2 (f). Multi-layered colloidal structure formation is linked to the fast evaporation rate of ethanol that limits the time available for the particles self-assembly before complete evaporation of the final colloidal

structure. Final scattering took place at 6.45 s after only 8.65 s from the deposition of colloidal suspension on the substrate.

In-situ data for the 25 wt. % silica suspension in pure water spun cast at 1000 rpm (given in Figure 7.3 accompanying movie https://youtu.be/oLrNrnShgis) shows that shear forces, induced by the rotational motion of the motor holding the colloidal suspension, dominates the process between 0.03 – 0.76 s. Evaporation of water starts once solvent was deposited on the substrate and prior to the start of the rotational motion. However, domination of evaporative thinning was observed at 0.76 s. Afterwards, water undergoes a uniform evaporation between 0.76 – 22.76 s. At 22.76 s, a clear laser scattering ring appeared indicating the formation of the final thin film where water was completely evaporated. The quantification of the hexagonal close – packing percentage (HCP %) using LabVIEW, as explained in section 2.1.1.3, confirmed the formation of a highly ordered colloidal structure with an HCP% of 72.4 % and a coverage area percentage of 99.6%. However, the HCP% calculated for the disordered colloidal structure fabricated in the case of pure ethanol was found to be 21.0 %. This could be attributed to the longer duration of the evaporative thinning stage for pure water (22.0 s) when compared to 8.65 s in the case of pure ethanol. Extending the evaporation period gives the colloidal particles opportunity to explore the optimum sites to occupy during self-assembly process efficiently. Hence, the formation of a monolayer colloidal crystals with a better ordering quality, while the fast evaporation of ethanol limits the self-organisation period and increases the shear forces which leads to the disruption of the colloidal ordering and the formation of a disordered structure.

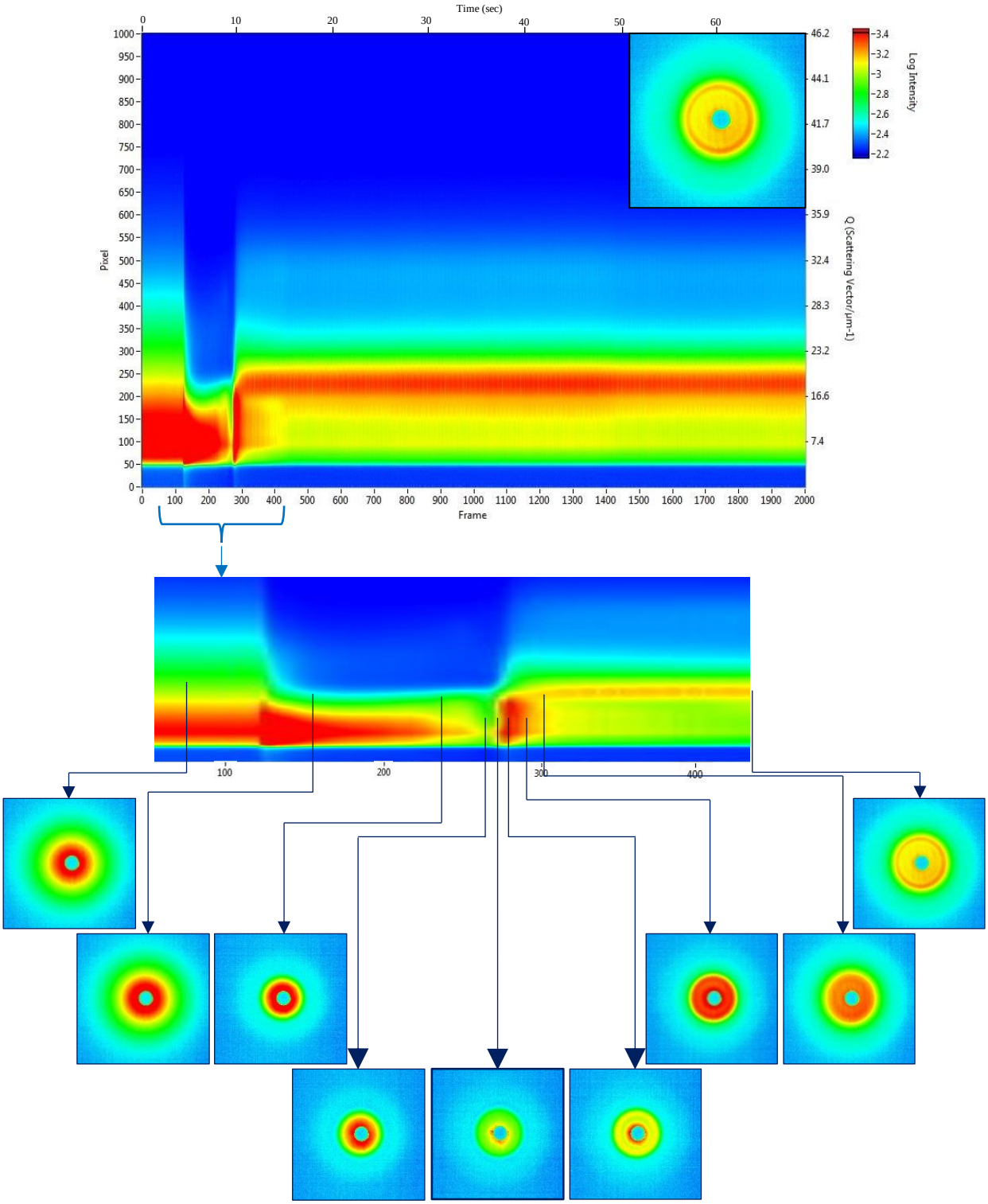

Figure 7.1: In-situ laser scattering chart for a 25 wt. % silica colloidal suspension in pure ethanol spun-cast at 1000 rpm.

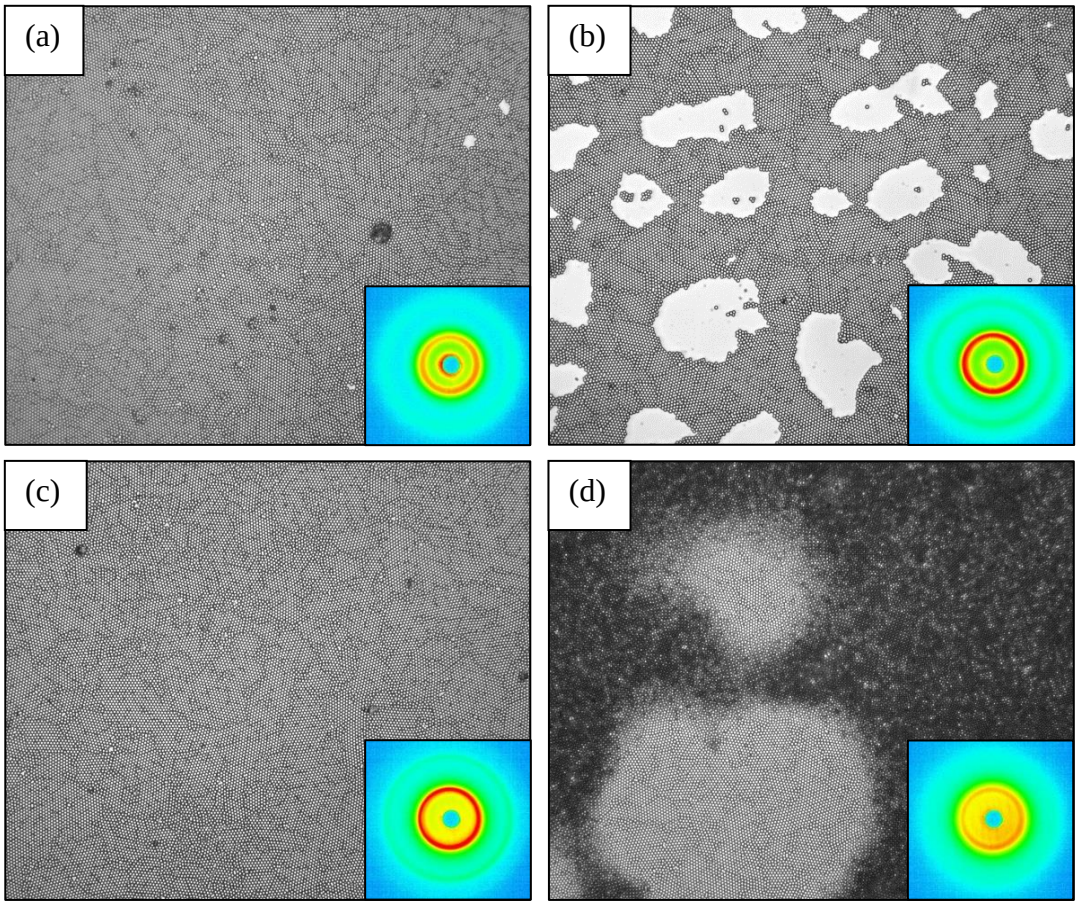

Figure 7.2: Microscopic images together with the laser scattering patterns for the final colloidal crystals obtained from 25 wt. % silica colloidal suspensions from different liquid solutions; A) water : Ethanol = 3:1, B) water : Ethanol = 3:2, C) water : Ethanol = 1:1 and D) pure Ethanol.

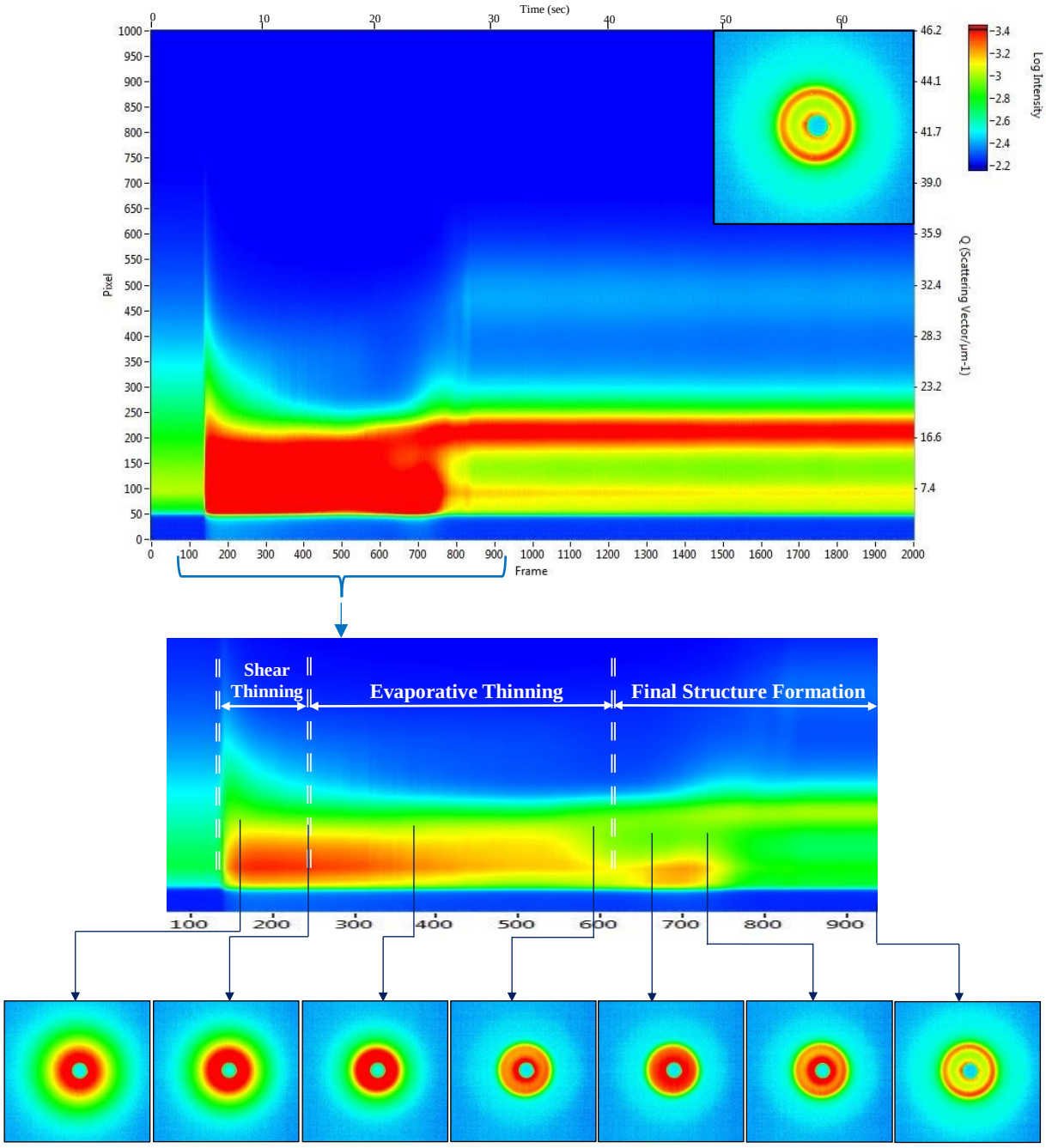

Figure 7.3: In-situ laser scattering chart for a 25 wt. % silica colloidal suspension in pure water spun-cast at 1000 rpm.

The 25 wt. % colloidal suspension spun cast at 1000 rpm from water – ethanol (1:3) mixture, given in Figure 7.4 accompanying movie https://youtu.be/BuTT9ffWQLI , initially shows a similar behaviour to that of pure water suspension where shear thinning starts at 0.03 s. however, the shift to evaporative thinning was observed at 7.03 s. *In-situ* chart for the 25 wt. % silica suspension in water – ethanol (1:3) mixture shows for the first time the appearance of two abrupt peaks in intensity during the evaporative thinning stage between 6.17 – 7.03 s. This behaviour could be attributed to a multistep evaporation of water when being in a mixture with ethanol [86]. Multistep evaporation mechanism enables water to evaporate in three consecutive stages gradually; “Network water”, “Intermediate water” and “Multimer water” (as shown in Figure 7.4). The whole evaporative thinning stage dominates for 11.0 s between 7.03 – 18.03 s. At 15.01 s, a scattering ring was observed indicating the emergence of an ordered colloidal structure. However, this scattering ring became weaker and weaker later. This could be attributed to the disruption of the primarily ordered structure due to the excessive shear induced by the fast evaporation of ethanol. At 18.03 s, the scattering ring became stable indicating the complete evaporation of the solvent. The disruption occurred to the scattering ring in case of water – ethanol (1:3) mixture looks similar to what happened in the case of pure ethanol. This confirms the negative impact of ethanol on the ordering quality of the final scattering rings regarding the high volatility that forces particles to be self-organised in a very limited time.

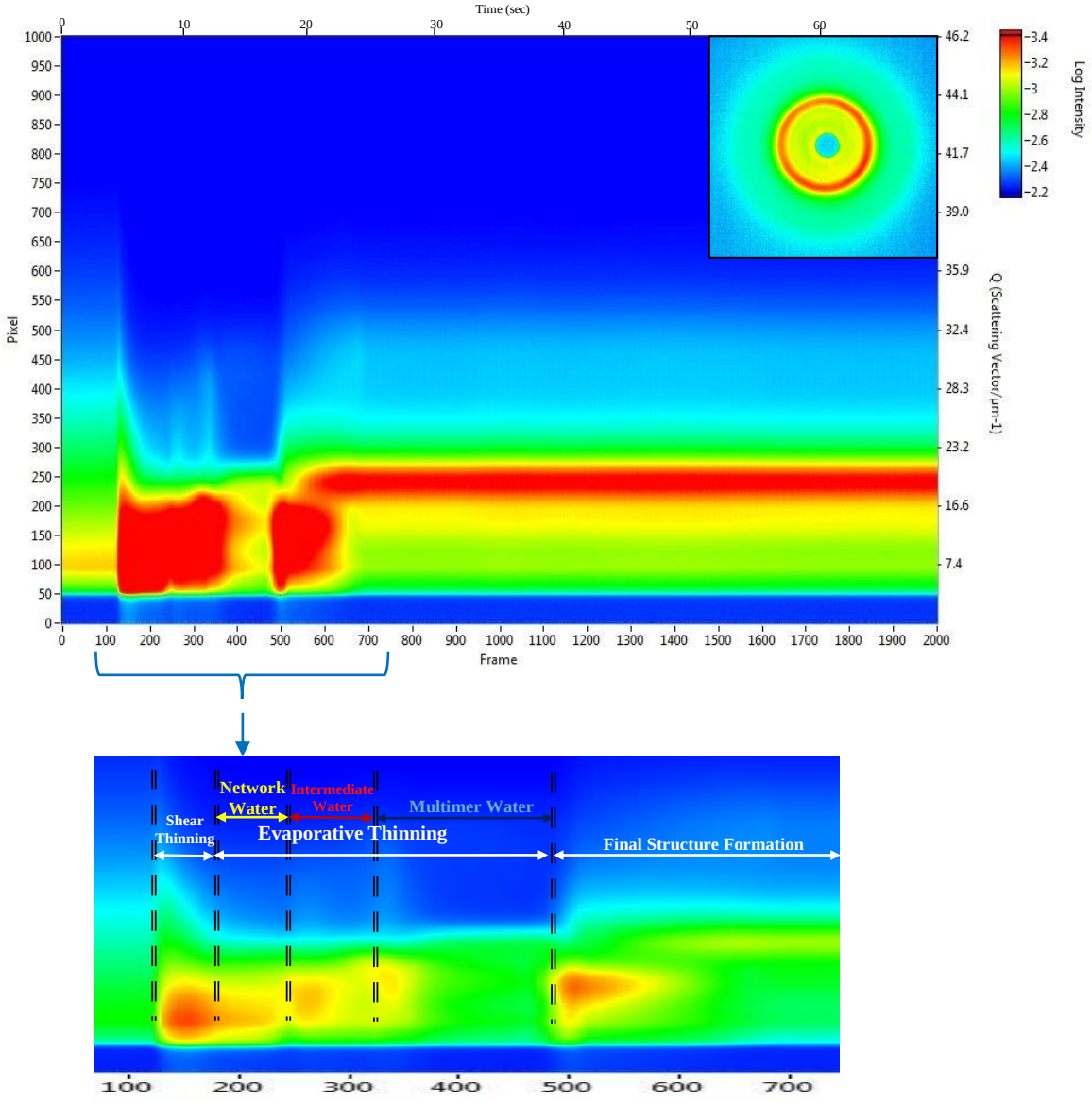

Figure 7.4: In-situ laser scattering chart for a 25 wt. % silica colloidal suspension in a water: ethanol mixture (1:3) spun-cast at 1000 rpm. Zooming shows the multistep evaporation stages of water in the water – ethanol mixtures; (1) Network water, (2) Intermediate water and (3) Multimer water.

The 25 wt. % colloidal suspension spun cast at 1000 rpm from water – ethanol (2:3) mixture, given in Figure 7.5 accompanying movie https://youtu.be/QJuKY2ExVUg , shows a similar behaviour to that of the suspension in water – ethanol (1:3) mixture. Herein, the two abrupt peaks observed in the case of the (1:3) suspension also appeared but with a little bit more intensity regarding the higher amount of water in the solvent mixture. However, the evaporative thinning stage duration was 15.28 s which is 3.28 s longer than that of the (1:3) suspension. This could be related to the higher content of water with respect to ethanol which decreases both the vapour pressure and the evaporation rate. Figure 7.6 accompanying movie https://youtu.be/Gykyji-gFeo shows the *in situ* laser scattering data for the 25 wt. % colloidal suspension spun cast at 1000 rpm from water – ethanol (1:1) mixture. This suspension behaves similarly to both (1:3) and (2:3) water – ethanol mixtures. However, it shows a longer evaporative thinning stage of 14.76 s between 7.24 – 22.0 s. This suspension develops an intermediate solvent volatility that gives colloidal particles the optimum time to reorganise themselves during self-assembly and before complete evaporation of the solvent. This leads to the formation of a highly ordered monolayer colloidal structure as confirmed by the microscopic image together with its FFT (given in Figure 7.7a), the SEM micrograph (given in Figure 7.7b) and the hexagonal close-packing percentage (HCP % = 84.5 %) calculated using LabVIEW software as shown in Figure 7.7c.

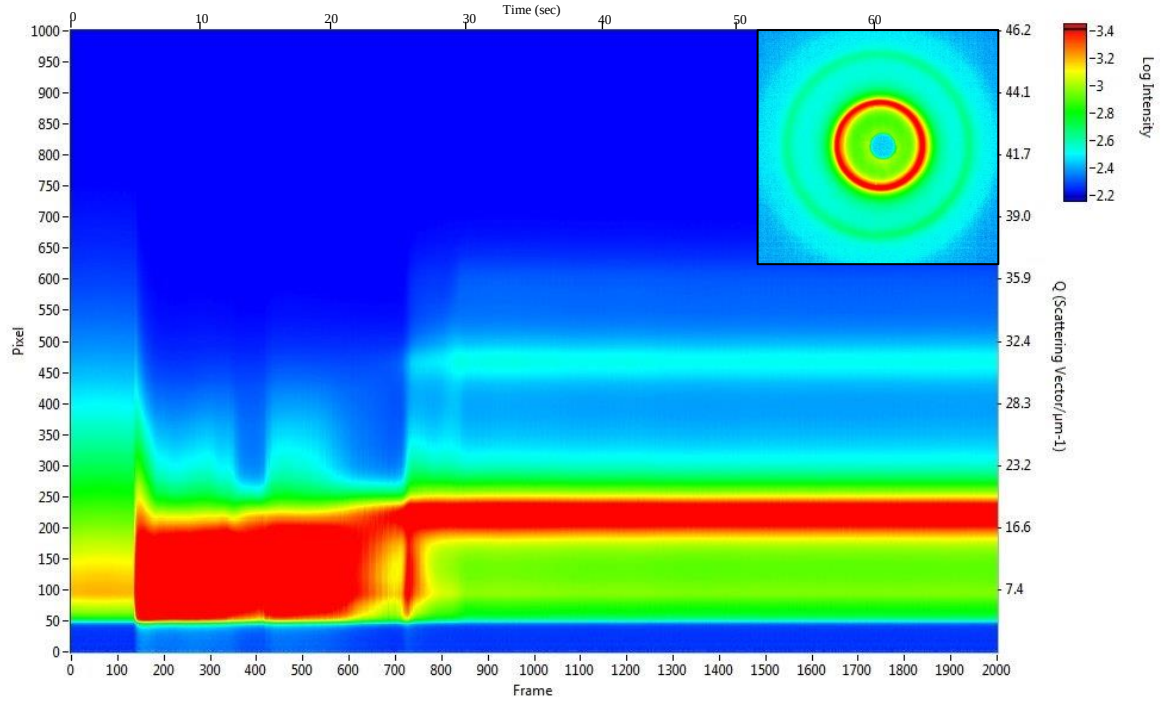

Figure 7.5: In-situ laser scattering chart for a 25 wt. % silica colloidal suspension in a water: ethanol mixture (2:3) spun-cast at 1000 rpm.

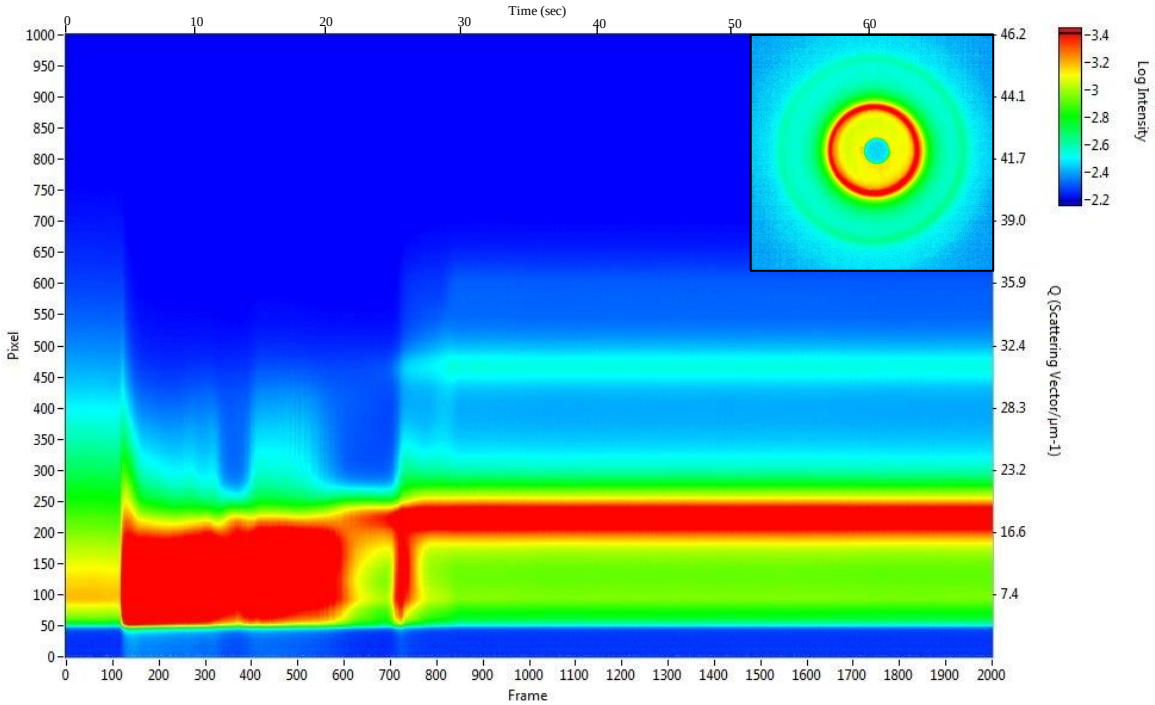

Figure 7.6: In-situ laser scattering chart for a 25 wt. % silica colloidal suspension in a water: ethanol mixture (1:1) spun-cast at 1000 rpm.

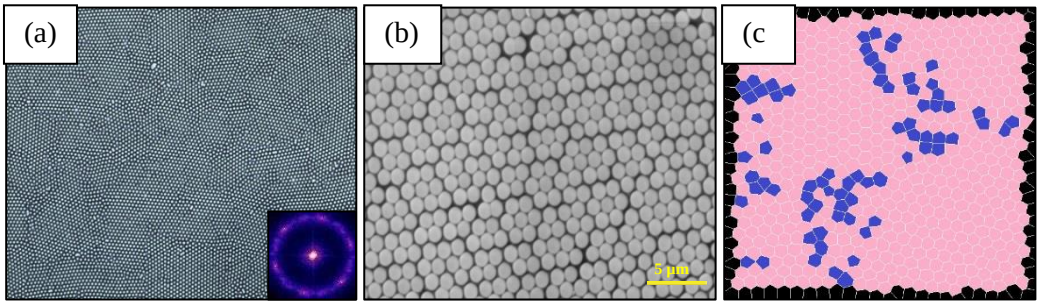

Figure 7.7: Data for the highly ordered monolayer colloidal crystals formed when a 25 wt. % silica colloidal suspension in a water – ethanol (1:1) mixture spun cast at 1000 rpm; (a) The microscopic image capture using a 40 × Nikon CFI S Plan Fluor ELWD objective (together with its FFT), (b) The SEM micrograph at a magnification of 4300 x and (c) Quantifying of hexagonal patterns in the a specific region of interest in the centre of the microscopic image using LabVIEW software shows a ***HCP % = 84.5 %*** *[pink areas indicate the hexagonal polygons, while blue areas are for other polygons] .*

The 25 wt. % colloidal suspension spun cast at 1000 rpm from a water – ethanol (3:2) mixture, given in Figure 7.8 accompanying movie https://youtu.be/a4wS8PZvXLs , behaves in an intermediate manner between the smooth evaporation of either pure water or pure ethanol and the multistep evaporation mechanism observed in case of either (1:3) or (2:3) suspensions. This indicates that the observed multistep evaporation phenomenon is linked to the amount of water in the water – ethanol mixture. As water content increases, suspension evaporates more uniformly like in the case of pure water suspension. However, decreasing the content of water in the water – ethanol mixtures increase the impact of the multistep evaporation of water during the colloidal self-assembly process.

The 25 wt. % colloidal suspension spun cast at 1000 rpm from water – ethanol (3:1) mixture, shown in Figure 7.9 accompanying movie https://youtu.be/I0KmV5TIZWE , confirms the previous conclusion that content of water in the water – ethanol mixtures control the multistep evaporation impact during the evaporative thinning. Herein, increasing the content of water to three times that of ethanol decreases the impact of the multistep evaporation of water. As a result, the stepwise evolution of the laser scattering patterns in the case of (3:1) suspension

follows a uniform ramp that looks similar to that of pure water suspensions. This explains why the colloidal structure formed in the case of (1:1) suspension that includes an evaporative thinning duration of 14.76 s is more ordered than the structure formed in the case of either (3:2) suspension or (3:1) suspension. However, both the (3:2) and the (3:1) suspensions have a longer evaporative thinning duration; 15.28 s and 20.01 s respectively, than that of the (1:1) suspension (14.79 s). This is attributed to the multistep evaporation mechanism involved in the case of the water – ethanol (1:1) mixture. This multistep evaporation mechanism creates an evaporation-induced self-assembly (EISA) that leads to the formation of a more ordered structure. Multistep evaporation of water in the water – ethanol (1:1) mixture provides different evaporation stages for different water components; network water, intermediate water and multimer water [86]. This mixture develops the optimum stepwise evaporation process that gives particles the opportunity to be self-organised gradually during several evaporation stages. On the other hand, the uniform evaporation in either water – ethanol (3:1) or pure water limits the evaporation process and leads to the formation of a less ordered colloidal structure.

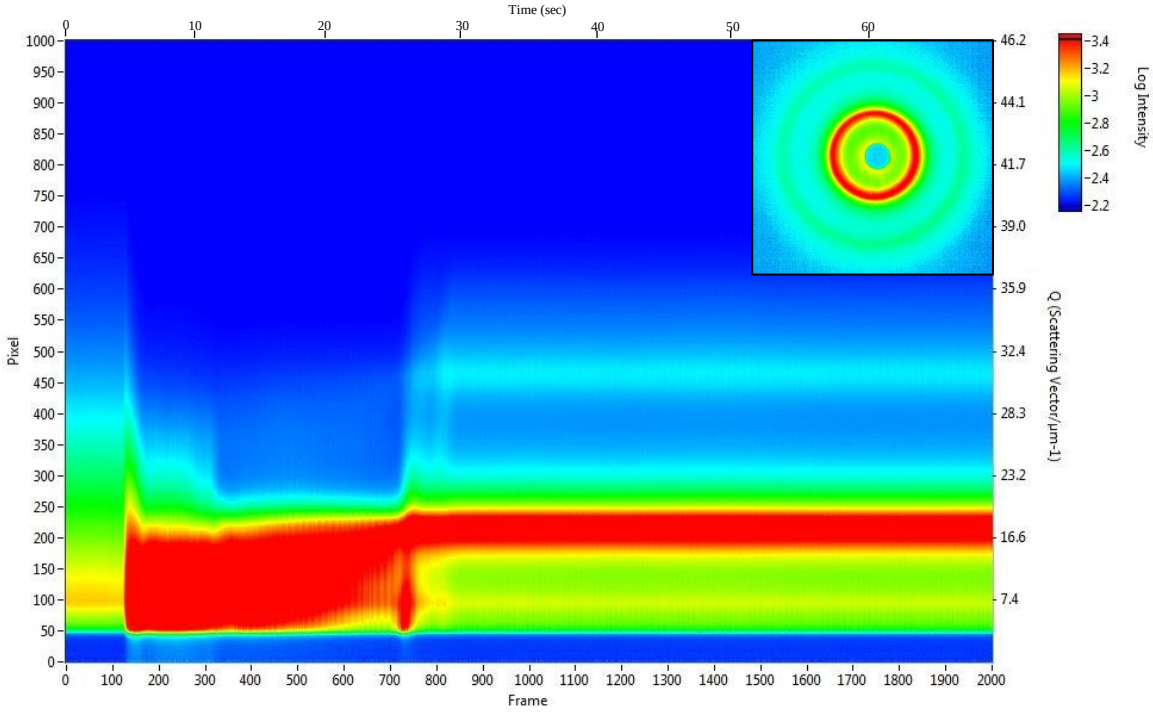

Figure 7.8: In-situ laser scattering chart for a 25 wt. % silica colloidal suspension in a water: ethanol mixture (3:2) spun-cast at 1000 rpm.

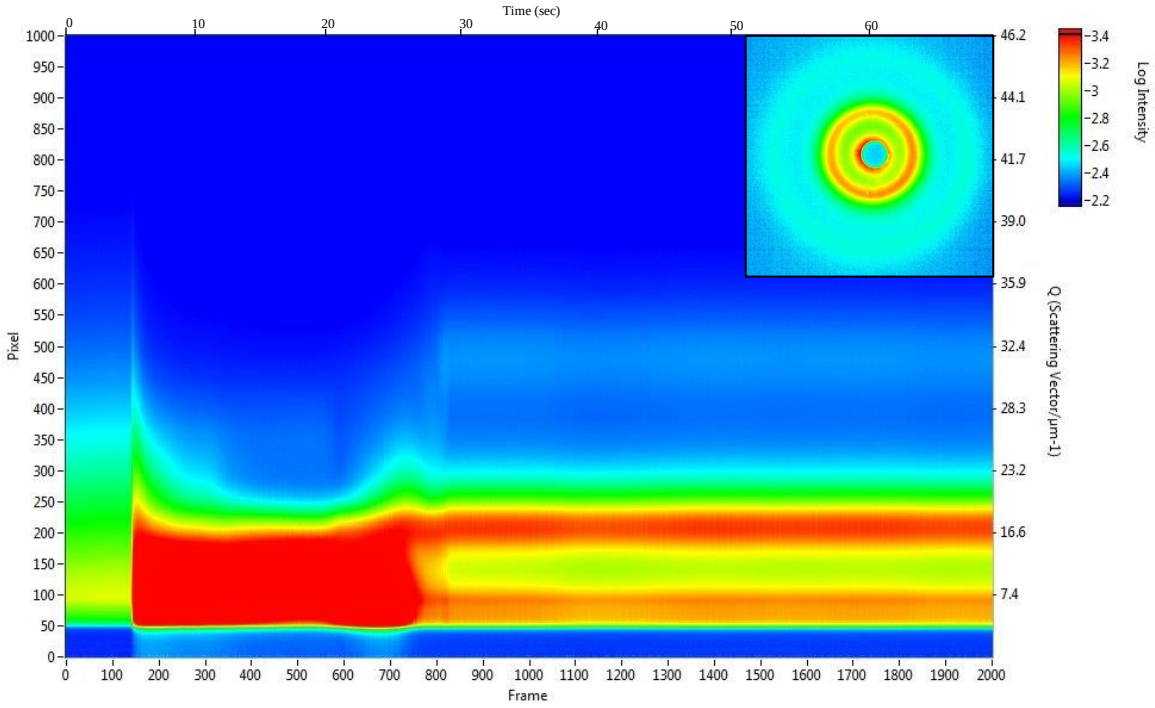

Figure 7.9: In-situ laser scattering chart for a 25 wt. % silica colloidal suspension in a water: ethanol mixture (3:1) spun-cast at 1000 rpm.

Table 7.1: Effect of solvent volatility on the hexagonal close-packing percentage (HCP %) of the final colloidal crystals after spin coating 25 wt. % Silica colloidal suspensions at 1000 rpm.

No.	Concentration , Wt. %	Speed, rpm	Solvent Nature	Evaporative Thinning Duration, sec	Coverage Area %	HCP %
1	25 %	1000	Pure Water	22.0	98.5	72.4
2			Water – Ethanol 3:1	20.01	75.4	64.5
3			Water – Ethanol 3:2	15.28	89.9	69.1
4			Water – Ethanol 1:1	14.76	99.2	84.5
5			Water – Ethanol 2:3	14.49	87.3	51.2
6			Water – Ethanol 1:3	11.0	Multilayer	43.2
7			Pure Ethanol	8.65	Multilayer	21.0

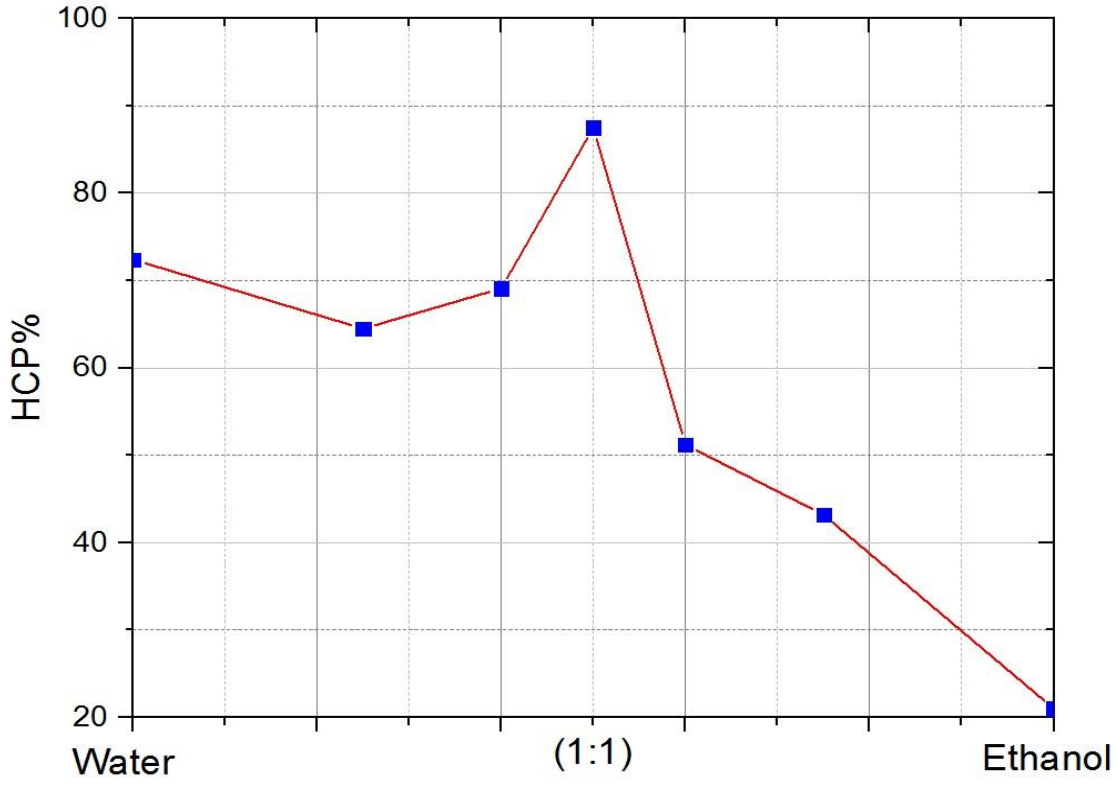

Figure 7.10: The impact of the water ratio with respect to Ethanol in the solvent mixture on the hexagonal close-packing percentage (HCP %) of the final colloidal crystals formed at the end of the spin coating process.

Data given in Figure 7.10 shows that water – ethanol (3:1) mixture produces a monolayer colloidal thin film with HCP % of 64.5% and an area coverage percentage of 75.4 %. These characterizations confirmed that introducing ethanol increases the solvent volatility and induces stronger shear forces. Thus, colloidal crystals with a lower ordering quality obtained with respect to quality obtained in the case of pure water as a solvent. As water amount increases in the mixture, both coverage area percentage and the HCP % were increased giving the highest ordering quality in the case of water – ethanol (1:1) mixture, as shown in Figure 7.10. The addition of water beyond this point was found to decrease the colloidal ordering quality forming multi-layered colloidal crystals. These results confirmed that colloidal ordering quality in the case of water – ethanol mixtures is governed by the multistep evaporation of water. This induces an evaporative-induced self-assembly (EISE) mechanism that helps particles to be self-ordered properly before complete evaporation of the solvent medium.

Chapter 8.
Conclusions and Future Work

8.0 Summary

In this thesis, I have investigated the colloidal self-assembly process that takes place during spin coating of colloidal suspensions either *ex-situ* or *in-situ* (in real time). Firstly, I have developed an *ex-situ* setup and processing to study the important factors that significantly affect the colloidal ordering quality, with respect to both coverage area percentages occupied by particles and the hexagonal close-packing percentages, in the final colloidal crystals. *Ex-situ* investigations helped to optimise the spin coating of colloidal suspensions from volatile solvents. Optimising the spin coating process facilitates the fabrication of highly ordered monolayer colloidal crystals. In addition, *ex-situ* stage highlighted the most important parameters that have the greatest impacts on the packing quality of colloidal crystals during the spin coating process.

Secondly, I have developed a new laser scattering setup to allow a real-time studying for the colloidal self-assembly taking place during the spin coating process of the colloidal silica suspensions. The *in-situ* laser scattering setup enables capture clear images of the laser scattering patterns refracted through the colloidal samples during spin coating process at a high frame rate of 29 fps. LabVIEW software was developed to enable tracking of any changes in laser scattering intensity with respect to time. *In-situ* data develops a deep insight into the spin coating process that enables real-time investigations of the factors that govern the colloidal self-assembly leading to the formation of the final colloidal crystals.

8.1 Conclusions and Future Work

Spinning speed was the first parameter to be investigated using the *in-situ* laser scattering setup. The *in-situ* setup enables to precisely visualise the onset of motor rotation, shear thinning stage, duration of the evaporative thinning stage and stepwise evolution of the final colloidal structure. *In situ* setup enables to link the spinning speed together with the duration of the evaporative thinning stage. The evaporative thinning stage is the stage at which solvent thins gradually and particles are self-assembled. The longer the evaporative thinning the higher the chance available for self-organisation of

particles in the colloidal array. As expected, increasing the rotational speed increases the evaporation rate of water. This limits the time available for colloidal particles to be self-organised properly before complete evaporation of water. As a result, increasing the spinning speed decreases the colloidal ordering quality dramatically in the final monolayer thin film. This result coincides with the *ex-situ* data at which 500 rpm produced the highest ordered colloidal structure with a coverage area percentage of 99.6% and a hexagonal close-packing percentage of 78.1%. These results confirm McLachlan's conclusions [45] regarding to the effect of liquid evaporation rate on the colloidal ordering quality of the final monolayer colloidal crystals. However, in this work I've used the rotational speed to control the solvent evaporation rate instead of temperature, which had been used by McLachlan in 2004.

The solids content was the second parameter to be investigated using the *in-situ* laser scattering setup. Herein, the effect of changing the concentration of colloidal silica particles on the colloidal self-assembly was studied. *In-situ* results showed that more concentrated suspensions produce sharper laser scattering patterns at the end of the spin coating process. Sharper laser scattering indicates the formation of a colloidal structure with a higher ordering quality. In addition, it was found that the shear thinning stage, evaporative thinning stage and stepwise structure formation stage appeared earlier at relatively higher concentrations. This could be attributed to the packing constraints induced at the higher concentrations of particles in the colloidal suspensions.

Ex-situ data showed that 25 wt. % silica colloidal suspensions spun cast at 1000 rpm developed highly ordered colloidal crystals with a coverage area percentage of 99.6 %. On the other hand, spin coating of 5 wt. % silica colloidal suspensions at the same speed led to the formation of an ordered colloidal islands separated by large voids with a total coverage area percentage of 43.4 %. *Ex-situ* results together with *in-situ* data confirm that higher concentrations of colloidal particles increase the volume fraction of colloidal suspension system during the self-assembly process. Consequently, the inter-particle distance between colloids in the colloidal suspension decreases. This helps particles to reorder themselves more uniformly during the spin

coating process. These conclusions coincide with Toolan's results [75], using the stroboscopic technique, that better organisation of colloids during the colloidal self-assembly is governed by the packing constraints that helps to fabricating regular structures of highly ordered particles. This suggests the following;

Future work (1): The *in situ* investigations for the colloidal self-assembly during spin coating process took place in this thesis were carried out using spherical silica particles with an average particle size of 1550 nm. Investigating colloidal suspensions composed of smaller particles sizes under the resolution of the microscopy; 1000 nm, 700 nm and 300 nm could be interesting.

The solvent volatility was the third parameter I have investigated using the *in-situ* laser scattering setup. Real-time data, as shown in Figure 8.1, showed that evaporative thinning stage duration in case of pure water was 22.0 s. While, when water was replaced by pure ethanol the evaporative thinning duration was found to be 8.65 s. Limited time and excessive shear forces induced by the fast evaporation of ethanol are the responsible for the formation of disordered colloidal structures in this case, as shown in Figure 8.2. Interestingly, *in-situ* charts given in Figure 8.3 showed for the first-time different peaks in the evaporative thinning stage in case of water – ethanol mixtures. These peaks are attributed to different stages of water evaporation in the evaporative thinning itself called a multistep evaporation. This conclusion coincides with Innocenzi's conclusions [86] regarding the evaporation mechanism of water in the water – ethanol mixtures. Multistep evaporation of water in the water – ethanol mixture develops different stages with gradual evaporation rates of water. This develops an evaporative-induced self-assembly (EISA) that gives colloidal particles the opportunity to be self-organised during a prolonged gradual evaporative thinning stage. This explains the reason why water – ethanol (1:1) mixture is the optimum solvent mixture that forms the highest ordered colloidal structure with a hexagonal close-packing percentage of 85.0 %. However, this mixture contains less amount of water when compared to either water – ethanol (3:2) or (3:1) mixtures which have longer evaporative thinning stages. This suggests the following as a future work;

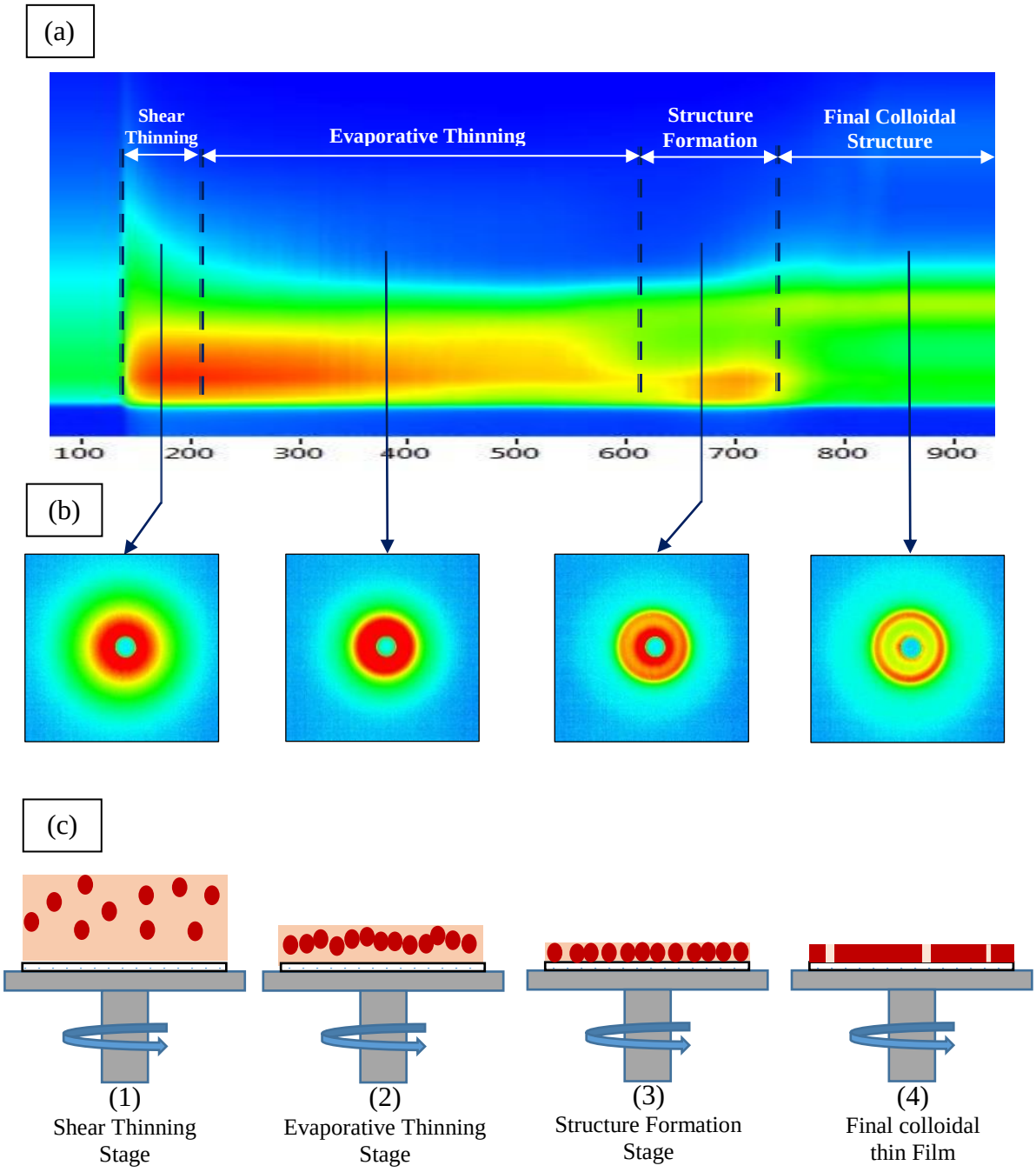

Figure 8.1: Schematic model describing the colloidal self-assembly taking place during spin coating from pure water as the volatile solvent medium; (a) combined laser scattering chart collected during spin coating process, (b) 2D-radial integration patterns and (c) Representation model describing the colloidal self-assembly during the evaporation of water.

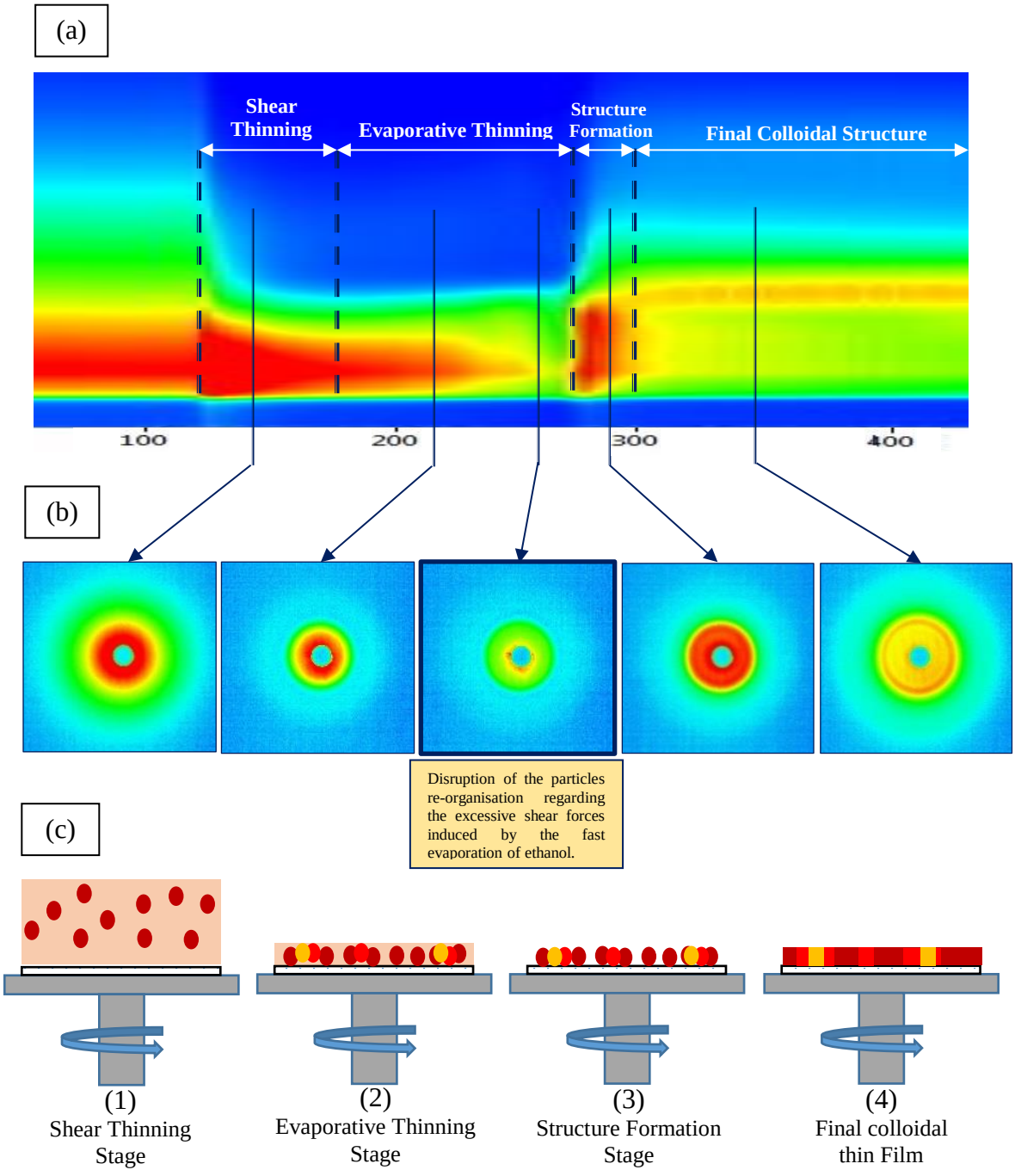

Figure 8.2: Schematic model describing the colloidal self-assembly taking place during spin coating from pure ethanol as the volatile solvent medium; (a) combined laser scattering chart collected during spin coating process, (b) 2D-radial integration patterns and (c) Representation model describing the colloidal self-assembly during the evaporation of pure ethanol.

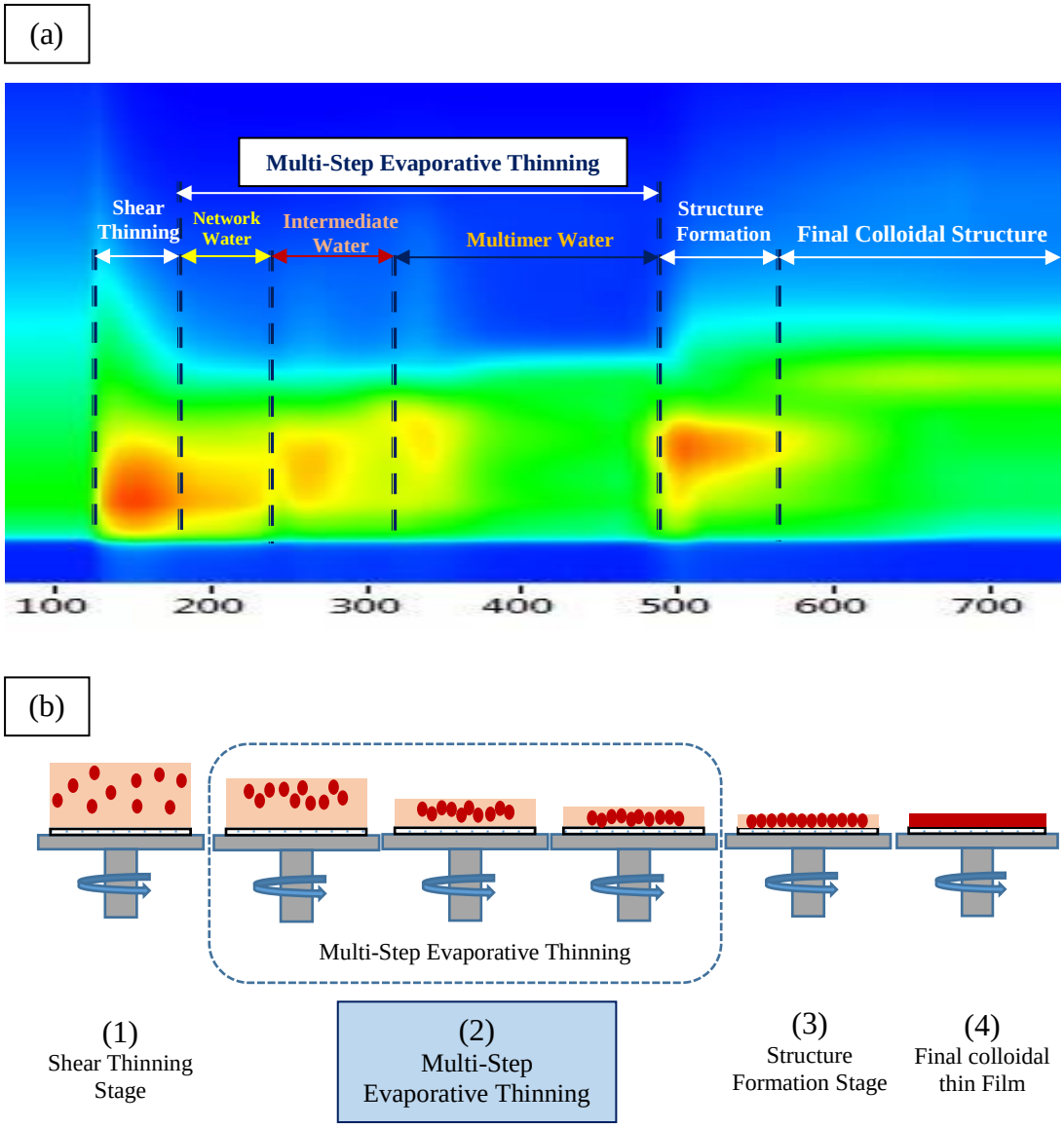

Figure 8.3: Schematic model describing the colloidal self-assembly taking place during spin coating from water – ethanol (1:1) mixture as the volatile solvent medium; (a) combined laser scattering chart collected during spin coating process, (b) 2D-radial integration patterns and (c) Representation model describing the impact of the multistep evaporation of water on the rearrangement of silica colloids.

Future work (2): Solvent volatility impact during spin coating of colloidal suspensions were examined using pure water, pure ethanol and different water – ethanol mixtures. Future work should aim to examine other binary solvent systems such as ethylene glycol – water mixtures and ethylene glycol – ethanol mixtures. In addition, the impact of tertiary systems such as ethylene glycol – water – ethanol mixtures could be investigated using the new *in situ* laser scattering setup.

Jiang [9] reported that the standard deviation of colloids is a crucial factor in the ordering quality of the fabricated arrays. Based on his work, particles with a polydispersity less than 8% develops brilliant colours when being illuminated with white light due to the highly-ordered structure, while particles with a polydispersity higher than 8% were white and opaque. In this thesis, I've investigated the impact of polydispersity on colloidal ordering quality using the developed *ex-situ* setup. Results showed that HCP % is inversely proportional with the polydispersity value. Particles with a polydispersity of 4% developed ordered structure with HCP % of 73.2%. On the other hand, particles possess a polydispersity of 11% lead to the fabrication of irregular structures with a HCP % of 47.6%. Figure 8.4 develops a schematic diagram that summaries the impact of polydispersity on the colloidal packing quality.

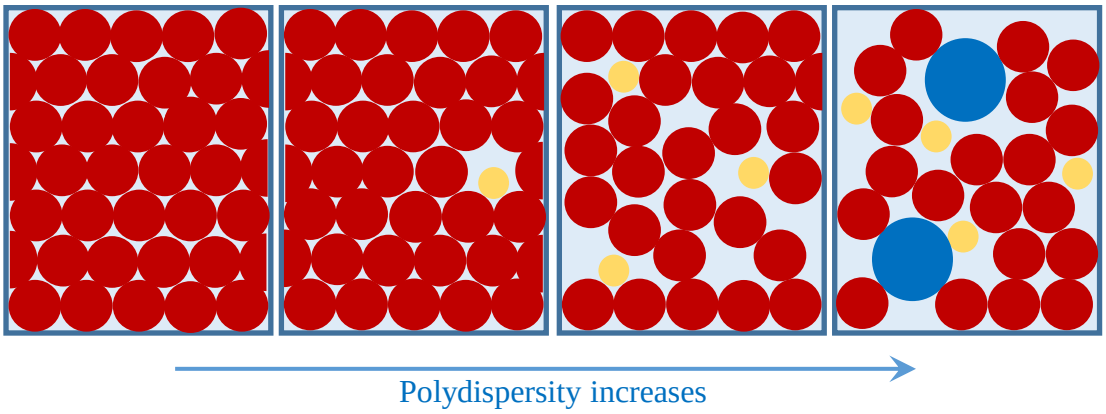

Figure 8.4: Schematic diagram showing the impact of particles polydispersity on the colloidal ordering quality of the final colloidal crystals fabricated at the end of spin coating. Higher the polydispersity induces larger degree of distortion in colloidal ordering pattern.

The impact of settling time on the particles packing quality was another factor under investigation using the *ex-situ* setup. Results showed that the settling time governs the particles sedimentation rate. This initiates the nucleation stage even before the start of the spinning which could favours the ordering mechanism. It was found that increasing the settling time before the onset of motor rotational motion significantly affect the final colloidal structure. Longer settling times increases the coverage area percentage occupied by particles. However, uncontrollable duration of the settling time develops multi-layered colloidal crystals. Figure 8.5 gives a schematic model showing the impact of settling time duration on the pre-ordering of colloids before starting the spinning motion.

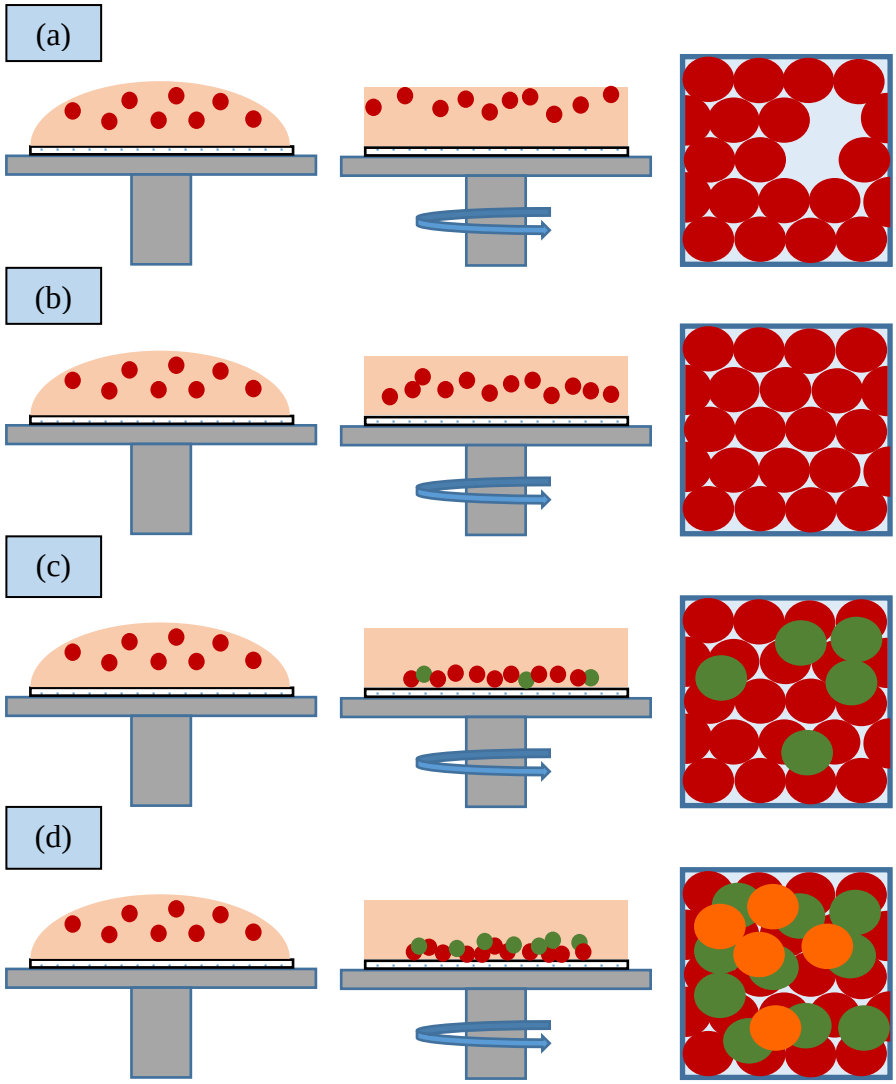

Figure 8.5: Schematic model describing the effect of prolonged settling time before the onset of rotation upon the self-assembly of colloids; (a) 0 s develops a regular structure with empty voids, (b) 30 s develops highly ordered structure, (c) 60 s fabricates some multi-layered areas and (d) 120 s produces a randomly multi-layered colloidal crystal.

Furthermore, the dependency of the coverage area percentage occupied by particles upon the acceleration rate was studied during the *ex-situ* stage. It was found that coverage area percentage is inversely proportional to the acceleration rate. This could be attributed to the increased shear forces accompanying the faster acceleration rates. As shear forces increases, particles loss the opportunity to explore properly the optimum sites to occupy during the colloidal self-assembly. This leads to the formation of irregular colloidal structures with relatively lower coverage area percentages. Figure 8.6 illustrates the effect of acceleration rate magnitude on the distribution of particles on the substrate at the early stage of the spin coating.

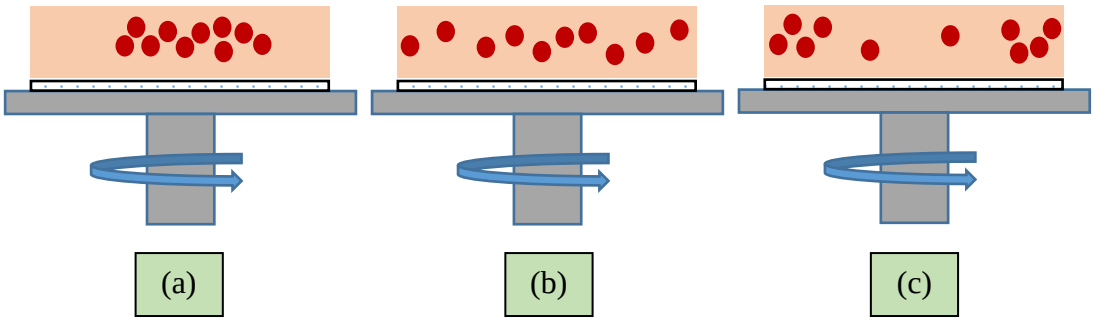

Figure 8.6: Schematic diagram describing the consequences of increasing the acceleration rate upon the distribution of particles on the substrate; (a) at low acceleration rates particles are evenly distributing around the centre, (b) at intermediate acceleration rates particles tend to pulled away from the substrate centre and (c) at fast acceleration rates particles are distributed at the edges rather than near the substrate centre.

Future work (3): My *in-situ* investigations for the colloidal self-assembly during spin coating process examined only the effect of spinning speed, solids content and solvent volatility. Future experiments should aim to study the effect of other important factors such as particles size distribution (polydispersity), settling time, acceleration rate, viscosity, and substrate shape and size.

Future work (4): *Ex situ* and *in situ* investigations examined only the self-assembly that took place during spin coating of colloidal suspensions. Future experiments should examine different types of polymer particles such as PMMA and PS. In addition, the *in-situ* setup should aim to examine different types of polymer blends to investigate the mechanisms that govern the crystallisation, topography and phase separation during the spin coating process of polymer blends.

Future work (5): Characterisation that took place during the *ex-situ* and *in-situ* investigations for the colloidal ordering quality of the fabricated monolayer colloidal crystals examined only area coverage percentage occupied by particles on substrate and the hexagonal close-packing density. However, studying the alignment and symmetry along the whole length scale could be crucial to fully characterise the colloidal ordering quality of these colloidal structures. Also, classification of dislocations as either point defects or line defects may develop important information regarding the cracks formation and how to be stabilised during the colloidal self-assembly through the spin coating process.

References

References

[1] P. Jiang and M. J. McFarland, “Large-scale fabrication of wafer-size colloidal crystals, macroporous polymers and nanocomposites by spin-coating,” *J. Am. Chem. Soc.*, vol. 126, no. 42, pp. 13778–13786, 2004.

[2] Z. Li, J. Wang, and Y. Song, “Self-assembly of latex particles for colloidal crystals,” *Particuology*, vol. 9, no. 6, pp. 559–565, Dec. 2011.

[3] and J. H. S. N. Ozer, H. Demiryont, “Optical properties of sol-gel spin-coated TiO2 films and comparison of the properties with ion-beam-sputtered films,” *Appl. Opt. 30, 3661-3666*.

[4] D. H. Everett., “Basic Principles of Colloid Science,” *R. Soc. Chem. London*, 1988.

[5] W. R. S. W. B. Russel, D. A. Saville, “Colloidal Dispersions,” *Cambridge Univ. Press. Cambridge.*, 1989.

[6] R. J. Hunter., “Introduction to Modern Colloid Science,” *Univ. Press. Oxford .*, 1993.

[7] J. Villa and A. Warshel, “Feature article,” pp. 7887–7907, 2001.

[8] J. Veinot, H. Yan, S. Smith, J. Cui, Q. Huang, and T. Marks, “Fabrication and properties of organic light-emitting ‘nanodiode’ arrays,” *Nano Lett.*, vol. 2, no. 4, pp. 333–335, 2002.

[9] P. Jiang, J. Bertone, and V. Colvin, “Single-crystal colloidal multilayers of controlled thickness,” *Chem. Mater.*, vol. 11, no. 25, pp. 2132–2140, 1999.

[10] T. Endo, Y. Yanagida, and T. Hatsuzawa, “Colorimetric detection of volatile organic compounds using a colloidal crystal-based chemical sensor for environmental applications,” *Sensors Actuators, B Chem.*, vol. 125, no. 2, pp. 589–595, 2007.

[11] J. Chen, P. Dong, D. Di, C. Wang, H. Wang, J. Wang, and X. Wu, “Controllable fabrication of 2D colloidal-crystal films with polystyrene nanospheres of various diameters by spin-coating,” *Appl. Surf. Sci.*, vol. 270, pp. 6–15, 2013.

[12] J. Accepted, “Hemispherical Arrays of Colloidal Crystals Fabricated by Transfer Printing,” 2013.

[13] P. N. Pusey, W. van Megen, and W. van Megen, “Phase behavior of concentrated suspensions of nearly hard colloidal spheres,” *Nature*, vol. 320, no. 6060, pp. 340–342, 1986.

[14] B. J. Ackerson and N. a. Clark, “Shear-induced melting,” *Phys. Rev. Lett.*, vol. 46, no. 2, pp. 123–126, 1981.

[15] X. Ye and L. Qi, “Recent advances in fabrication of monolayer colloidal crystals and their inverse replicas,” *Sci. China Chem.*, vol. 57, no. 1, pp. 58–69, 2014.

[16] P. N. Pusey and W. van Megen, “Observation of a Glass transition in suspension of spherical colloidal particles,” *Phys. Rev. Lett.*, vol. 59, no. 18, pp. 2083–2086, 1987.

[17] J. Zhu, M. Li, R. Rogers, and W. Meyer, “Crystallization of hard-sphere colloids in microgravity,” *Nature*, vol. 387, no. June, pp. 883–885, 1997.

[18] M. Holgado, F. García-Santamaría, a. Blanco, M. Ibisate, a. Cintas, H. Míguez, C. J. Serna, C. Molpeceres, J. Requena, a. Mifsud, F. Meseguer, and C. López, “Electrophoretic deposition to control artificial opal growth,” *Langmuir*, vol. 15, no. 14, pp. 4701–4704, 1999.

[19] A. L. Rogach, N. A. Kotov, D.S.Koktysh, J. W. Ostrander, G. A. Ragoisha, D. S. Koktysh, J. W. Ostender, and G. A. Ragoisha, “Electrophoretic Deposition of Latex-Based 3D Colloidal Photonic Crystals: A Technique for Rapid Production of High-Quality Opals,” *Chem. Mater*, vol. 12, no. 9, pp. 2721–2726, 2000.

[20] P. Kumnorkaew, Y. K. Ee, N. Tansu, and J. F. Gilchrist, “Investigation of the deposition of microsphere monolayers for fabrication of microlens arrays,” *Langmuir*, vol. 24, no. 21, pp. 12150–12157, 2008.

[21] Q. B. Meng, C. H. Fu, Y. Einaga, Z. Z. Gu, a. Fujishima, and O. Sato, “Assembly of highly ordered three-dimensional porous structure with nanocrystalline TiO2 semiconductors,” *Chem. Mater.*, vol. 14, no. 1, pp. 83–88, 2002.

[22] A. Stein, B. E. Wilson, and S. G. Rudisill, “Design and functionality of colloidal-crystal-templated materials—chemical applications of inverse opals,” *Chem. Soc. Rev.*, vol. 42, no. 7, pp. 2763–2803, 2013.

[23] J. Rybczynski, U. Ebels, and M. Giersig, “Large-scale, 2D arrays of magnetic nanoparticles,” *Colloids Surfaces A Physicochem. Eng. Asp.*, vol. 219, no. 1–3, pp. 1–6, 2003.

[24] S. M. Weekes, F. Y. Ogrin, W. a. Murray, and P. S. Keatley, “Macroscopic arrays of magnetic nanostructures from self-assembled nanosphere templates,” *Langmuir*, vol. 23, no. 3, pp. 1057–1060, 2007.

[25] M. a. Ray and L. Jia, “Micropatterning by non-densely packed interfacial colloidal crystals,” *Adv. Mater.*, vol. 19, no. 15, pp. 2020–2022, 2007.

[26] P. I. Stavroulakis, N. Christou, and D. Bagnall, “Improved deposition of large scale ordered nanosphere monolayers via liquid surface self-assembly,” *Mater. Sci. Eng. B*, vol. 165, no. 3, pp. 186–189, 2009.

[27] C. Arcos, K. Kumar, W. González-Viñas, R. Sirera, K. M. Poduska, and A. Yethiraj, “Orientationally correlated colloidal polycrystals without long-range positional order,” *Phys. Rev. E*, vol. 77, no. 5, p. 50402, 2008.

[28] G. R. S. of Britain, “Thomas Graham 1861,” *Vasa*, vol. 151, no. 1861, pp. 183–224, 1894.

[29] *Manipulation of colloidal crystallization*. PhD Thesis, Debye Institute for NanoMaterials Science, Utrecht University, Nonember 2008.

[30] R. Al Jones, *Soft Condensed Matter*. 2002.

[31] R. Brown, “Character and description of Kingia: a new genus of plants found on the south-west coast of New Holland, with observations on the structure of its unimpregnated ovulum, and on the female flower of Cycadeae and Coniferae.,” *Linn. Soc. (London).*, 1827.

[32] C. C. Beads, D. Technique, and T. Application, “Colloidal crystals,” pp. 592–596, 2008.

[33] P. Habdas and E. R. Weeks, “Video microscopy of colloidal suspensions and colloidal crystals,” *Curr. Opin. Colloid Interface Sci.*, vol. 7, no. 3–4, pp. 196–203, 2002.

[34] S. Auer and D. Frenkel, “Suppression of crystal nucleation in polydisperse colloids due to increase of the surface free energy.,” *Nature*, vol. 413, no. 6857, pp. 711–713, 2001.

[35] A. P. Gast and W. B. Russel, “Simple Ordering in Complex Fluids,” *Phys. Today*, vol. 51, no. 12, p. 24, 1998.

[36] D. Thomas and W. Toolan, “In situ studies of polymer films,” no. May, 2014.

[37] L. V. Woodcock, “Entropy difference between the face-centred cubic and hexagonal close-packed crystal structures,” *Nature*, vol. 385, no. 6612. pp. 141–143, 1997.

[38] S.-C. Mau and D. Huse, “Stacking entropy of hard-sphere crystals,” *Phys. Rev. E*, vol. 59, no. 4, pp. 4396–4401, 1999.

[39] X. Wang, T. S. Bailey, and X. Qian, “Inverse Colloidal Crystal Membranes: Formation, Surface modification and Applications,” PhD Thesis, Colorado State University, 2010.

[40] Y. K. Koh and C. C. Wong, “In situ monitoring of structural changes during colloidal self-assembly.,” *Langmuir*, vol. 22, no. 5, pp. 897–900, 2006.

[41] N. Denkov, O. Velev, P. Kralchevski, I. Ivanov, H. Yoshimura, and K. Nagayama, “Mechanism of formation of two-dimensional crystals from latex particles on substrates,” *Langmuir*, vol. 8, no. 12, pp. 3183–3190, 1992.

[42] P. a. Kralchevsky and N. D. Denkov, “Capillary forces and structuring in layers of colloid particles,” *Curr. Opin. Colloid Interface Sci.*, vol. 6, no. 4, pp. 383–401, 2001.

[43] “A. B. El Bediwi, W. J. Kulnis, Y. Luo, D. Woodland and W. N. Unertl (1994). Distributions of Latex Particles Deposited from Water Suspensions. MRS Proceedings, 372, 277 doi:10.1557/PROC-372-277.”

[44] J. 2000 Deegan, “Contact line deposits in an evaporating drop,” *Phys. Rev. E - Stat. Physics, Plasmas, Fluids, Relat. Interdiscip. Top.*, vol. 62, no. 1 B, pp. 756–765, 2000.

[45] M. A. McLachlan, N. P. Johnson, R. M. De La Rue, and D. W. McComb, “Thin film photonic crystals: synthesis and characterisation,” *J. Mater. Chem.*, vol. 14, no. 2, pp. 144–150, 2004.

[46] A. S. Dimitrov and K. Nagayama, “Continuous Convective Assembling of Fine Particles into Two-Dimensional Arrays on Solid Surfaces,” *Langmuir*, vol. 12, no. 5, pp. 1303–1311, 1996.

[47] Y. K. Koh, C. H. Yip, Y. M. Chiang, and C. C. Wong, “Kinetic stages of single-component colloidal crystallization,” *Langmuir*, vol. 24, no. 12, pp. 5245–5248, 2008.

[48] I. M. Krieger and F. M. O’Neill, “Diffraction of light by arrays of colloidal spheres,” *J. Am. Chem. Soc.*, vol. 90, no. 12, pp. 3114–3120, 1968.

[49] C. D. Dushkin, K. Nagayama, T. Miwa, and P. a Kralchevskyt, “Colored Multilayers from Transparent Submicrometer Spheres,” *Langmuir*, vol. 9, no. 8, pp. 3695–3701, 1993.

[50] C. D. Dushkin and H. Yoshimura, “Nucleation and Growth of Colloidal Crystals,” *Phys. Rev. Lett.*, vol. 57, no. 14, p. 1733, 1986.

[51] a. S. Dimitrov, C. D. Dushkin, H. Yoshimura, and K. Nagayama, “Observations of Latex Particle Two-Dimensional-Crystal Nucleation in Wetting Films on Mercury, Glass and Mica,” *Languir*, vol. 10, no. 7, pp. 432–440, 1994.

[52] M. Yamaki, J. Higo, and K. Nagayama, “Size-Dependent Separation of Colloidal Particles in 2-Dimensional Convective Self-Assembly,” *Langmuir*, vol. 11, no. 8, pp. 2975–2978, 1995.

[53] N. Metropolis, A. W. Rosenbluth, M. N. Rosenbluth, A. H. Teller, and E. Teller, “Equation of State Calculations by Fast Computing Machines,” *J. Chem. Phys.*, vol. 21, no. 6, pp. 1087–1092, 1953.

[54] K. Nagayama, “Two-dimensional self-assembly of colloids in thin liquid films,” *Colloids Surfaces A Physicochem. Eng. Asp.*, vol. 109, pp. 363–374, 1996.

[55] R. D. Deegan, O. Bakajin, T. F. Dupont, G. Huber, S. R. Nagel, and T. a Witten, “Capillary flow as the cause of ring stains from dried liquid drops,” *Lett. to Nat.*, vol. 389, pp. 827–829, 1997.

[56] S. H. Im, M. H. Kim, and O. O. Park, “Thickness control of colloidal crystals with a substrate dipped at a tilted angle into a colloidal suspension,” *Chem. Mater.*, vol. 15, no. 9, pp. 1797–1802, 2003.

[57] S. H. Im, T. Herricks, Y. T. Lee, and Y. Xia, “Synthesis and characterization of monodisperse silica colloids loaded with superparamagnetic iron oxide nanoparticles,” vol. 401, pp. 19–23, 2005.

[58] L. K. Teh, N. K. Tan, C. C. Wong, and S. Li, “Growth imperfections in three-dimensional colloidal self-assembly,” *Appl. Phys. A Mater. Sci. Process.*, vol. 81, no. 7, pp. 1399–1404, 2005.

[59] Y. Koh, Y. Chiang, and C. Wong, “Ordering Control of Self-Assembled Colloidal Crystals,” *Dspace.Mit.Edu*, pp. 1–4, 2007.

[60] L. Meng, H. Wei, A. Nagel, B. J. Wiley, L. E. Scriven, and D. J. Norris, “The role of thickness transitions in convective assembly,” *Nano Lett.*, vol. 6, no. 10, pp. 2249–2253, 2006.

[61] M. Ishii, M. Harada, and H. Nakamura, “In situ observations of the self-assembling process of colloidal crystalline arrays,” *Soft Matter*, vol. 3, no. 7, p. 872, 2007.

[62] Q. Yan, Z. Zhou, and X. S. Zhao, “Inward-growing self-assembly of colloidal crystal films on horizontal substrates,” *Langmuir*, vol. 21, no. 7, pp. 3158–3164, 2005.

[63] Q. Yan, L. Gao, V. Sharma, Y. M. Chiang, and C. C. Wong, “Particle and substrate charge effects on colloidal self-assembly in a sessile drop,” *Langmuir*, vol. 24, no. 20, pp. 11518–11522, 2008.

[64] K. W. Tan, G. Li, Y. K. Koh, Q. Yan, and C. C. Wong, “Layer-by-layer growth of attractive binary colloidal particles.,” *Langmuir*, vol. 24, no. 17, pp. 9273–8, 2008.

[65] R. J. "Foundations of C. S. C. . N. Y. (1987): 244-250. Hunter, “No Title.”

[66] K. W. Tan, Y. K. Koh, Y.-M. Chiang, and C. C. Wong, “Particulate mobility in vertical deposition of attractive monolayer colloidal crystals.,” *Langmuir*, vol. 26, no. 10, pp. 7093–100, 2010.

[67] spin coating-basic Lab., “Spin coating,” vol. 5, no. 12, p. 62, Dec. 2002.

[68] J. Chen, P. Dong, D. Di, C. Wang, H. Wang, J. Wang, and X. Wu, “Controllable fabrication of 2D colloidal-crystal films with polystyrene nanospheres of various diameters by spin-coating,” *Appl. Surf. Sci.*, vol. 270, pp. 6–15, Apr. 2013.

[69] A. G. Emslie, F. T. Bonner, and L. G. Peck, “Flow of a viscous liquid on a rotating disk,” *J. Appl. Phys.*, vol. 29, no. 5, pp. 858–862, 1958.

[70] D. Meyerhofer, “Characteristics of resist films produced by spinning,” *J. Appl. Phys.*, vol. 49, no. 7, p. 3993, 1978.

[71] A. Mihi, M. Ocaña, and H. Míguez, “Oriented colloidal-crystal thin films by spin-coating microspheres dispersed in volatile media,” *Adv. Mater.*, vol. 18, no. 17, pp. 2244–2249, 2006.

[72] V. Sharma, Q. Yan, C. C. Wong, W. C. Carter, and Y.-M. Chiang, “Controlled and rapid ordering of oppositely charged colloidal particles.,” *J. Colloid Interface Sci.*, vol. 333, no. 1, pp. 230–6, 2009.

[73] M. Giuliani, W. González-Viñas, K. M. Poduska, and A. Yethiraj, “Dynamics of crystal structure formation in spin-coated colloidal films,” *J. Phys. Chem. Lett.*, vol. 1, pp. 1481–1486, 2010.

[74] D. T. W. Toolan, R. Hodgkinson, and J. R. Howse, “Stroboscopic microscopy-direct imaging of structure development and phase separation during spin-coating,” *J. Polym. Sci. Part B Polym. Phys.*, vol. 52, no. 1, pp. 17–25, Jan. 2014.

[75] D. T. W. Toolan, S. Fujii, S. J. Ebbens, Y. Nakamura, and J. R. Howse, “On the mechanisms of colloidal self-assembly during spin-coating.,” *Soft Matter*, vol. 10, pp. 8804–8812, 2014.

[76] A. F. Routh and W. B. Zimmerman, “Distribution of particles during solvent evaporation from films,” *Chem. Eng. Sci.*, vol. 59, no. 14, pp. 2961–2968, 2004.

[77] Y. Reyes and Y. Duda, “Modeling of drying in films of colloidal particles.,” Langmuir, vol. 21, no. 15, pp. 7057–60, 2005.

[78] http://toruhara.page.tl/, "Electrochemistry: The Basic of the basic”.

[79] Ph.D, HORIBA Scientific, “Introduction to Laser Diffraction Jeffrey Bodycomb,” 2016. [Online]. Available: www.horiba.com/us/particle.

[80] MEE, “Handbook of Analytical Methods for Materials,” pp. 39–42, 2014.

[81] E. Bash, “PREPARATION AND CHARACTERIZATION OF SPIN-COATED COLLOIDAL TEMPLATES AND PATTERNED ELECTRODEPOSITED COBALT,” PhD Propos., vol. 1, 2015.

[82] “Enhanced Flame Retardant Polymer Nanocomposites Sherif Elbasuney,” PhD Propos. Univ. Nottingham, 2012.

[83] M. Park, “NanoSight Software Operating Manual,” pp. 1–88, 2012.

[84] J. Uhlig, “Nanoparticle Tracking Analysis . NanoSight Limited The NanoSight System is Widely Applicable.”

[85] Malvern, “MAL - DIF Mastersizer 3000-3000E IESMAT, SMARTER PARTICLE SIZING Brochure.,” p. 182, 2013.

[86] P. Innocenzi, L. Malfatti, S. Costacurta, T. Kidchob, M. Piccinini, and A. Marcelli, “Evaporation of ethanol and ethanol-water mixtures studied by time-resolved infrared spectroscopy,” J. Phys. Chem. A, vol. 112, no. 29, pp. 6512–6516, 2008.